Measurements of W^+W^- production cross sections in pp collisions at $\sqrt{s}$ = 13 TeV with the ATLAS detector

A thesis submitted for the degree of
Doctor of Philosophy

Jack Cameron MacDonald
Supervisor: Dr Kristin Lohwasser

Department of Physics and Astronomy
The University of Sheffield

31st March 2022

Abstract

In this thesis, measurements of cross sections for the production of pairs of oppositely charged W bosons in association with hadronic jets are presented. Integrated and differential fiducial cross sections are obtained using data corresponding to an integrated luminosity of $139\,\mathrm{fb}^{-1}$ collected in $\sqrt{s} = 13\,\mathrm{TeV}$ proton-proton collisions with the ATLAS detector. These measurements provide an important test of the Standard Model, in particular of the electroweak theory and perturbative quantum chromodynamics. In addition, a precise understanding of W boson pair production is required in measurements of resonant Higgs boson production, and in searches for physics beyond the Standard Model, where it constitutes a dominant background. Events are selected with exactly one electron and one muon of opposite charge, and different requirements are placed on the number of hadronic jets. For the first time at the LHC, measurements are included where no requirements are placed on the jet activity. Background contributions are estimated using a combination of simulation and data-driven techniques. The dominant background from top quark events is precisely estimated using a data-driven method that significantly reduces experimental and modelling uncertainties. The integrated cross section obtained in a fiducial phase space with at least one jet is found to be $258 \pm 4\,\mathrm{(stat.)}\, \pm 25\,\mathrm{(syst.)}\,\mathrm{fb}$, whilst the result in a phase space with any number of jets is $668 \pm 5\,\mathrm{(stat.)}\, \pm 34\,\mathrm{(syst.)}\,\mathrm{fb}$. Both results are consistent with a range of state-of-the-art theoretical predictions. Cross section measurements in a phase space with a dynamic requirement on the event jet activity are also presented.

Contributions

Listed below are the contributions made by the author to the measurements presented in this thesis. Some of this work was carried out in collaboration with other members of the analysis team. The specific techniques or concepts referenced here will be discussed in depth in the relevant sections.

Measurements of W^+W^- production in a one jet inclusive phase space: Optimisation of the event selection; Unfolding, including the calculation of efficiencies and migrations based on simulated samples as well as optimisation of the number of iterations, propagation of systematic and statistical uncertainties, calculation of signal uncertainties, and calculation of the final covariance matrices.

Measurements of W^+W^- production in fully jet inclusive, dynamic jet veto and jet veto phase spaces: Responsible for the full data analysis chain, excluding the fake lepton background estimate, including the optimisation of the event selection and binning, processing of simulated signal samples, running of the top background estimates, and unfolding; Analysis of the W^+W^- charge asymmetry.

Acknowledgements

The completion of this thesis would not have been possible without the exceptional supervision of Kristin Lohwasser, Hannes Mildner, and Philip Sommer. All have been very engaged in my work at different stages, demonstrated remarkable patience, and helped to create a very welcoming and supportive environment in Sheffield. I am also very grateful to the ATLAS WW analysis team, without whose collaboration there would be no results to present.

I would like to thank Pauline Chouraki, Kristin Lohwasser, Christyanne MacDonald, Julian MacDonald, and Hannes Mildner for proofreading sections, or in some cases all, of this thesis and providing helpful comments from both physicist and non-physicist perspectives, even at the last minute. I take full responsibility for any remaining typos.

A final thank you goes to my family and friends, who have always been there to provide their love and support, and to remind me that there is in fact more to life than W bosons!

Contents

Introduction

The Standard Model (SM) of particle physics is arguably the most successful physical model ever devised. It was developed over a number of years using information from experimental measurements and theoretical constraints, with its current form able to describe the properties and interactions of all the known fundamental particles with unprecedented accuracy and precision. The most precise theoretical predictions of the SM to date are able to match the results of experimental measurements up to one part in 10^{11} [1]. Theoretical arguments based on the assumed symmetries of the SM were also able to predict the existence of the W, Z and Higgs bosons, as well as quarks and gluons, prior to their discoveries in high energy particle colliders.

Despite the great success of the SM, it suffers from certain limitations. It only accounts for three of the known fundamental forces, namely the electromagnetic (EM) force, and the strong and weak nuclear forces, with a complete quantum theory of gravity currently unknown. Astrophysical observations suggest the presence of a new form of matter, referred to as dark matter, making up a significant proportion of the energy density of the universe, and whose origin is unclear.Neutrino oscillation experiments indicate that neutrinos are massive particles, although this fact is not incorporated into the SM in its current form. These problems suggest extensions to the SM, referred to as beyond the SM (BSM) physics, are required, and experimental measurements are essential for providing the necessary constraints.

Direct evidence in the form of new particles, or resonances, that may be able to solve some or all of the problems listed above is currently lacking. Although there is still the potential for such discoveries in the near future, another avenue is precision measurements of known processes or physical quantities that can be compared to the latest high precision calculations from the theory community. At the time of writing, this approach would appear fruitful, with the muon $g - 2$ anomaly measurement [2] and tests of lepton flavour universality in B hadron decays [3] being two recent examples where precision experimental results present tensions with the SM predictions.

One class of precision measurements involves the study of particle production rates, or cross sections, in high energy collisions. The measurements presented in this thesis concern the production of pairs of oppositely charged W bosons in proton-proton (pp) collisions, performed using the ATLAS (A Toroidal LHC ApparatuS) detector [4] based at the Large Hadron Collider (LHC) [5] at the European Organisation for Nuclear Research (CERN) near the city of Geneva, Switzerland. Such measurements provide a test of the electroweak (EW) sector of the SM, in particular the nature of EW symmetry breaking (EWSB), the mechanism responsible for giving masses to the gauge bosons. The interplay between the couplings of the EW and Higgs bosons is delicately balanced in the theory, with even small deviations resulting in unphysical divergences in the resulting cross sec-

tions. Precise measurements provide an opportunity for testing these relationships. Measurements of W boson pair production also allow for the testing of perturbative quantum chromodynamics (QCD) through higher order corrections to the leading cross section calculation.

Since W bosons are unstable, only their decay products are directly measurable in the detector. The leptonic decays provide the cleanest signature, and so are targeted in the measurements presented in this thesis. The experimental signature is therefore a pair of oppositely charged leptons and missing energy from the W boson decay neutrinos. Real emissions of quarks or gluons additionally result in collimated streams of hadrons, known as jets.

Although not necessarily designed as a precision machine, the LHC has delivered recent measurements of integrated W boson pair production cross sections at percent-level precision [6–9], almost matching that of the latest theoretical predictions [10, 11]. In many of these measurements, events were selected such that there was minimal hadronic activity produced in association with the W boson pair. This was achieved by placing restrictions on the number of jets, and was done to limit contributions from processes involving the production of pairs of top quarks, whose experimental signature is otherwise very similar to the signal process. In this thesis, results from a recent publication [12] will be summarised in which differential cross sections are measured for the first time in a jet inclusive phase space. This is feasible due to the use of an accurate and precise data-driven estimate for the dominant background from top-related events. So far unpublished results for cross section measurements in phase spaces with any number of jets, and with a dynamic requirement in which the cut placed to limit jet activity varies on an event-by-event basis, will also be presented. Finally, studies of the sensitivity to the W boson pair charge asymmetry will be shown.

This thesis is divided into seven chapters. Chapter 1 provides a brief overview of the theoretical construction of the SM, as well as some of the phenomenological details of how predictions are made for the results of measurements performed in the hadron collider environment. In Chapter 2, a more detailed summary of the EW sector of the SM will be presented in addition to a summary of the theoretical predictions and previous measurements of W boson pair production cross sections. In Chapter 3, the components of the ATLAS detector are summarised in detail, whilst in Chapter 4 the process of combining signals in the detector to build the physics objects used in analyses will be summarised. Chapter 5 provides an overview of the statistical methods used in the experimental measurement, including a description of the unfolding process in which cross sections are obtained with detector resolution effects removed. The final two chapters present the results for the most recent ATLAS measurements of W boson pair production, with Chapter 6 including a description of event selections, background estimates, and the unfolding procedure, and Chapter 7 containing the final results.

1

Theoretical overview

In this chapter the theoretical background necessary for interpreting the results of experiments involving the scattering of high energy particles will be reviewed. A summary of the current status of the Standard Model (SM) of particle physics will be presented, as well as an outline of some of the methods used for deriving the theoretical predictions relevant for the collider environment.

1.1 The Standard Model

The probabilities, or rates, for particle scattering processes may be calculated within the framework of quantum field theory (QFT). For high energy particle scattering processes, such as the collisions that take place at the LHC, the appropriate QFT is the SM, which incorporates both the unified EW theory [13–15] and the theory of strong interactions, known as quantum chromodynamics (QCD) [16–18]. The SM therefore encapsulates our current understanding of elementary particle interactions under all the known fundamental forces except gravity.

1.1.1 Symmetries

The principle of symmetry is an integral part of the construction of the SM, since symmetries imply the existence of conserved quantities. These are usually given as a set of quantum numbers, that are related to the way in which a given particle transforms under the corresponding symmetry. Particles in the SM are required to transform under the internal symmetry group given by

$$G = \mathrm{SU}(3) \times \mathrm{SU}(2) \times \mathrm{U}(1),$$

(1.1)

where SU(3) is the symmetry group of QCD, with the associated quantum number of colour, and SU(2) × U(1) is the symmetry group of the EW interactions, with the associated quantum numbers

of weak isospin, I, and weak hypercharge, Y. This symmetry is additionally required to be local, in the sense that the transformations may take different values at different space-time points. The locality requirement promotes the symmetry to a gauge symmetry, and necessitates the introduction of gauge boson fields.

The EW symmetry is spontaneously broken in such a way that masses for the gauge bosons are generated in a gauge invariant way. This result, known as EW symmetry breaking (EWSB), or the Higgs mechanism, was arrived at almost simultaneously by three independent groups [19–21]. The symmetry is broken as $\mathrm{SU}(2) \times \mathrm{U}(1) \to \mathrm{U}(1)$ by the non-zero vacuum expectation value (VEV) of the Higgs field[1], leaving only the EM U(1) symmetry, with associated quantum number of electric charge, Q. The resulting EW boson masses and coupling parameters, discussed further in Sections 1.1.3 and 2.1.1, are related due to the gauge symmetry.

1.1.2 Particle content

The classification of the SM particles is done with respect to their quantum numbers. All particles in the SM have a spin quantum number. Those with half-integer spin are fermions and those with integer spin are bosons, so the SM can be broadly divided into the fermionic sector, consisting of quarks and leptons, and the bosonic sector, consisting of gauge bosons and the Higgs boson. The full particle content after EWSB is shown in Table 1.1.

Particles in the fermionic sector are further divided into three generations. The first generation contains two different flavour leptons: the electron and the electron neutrino, and two different flavour quarks: the up quark and the down quark. Higher generations contain more massive versions of these particles with all other quantum numbers identical. Neutrinos are the only fermions that do not have an electric charge, and so do not interact via the EM force. Only quarks are charged under SU(3) and so interact via the strong force. Fermions are also said to be chiral, meaning they have an intrinsic handedness which may be left-handed or right-handed. In the high energy or massless limit, chirality corresponds to the projection of the spin of the particle along its direction of motion, known as the helicity. Only left-handed fermions are charged under the SU(2) symmetry group. For each particle there is also an associated antiparticle with identical mass but opposite signs for all additive quantum numbers.

As mentioned in Section 1.1.1, the SM is a gauge theory and so contains gauge bosons. There are eight such massless bosons known as gluons associated with the strong force. After EWSB there are two massive W bosons and one massive Z boson associated with the weak force, and one massless photon associated with the EM force. Additionally there is the Higgs boson, which is not a gauge boson, but is associated with the mechanism of EWSB.

1.1.3 Interactions

Particle interactions are described using the Lagrangian formalism within the QFT framework. The SM Lagrangian contains fields corresponding to each of the particles discussed in Section 1.1.2 and is required to respect the symmetries given in Section 1.1.1. Each interaction term in

---

[1]The tree-level Higgs VEV is the value of the Higgs field at the minimum of the Higgs potential.

		s	Q	I^3	SU(3)	m
	electron	e	1/2	-1	$-1/2$		0.511 MeV
	electron neutrino	ν_e	1/2	0	$+1/2$		< 0.8 eV
I	up quark	u	1/2	$+2/3$	$+1/2$	$*$	2.16 MeV
	down quark	d	1/2	$-1/3$	$-1/2$	$*$	4.67 MeV
	muon	μ	1/2	-1	$-1/2$		106 MeV
	muon neutrino	ν_μ	1/2	0	$+1/2$		< 0.8 eV
II	charm quark	c	1/2	$+2/3$	$+1/2$	$*$	1.27 GeV
	strange quark	s	1/2	$-1/3$	$-1/2$	$*$	95 MeV
	tau	τ	1/2	-1	$-1/2$		1.78 GeV
	tau neutrino	ν_τ	1/2	0	$+1/2$		< 0.8 eV
III	top quark	t	1/2	$+2/3$	$+1/2$	$*$	173 GeV
	bottom quark	b	1/2	$-1/3$	$-1/2$	$*$	4.18 GeV
	$W^\pm$ boson	$W^\pm$	1	±1	±1		80.4 GeV
	Z boson	Z	1	0	0		91.2 GeV
	photon	γ	1	0	0		-
	gluon	g	1	0	0	$*$	-
	Higgs boson	h	0	0	$-1/2$		125 GeV

Table 1.1: The particle content of the SM after EWSB. The fermions are grouped according to generation. The values of spin, s, EM charge, Q, third component of weak isospin for left-handed fermions, I^3, and mass, m, are listed. The presence of the $*$ symbol in the SU(3) column indicates that the corresponding particle interacts via the strong force. Quark masses are current masses. Quark, boson and charged lepton masses are taken from [22], whilst neutrino mass limits are taken from [23].

the Lagrangian consists of a product of fields that encodes the way in which the corresponding particles interact, as well as a coupling parameter which indicates the strength of the associated interaction. The strong and EW interaction strengths are specified in terms of the strong coupling, g_s, the EM coupling, e, and the weak mixing angle, θ_w. Coupling strengths related to interactions involving the Higgs boson additionally include the Higgs VEV, v, as well as the masses of the other particles involved in the interaction. An important feature of SM couplings is that they are functions of the energy scale of the interaction, and so are said to run with energy. This feature is related to the presence of loops of virtual particles that change the effective strength of the given interaction. It is useful to define the couplings $\alpha_s = g_s^2/4\pi$, $\alpha = e^2/4\pi$ and $\alpha_w = \alpha/\sin^2\theta_w$. At energies close to the Z boson mass, the strong and EW couplings have the characteristic strengths of $\alpha_s \sim 0.1$, $\alpha \sim 0.008$ and $\alpha_w \sim 0.03$ [22]. Therefore, at LHC energy scales the strong force is the strongest, followed by the weak and EM forces. At lower energies, the weak force is weakest due to a suppression from vector boson masses.

1.1.4 Matrix elements and cross sections

The probabilities for particle scattering may be calculated in QFT, and are usually given in the form of cross sections. The differential cross section for two-particle scattering may be written as [24]

$$d\hat{\sigma}_{ij \to X} = \frac{1}{2E_i \, 2E_j \, |\boldsymbol{v}_i - \boldsymbol{v}_j|} \, |\mathcal{M}(ij \to X)|^2 \, d\Pi, \tag{1.2}$$

where E_i, E_j, $\boldsymbol{v}_i$ and $\boldsymbol{v}_j$ are the energies and velocities of the two initial state particles i and j in a given reference frame respectively, $d\Pi$ is the Lorentz invariant phase space element to be integrated over, and $\mathcal{M}(ij \to X)$ is the matrix element (ME) for the scattering process $ij \to X$, with X representing the set of final state particles. The ME encodes all the details of the interaction between the two particles, described by the SM Lagrangian. In the energy regime in which the couplings are small, it may be calculated using perturbative methods involving Feynman diagrams. The diagrams are organised according to their order in the strong and EW couplings. The leading order (LO) Feynman diagrams are at the lowest order for a given process, and usually provide the largest contribution, with higher order diagrams needed to improve the accuracy and precision of the prediction.

1.2 Collider phenomenology

Experiments at the LHC are mostly concerned with the scattering of initial state hadrons, in particular protons. At the high energies involved, the hard scattering is between the proton constituents, quarks and gluons, known collectively as partons. As described in Section 1.1.4, the probability for the two-parton hard scatter (HS) process may be calculated in perturbative QFT. The initial parton momenta are obtained from proton probability distributions, as will be discussed in Section 1.2.2. Scattering processes involving partons in the initial or final state may also include additional QCD radiation that manifests itself in the form of hadronic jets, discussed in more detail in Section 1.2.4.

1.2.1 QCD coupling

The QCD coupling, α_s, as with other SM parameters, is found to be a function of the energy scale Q of the interaction, as was mentioned in Section 1.1.3. This running of the strong coupling with energy may be calculated in perturbative QCD, and is given by

$$\alpha_s(Q^2) = \frac{\alpha_s(\mu_R^2)}{1 - \alpha_s(\mu_R^2)\beta_0 \ln Q^2/\mu_R^2} = \frac{1}{\beta_0} \frac{1}{\ln Q^2/\Lambda_{\text{QCD}}^2}, \tag{1.3}$$

where $\beta_0 = \frac{33-2n_f}{12\pi}$ is the QCD one-loop β-function and n_f is the number of active quark flavours. The running is shown graphically in Figure 1.1, along with values extracted from experimental measurements. The renormalisation scale, μ_R, is in principle arbitrary, but it is useful to set it equal to the typical energy scale of the process in order to reduce the impact of higher order corrections in the perturbative expansion. The second equality in Eq. (1.3) defines the scale $\Lambda_{\text{QCD}} \sim 1\,\text{GeV}$ [22] where the coupling diverges and perturbation theory breaks down. This corresponds to the regime of confinement, where quarks and gluons exist only as bound states. On the converse, the
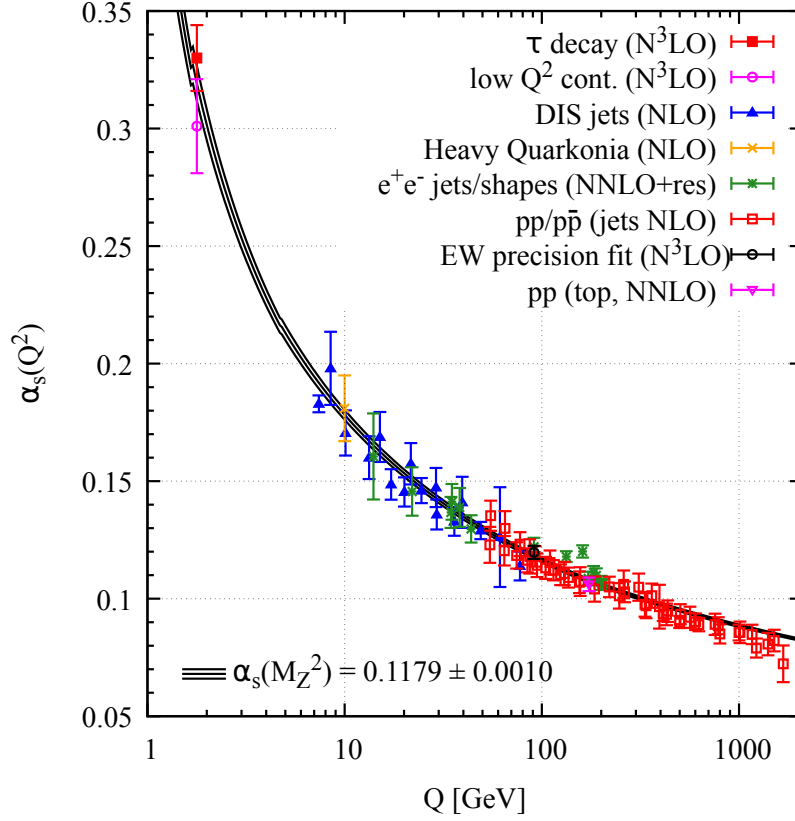
Figure 1.1: The running of the strong coupling α_s with energy scale Q. The markers show the results of extracting values for α_s from various experimental measurements. The precision of the calculation of the process from which α_s is extracted is indicated in brackets. The current best average value for $\alpha_s(m_Z^2)$ is given along with its calculated running (black line). Taken from [22].

strength of the coupling is observed to decrease as the energy scale increases, a feature known as asymptotic freedom [17, 18]. This in principle allows for perturbative calculations to be performed at the high energy scales of colliders, with non-perturbative methods needed only to describe initial and final state hadrons.

1.2.2 Parton distribution functions

Since protons are bound states of quarks and gluons, their description is not amenable to perturbative treatment. However, in the case that there is a sufficient separation of scales between the hard and soft processes, such that the principle of factorisation holds [25, 26], the inclusive differential cross section for a $pp \to X$ scattering process may be given as[2]

$$d\sigma_{pp \to X} = \sum_{i,j} \int dx_1 dx_2 \, f_i(x_1, \mu_F^2) \, f_j(x_2, \mu_F^2) \, d\hat{\sigma}_{ij \to X}(x_1 x_2 s, \mu_R^2, \mu_F^2), \qquad (1.4)$$

where $d\hat{\sigma}_{ij \to X}$ is the differential HS cross section of Section 1.1.4, $\sqrt{s}$ is the centre-of-mass energy for the pp system, and x_1 and x_2 are the fractions of the longitudinal proton momentum carried by the respective partons. The quantity $f_i(x, \mu_F^2)$ is the probability density function for the fraction

---

[2]Factorisation means that this expression is valid up to corrections of the order Λ_{QCD}^2/Q^4, where Q is the characteristic energy scale of the HS process.
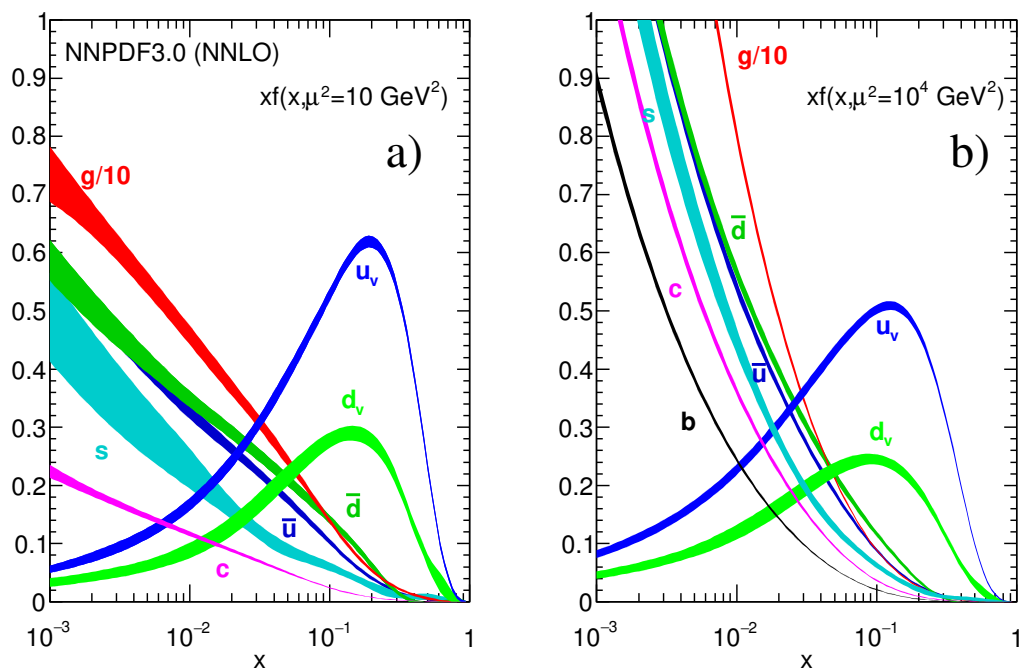
Figure 1.2: The next-to-next-to-LO (NNLO) NNPDF3.0 proton PDFs for quarks and gluons, evaluated at two different values of the factorisation scale. The subscript v on the u and d quark lines indicates that these are valence quarks. All other quark and antiquark types are referred to as sea quarks. The distributions for s, c and b are equivalent to their antiquark variations. Taken from [22] using results from [31].

of the proton momentum carried by the parton i, known as the parton distribution function (PDF). The PDF is a non-perturbative quantity that must be obtained from fits to experimental data. Some example PDFs are shown in Figure 1.2. The scale μ_F is known as the factorisation scale. Analogously to the renormalisation scale, this is the point at which collinear divergences are absorbed into the PDF and can be understood intuitively as the transverse momentum scale that separates the hard process from the soft process. As for the renormalisation scale, the factorisation scale is arbitrary, but it is common to choose a value close to the energy scale of the HS process to minimise higher order corrections. Although the absolute values of the PDFs are usually obtained from data, their energy scale dependence is calculable in perturbation theory and results in the DGLAP evolution equations [27–30]. Importantly, by virtue of the principles of factorisation, it is expected that the PDFs are universal, in the sense that the same PDF can be used for many different HS processes if the initial state hadrons are the same. In experimental measurements, systematic uncertainties related to the PDF may be estimated by simulating signal and background events with different PDF sets. The different sets are obtained from fits by different groups and usually contain a nominal PDF for each parton type, as well as variations corresponding to fit uncertainties.

1.2.3 Hard scatter process

As mentioned previously, the differential HS cross section of Eq. (1.2), used in Eq. (1.4), may be computed at an energy scale Q to a given order in perturbation theory. In general, this results in an

expansion in terms of the strong and EW coupling constants, which may be written as [32]

$$d\hat{\sigma}_{ij \to X} = \alpha_s^k \alpha^l \sum_{m,n=0}^{\infty} c_{mn} \alpha_s^m \alpha^n. \tag{1.5}$$

The coefficient c_{00} parameterises the LO contribution, whilst the remaining coefficients c_{mn} account for higher order real and virtual QCD and EW corrections. The coefficients are in general functions of Q, μ_R and μ_F as well as potentially other relevant energy scales in the event, such as jet transverse momentum thresholds. The LO expression for the cross section may itself include a finite number of powers of α_s and α, indicated by the exponents k and l. Since at typical energy scales probed by the LHC the coupling α_s is larger in magnitude than the equivalent EW couplings, purely QCD contributions usually dominate the higher order corrections. Pure EW and mixed corrections may become important for higher precision calculations or in the tails of certain kinematic distributions.

In Eq. (1.5) the couplings α_s and α are understood to be evaluated at a particular choice of renormalisation scale, μ_R. Physical observables should be independent of this choice, yet since in fixed order perturbation theory the sum is truncated, there is some residual higher order scale dependence in cross section predictions. This enters experimental results as a theoretical uncertainty on the choice of renormalisation scale, and can be interpreted as an estimate of the size of missing higher order terms. This truncation generates similar uncertainties related to the choice of factorisation scale, μ_F, in the total pp cross section in Eq. (1.4).

1.2.4 QCD radiation and jets

QCD processes may be associated with additional quark and gluon radiation from coloured particles in the initial or final state, respectively referred to as initial state radiation (ISR) and final state radiation (FSR)[3]. The probability for hard emissions is expected to be suppressed by additional powers of α_s, whereas soft or collinear emissions are enhanced. This in general results in a set of well-separated collimated parton emissions, known as jets. Additional emissions reduce the energy scale, until the threshold value of ~ 1 GeV is reached and hadronisation takes place. The experimental signature is then a set of collimated beams of colourless hadrons, whose properties correlate strongly with the underlying hard parton emissions. Since jets themselves are not fundamental objects, the systematic characterisation of the associated emissions is achieved with the introduction of a jet definition. For ease of use this is usually chosen such that the resulting jet properties hold on the level of both partons and hadrons, as well as for detector deposits.

There are additional requirements on the jet definition that ensure theoretical calculations to any order are possible. In particular, it is required that all real and virtual contributions needed for the cancellation of infrared (IR) divergences in QCD corrections to partonic final state cross sections, as specified by the Kinoshita-Lee-Nauenberg (KLN) theorem [33, 34], are included at all orders. This means that the jet definition should be insensitive to collinear or soft splitting of final state partons. Such definitions are referred to as IR safe.

---

[3]ISR and FSR can also refer to EW emissions, usually photons.

Although IR divergences may be made to cancel by a careful choice of observable, in less inclusive cases the cancellation is incomplete, which can lead to residual large logarithms. This for example can happen when the transverse momentum threshold for the definition of a jet, $p_{\mathrm{T}}^{\mathrm{jet}}$, is small compared to the relevant energy scale of the event, Q, where logarithms of $p_{\mathrm{T}}^{\mathrm{jet}}/Q$ may emerge. In this case, all orders in the perturbative expansion may be equally important and a resummation may be needed. Resummation of all terms with two powers of a large logarithm per power of α_s is known as leading logarithmic (LL) resummation. Summation of terms with one fewer logarithmic power per power of α_s is referred to as next-to-LL (NLL) resummation, and so on. A typical theoretical prediction may therefore include a fixed order calculation of the HS process, accompanied with some resummation of large logarithms, for example in the case that a phase space restriction introduces disparate scales.

1.2.5 Event generation

Even though observations are made on the level of hadrons, fixed order parton-level predictions can adequately describe the main energy flow in events. However, for more exclusive cases such calculations are often insufficient to account for all aspects of kinematic distributions, such as detailed jet substructure or specific hadron properties. In addition, for large numbers of final state particles, computations of cross sections via analytic methods become increasingly complex due in part to the high dimensional phase space integrals required. These challenges can be met with a combination of Monte Carlo (MC) methods, parton shower (PS) algorithms and hadronisation models, shown schematically in Figure 1.3. A detailed summary of such methods can be found in Ref. [35]. The tools described here are ubiquitous in predictions for signal and background estimates in measurements at the LHC. Similarly to the choice of PDF set, systematic uncertainties on these estimates related to the event simulation process may be obtained by comparing results produced using different generators.

Fixed order matrix elements

The ME enters the calculation of the differential cross section for the HS process, as given by Eq. (1.2). As mentioned in Sections 1.1.4 and 1.2.3, for few particle final states the expression for the ME can be calculated to a given fixed order in the strong and EW coupling parameters using Feynman diagram techniques. A phase space integral then needs to be performed in order to calculate cross sections, and in many cases MC methods are the appropriate calculational tool. The MC sampling procedure produces a set of events, each consisting of a specific configuration of final state momenta, similar to those that would be obtained in data. In general each event is associated with some MC weight related to the value of the ME at that point in phase space. Since the statistical uncertainty decreases as the number of events increases, typically many more MC events are simulated than would be expected in data. The event weights are then additionally chosen such that the distributions are normalised to the correct cross section, which may be from a higher order calculation than that used for the simulation.
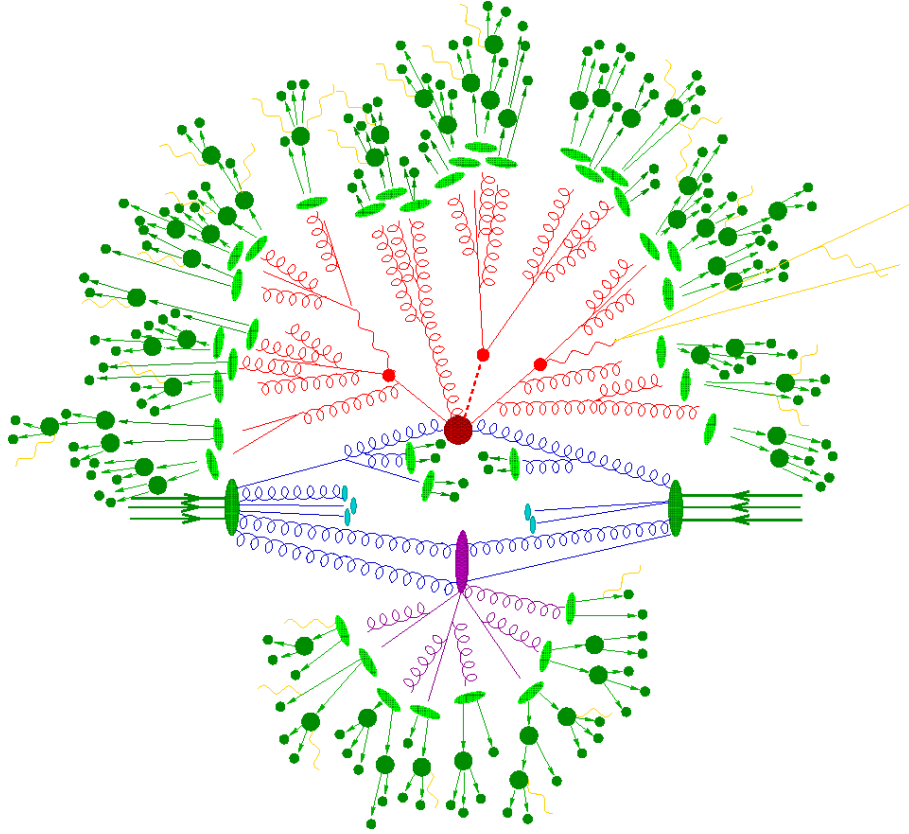
Figure 1.3: A *pp* collision from the point of view of a general purpose MC event generator. The dark red circle corresponds to the HS process, where two partons fuse to form a multi-particle final state. Additional soft and collinear emissions composing the PS are shown in red, with the resulting hadrons shown in light green. These hadrons may themselves subsequently decay into more stable hadrons, as shown in dark green. The purple oval and associated emissions correspond to multiple parton interactions (MPI) composing the underlying event (UE). Yellow lines correspond to EM radiation, which may be emitted at any stage. Taken from [36].

Parton showers

Although MEs at fixed order produce reliable predictions for a small number of hard and well-separated partons, they perform less well in cases where there is a large amount of additional soft and collinear radiation, as mentioned in Section 1.2.4. This issue can be resolved by the intro-duction of a semi-classical PS, which can be considered as an MC approach to LL resummation of associated large logarithms. Being a stochastic process, the PS produces multiple many-parton final states, analogous to the events generated for ME integrals, allowing for the more detailed sim-ulation of distributions for jet-related observables. The basic principle of PS algorithms is to split a given parton at a high value of some ordering variable, ρ, into two daughter partons at lower values of ρ with some probability related to the Sudakov form factor[4]. The momentum fractions of the daughter partons are then determined probabilistically according to a distribution containing the appropriate DGLAP splitting kernels[5]. The ordering variable may for example be the transverse momentum of the daughter parton with respect to its parent, or the angular separation between

---

[4]The Sudakov form factor represents the probability for no emission between two values of the ordering parameter.
[5]These may be supplemented with PDFs in the case of an initial state PS.

them. This splitting process is repeated on each subsequent parton until some lower cut-off value of order Λ_{QCD} in the ordering variable is reached and the resulting partons are fed into hadronisation simulations.

Given the complementary nature of fixed order ME calculations and PS simulations in describing different energy scales of the same event, it is desirable to combine the approaches for highest accuracy. This is done via a combination of matching and merging schemes, where care is taken to ensure double counting of emissions is avoided, for example by placing a momentum cut-off to separate the hard ME emissions from those of the PS. The state-of-the-art for most processes involves next-to-LO (NLO) MEs, and a range of matching and merging schemes are available, as will be discussed further in Section 2.1.2.

Hadronisation and the underlying event

The final stages of event simulation involve the conversion of low energy partons at the end of the PS into a set of hadrons, which may themselves decay into further hadrons considered stable on the timescales of the detector. Given hadronisation occurs at scales of order Λ_{QCD}, it is a non-perturbative transition for which there is currently no first principles calculation. Instead, various phenomenological models, including for example the Lund string model [37] or the cluster model [38], are used in most event generators.

An additional non-perturbative aspect of events comes from the underlying event (UE), which here will refer to all additional soft QCD processes that are not directly related to the primary HS process and its associated PS. Examples include scattering between different partons within the same proton, known as multiple parton interactions (MPI), and remnants from the proton beam. These predominantly soft processes are accounted for using additional models.

2

Overview of W^+W^- production

In this chapter, the phenomenology related to the production of pairs of oppositely charged W bosons will be discussed, and a summary of previous measurements will be given. Starting from a general introduction to the structure of the EW sector of the SM and a brief discussion of its history, a review of the developments in the theoretical predictions for W^+W^- (WW) production cross sections will be provided. In the second half of this chapter, previous measurements of WW production performed at LEP (Large Electron-Positron), the Tevatron and the LHC will be reviewed.

2.1 Phenomenology of W^+W^- production

Measurements of the production of oppositely charged W boson pairs, such as those that will be presented in Chapter 7, provide a test of the EW gauge structure of the SM. To this end, theoretical predictions for WW production in the collider environment are needed. The first predictions [39–41] for $pp \to W^+W^-$ cross sections with and without hard jets in the final state were made a number of years ago, with more recent calculations incorporating higher orders in the strong and EW coupling parameters, as well as improved PDF and PS inputs. In this section, an overview of these predictions will be given in the context of the EW sector of the SM.

2.1.1 The electroweak sector of the Standard Model

The EW sector of the SM incorporates both the EM and weak interactions [13–15]. Above the EWSB scale, of the order $v \approx 246\,\text{GeV}$, the EM and weak forces are understood to be unified, with the corresponding EW symmetry spontaneously broken at lower energy scales, such as those currently probed by the LHC. The details of this symmetry breaking are reflected in the properties of the EM and weak bosons, providing a window for testing the EW theory through precision

13

measurements.

Theoretical overview of the electroweak sector

The EW sector is based on the SU(2) × U(1) symmetry group. As mentioned in Section 1.1, local gauge invariance of the SM Lagrangian under this symmetry requires the presence of gauge bosons. Before EWSB, there are four massless spin-1 gauge bosons associated with the SU(2) × U(1) gauge symmetry. The three bosons associated with the SU(2) symmetry are called W^1, W^2 and W^3, and the boson associated with the U(1) symmetry is called B. The physical W^+ and W^- bosons are then defined as the linear combinations

$$W^\pm = \frac{1}{\sqrt{2}} \left(W^1 \mp iW^2 \right),\tag{2.1}$$

where the signs correspond to EM charges, whereas the electrically neutral photon, A, and Z boson can be written as

$$A = W^3 \sin\theta_w + B\cos\theta_w \quad \text{and} \quad Z = W^3 \cos\theta_w - B\sin\theta_w.\tag{2.2}$$

After EWSB, mass terms for these bosons are generated, which are diagonal in the $W^\pm$, A and Z basis. The photon remains massless and is the gauge boson associated with the remaining U(1) symmetry, whereas the W and Z bosons acquire the masses

$$m_W = \frac{ve}{2\sin\theta_w} \quad \text{and} \quad m_Z = \frac{m_W}{\cos\theta_w}\tag{2.3}$$

respectively. The $W^\pm$ bosons are therefore predicted to have the same mass, whereas the Z boson is predicted to be heavier than the W bosons. These predictions are consistent with the observations given in Table 1.1.

The interactions of the EW bosons amongst themselves and with quarks and leptons are described by the EW sector of the SM Lagrangian. The fact that the underlying EW symmetry group is non-abelian means that self-interactions between the gauge bosons are possible. In particular, both interactions involving three EW bosons, known as triple gauge couplings, and interactions involving four EW bosons, known as quartic gauge couplings, are possible, as well as couplings between these bosons and the Higgs boson. The SM interaction terms involving EW bosons are shown in Table 2.1, along with their characteristic coupling strengths. Each interaction term corresponds to a possible vertex in a Feynman diagram involving the associated particles. The relationships between the parameters, e, θ_w, and v, and the EW boson masses and coupling strengths are unique predictions of the EWSB mechanism of the SM. Any measured inconsistencies amongst these parameters would therefore indicate the presence of BSM physics.

The EW bosons additionally interact with fermions. The interaction terms in the Lagrangian involve a pair of fermion fields and one EW boson, and are referred to as currents. The interaction terms and their coupling strengths are summarised in Table 2.2. Pure EM interactions, involving only photons, form currents with charged fermions of the same flavour. The coupling is simply related to the EM charge of the fermion. For weak interactions, the W bosons form charged currents

Interaction term	Coupling strength
$W^+W^-\gamma$	e
W^+W^-Z	$e\cot\theta_w$
$W^+W^-W^+W^-$	$e^2/\sin^2\theta_w$
$W^+W^-\gamma\gamma$	e^2
W^+W^-ZZ	$e^2\cot^2\theta_w$
$W^+W^-\gamma Z$	$e^2\cot\theta_w$
W^+W^-h	m_W^2/v
ZZh	m_Z^2/v
W^+W^-hh	m_W^2/v^2
$ZZhh$	m_Z^2/v^2

Table 2.1: Interaction terms for EW bosons and the Higgs boson along with their characteristic coupling strengths. The table is divided into triple EW gauge couplings, quartic EW gauge couplings, and couplings involving both EW bosons and Higgs bosons. All coupling strengths are taken from [24].

Interaction term	Coupling strength
$f_L f_L \gamma, f_R f_R \gamma$	eQ
$e_L \nu_L W$	$e/\sqrt{2}\sin\theta_w$
$u_L^i d_L^j W$	$eV^{ij}/\sqrt{2}\sin\theta_w$
$f_L f_L Z$	$e(I^3 - Q\sin^2\theta_w)/\sin\theta_w\cos\theta_w$
$f_R f_R Z$	$eQ\tan\theta_w$

Table 2.2: Interaction terms between EW bosons and fermions, along with the associated coupling strengths. For the interaction terms, f denotes a generic fermion, whilst e corresponds to an electron, muon or tau, ν to an electron, muon or tau neutrino, u to an up, charm or top quark, and d to a down, strange or bottom quark. The subscripts L and R correspond to left- and right-handed chirality respectively. For the coupling strengths, Q is the EM charge on the associated fermion in units of e, I^3 is the third component of weak isospin, and V^{ij} is an element of the CKM matrix, mixing fermion generations i and j. All coupling strengths are taken from [24].

which connect fermions of different flavour. Interactions involving W bosons are maximally parity violating, which means that the rate for such interactions is not preserved under a reflection in space. This is a result of the fact that W bosons only couple to fermions with left-handed chirality, defined in Section 1.1.2. Another feature of W bosons is that they are able to induce transitions between quark generations, with the coupling strengths proportional to entries of the Cabibbo-Kobayashi-Maskawa (CKM) matrix [42, 43]. The CKM matrix is mostly diagonal, meaning mixing between different generations is heavily suppressed. The remaining weak boson is the Z boson, which forms neutral currents with fermions of the same flavour. Unlike for W bosons in charged current interactions, Z bosons couple to both left-handed and right-handed fermions, although unlike pure EM interactions, the coupling strengths are not equal.

Development of the electroweak theory

The EW theory was devised over a number of years, using information from a variety of exper-
imentals, as well as theoretical constraints. In 1957, parity violation within the weak sector was
measured for charged current interactions via experiments involving the beta decay of ^{60}Co isotopes
[44]. This quickly led to the development of a theory for weak interactions involving the observed
maximal parity violation, known as vector $-$ axial, or V $-$ A, theory [45, 46]. This was done mostly
within the context of the Fermi interaction, which describes weak decays as four-fermion vertices
with a coupling strength given by the Fermi constant, G_F. Such interaction terms were realised
to lead to unphysical divergences in cross sections at high energies, so a gauge theory based on
the SU(2) × U(1) group and involving spin-1 W bosons that mediated the weak interaction was
considered [13–15]. The theory not only predicted massive W bosons, but also a massive neutral
Z boson expected to generate neutral current interactions. In 1973, electron-neutrino and hadron-
neutrino scattering experiments performed at the Gargamelle bubble chamber at CERN confirmed
the existence of such neutral currents [47, 48]. In 1983, observations of W and Z boson resonances
were made at values consistent with their predicted masses using $\sqrt{s} = 540\,\text{GeV}$ proton-antiproton
($p\bar{p}$) collisions at the UA1 and UA2 experiments on the Super Proton Synchrotron (SPS) at CERN
[49–52]. Although the mass generation mechanism for the EW bosons was known prior to their
discovery, one of the consequences of this mechanism, the existence of an uncharged scalar boson,
known as the Higgs boson, had yet to be confirmed. Minimum bounds on the Higgs mass were
obtained from previous experiments, whereas an upper limit of about 1 TeV was set by theoretical
constraints [53]. This motivated the design and construction of the LHC, with a resonance con-
sistent with the Higgs boson finally being discovered in 2012 by both the ATLAS [54] and CMS
(Compact Muon Solenoid) [55] experiments.

2.1.2 Calculations of W^+W^- production cross sections

The couplings and masses of the EW bosons may be described in the SM using only the three
parameters, e, θ_w and v, or equivalently α, $\sin^2 \theta_w$ and G_F. The ability to make multiple measure-
ments of different processes allows for the testing of the relationships between these parameters,
providing a consistency check of the EW sector of the SM. One such set of measurements involves
the production of pairs of oppositely charged W bosons. These pairs may be produced in a va-
riety of ways, including both e^+e^- and pp scattering, where in the latter case the hard collision
may be between the partons in the protons, or between EW bosons that radiate off the protons. The
measurements presented in this thesis focus on parton-induced production mechanisms, which pro-
vide larger cross sections. The LO Feynman diagrams for quark-antiquark-induced W boson pair
production, denoted $q\bar{q} \rightarrow W^+W^-$, are shown in Figure 2.1. The left-hand diagram is known
as a t-channel diagram, whereas the right-hand diagram is known as an s-channel diagram. The
s-channel diagram involves a Z or photon exchange, where the associated particle is described as
being virtual, or off-shell[1]. From these diagrams, it is clear that W boson pair production pro-
vides sensitivity to the $W^+W^-\gamma$ and W^+W^-Z triple gauge couplings. In principle, s-channel
diagrams involving a Higgs exchange should also be included, but since the associated Higgs-

---

[1]This refers to the fact that the relativistic dispersion relation is in general not satisfied for these particles.
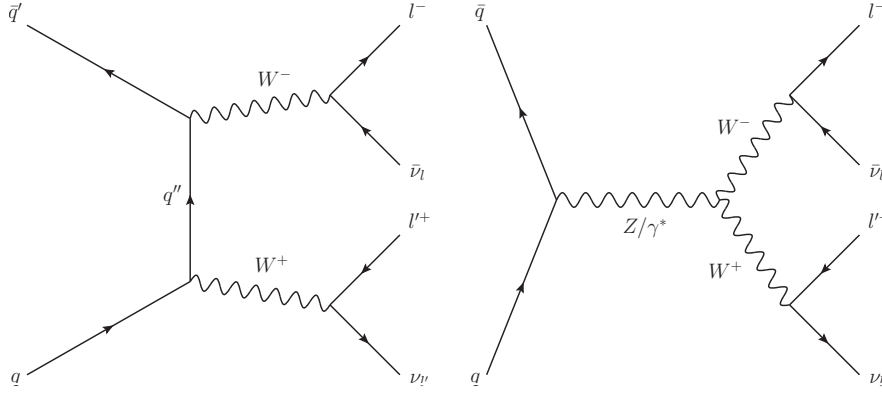
Figure 2.1: LO Feynman diagrams for the $q\bar{q} \rightarrow W^+W^-$ process. Initial state particles are represented by lines entering the diagram from the left, with final state particles represented by lines leaving the diagram towards the right. Shown are both the t-channel (left) and s-channel (right) diagrams. The q line corresponds to a quark and the $\bar{q}$ line to an antiquark, whilst the ν line corresponds to a neutrino and the $\bar{\nu}$ line to an antineutrino. The primes on the quark and lepton lines are used to differentiate flavours. The asterisk in the s-channel diagram indicates that the Z boson or photon is off-shell.

decay mode	BR / %
$e^{\pm}\nu_e$	10.7 ± 0.2
$\mu^{\pm}\nu_\mu$	10.6 ± 0.2
$\tau^{\pm}\nu_\tau$	11.4 ± 0.2
$q\bar{q}'$	67.4 ± 0.3

Table 2.3: Decay modes and measured BRs for W bosons. $q\bar{q}'$ corresponds to a quark-antiquark pair of different flavour. Decay modes with smaller BRs have been neglected. All BR values are taken from [22].

fermion-fermion Yukawa coupling strength is proportional to the fermion mass, which is small in the case of e^+e^- and light quark initial states, these contributions are usually neglected.

Due to the relatively large mass of the W boson, decays to lighter particles are kinematically possible, and as shown in Table 2.2, the necessary interaction terms exist in the SM Lagrangian. These two facts result in the W boson being unstable, as characterised by its non-zero total decay width, $\Gamma_W = 2.1\,\mathrm{GeV}$ [22], corresponding to a mean lifetime of $3.1 \times 10^{-25}\,\mathrm{s}$. The decay modes and associated branching ratios (BRs)[2] are shown in Table 2.3. For the measurements presented in this thesis, only W decays to leptons, in particular $e\nu_e$ and $\mu\nu_\mu$ final states, are considered.

Fixed order calculations

The first LO calculations for on-shell stable WW production cross sections for e^+e^-, pp and $p\bar{p}$ initial states were performed in 1979 prior to the W or Z boson discoveries [39]. The lepton- or quark-induced process has a $\frac{\ln \hat{s}}{\hat{s}}$ dependence at large values of the centre-of-mass energy of the lepton or quark system, $\sqrt{\hat{s}}$. The cross section in pp collisions is predicted to rise with $\sqrt{s}$ up to at least $1.6\,\mathrm{TeV}$. Cancellations between the two diagrams of Figure 2.1 needed to avoid unitarity

---

[2]The BR of a given decay mode is defined as the ratio of the decay rate for that mode to the total decay rate.
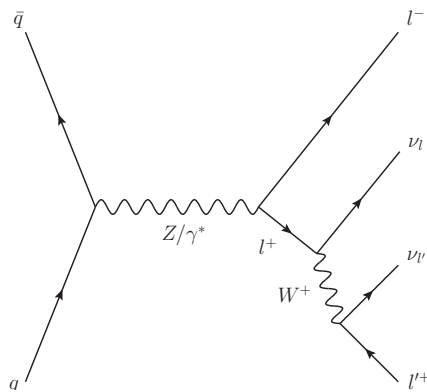
Figure 2.2: An example of a single-resonant Feynman diagram that contributes when final state leptons are considered.

violations are shown to occur only for the specific relationships between the coupling parameters described in Section 2.1.1. Diagrams involving a Higgs exchange, as mentioned previously, are additionally required to cancel these divergences in the case where fermion masses are not neglected, but the resulting contributions to the cross section are usually negligible [53].

Higher order calculations for $pp \rightarrow W^+W^-$ production include both QCD and EW corrections. Given the relatively large size of α_s compared to α at LHC energies, QCD corrections normally dominate, as mentioned in Section 1.2.3. NLO corrections at $\mathcal{O}(\alpha_s)$ in the cross section involve real and virtual one loop corrections to the $q\bar{q}$ channel, as well as the opening of qg and $\bar{q}g$ channels with real quarks in the final state [56, 57]. The NLO contributions can increase the total inclusive cross section by around 50% relative to the LO process depending on the centre-of-mass energy, with significant corrections to the shapes of certain differential distributions, mostly in high energy tails. The inclusion of leptonic decay products for the W bosons provides more realistic calculations involving spin correlations, and allows for application of experimental cuts. NLO calculations involving final state leptons with on-shell W bosons [58–60] and separately those accounting for finite-width effects [61] have been available for a number of years. When leptons are included in the final state, additional single-resonant diagrams may also contribute that cannot be interpreted as W boson pair production and subsequent decay. These diagrams can have substantial effects, particularly in the tails of distributions [62]. An example diagram of this type is shown in Figure 2.2.

There are also gg channels that proceed at LO via one loop diagrams, as shown in Figure 2.3. These contribute $\mathcal{O}(\alpha_s^2)$ corrections to the $pp \rightarrow W^+W^-$ cross section, and so are formally considered as NNLO corrections. However, these contributions are enhanced due to the relatively large gluon PDF for small momentum fractions at LHC energies, which somewhat compensates for the extra power of α_s. As a result, these diagrams often supplement the NLO corrections. There is no interference or overlap at this order due to the different initial states, so these contributions can be calculated separately. A Higgs exchange diagram via a quark loop is also included here since heavy-flavour quarks with non-negligible couplings to the Higgs may be present in the loop. The Higgs contribution is however small when the invariant mass of the W boson system is far from the Higgs mass [56], although interferences between the Higgs and continuum gg-induced processes
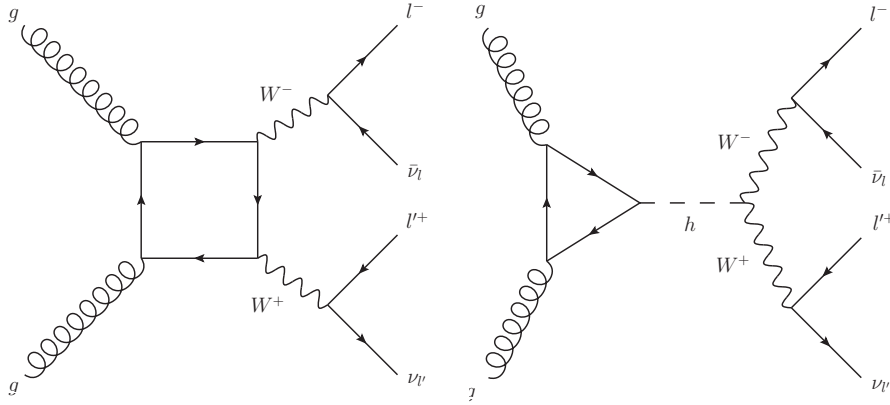
Figure 2.3: LO Feynman diagrams for the $gg \rightarrow W^+W^-$ subprocess contributing $\mathcal{O}(\alpha_s^2)$ corrections to $pp \rightarrow W^+W^-$. The loop in both diagrams involves quarks

can be relevant. In principle, diagrams where the Higgs is replaced with a Z boson or photon can also contribute, although it can be shown that both terms vanish on-shell [63, 64]. Corrections to account for W boson decays to leptons and finite-width effects in the gg channel have also been calculated [65–67].

Full NNLO QCD corrections have been calculated for stable W bosons [68] and more recently taking into account decays to leptons [69], providing corrections to the total cross section of the order of 10%. NLO corrections to the gg-induced process, formally of $\mathcal{O}(\alpha_s^3)$ and so contributing to the next-to-NNLO (N³LO) corrections to $pp \rightarrow W^+W^-$, have also been calculated [11, 70], providing a correction of about 2% to the total NNLO cross section.

In addition to the QCD corrections, increasingly precise measurements call for the inclusion of EW corrections. Such corrections involve virtual EW boson exchanges as well as real emissions, potentially opening up channels such as $q\gamma$ involving photons in the initial state. Although nominally subdominant to QCD corrections in inclusive cross sections, the EW contributions can be sizeable in regions of phase space where the energy scale is significantly larger than the EW scale, due to the presence of large logarithms [71]. NLO EW corrections at $\mathcal{O}(\alpha^3)$ have been calculated for stable W bosons [72–74], and at $\mathcal{O}(\alpha^5)$ when fully including lepton decays and off-shell effects [62]. Combinations of EW and QCD corrections have also been made, including at NLO QCD+EW [75] and, more recently, at NNLO QCD+NLO EW [10] within the MATRIX+OpenLoops computational framework [76–78]. Such combinations are usually approximate, with both additive and multiplicative schemes in use, where the pure QCD and EW correction factors to the LO cross section are added or multiplied together respectively.

Dedicated calculations for WW production with hard jets[3] in the final state have also been performed, although since the LO process is of $\mathcal{O}(\alpha_s)$, typically only lower order predictions are available compared to the fully jet inclusive or jet veto cases. Example LO Feynman diagrams for $pp \rightarrow W^+W^-$+jet are shown in Figure 2.4. Virtual diagrams are not needed to cancel soft and collinear divergences at this order since the jets are required to be hard and well-separated. The first calculations with up to two jets were performed at LO [40, 41]. There has been a recent effort to calculate the one jet process at NLO QCD [79–82], as well as to estimate NLO EW corrections

---

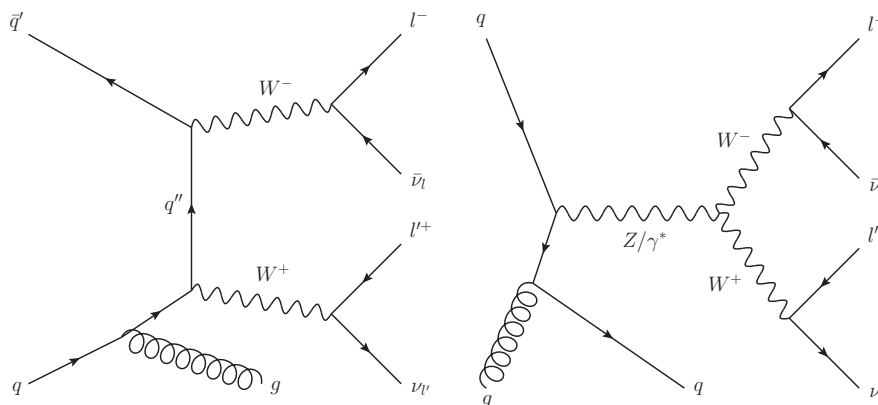[3]A hard jet in this context means that some minimum p_{T} requirement is placed on the final state partons.

Figure 2.4: LO Feynman diagrams contributing to $pp \rightarrow W^+W^-$+jet. These same diagrams contribute to exclusive $pp \rightarrow W^+W^-$ at NLO, where the jet is not resolved.

[83] and to perform NLO QCD+NLO EW combinations including off-shell effects [84]. In addition, NLO QCD corrections have been calculated for final states with up to two jets [85, 86] and, more recently, up to three jets [87]. Events generated using the inclusive cross section calculations previously discussed can also be used to provide predictions for a given number of hard jets, but the order in α_s falls by one from the quoted value for each extra jet considered.

Predictions with parton showers

In addition to the fixed order calculations described above, predictions are available that also include PS algorithms to better model jet distributions, as discussed in Section 1.2.5. A range of generator and PS combinations are available for generating exclusive $pp \rightarrow W^+W^-$ events with MEs at NLO QCD. Common PS programs include those provided by the SHERPA [88], PYTHIA [89, 90] and HERWIG [91, 92] event generators. Various aspects of the PS development are determined by a set of parameters tuned to agree with data. Additional tunes are used to describe hadronisation and the UE. When interfacing the ME calculation to the PS, it is important to ensure there is no double counting of emissions, which can be achieved with matching and merging techniques. Matching methods modify the hardest emission of the PS such that it agrees with the same result from the NLO accurate ME. Common prescriptions include MC@NLO [93] and POWHEG [94, 95]. Multi-jet merging methods involve splitting the phase space into two regions according to a merging scale, where each region is then described either by the hard LO ME or by the soft PS [96]. Such methods were first used by HERWIG, with subsequent adaptations resulting in the now widely used CKKW [97] and CKKW-L [98] methods. Extensions to multi-jet merging methods, such as FxFx merging [99], MEPS@NLO [100] and MINLO [101], incorporate MEs at NLO accuracy, whilst the recent MINNLO [102] method provides NNLO accuracy. The accuracy of the fixed order calculation used in predictions interfaced to a PS is typically lower than that of pure fixed order calculations due to the added complication of the matching and merging procedures.

As mentioned in Sections 1.2.2 and 1.2.3, uncertainties on all theoretical predictions arise from ambiguities about the choice of renormalisation and factorisation scales, and from uncertainties in the PDF. The scale dependence of cross sections typically reduces as higher orders are included in the calculation. Nominal values and uncertainties will be discussed for the relevant signal predic-

tions when comparing them to the experimental results presented in Chapter 7.

2.2 Previous measurements of W^+W^- production

As mentioned in Section 2.1.2, pairs of oppositely charged W bosons may be produced by a variety of initial states. Measurements of WW production have therefore been made at all the previous particle colliders capable of delivering a high enough centre-of-mass energy to produce such pairs. The first such measurements were performed using e^+e^- collisions at LEP [103], with measurements using $p\bar{p}$ collisions and pp collisions following at the Tevatron [104] and LHC respectively. Circular e^+e^- colliders tend to produce more precise measurements due to the fact that the initial energy of the colliding particles is known, the centre-of-mass frame coincides with the laboratory frame, there is a lack of UE, and backgrounds are typically smaller. However, in general they cannot deliver the same centre-of-mass energies as the equivalent hadron colliders due to the increased energy loss from synchrotron radiation.

2.2.1 Measurements at LEP

LEP was a circular e^+e^- collider, operational from 1989 until 2000, and reached a final centre-of-mass energy of $\sqrt{s} = 209\,\text{GeV}$. This allowed for the production of pairs of on-shell W bosons for the first time. LEP remains the highest energy lepton collider ever constructed, collecting an integrated luminosity above the Z peak during the LEP-II program of about $3\,\text{fb}^{-1}$, during which time a number of precision measurements of EW processes were made. As with the LHC, there were four experiments located around the LEP ring, each associated with its own IP, namely ALEPH (Apparatus for LEP pHysics at CERN) [105], DELPHI (DEtector with Lepton, Photon and Hadron Identification) [106], OPAL (Omni-Purpose Apparatus for LEP) [107], and L3 [108].

Measurements of W boson pair production were made at all four detectors in the all-hadronic, semi-leptonic, and fully-leptonic final states [109]. The measurement uncertainty was around 2% for most of the centre-of-mass energies considered. The combined results as a function of the centre-of-mass energy are compared to theoretical predictions in Figure 2.5a. Additionally shown are two predictions where either the W^+W^-Z vertex is not considered or only the ν_e exchange t-channel diagram is considered. It is clear that the interference of all three diagrams is essential to match the data, providing strong evidence for the non-abelian nature of the EW symmetry group. The fitted ratios of the measured cross sections to the theoretical predictions at each energy, and the same ratio including all energies, are shown in Figure 2.5b.

2.2.2 Measurements at the Tevatron

The Tevatron was a $6.28\,\text{km}$ synchrotron $p\bar{p}$ accelerator and collider located at the Fermi National Accelerator Laboratory (Fermilab) in Illinois, United States. It ran from 1983 until 2011 and achieved a maximum centre-of-mass energy of $\sqrt{s} = 1.96\,\text{TeV}$. There were two experiments located around the ring, namely CDF (Collider Detector at Fermilab) [113] and DØ [114]. One of the most noteworthy contributions of the Tevatron was the discovery of the top quark in 1995 [115, 116], but the first measurements of hadronic WW production cross sections were also made.
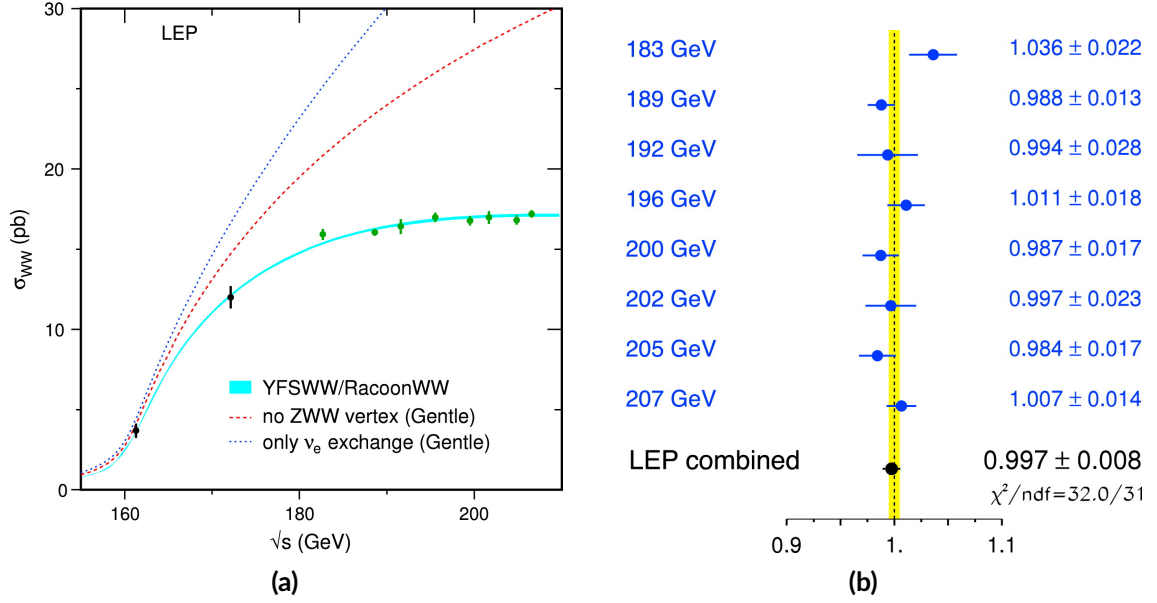
Figure 2.5: **(a)** The total WW production cross section as a function of the centre-of-mass energy $\sqrt{s}$, both measured in data and calculated using the YFSWW [110] and RacoonWW [111] generators including all diagrams, and the GENTLE [112] program without the W^+W^-Z vertex or with only the ν_e exchange t-channel diagram. The blue shaded area indicates the theoretical uncertainty on the prediction. **(b)** The fitted ratio of the measured cross section to that predicted by the RacoonWW generator for each centre-of-mass energy separately and combined. The yellow band indicates the theoretical uncertainty. Adapted from [109].

Evidence for W boson pair production in fully-leptonic final states at $\sqrt{s} = 1.8\,\text{TeV}$ was obtained in 1997 by the CDF collaboration using $108\,\text{pb}^{-1}$ of data collected during the Tevatron Run-I [117]. A jet veto was applied, whereby events were rejected if they contained reconstructed jets with a transverse momentum above $10\,\text{GeV}$, in order to reduce background from $t\bar{t}$ production. A total of 3.8 signal events were observed, corresponding to a total inclusive cross section of

$$\sigma(p\bar{p} \to W^+W^-, \ \sqrt{s} = 1.8\,\text{TeV}) = 10.2^{+6.3}_{-5.1}\,(\text{stat.}) \pm 1.6\,(\text{syst.})\,\text{pb},$$

with a combined relative uncertainty of about 60%. The result was found to be consistent with the NLO theoretical predictions. Subsequent measurements of this process were made by both the DØ [118, 119] and CDF [120, 121] collaborations at $\sqrt{s} = 1.96\,\text{TeV}$ during Run-II, with the highest precision of about 15% achieved by CDF in 2010 [121]. The final inclusive cross section was measured in a fit to be

$$\sigma(p\bar{p} \to W^+W^-, \ \sqrt{s} = 1.96\,\text{TeV}) = 12.1 \pm 0.9\,(\text{stat.})^{+1.6}_{-1.4}\,(\text{syst.})\,\text{pb},$$

using $3.6\,\text{fb}^{-1}$ of data, corresponding to about 334 signal events. This was found to be in agreement with the SM prediction. A later analysis using the full Run-II dataset of $9.7\,\text{fb}^{-1}$ was presented in 2015 [122], with a reduction in the total relative uncertainty to about 10%. A multivariate discriminator was used to separate signal from background, and an iterative unfolding method, discussed further in Section 5.4.3, was used to correct for detector effects to obtain the first differential cross
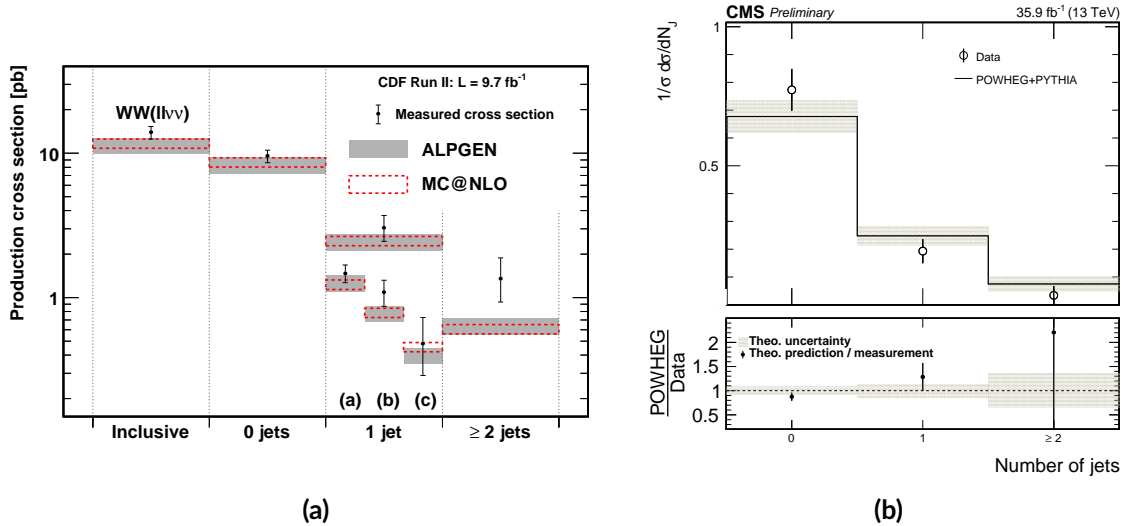
Figure 2.6: **(a)** The jet multiplicity and leading jet energy distributions obtained by the CDF collaboration. The cross section in the one jet phase space is measured in bins of the leading jet transverse energy, E_T, corresponding to (a) $15 < E_T < 25\,\text{GeV}$, (b) $25 < E_T < 45\,\text{GeV}$ and (c) $E_T > 45\,\text{GeV}$. The measured distributions are compared to predictions from the MC@NLO [93] and ALPGEN [123] generators. Taken from [122]. **(b)** The normalised jet multiplicity distribution obtained by CMS. The result is compared to a POWHEG+PYTHIA [89, 90, 94, 95] prediction, with the lower panel showing the ratio of the prediction to the measurement. Taken from [9].

sections in jet multiplicity and leading jet energy, as shown in Figure 2.6a.

2.2.3 Measurements at the LHC

A number of measurements of $pp \rightarrow W^+W^-$ cross sections with fully-leptonic final states have been made by both the ATLAS and CMS collaborations since 2011 at centre-of-mass energies of $\sqrt{s} = 7\,\text{TeV}$ [6, 7, 124–126], $\sqrt{s} = 8\,\text{TeV}$ [127–130] and $\sqrt{s} = 13\,\text{TeV}$ [8, 9, 131]. As with most measurements at the Tevatron, the majority of these analyses placed restrictions on the amount of hard jet activity in order to suppress the background from $t\bar{t}$ events. Extrapolation factors were usually applied to obtain fully inclusive cross section results. Differential fiducial cross section results were obtained for phase spaces with at most one hard jet in the final state.

Measurements at $\sqrt{s} = 7\,\text{TeV}$ were made by the ATLAS and CMS detectors using $4.6\,\text{fb}^{-1}$ and $4.9\,\text{fb}^{-1}$ of data respectively [6, 7]. A jet veto was applied in both cases. The measured total cross sections had a relative uncertainty of about 9% for both detectors, with the ATLAS result obtained in a fit being given by

$$\sigma(pp \rightarrow W^+W^-,\ \sqrt{s} = 7\,\text{TeV}) = 51.9 \pm 2.0\,(\text{stat.}) \pm 4.4\,(\text{syst.})\,\text{pb},$$

consistent with the theoretical predictions. The most recent ATLAS measurement [8] of integrated and differential fiducial cross sections was also performed in a jet veto phase space with a jet p_T threshold of $35\,\text{GeV}$, requiring one electron and one muon in the final state, and using $36.1\,\text{fb}^{-1}$ of data corresponding to about 7,690 expected signal events. The integrated fiducial cross section result was obtained using a cut-based analysis where an extrapolation factor was used to correct
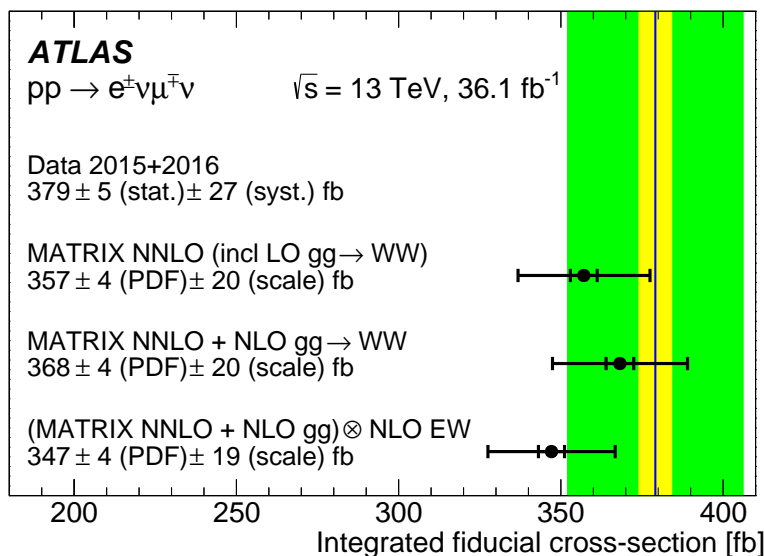
ATLAS
$pp \rightarrow e^{\pm}\nu\mu^{\mp}\nu$ $\sqrt{s}$ = 13 TeV, 36.1 fb^{-1}

Data 2015+2016
379 ± 5 (stat.)± 27 (syst.) fb

MATRIX NNLO (incl LO $gg \rightarrow$ WW)
357 ± 4 (PDF)± 20 (scale) fb

MATRIX NNLO + NLO $gg \rightarrow$ WW
368 ± 4 (PDF)± 20 (scale) fb

(MATRIX NNLO + NLO gg)$\otimes$ NLO EW
347 ± 4 (PDF)± 19 (scale) fb

Integrated fiducial cross-section [fb]

Figure 2.7: The integrated fiducial cross section measured in $W^+W^- \rightarrow e^{\pm}\nu_e\mu^{\mp}\nu_{\mu}$ events with an applied jet veto. Statistical uncertainties are shown by the yellow band, whereas the green band additionally includes systematic uncertainties. Also shown are three NNLO QCD theoretical predictions using the MATRIX framework [77], including two with the NLO gg-induced calculation [70], and one also including NLO EW effects [62]. The inner bar corresponds to PDF uncertainties, whereas the outer bar also includes scale uncertainties. Taken from [8].

for detector effects. The final result was

$$\sigma^{\mathrm{fid}}(pp \rightarrow W^+W^- \rightarrow e^{\pm}\nu_e\mu^{\mp}\nu_{\mu},\ \sqrt{s} = 13\,\mathrm{TeV}) = 379.1 \pm 5.0\,(\mathrm{stat.}) \pm 26.6\,(\mathrm{syst.})\,\mathrm{fb},$$

with a corresponding total relative uncertainty of about 7%. This result is shown and compared to theoretical predictions in Figure 2.7, where good agreement is seen.

In addition to jet veto measurements, a selection of analyses allowed for additional hard jets in the measurement phase space [9, 129, 130]. Cuts were still applied on the number of b-tagged jets in order to reduce the background from $t\bar{t}$ events, using techniques similar to those that will be described in Section 4.5.3. Excluding the measurements to be discussed in Chapters 6 and 7, the most recent ATLAS analysis to use a one jet requirement measured both fiducial and inclusive cross sections at $\sqrt{s} = 8\,\mathrm{TeV}$ [130]. The one jet integrated fiducial cross section was obtained in a simultaneous fit to data combining information from a previous jet veto measurement [128] as

$$\sigma^{\mathrm{fid}}(pp \rightarrow W^+W^- \rightarrow e^{\pm}\nu_e\mu^{\mp}\nu_{\mu},\ \sqrt{s} = 8\,\mathrm{TeV}) = 136 \pm 6\,(\mathrm{stat.}) \pm 14\,(\mathrm{syst.})\,\mathrm{fb},$$

with a total relative uncertainty of about 15%, in agreement with theoretical predictions. CMS recently performed a measurement of differential cross sections including at most one jet in the fiducial phase space at $\sqrt{s} = 13\,\mathrm{TeV}$ using an integrated luminosity of 35.9 fb^{-1} [9]. Two analyses were performed in which background contributions were reduced using either kinematic cuts or a multivariate technique. In both cases the signal normalisation was extracted in a fit across a number of signal and control regions, with the normalisation multiplied by the NNLO theoretical prediction [68] to give the final result. The cut-based analysis gave a result for the total inclusive cross section

of

$$\sigma(pp \to W^+W^-, \sqrt{s} = 13\,\text{TeV}) = 117.6 \pm 1.4\,(\text{stat.}) \pm 6.6\,(\text{syst.})\,\text{pb},$$

with a total relative uncertainty of about 6%. Cross section measurements were also presented for a fiducial region containing at most one jet, and for a jet veto fiducial region where the jet p_T threshold was varied, both of which were obtained using fits. In addition to differential cross section measurements in a fiducial phase space with at most one jet, the jet multiplicity was measured differentially as shown in Figure 2.6b.

3

The ATLAS detector

The results presented in this thesis use data collected by ATLAS, one of the four detectors found along the ring of the LHC, located at CERN near the city of Geneva, Switzerland. In this chapter, components of the ATLAS detector that allow for the identification of particles produced in pp collisions will be summarised in some detail. The interpretation of the signals produced in the various detector components in terms of final state physics objects will be discussed in Chapter 4.

3.1   The Large Hadron Collider

The LHC [5] is the most recent addition to the accelerator arsenal located at CERN, and is the world's largest and highest-energy hadron-hadron accelerator and collider. It is a circular synchroton with a circumference of 27 km located on average some 100 m beneath the France-Switzerland border. Construction of the LHC took place between 1998 and 2008, with the tunnel and much of the existing infrastructure left over from LEP [103] being reused. The LHC became operational in 2008, with the first pp collisions taking place in 2009 at a centre-of-mass energy of $\sqrt{s} = 900$ GeV, eventually reaching 2.36 TeV and therefore surpassing the previous $p\bar{p}$ record of 1.96 TeV held by the Tevatron [104]. Early 2010 saw the beginning of the main physics program, with collisions reaching $\sqrt{s} = 7$ TeV.

Periods during which particle collisions are taking place at the LHC are referred to as *runs*, and are interspersed with periods of maintenance and upgrades referred to as *shutdowns*. Collisions mostly take place between pairs of protons, although for smaller time periods during a run, collisions between pairs of heavy ions, or between protons and heavy ions, may also be facilitated. So far, there have been two run periods, with Run-I colliding protons at a maximum $\sqrt{s} = 8$ TeV and the most recent Run-II achieving $\sqrt{s} = 13$ TeV. At the time of writing, the LHC is emerging from the Long Shutdown (LS) 2, during which time preparations have been made for Run-III, expected

to commence in mid-2022, as well as for the High Luminosity LHC (HL-LHC), the successor to the LHC expected to be operational at the end of 2027 at the earliest.

3.1.1 LHC accelerator complex

Protons are accelerated in stages before being injected into the main LHC ring where they undergo an additional acceleration to reach the final target collision energy. In the initial stages, negatively charged hydrogen ions (H^-) are accelerated to 160 MeV by the Linac4 [132] linear accelerator, before their outer electrons are stripped and they are accelerated further to 2 GeV by the Proton Synchrotron Booster (PSB), to 26 GeV by the Proton Synchrotron (PS), and to 450 GeV by the SPS. The final accelerating stage happens inside the main LHC ring itself. A diagram showing the LHC and its associated accelerator system is given in Figure 3.1.

The main LHC ring consists of two parallel beamlines with the protons in each beam made to accelerate in opposite directions. Acceleration is facilitated by a series of superconducting radio frequency (RF) cavities whose electric fields are made to oscillate at a frequency of 400 MHz. This produces a set of proton bunches, separated in time by 25 ns, with each proton carrying close to the target energy of 6.5 TeV. Protons are maintained on their circular paths via 1,232 superconducting dipole magnets with a strength of 8.3 T located at various points around the ring, whilst an additional 392 quadrupole magnets keep the proton beams focused. Additional quadrupole magnets help to further focus the proton beams prior to collision [133].

Accelerated particles are brought to collide at four points around the main LHC ring, where the properties of particles produced in such collisions are measured. Each of the detectors, ALICE (A Large Ion Collider Experiment) [134], ATLAS [4], CMS [135] and LHCb (LHC beauty) [136] is associated with its own collision point. ATLAS and CMS are general purpose detectors, whilst ALICE and LHCb are specialised to heavy ion and b quark physics respectively.

3.1.2 Luminosity and pile-up

In the context of particle collisions, the luminosity is related to the number of events expected to be observed for a given process. The instantaneous luminosity, L, is the constant of proportionality between the number of events expected per second and the cross section, σ,

$$\frac{dN}{dt} = L\sigma, \tag{3.1}$$

which motivates the definition of the integrated luminosity, $\mathcal{L}$, as

$$\mathcal{L} = \int dt\, L = \frac{N}{\sigma}. \tag{3.2}$$

Here, N is the total number of events expected for a given process over a given time period. The instantaneous luminosity for collisions of bunches of protons may be expressed in closed form under the Gaussian beam approximation as [138]

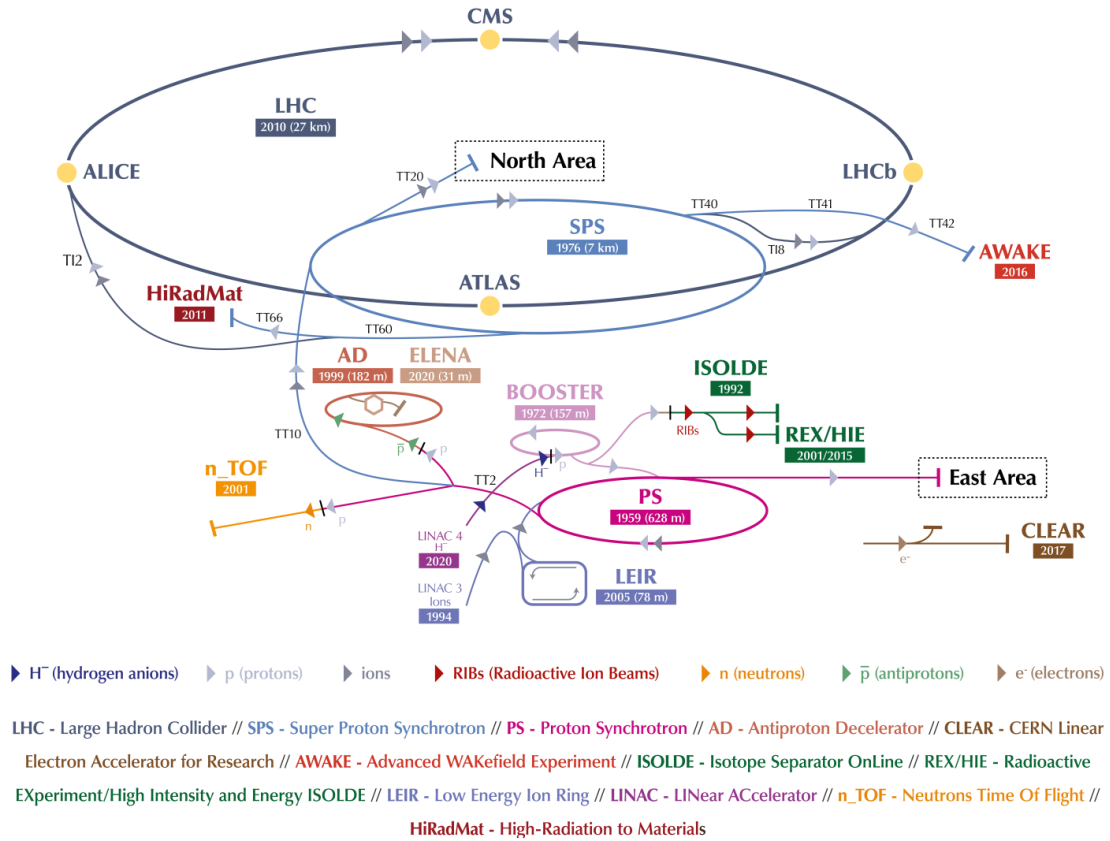$$L = \frac{n_b^2 N_b f}{4\pi w^2}, \tag{3.3}$$

Figure 3.1: The LHC and its accelerator system. As described in the text, particles are accelerated in stages using the Linac4, PSB, PS and SPS systems before being injected into the main LHC ring where they undergo a final acceleration. Adapted from [137].

where n_b is the number of protons per bunch, N_b is the number of bunches per beam, f is the revolution frequency, and w is the beam width. Some additional assumptions have been made for simplicity, including amongst others that the number of protons in each colliding bunch is the same, the beams have circular cross sections, the collision is head-on, and the bunch crossing angle is zero. Additional parameters may be included that account for deviations from these assumptions. Notwithstanding these corrections, the expression in Eq. (3.3) shows how the luminosity may be enhanced by increasing the number of protons per bunch, the number of bunches, the revolution frequency, or by reducing the beam width. Currently the LHC bunches contain on the order of 10^{11} protons each, and are a few micrometres in width. There are 2,808 bunches per proton beam with a revolution frequency of 11 kHz, corresponding to an instantaneous luminosity of the order $10^{34}\,\mathrm{cm}^{-2}\,\mathrm{s}^{-1}$ ($10\,\mathrm{nb}^{-1}\,\mathrm{s}^{-1}$). This luminosity is calibrated in so-called van der Meer scans [139], along with the effective beam width. The increase in the integrated luminosity recorded at the LHC over the Run-II data-taking period is shown in Figure 3.2a.

Due to the fact that large bunches of protons are made to collide at a given interaction point (IP), it is often the case that there are multiple pp interactions in a typical event, or bunch crossing. Many of these interactions will be soft and hence uninteresting from the point of view of producing high mass resonances. However, they can produce final state particles whose detector signals overlap with those from the main HS process, and so must be accounted for. Additional inelastic
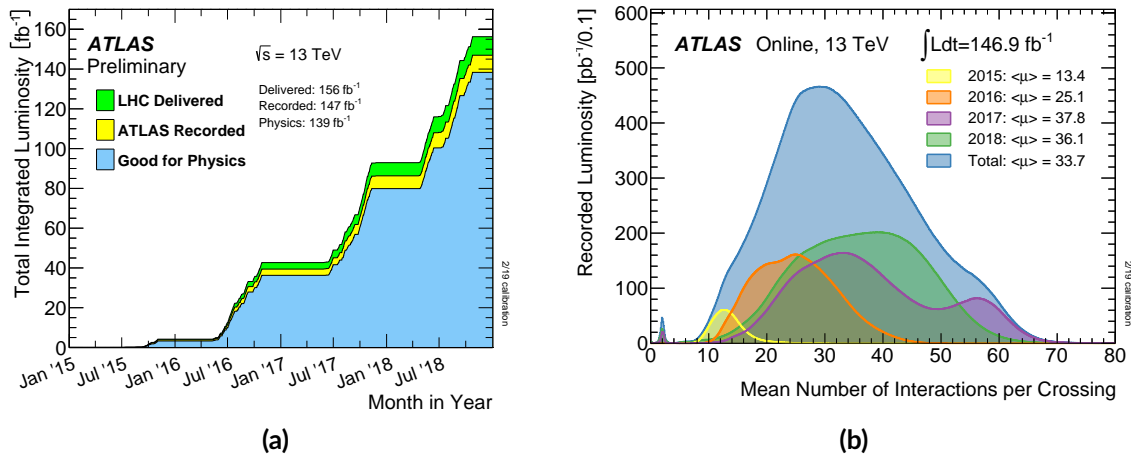
Figure 3.2: (a) The integrated luminosity delivered by the LHC during Run-II, compared to the luminosity recorded by the ATLAS detector, and that useful for physics analysis. **(b)** The luminosity-weighted mean number of pp interactions per bunch crossing, shown for the whole of Run-II and for each year separately. Also shown is the $\langle\mu\rangle$ value for each data-taking year, and the total luminosity recorded by ATLAS for the Run-II period. Taken from [140].

pp interactions in a given bunch crossing produce detector signals referred to as in-time pile-up (PU). Due to time delays between the interaction of a particle in the detector and the subsequent readout, in-time PU events from previous bunch crossings can influence the measurements made in future bunch crossings. Such additional PU is referred to as out-of-time PU. The mean number of pp interactions per bunch crossing, μ, in general varies throughout a run, as shown in Figure 3.2b. The mean value of μ for the whole of Run-II was $\langle\mu\rangle = 33.7$ [140]. Its value in general increases with the luminosity and so is expected to be larger for the HL-LHC. Higher numbers of interactions per bunch crossing are desirable in searches for rare processes whose cross sections are expected to be small, but may present challenges for more exclusive analyses due to the increased PU.

3.2 The ATLAS detector

The ATLAS detector is the largest of the four detectors at the LHC. It is a general purpose detector and therefore seeks to record the properties of all the particles produced in pp collisions with the highest possible accuracy and precision. The ATLAS detector is divided into several sub-components forming layers around the IP. The sub-detectors in general consist of a single barrel and two end-cap regions, together providing an almost 4π coverage in solid angle around the IP. This allows for the reconstruction of particles produced at almost any angle from a given pp collision. The ATLAS sub-detectors include the inner detector (ID), providing tracking information for charged particles, the EM and hadronic sampling calorimeters, and the muon spectrometer (MS). A diagram of the ATLAS detector is shown in Figure 3.3.

3.2.1 Coordinate system

The LHC has a toroidal geometry. The ATLAS coordinate system is defined with the x-axis directed towards the centre of the LHC ring, and the y-axis directed vertically upwards. The z-axis
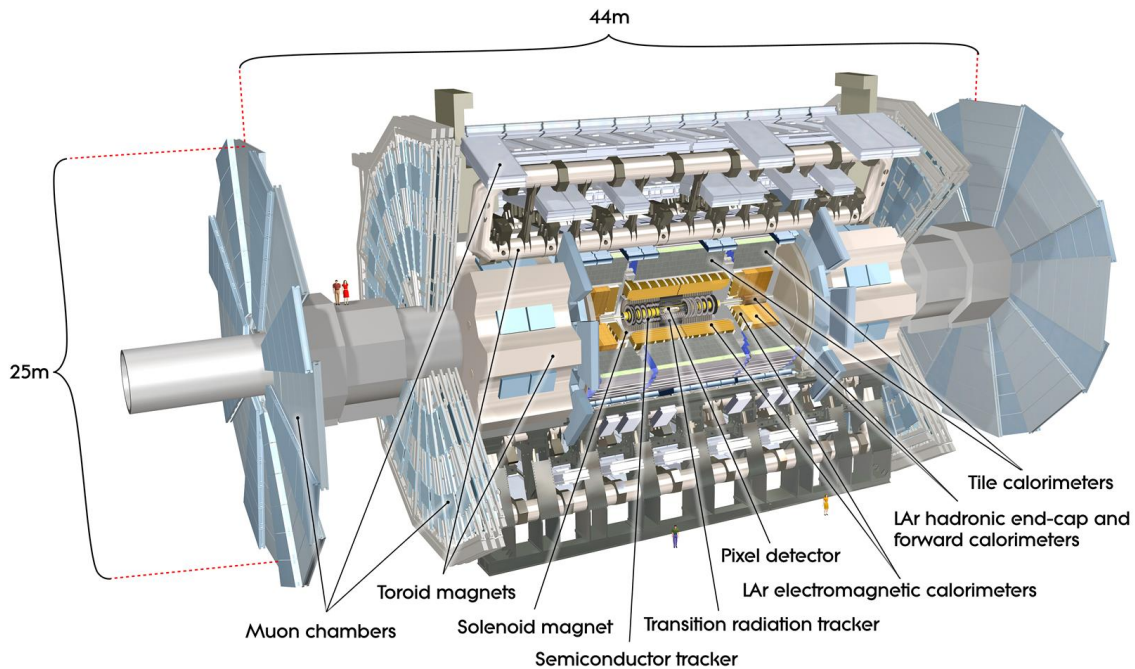
Figure 3.3: The ATLAS detector. The pixel detector, semiconductor tracker (SCT) and transition radiation tracker (TRT) make up the ID, which is surrounded by solenoid magnets. The next layer contains the EM and hadronic calorimeters, surrounded by toroid magnets and muon chambers. Taken from [141].

is oriented according to the right-hand rule, and hence is parallel to the beam axis. The azimuthal and polar angles, ϕ and θ, are defined with respect to the x- and z-axis respectively, as shown in Figure 3.4a. The symbol R is used to refer to distances perpendicular to the beam axis. Usually the angle θ is substituted for the pseudorapidity, η, defined as

$$\eta = -\ln\left[\tan\left(\frac{\theta}{2}\right)\right] = \frac{1}{2}\ln\left(\frac{|\boldsymbol{p}| + p_z}{|\boldsymbol{p}| - p_z}\right). \tag{3.4}$$

The second equality expresses η in terms of the momentum, $\boldsymbol{p}$, of a particle of mass m and energy E travelling at the polar angle θ such that its longitudinal momentum is $p_z = |\boldsymbol{p}|\cos\theta$. In the high energy limit, $E \approx |\boldsymbol{p}| \gg m$, this definition of η coincides with that of the rapidity, y, associated with a longitudinal boost to the frame in which the momentum of the particle has only transverse components, that is

$$y = \frac{1}{2}\ln\left(\frac{E + p_z}{E - p_z}\right) \approx \eta \quad \text{for} \quad |\boldsymbol{p}| \gg m. \tag{3.5}$$

Differences in y are Lorentz invariant, whilst differences in η are only Lorentz invariant in the massless or high energy limit. It is in general easier to measure η since it depends only on geometrical quantities, but y may be more appropriate for composite objects such as jets whose mass cannot be neglected [142]. Values of θ and the corresponding values of η are shown in Figure 3.4b. The Lorentz invariant measure of angular separation between two objects may be calculated from
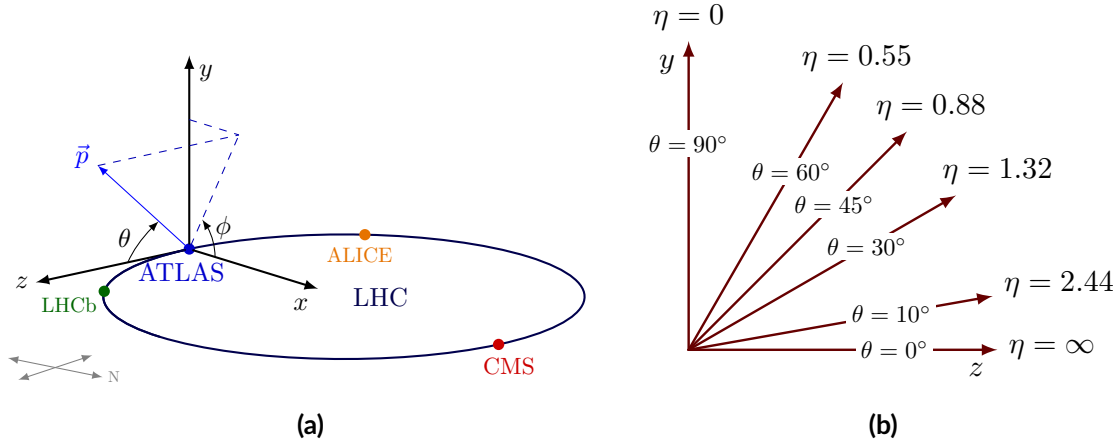
Figure 3.4: The ATLAS coordinate system. **(a)** The orientation of the x-, y- and z-axis, along with the angles ϕ and θ. **(b)** Values of θ and the corresponding values of pseudorapidity, η. Taken from [143].

differences in their y, or η, and ϕ values as

$$\Delta R = \sqrt{(\Delta y)^2 + (\Delta\phi)^2} \approx \sqrt{(\Delta\eta)^2 + (\Delta\phi)^2}, \tag{3.6}$$

where again the approximation corresponds to the limit of massless or high energy particles.

In pp collisions, the interacting particles are usually the constituent partons which carry an unknown fraction of the longitudinal momentum of the proton. As a result, the total initial momentum in the longitudinal direction is unknown, so conservation of momentum along the z-axis cannot be used to infer the presence of undetected particles. On the other hand, to a very good approximation, the constituent partons involved in the HS process carry no momentum in the transverse plane. Consequently, the transverse projection of the momentum, known as the transverse momentum and denoted by p_T, is the quantity of interest for many physics analyses. So-called missing transverse momentum, with magnitude p_T^{miss}, may be calculated using transverse momentum conservation, and can be used to infer the presence of additional undetected particles, such as neutrinos, as will be discussed in more detail in Chapter 4. Meanwhile, events containing final state particles with large values of p_T indicate hard collisions, potentially corresponding to the production of heavy resonances.

3.2.2 Inner detector

The purpose of the ID [144, 145] is to measure in a non-destructive manner the charge and momentum of electrically charged particles produced at the IP. Charged particles passing through the ID layers deposit energy as a series of discrete points called hits, which may be used to determine the particle trajectory as well as the location of its primary and, in the case of particles such as B hadrons and τ leptons, secondary decay vertices. The ID is 2.3 m in diameter and 7 m in length, consisting of the pixel detector, semiconductor tracker (SCT) and transition radiation tracker (TRT), as shown in Figure 3.5, and provides a coverage over $|\eta| < 2.5$. It is surrounded by a superconducting solenoid magnet system providing a 2 T magnetic field parallel to the beamline
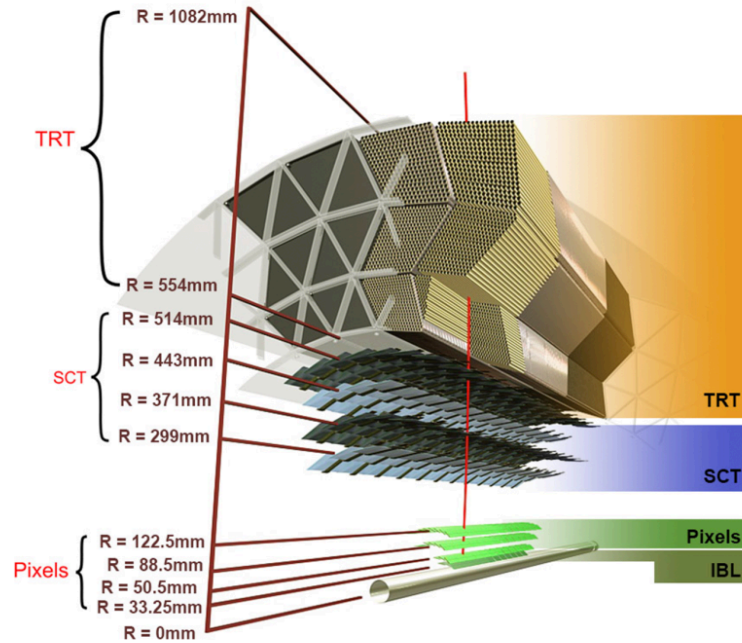
Figure 3.5: The ATLAS ID barrel layers. The insertable B-layer (IBL) surrounds the beam pipe, followed by three further layers making up the pixel detector. This is surrounded by the four layers of the SCT and the straw tubes of the TRT. Taken from [146].

for bending the paths of charged particles in the transverse plane.

Pixel detector

The pixel detector [147, 148] is the innermost layer of the ID. The active region of the detector consists of three layers parallel to the z-axis, referred to as barrel layers, as well as disc layers perpendicular to the beam axis forming a pair of end-caps with three layers each. The layers consist of a set of modules containing the silicon semiconductor sensors, read-out chips and other electronics. Incident ionising particles generate electron-hole pairs in the silicon, which migrate under an electric field to produce a signal. The nominal pixel size is $50\,\mu$m $\times$ $400\,\mu$m ($R\phi \times z$), corresponding to about 80.4 million read-out channels in the barrel. The intrinsic resolution is $10\,\mu$m $\times$ $115\,\mu$m ($R\phi \times z$), thus providing very high precision tracking information close to the IP. In preparation for Run-II, a fourth layer known as the insertable B-layer (IBL) [149] was added between a smaller radius beam pipe and the first pixel layer (B-layer). The main motivation for this instalment was to counteract possible irreversible radiation damage to the B-layer, as well as to provide improved impact parameter reconstruction for tagging of B hadrons.

Semiconductor tracker

The pixel detector is surrounded by the SCT [150], which is composed of narrow silicon microstrips utilising similar semiconductor technology to the pixel detector. There are four cylindrical layers forming the barrel region, with nine discs in each of the two end-caps. The silicon sensors in the barrel layers have a length of about 6 cm (z) with a constant read-out strip pitch of $80\,\mu$m ($R\phi$).

There are two such sensors on each side of a module with a stereo angle of 40 mrad, with the offset providing a 2D space-point for each layer of the SCT. In total the SCT comprises approximately 6.3 million read-out channels, with an intrinsic spatial resolution of $17\,\mu\mathrm{m} \times 580\,\mu\mathrm{m}$ ($R\phi \times z$).

Transition radiation tracker

The TRT [151, 152] is the final layer of the ID. It consists of barrel and end-cap regions composed respectively of 73 and 2×160 layers of 4 mm diameter proportional drift tubes, also known as straws. At the centre of each straw is a $31\,\mu\mathrm{m}$ diameter gold-plated tungsten wire, with the straw wall held at a potential difference of $-1.5\,\mathrm{kV}$ with respect to the wire. The space within each straw is filled with a 70% Xe gas mixture, which becomes ionised when traversed by a charged particle. The free electrons drift under the electric field towards the anode wire, generating a signal. The drift time may be used to infer the drift circle radius. Polypropylene fibres occupy the spaces between the straws resulting in transition radiation. This is the emission of X-ray photons by highly relativistic charged particles when traversing a material boundary. These photons are absorbed by Xe atoms, increasing the energy in the gas and generating larger signals. Since the transition radiation effect is strongest for electrons, given that the amount of transition radiation increases with the Lorentz factor, the TRT can provide particle identification information. In the barrel region, there are 52,544 straws of length 144 cm oriented parallel to the beam axis, whereas for each end-cap, there are 122,880 straws of length 37 cm oriented radially, corresponding to around 350,000 read-out channels in total. The intrinsic resolution is $130\,\mu\mathrm{m}$ ($R\phi$), which although larger than the silicon detectors, is somewhat compensated for by a larger number of hits per track.

3.2.3 Calorimeters

Surrounding the ID is the calorimeter system [153], consisting of the EM calorimeter (ECal) and hadronic calorimeter (HCal), as shown in Figure 3.6. As with the ID, the calorimeters are divided into barrel and end-cap regions, providing a coverage of $|\eta| < 4.9$. The purpose of the calorimeters is to measure the energy of both charged and neutral particles, including electrons, photons and hadrons. Unlike the ID, the measurement process is inherently destructive in the sense that the energy of the incident particles is fully absorbed by the detector material. This manifests itself as a cascade, or shower, of secondary particles. ATLAS uses sampling calorimeters, whereby the material that produces the shower is separate from the material that measures the deposited energy[1].

Calorimeter showers

The development of a calorimeter shower depends on the incident particle and the absorbing material [155]. For EM showers, the dominant material interaction for electrons with an energy greater than about 1 GeV is radiation, or bremsstrahlung, resulting in photons. At high energies, such photons predominately undergo pair production, generating electron-positron pairs which radiate further photons. The particle multiplicity increases until the critical energy threshold, E_C, is reached[2]. The radiation length, X_0, characterises the longitudinal shower shape, and corresponds

---

[1]This is distinct from homogeneous calorimeters, where a single medium performs both functions.
[2]E_C is the energy at which the rate of energy loss from ionisation equals that due to bremsstrahlung.
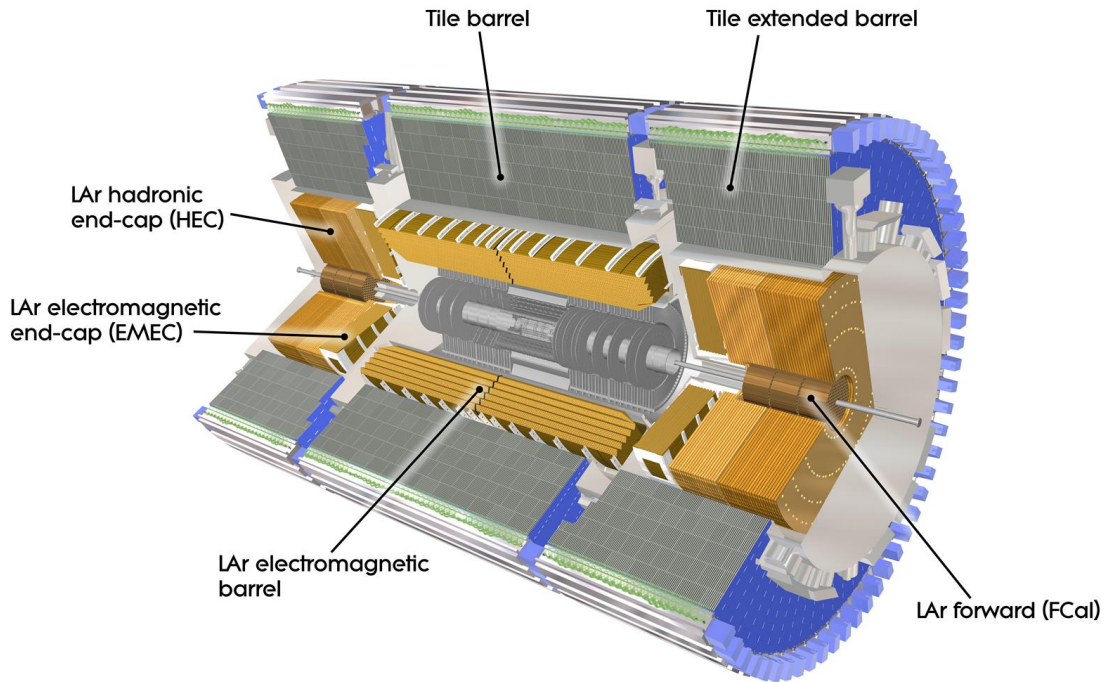
Figure 3.6: The ATLAS calorimeters, consisting of the EM and tile barrels, EM and hadronic end-caps, and the forward calorimeter (FCal). Taken from [154].

to the average distance over which an electron loses 63% of its energy. Lateral shower development is driven by multiple scattering at low X_0, with more isotropic processes dominating at high X_0, and is characterised by the Molière radius, $\rho_M \sim X_0/E_C$.

Hadronic showers involve strong interactions in addition to EM interactions, and so the shower development is in general more complex. Neutral pions may be produced that decay primarily into photon pairs, which generate EM showers. Nuclear interactions also involve undetectable energy deposits, where the missing energy may used in overcoming the nuclear binding energy or is carried by neutrinos. The hadronic shower shape is parameterised in terms of the average distance a hadron travels before undergoing a nuclear interaction, known as the nuclear interaction length, λ_{int}. Due to invisible energy, the ATLAS calorimeters are non-compensating, meaning that the ratio, e/π, of the EM to hadronic signal for showers of the same energy is greater than unity.

Electromagnetic calorimeter

The ATLAS ECal [156] is composed of alternating layers of lead absorber and active liquid argon (LAr) with read-out electrodes arranged in an accordion geometry in order to provide complete ϕ coverage without azimuthal cracks, as shown in Figure 3.7a. The barrel region extends to $|\eta| = 1.475$, and the EM end-caps (EMECs) are divided into two coaxial wheels, with the outer wheel covering $1.375 < |\eta| < 2.5$ and the inner wheel covering $2.5 < |\eta| < 3.2$. The calorimeter is divided into at most three separate sections of varying depth and granularity. For $|\eta| < 1.8$, an additional LAr presampler layer with granularity 0.025×0.1 ($\Delta\eta \times \Delta\phi$) provides a sampling for particles that start showering before the EM calorimeters in order to correct for upstream energy
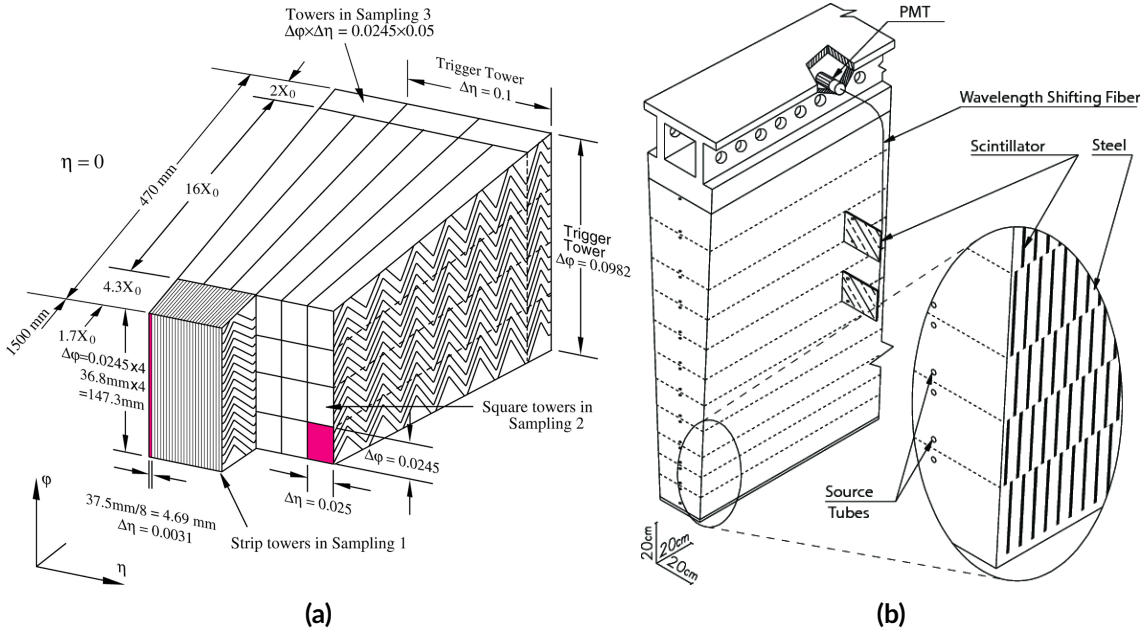
Figure 3.7: The ATLAS ECal and tile calorimeter. **(a)** A section of the ECal in the barrel region for $\eta = 0$ with its accordion geometry, showing three sampling layers and the trigger towers with their thicknesses and granularity. **(b)** A section of the tile calorimeter in the barrel showing the alternating steel and scintillator layers and read-out devices. The source tubes are used for calibration. Taken from [4].

losses [157], and has a thickness of 1.1 cm ($0.08X_0$) and 0.5 cm ($0.04X_0$) in the barrel and end-cap regions respectively. The first calorimeter layer has a relatively high granularity of $0.025/8 \times 0.1$ ($\Delta\eta \times \Delta\phi$) for $|\eta| < 1.4$ in order to distinguish between prompt photon showers and those from neutral pion decays. The most forward region of $2.5 < |\eta| < 3.2$ has a coarser granularity of 0.1×0.1 ($\Delta\eta \times \Delta\phi$). The total thickness of the ECal is approximately $22X_0$ in the barrel and $24X_0$ in the end-caps. There are over 170,000 read-out channels in total. The EM forward calorimeter (FCal) covers $3.1 < |\eta| < 4.9$. It consists of a single layer with electrode rods parallel to the beam axis embedded in an absorbing copper matrix. A small gap between the rods and the outer copper tubes is filled with LAr, providing the active medium. The granularity of the EM FCal for most of the η range is $3.0\,\text{cm} \times 2.6\,\text{cm}$ ($\Delta x \times \Delta y$).

Hadronic calorimeter

The HCal [158] consists of alternating layers of steel absorbers and active scintillating tiles with the central barrel region covering $|\eta| < 1.0$, and the two extended barrel sections covering $0.8 < |\eta| < 1.7$. The scintillating tiles are arranged in the plane perpendicular to the beam direction as shown in Figure 3.7b, and at $\eta = 0$ provide a depth of about $9.7\lambda_{\text{int}}$. This is sufficient to absorb most of the energy deposited by hadrons and to limit punch-through to the MS. A signal is produced by reading both sides of the tiles with wavelength shifting fibres into two separate photomultiplier tubes (PMTs). There are three layers in the tile, with a typical granularity of 0.1×0.1 ($\Delta\eta \times \Delta\phi$). The total number of read-out channels is about 10,000. The hadronic end-caps (HECs) are copper-LAr sampling calorimeters divided into two coaxial wheels of four layers each,
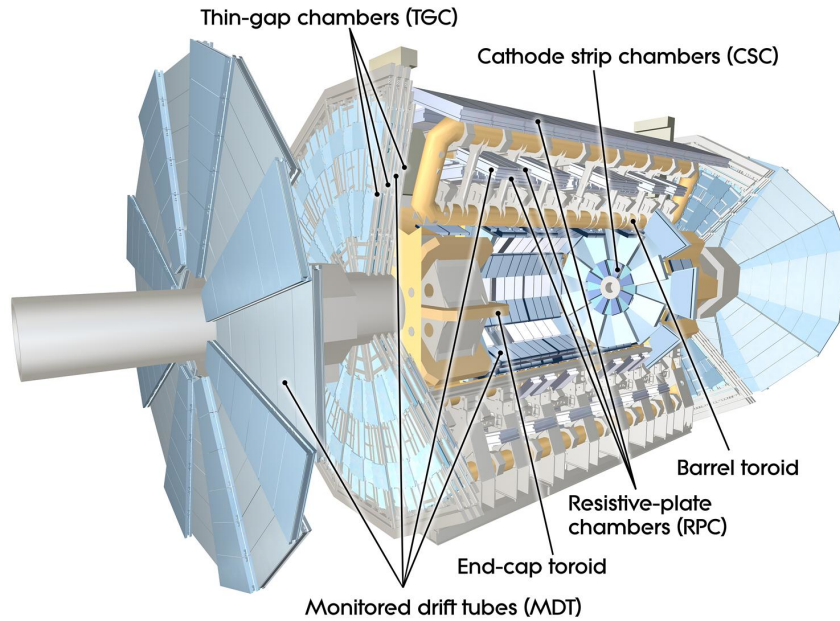
Figure 3.8: The ATLAS muon system, consisting of the barrel and end-cap toroids, MDTs and CSCs for precision tracking, and RPCs and TGCs for triggering. Taken from [160].

providing a coverage of $1.5 < |\eta| < 3.2$. As with the ECal, the coverage of the HCal is extended to $|\eta| = 4.9$ with the hadronic FCal, consisting of two layers of tungsten-LAr calorimeters with the same structure as the EM FCal. For most of the η coverage, the granularity is $3.3\,\text{cm} \times 4.2\,\text{cm}$ ($\Delta x \times \Delta y$) for the first layer, and $5.4\,\text{cm} \times 4.7\,\text{cm}$ ($\Delta x \times \Delta y$) for the second layer.

3.2.4 Muon spectrometer

Muons do not interact significantly with either the ECal or HCal. This is due to their relatively large mass, corresponding to a critical energy of the order $100\,\text{GeV}$, making them minimum-ionising particles (MIPs). Consequently muons are detected in the dedicated MS [159]. This detector system involves three superconducting air-core toroidal magnets with eight coils each for deflecting the muons, as well as monitored drift tubes (MDTs), cathode strip chambers (CSCs), resistive plate chambers (RPCs) and thin gap chambers (TGCs) for precision tracking in $|\eta| < 2.7$, and triggering over $|\eta| < 2.4$, as shown in Figure 3.8. The muon chambers in the barrel are arranged in three concentric cylindrical shells and form octants divided into a large and a small sector overlapping slightly in ϕ. There are four layers of chambers in each of the two end-caps.

Monitored drift tubes

The MDTs cover $|\eta| < 2.7$ for all but the innermost layer, where the coverage is for $|\eta| < 2.0$, and provide most of the precision muon tracking. Each chamber consists of three to eight layers of pressurised drift tubes, filled with 97% Ar and containing a $50\,\mu\text{m}$ tungsten-rhenium anode wire. The tubes are arranged along the ϕ direction in both the barrel and end-caps. There are in total 1,088 MDT chambers with a resolution of $80\,\mu\text{m}$ per tube.

Cathode strip chambers

Precision tracking in the range $2.0 < |\eta| < 2.7$ is covered by the CSCs, where the higher particle density prevents the use of MDTs. They are multiwire proportional chambers, with the wires oriented radially. One set of cathode strips is oriented parallel to the wires, with the other set perpendicular. The hit position may be obtained by interpolating between the charges induced on neighbouring cathode strips. There are 32 chambers in total, with a resolution of $40\,\mu$m in the bending plane and 5 mm in the transverse plane.

Resistive plate chambers

The RPCs constitute one of the two types of muon trigger chambers, the other being the TGCs. The trigger will be discussed in more detail in Section 3.2.5. The main purpose of the trigger chambers is to provide fast information on the multiplicity and energy range of muon tracks, which cannot be provided by the MDTs or CSCs due to the long drift time. There are three layers of RPCs in the barrel with a total of 260 chambers, providing a coverage of $|\eta| < 1.05$. Each RPC is a gaseous parallel electrode-plate detector, with an applied electric field of about $4.9\,\text{kVmm}^{-1}$. Ionised particles create avalanches that register on the 2 mm separated plates as electrical signals. Orthogonal strips provide positional information in both η and ϕ, and the typical space-time resolution is 1 cm $(R\Delta\phi) \times 1$ ns.

Thin gap chambers

The TGCs cover the end-cap region $1.05 < |\eta| < 2.4$. In addition to trigger capabilities, the TGCs provide an azimuthal coordinate to complement the η coordinate given by the MDTs. The TGC system consists of 3,588 multiwire proportional chambers, with a 2.8 cm gap and 1.8 mm spacing between the wires, providing a typical time resolution smaller than the 25 ns bunch crossing time.

3.2.5 Trigger system

Since the typical pp collision rate is much higher than the rate at which data can be written to disk, and storage space is limited, it is necessary to select only the most interesting subset of available events for future study. This is the purpose of the ATLAS trigger system [161], which provides such a decision on an event-by-event basis. The trigger and data acquisition (TDAQ) system is composed of the hardware-based first-level trigger (L1), using information from the calorimeter and muon systems, and the software-based high-level trigger (HLT), which uses information from all the detector subsystems. L1 is designed to make a decision in less than $2.5\,\mu$s, and when combined with the HLT reduces the event rate from 40 MHz to about 1 kHz, with a typical event size of 1 MB.

The L1 trigger searches for physics objects with high transverse momentum, in addition to identifying so-called regions of interest (RoIs) in η and ϕ that are used as input to the HLT. As mentioned in Section 3.2.4, high transverse momentum muons are identified with the trigger chambers. Calorimeter information is obtained from reduced-granularity trigger towers of typical size 0.1×0.1 ($\Delta\eta \times \Delta\phi$), as shown in Figure 3.7a.

The HLT provides more granular information on the subset of events selected by the L1 trigger.

Typically this involves calorimeter clustering algorithms to obtain information on shower shapes, algorithms to reconstruct tracks in the ID and MS, and algorithms for track-to-cluster matching. These algorithms are similar to those used in the full offline event reconstruction, to be discussed further in Chapter 4.

3.2.6 Computational infrastructure

Despite the ability of the trigger system to filter out the vast majority of events, a significant amount of data is still recorded. The ATLAS computational infrastructure is required to process these large data sets. As well as the passing of both real and MC generated data through complex reconstruction algorithms, the entire ATLAS detector must be simulated. All of this is facilitated by a streamlined event-processing workflow.

Detector simulation

As mentioned in Section 1.2.5, MC event generators are able to produce a large number of weighted data-like events that sample the available phase space for a given process. These events are said to be on particle-level. The equivalent detector-level event may be obtained by simulating the passage of its final state particles through the detector. This simulation is done within the ATLAS simulation infrastructure [162], integrated into the main ATLAS software framework, Athena [163], and utilising the GEANT4 [164] simulation toolkit.

Generated events are produced as EVNT files, based on the HepMC format [165], and contain all final-state particles considered stable enough to interact with the detector [3]. The ATLAS detector sub-components are represented in the simulation in terms of their geometry and constituent materials. GEANT4 handles the simulation of particle interactions within the detector materials, as well as their trajectories through the magnetic field. The particle is propagated through a certain distance and a decision is made on whether to induce a decay or interaction, with this process repeated on the daughter particles until some minimum step length is reached. At each stage, the energy deposited in sensitive detector components at given positions and times is recorded, with the output stored in a HITS file. Information on the particle that left the deposit, known as truth-level information, is also stored. The digitisation stage converts the hits into detector responses, which includes a simulation of the L1 trigger and the introduction of noise. The resulting raw data object (RDO) files, of a similar format to RAW data files, can then be passed to the HLT and reconstruction algorithms. PU interactions originating from the same or neighbouring bunch crossings are usually simulated by overlaying hits from the HS signal process with those from separately generated inelastic pp events.

Given the time-consuming nature of the full simulation, various fast simulation alternatives have been developed. These may for example use a simplified detector geometry and magnetic field, along with pre-simulated or parameterised calorimeter showers. Compromises are made on the accuracy of the simulation as a result.

---

[3]*Stable* here means that the proper lifetime of the particle, τ, satisfies $c\tau > 10\,\mathrm{mm}$.

Data processing

Most of the generation or processing of large input data sets is done via the worldwide LHC distributed computing grid, often simply referred to as the *grid*. Reconstruction algorithms running within the Athena framework produce physics objects from the detector signals, with the output stored in event summary data (ESD) files of typical size 1-10 MB/event, that may then be converted to smaller analysis object data (AOD) files with about 0.1-1 MB/event. Further processing to remove unwanted branches or events results in derived AOD (DAOD) files, reducing the dataset size to about 10-100 kB/event. Additional reductions in file size are possible depending on the needs of the analysis, but at this stage datasets are usually small enough to be amenable to local processing, for which a range of dedicated frameworks exist.

4

Analysis objects

Detector-level objects used in the analysis of ATLAS data are designed to represent as closely as possible the truth-level particles in a given event. Signals in the detector are first combined to build particles or physics objects in a process called reconstruction. Although some low-level reconstruction is performed by the trigger, precision reconstruction happens offline and utilises a set of highly optimised object-specific algorithms. Additional criteria are applied to select genuine particles with high efficiency and purity. A relatively recent development in ATLAS is the introduction of a particle flow algorithm, which incorporates information from multiple sub-detectors for optimal reconstruction. In this chapter the various reconstruction algorithms will be discussed, with emphasis on those relevant for the measurements presented in this thesis, along with details on the various triggers, and strategies used to reject backgrounds.

4.1 Tracks, vertices and topo-clusters

All reconstruction algorithms for high-level physics objects use a common set of reconstructed base-level objects, which include tracks, vertices and topo-clusters. Tracks and vertices are formed by combining deposits in the ID and potentially the MS, whilst topo-cluster reconstruction uses information from the EM and hadronic calorimeters.

4.1.1 Track and vertex reconstruction

As described in Sections 3.2.2 and 3.2.4, charged particles travelling through the ID and MS may deposit small fractions of their energy as a series of discrete hits, also known as space-points. Track reconstruction uses these hits to reproduce the trajectory of the particle. The curvature of the resulting track can be used to obtain the particle momentum, and the orientation provides the sign of the electric charge. A set of tracks may intersect at a point, known as a vertex, corresponding to
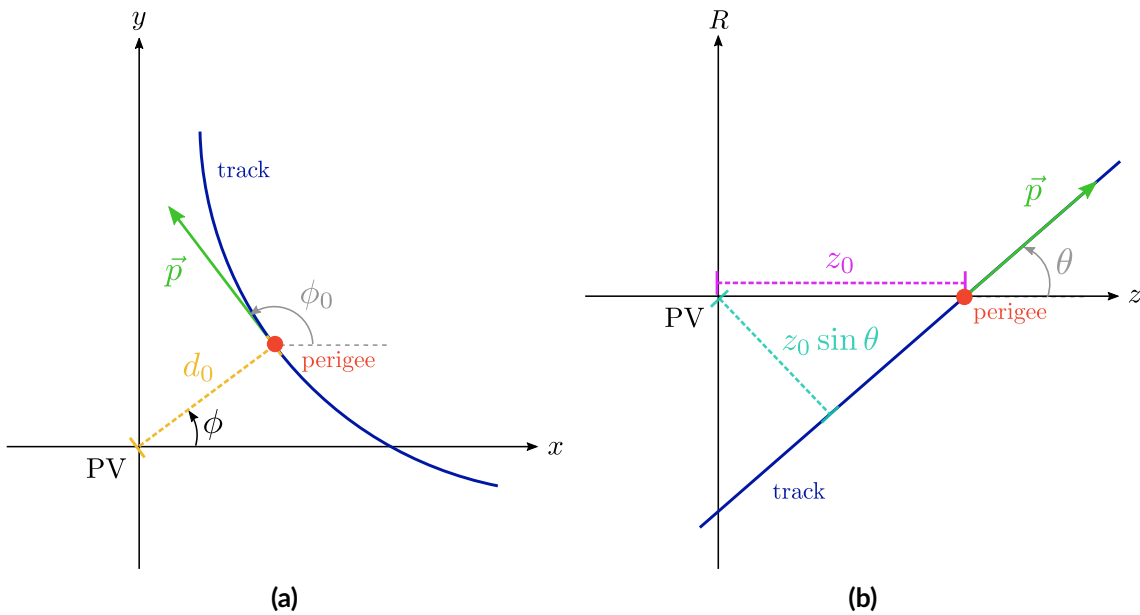
Figure 4.1: The track parameters at the perigee (red) relative to a PV, which may for example be the HS vertex. **(a)** The transverse plane showing the momentum vector of a charged particle (green) and its track (blue), along with d_0, ϕ_0 and the ATLAS ϕ coordinate. For a given value of ϕ_0 there are two possible ϕ values, separated by π, which are resolved by the sign of d_0. The configuration shown here is for a positive d_0. **(b)** The longitudinal projection showing z_0 and θ.

the location where the associated interaction took place. In a given process, particles may be considered primary or secondary. Primary, or prompt, particles are those that arise directly from the pp interaction. Secondary, or non-prompt, particles are those produced in the decays or material interactions of primary particles, where the initial particle travels a finite and resolvable distance in the detector before decaying or interacting. Tracks may therefore be classified as either primary or secondary, depending on whether or not they correspond to primary or secondary particles respectively. Primary tracks intersect at primary vertices (PVs), and secondary tracks at secondary vertices.

Tracks are fully described in terms of five track parameters, given with respect to the point of closest approach to the beam axis, known as the perigee. The parameters are usually taken to be the longitudinal distance from the IP, z_0, the signed[1] transverse impact parameter, d_0, the azimuthal and polar angles of the momentum vector, ϕ_0 and θ respectively, and the ratio of the signed charge to the absolute value of the momentum, q/p. These parameters are visualised in Figure 4.1.

Inner detector tracks

Primary tracks are reconstructed using an inside-out algorithm [166, 167]. Initially, groups of three space-points within the silicon layers are formed and used as track seeds to provide an initial crude estimate of the track perigee parameters, and to filter out lower-quality track candidates early. Where possible, track seeds are extended using a Kalman filter [168] to include additional hits within a window around the track direction, forming track candidates. A large number of track

---

[1] d_0 is signed to resolve the ambiguity between the two possible azimuthal positions for a given ϕ_0. The sign of d_0 is taken as positive if the momentum at the perigee points anticlockwise about the positive z-axis.

candidates result from this step, many of which share hits, are incomplete, or correspond to combinatorial tracks. This ambiguity is resolved using a scoring system, where each track candidate receives a score based on factors such as the quality of a χ^2 fit, the number of holes, and in which layers the hits are located. Higher-scoring tracks are preferred in the final track collection, with overlapping lower-scoring tracks rejected. Finally, tracks are extended to include hits in the TRT, and a global χ^2 fit is performed to obtain the final track parameters [169]. A typical charged particle would be expected to leave 4 pixel hits, 8 SCT hits, and more than 30 TRT hits.

An outside-in algorithm may be used to identify secondary tracks from particles that do not produce seeds in the silicon layers. Track segments are formed in the TRT layer, excluding hits already assigned to tracks during the inside-out stage, and extended into the silicon layers with a backtracking approach.

Nominally reconstructed tracks are required to have a $p_T > 400$ MeV. The central inverse transverse momentum resolution achieved for tracks reconstructed in the combined ID system closely matches the design specification given by [170]

$$\sigma \left(\frac{1}{p_T} \right) \cdot p_T = 0.036\% \cdot p_T \oplus 1.3\%, \tag{4.1}$$

where the momentum values are in GeV and $\oplus$ denotes the sum in quadrature. As expected, the resolution deteriorates as the particle momentum increases, as a result of the reduced track curvature. The constant term is related to multiple scattering processes [171].

Muon spectrometer tracks

Tracks are also reconstructed in the MS [172]. Track segments are formed from hits in the MDT or CSC chambers, with hits in the RPC and TGC chambers providing the coordinate orthogonal to the bending plane. Muon track candidates are built by combining segments from different layers. A global χ^2 fit is performed and ambiguities are resolved according to specified quality criteria.

Vertex reconstruction

PV reconstruction in the ID proceeds via an iterative approach [173]. Reconstructed tracks within the vicinity of a vertex seed are used to improve the estimate of the vertex location using a χ^2-based fitting algorithm. Tracks displaced by more than 7σ from the vertex candidate seed new vertices, and the process repeats until there are no remaining tracks or no additional vertices can be found. In the presence of PU, multiple PVs are typically reconstructed. The vertex whose associated tracks give the largest $\sum p_T^2$ is usually taken to be the HS vertex. The reconstruction of secondary vertices is relevant for the identification of jets containing B hadrons, as will be discussed in Section 4.5.3.

4.1.2 Topo-clusters

Both charged and neutral particles deposit energy in the cells of the calorimeter system, as described in Section 3.2.3. The shower that develops from a single incident particle can deposit energy in multiple calorimeter cells, so these need to be combined to correctly account for the incident particle energy. The ATLAS design specifies an energy resolution for single pions in the centre of

the detector of [170]

$$\frac{\sigma_E}{E} = 50\% \sqrt{\frac{\text{GeV}}{E}} \oplus 3.4\% \oplus 1\% \frac{\text{GeV}}{E}. \tag{4.2}$$

The first term corresponds to the stochastic nature of the shower development. The second constant term arises from a variety of sources such as energy leakage, inactive material, and inhomogeneities in the calorimeter response. The final term corresponds to electronic and PU noise. In contrast to the momentum resolution in Eq. (4.1), the calorimeter resolution improves as the energy of the incident particle increases.

The formation of clusters within ATLAS proceeds via a topological cell clustering algorithm [174], superseding previous sliding-window clustering algorithms based on fixed-size clusters [175] by instead introducing a dynamical clustering. The algorithm groups individual cells into 3D topological clusters, or topo-clusters, of variable size. One of the aims of such an algorithm is to extract the significant signal, whilst suppressing contributions from electronic noise and PU. To this end, the cell significance is used. It is defined as

$$\zeta_{\text{cell}}^{\text{EM}} = \frac{E_{\text{cell}}^{\text{EM}}}{\sigma_{\text{noise,cell}}^{\text{EM}}}, \tag{4.3}$$

where $E_{\text{cell}}^{\text{EM}}$ is the energy deposited in a given cell and $\sigma_{\text{noise,cell}}^{\text{EM}}$ is the expected noise in that cell. The "EM" superscript indicates that the energies are measured on the EM scale. This scale correctly reconstructs the energy of electrons and photons, but does not correct for signal losses associated with hadronic interactions in the HCal. The cell significance is used to build topo-clusters following the *4-2-0* topo-clustering algorithm, as shown in Figure 4.2. Firstly, all cells satisfying $|\zeta_{\text{cell}}^{\text{EM}}| \geq 4$ are selected as seeds and sorted in decreasing order of significance. Cells satisfying $|\zeta_{\text{cell}}^{\text{EM}}| \geq 2$ that neighbour those from the previous step are added to the cluster iteratively. For recovery of genuine signal below the noise threshold, all cells satisfying $|\zeta_{\text{cell}}^{\text{EM}}| \geq 0$ that neighbour any cells already selected are also included. An additional algorithm is run to split the resulting clusters into n smaller clusters if they contain n local maxima, producing the final set of topo-clusters. Topo-cluster kinematic properties such as angular coordinates and energy, as well as higher order moments, are calculated using geometrically weighted sums of the constituent cell properties.

4.2 Electrons

Electrons are charged particles and so interact with both the ID and ECal, forming tracks and EM topo-clusters. Electrons interacting with the detector material may lose a significant amount of their energy due to bremsstrahlung. The photons radiated in this process may then themselves convert to electron-positron pairs, potentially forming additional tracks. As a result, a given EM topo-cluster may be associated with multiple tracks [176]. In addition, well-separated electrons or photons produced in the material interactions of the initiating particle may seed separate topo-clusters.
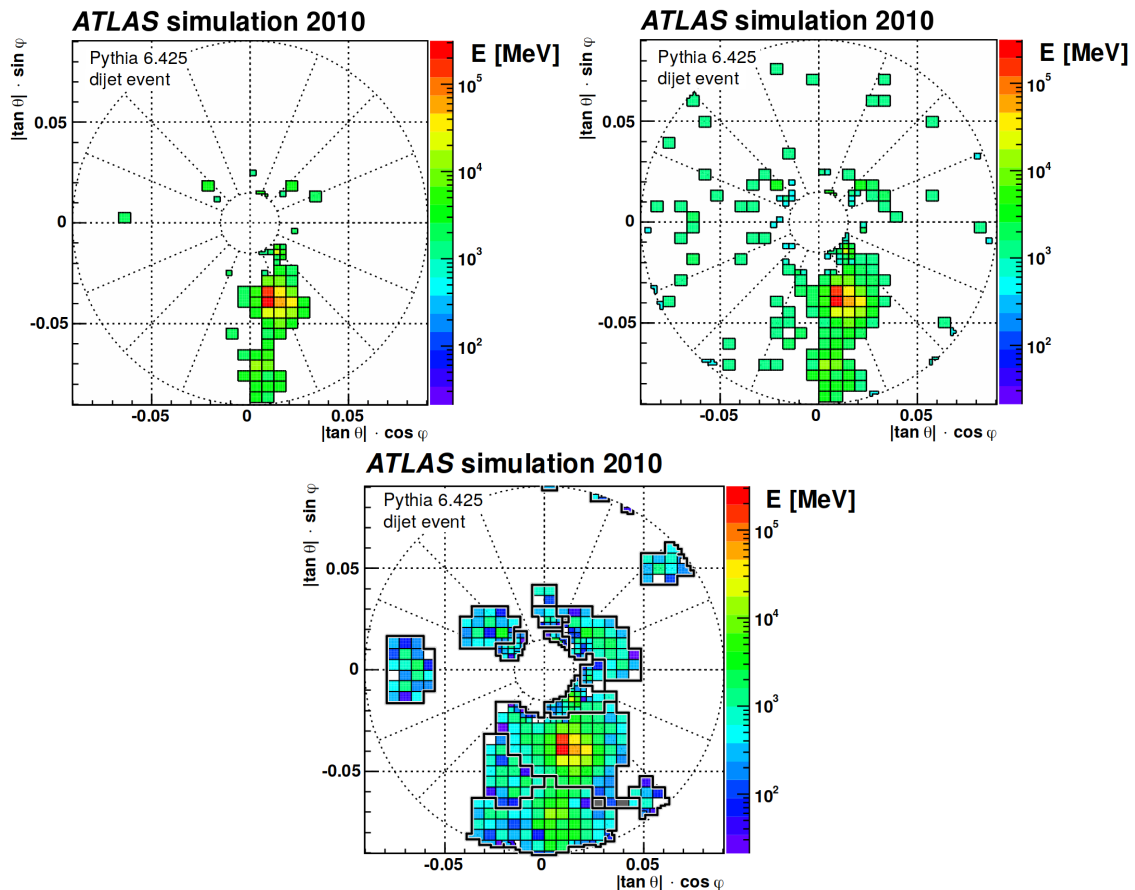
Figure 4.2: The formation of topo-clusters in the first layer of the FCal (FCAL0) using MC simulated dijet events. The upper left and right images show all cells satisfying $|\zeta_{cell}^{EM}| \geq 4$ and $|\zeta_{cell}^{EM}| \geq 2$ respectively. The clustering algorithm is run as described in the text, with the bottom image showing the resulting topo-clusters outlined in black. PU is not included but electronic noise is modelled. White cells within a topo-cluster correspond to negative cell signals. Taken from [174].

4.2.1 Electron reconstruction

Given the above considerations, single electron candidates are built using a combination of ID tracks and EM topo-clusters, where a matching of tracks to topo-clusters is performed [177]. Only reconstruction in the central region, $|\eta| < 2.5$, is discussed here.

Track-cluster matching

The standard track fitting procedure is based on a pion hypothesis, and so a modified tracking algorithm, referred to as a Gaussian sum filter (GSF) algorithm [178], is needed to account for electron energy losses via bremsstrahlung. The GSF algorithm is applied to tracks loosely matched to fixed-size clusters. The matching to EM topo-clusters is then achieved by extrapolating tracks from the perigee to the second layer of the calorimeter and comparing the angular coordinates. In the case of multiple track matches, tracks are ranked according to the number of silicon layer hits and the ΔR between the extrapolated track and cluster. The highest-ranked track, referred to as the *best-matched* track, is used to obtain the electron directional information.

Add all clusters within 3 × 5 window around seed cluster.

Seed, secondary cluster **match the same track**.

5 × 0.025

3 × 0.025

12 × 0.025

5 × 0 .025

Seed cluster

Satellite

Figure 4.3: The creation of electron superclusters. All satellite topo-clusters (blue) within a 0.075×0.125 $(\Delta\eta \times \Delta\phi)$ window around the seed cluster (red) are included in the supercluster, as well as any topo-cluster in a 0.125×0.3 $(\Delta\eta \times \Delta\phi)$ window around the seed cluster whose *best-matched* track is that of the seed cluster. Adapted from [177].
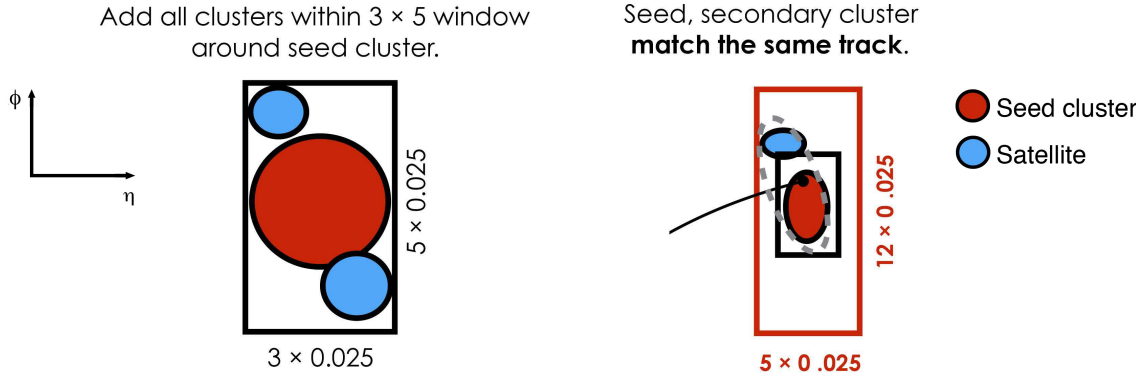
Superclusters

The energy of a single incident electron may be distributed amongst a set of topo-clusters as a result of bremsstrahlung, and so a prescription is made for grouping these topo-clusters into composite objects called superclusters. Topo-clusters are first sorted in order of decreasing transverse energy[2], E_{T}. Starting with the highest energy, each topo-cluster is used to seed a supercluster, where any topo-cluster already belonging to a supercluster is not considered. Any topo-clusters within a window around a selected seed, referred to as satellite clusters, are included if they satisfy a set of criteria as summarised in Figure 4.3, with the resulting object forming the supercluster. Superclusters undergo an initial calibration before track-supercluster matching is done. The supercluster together with its set of tracks defines the electron.

Electron energy calibration

The electron candidate energy resolution is corrected to account for effects such as energy lost in material upstream or downstream of the ECal, with the correction applied to both data and simulation [179]. Intercalibration of the different calorimeter layers and non-uniformities in the calorimeter response generate additional corrections that are applied to data. The absolute energy scale and resolution of electron candidates is calibrated using measurements of $Z \rightarrow ee$ decays, where the agreement between parameterised distributions of the dielectron invariant mass in data and simulation is optimised. The energy scale correction is applied to data, whereas the resolution correction is applied to simulation.

4.2.2   Electron identification and isolation

The electron reconstruction algorithm provides a set of electron candidates, which have a non-zero probability to be constructed from detector signals generated by objects other than genuine electrons. Therefore, after such electron candidates are built, additional variables are calculated that aid in the discrimination of genuine prompt electrons from a variety of background processes, in-

---

[2]For an object of energy E and pseudorapidity η, the transverse energy is defined as $E_{\mathrm{T}} = E/\cosh\eta$.
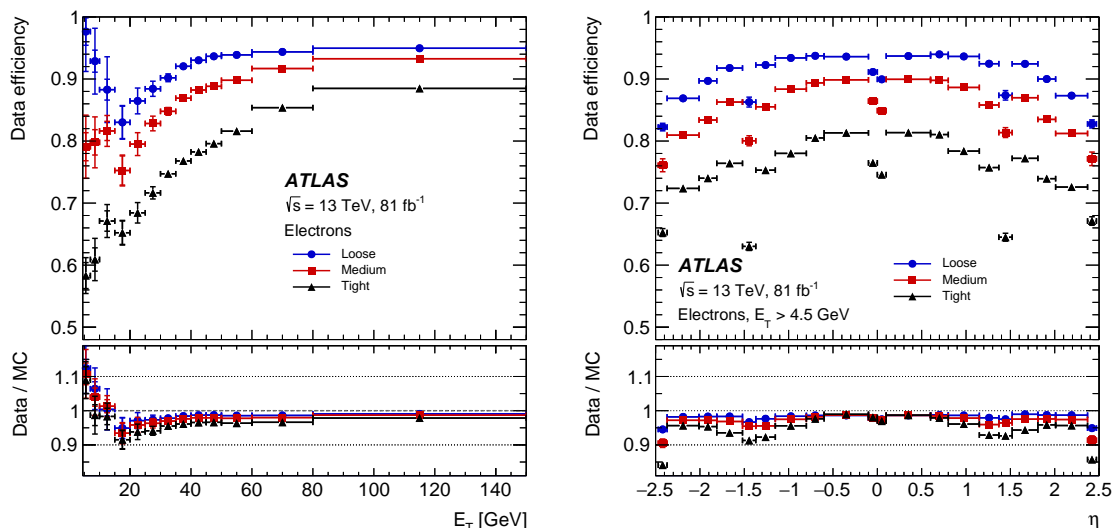
Figure 4.4: Electron identification efficiencies for the `Loose`, `Medium` and `Tight` operating points in $Z \to ee$ events in data. Data efficiencies are obtained in $J/\psi \to ee$ and $Z \to ee$ events, and the corresponding data-to-simulation efficiency ratios applied to simulated $Z \to ee$ events to get the data efficiencies shown. The inner uncertainties are statistical only, whereas the outer uncertainties include both statistical and systematic uncertainties. The bottom panels show the data to simulation ratio. Taken from [177].

cluding jets that mimic the signature of prompt electrons, photons that convert to electron-positron pairs via material interactions, and non-prompt electrons from the decays of hadrons containing heavy-flavour quarks. These variables are used to define identification and isolation criteria.

Electron identification

The full set of variables used for determining identification quality criteria are given in Ref. [177]. They relate to shower shapes, and the quality of electron candidate tracks and track-cluster matching. A discriminant is formed as a ratio of likelihoods (LHs) for signal and background electrons, themselves calculated from the probability density functions (pdfs) for the identification variables as functions of E_T and η. Three operating points, namely `Loose`, `Medium` and `Tight`, corresponding to increasing LH discriminant thresholds, are defined in order of increasing background rejection, with average efficiencies to select a signal electron of 93%, 88% and 80% respectively. The efficiencies measured in data as a function of E_T and η are shown in Figure 4.4.

Electron isolation

There is a relatively high efficiency for non-prompt electrons or misidentified jets associated with additional tracks or calorimeter activity to pass the identification criteria discussed above. In this case, isolation variables may be used to further reject these background electrons. Such variables are constructed by summing the transverse energies of clusters or tracks in the vicinity of an electron candidate, excluding those from the candidate itself.

The calorimeter isolation is obtained by summing the transverse energies on the EM scale of topo-clusters whose barycentres fall within a cone of size $\Delta R = 0.2$ around the barycentre of the

electron cluster. To exclude the electron candidate itself, cells within a window of size 0.125×0.175 ($\Delta\eta \times \Delta\phi$) centred on the electron cluster barycentre are removed. Corrections are made for signal leakage outside this window, as well as for contributions from PU and the UE.

The track isolation is calculated by summing the transverse momentum of sufficiently high-quality tracks within a cone around the electron candidate track, with tracks matched to the electron candidate excluded. The maximum cone size is $\Delta R_{\mathrm{max}} = 0.2$ and decreases as the momentum of the candidate electron increases to account for the more collimated nature of additional activity associated with high-momentum non-prompt electrons.

The way in which electron isolation variables are implemented is analysis-dependent, given that there is a compromise to be made between selecting genuine prompt electrons with high efficiency in both isolated and dense environments, and rejecting non-prompt or misidentified contributions. A variety of isolation operating points are defined, including the `Gradient` working point, used for the measurements presented in this thesis, which is defined to select electrons with a specified efficiency of $\epsilon = 0.1143\% \times p_{\mathrm{T}}\,(\mathrm{GeV}) + 92.14\%$.

4.2.3 Electron trigger

As mentioned in Section 3.2.5, the ATLAS detector utilises a two-level trigger system, and a dedicated sequence of trigger algorithms is available for selecting events containing at least one electron [180]. The L1 trigger builds EM RoIs using 4×4 calorimeter trigger towers in a sliding-window algorithm, using the E_{T} value calculated from the central 2×2 region as the EM transverse energy. Electron candidates can be rejected if there is significant energy in hadronic towers or in EM trigger towers surrounding the central region. L1 RoIs are passed to the HLT, which runs a fast followed by a higher-precision calorimeter reconstruction algorithm on electron candidates now including cluster-matched ID tracks from the RoI. A LH discriminant matching as closely as possible the offline version is used for electron identification, and an optional track isolation may additionally be used. For the measurements presented in this thesis, single-electron triggers are used to select events containing leptonic W decays. A minimum trigger threshold of $E_{\mathrm{T}} = 24\,\mathrm{GeV}$ was used in 2015 data-taking, and this increased to $26\,\mathrm{GeV}$ for 2016-2018. Both triggers are additionally associated with LH-based identification criteria and isolation criteria. The lower rate at higher energies allows for the removal of the isolation requirement and for looser identification criteria to be applied, increasing the trigger selection efficiency.

4.3 Muons

Muons form tracks in both the ID and the MS. They may additionally deposit small amounts of energy in the calorimeters. As a result, muon reconstruction incorporates information from both tracking systems and the calorimeter system [181].

4.3.1 Muon reconstruction

There are five muon types corresponding to different reconstruction strategies, although only two, namely the combined (CB) and inside-out combined (IO) types, are used in the measurements

presented in this thesis due to their relatively high purity in the central region, $|\eta| < 2.5$. Potential overlaps between different muon types are resolved before use in analyses.

Track reconstruction is run independently in the ID and MS. To form CB muons, track candidates from the MS are matched to those in the ID using an outside-in approach. A global fit is performed including hits from both sub-detectors, taking into account energy losses in the calorimeters. MS hits may be added to or removed from the resulting track to improve the fit quality. Similarly to CB muons, IO muons combine tracks from the ID and MS, but an inside-out approach is used. The method extrapolates tracks from the ID to the MS and searches for at least three additional loosely-aligned hits. This approach improves the muon reconstruction efficiency for low-p_{T} muons, or in cases where the MS provides poor coverage.

Muon momentum calibration

Inaccuracies in the ATLAS detector simulation, for example from mismodelling of the magnetic field, or energy losses from the calorimeter and other sources, lead to discrepancies between the muon momentum scale and resolution in data and simulation. Calibration is therefore performed using $J/\psi \to \mu\mu$ and $Z \to \mu\mu$ decays, with the corrections applied to the muon momentum in simulation [172]. CB muons are used to extract the calibration parameters from data in a maximum-LH fit of the dimuon invariant mass distribution.

4.3.2 Muon identification and isolation

As in the case of electrons, high-quality muons can be selected by placing requirements on the reconstructed muon candidates that help to reduce background from non-prompt muons. Non-prompt muons may arise from light and heavy-flavour hadrons. Variables related to the track properties, the compatibility of measurements in the different sub-detectors, and the presence of associated activity are used to define the identification and isolation criteria.

Muon identification

Three working points are defined, namely `Loose`, `Medium` and `Tight`, in order of increasing purity and decreasing efficiency. For all working points, muons are required to pass quality criteria related to the number of hits in the ID tracks. Additional requirements on the number of MS stations containing hits, the quality of the track χ^2 fit, and the agreement between the p_{T} values measured in the ID and MS, define the working points. The identification efficiency for selecting prompt muons is shown as a function of p_{T} and η in Figure 4.5. The drop in efficiency visible at central values of η is due to a reduced coverage of the MS in this region.

Muon isolation

Most of the background from light hadrons is removed by the identification requirements, but some background from heavy-flavour hadron decays remains. This can be effectively removed with isolation requirements. ID track and calorimeter isolation variables are defined similarly to those for electrons discussed in Section 4.2.2. The `Tight_FixedRad` working point, used for the measure-
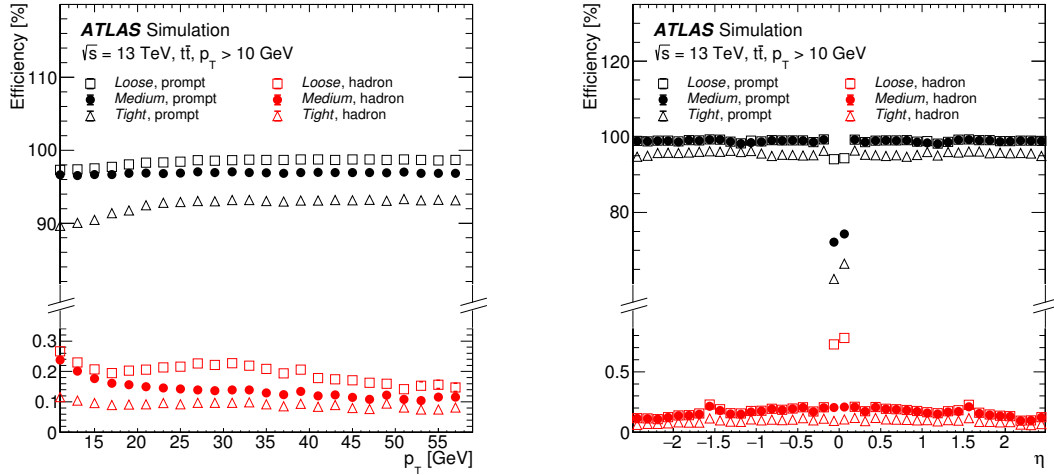
Figure 4.5: Identification efficiencies for the `Loose`, `Medium` and `Tight` working points in simulated $t\bar{t}$ events, shown for both prompt muons and muons from light hadron decays. The efficiency is calculated as the fraction of ID tracks associated with a reconstructed muon that satisfy the criteria for each working point. ID tracks are matched to either truth-level prompt muons or light hadrons. Taken from [181].

ments presented in this thesis, employs a variable-cone track isolation, $p_{\mathrm{T}}^{\mathrm{varcone30}}$, for $p_{\mathrm{T}} < 50\,\mathrm{GeV}$, with a maximum of $\Delta R = 0.3$, and a fixed-cone isolation, $p_{\mathrm{T}}^{\mathrm{cone20}}$, with $\Delta R = 0.2$, to improve hadronic background rejection for $p_{\mathrm{T}} > 50\,\mathrm{GeV}$. The calorimeter isolation, $E_{\mathrm{T}}^{\mathrm{topocone20}}$, is defined as the sum of the E_{T} values of topo-clusters within a cone of $\Delta R = 0.2$ around the position of the muon extrapolated to the calorimeter, with corrections applied to account for PU and the UE. The `Tight_FixedRad` working point then requires $p_{\mathrm{T}}^{\mathrm{varcone30}} < 0.04 \times p_{\mathrm{T}}$ and $E_{\mathrm{T}}^{\mathrm{topocone20}} < 0.15 \times p_{\mathrm{T}}$.

4.3.3 Muon trigger

As described in Section 3.2.4, the RPC and TGC sub-detectors provide fast information on muon candidates that may be utilised by the muon trigger [182]. The L1 trigger estimates the p_{T} of the muon candidate using its hit positions in the trigger chambers and forms RoIs of typical size 0.1 $\times$ 0.1 ($\Delta\eta \times \Delta\phi$) in the RPCs and 0.03 $\times$ 0.03 ($\Delta\eta \times \Delta\phi$) in the TGCs. The HLT is divided into fast and precision stages. The fast stage includes both MDT hits within the RoI and ID tracks to improve the resolution of the p_{T} estimate. The precision step uses algorithms similar to those used in the offline reconstruction, with muon candidates formed by fitting hits in either the MS alone, or a combination of the MS and ID, optionally with some track isolation criteria applied. The minimum p_{T} threshold of the single-muon trigger increased from 20 GeV in 2015 to 26 GeV for 2016-2018. As with the single-electron trigger, isolation and other quality requirements are made less stringent with increasing p_{T} to improve efficiency.

4.4 Particle flow

In Sections 4.1.1 and 4.1.2, the typical momentum and energy resolutions were given for the AT-LAS tracker and calorimeter systems respectively. An important observation is that the tracker momentum resolution deteriorates at high p_T, whereas the calorimeter energy resolution improves at high energy. Tracks are also only reconstructed for charged particles. On the other hand, tracks typically provide better spatial resolution, can be associated to vertices, which aids in the rejection of in-time PU, and allow for reconstruction of lower energy particles when compared to topo-clusters in the calorimeter. In general, it is therefore desirable to combine information from both the tracker and the calorimeter for optimal reconstruction performance. The combination of information from different sub-detectors is referred to as particle flow. This approach is to some extent implemented in the electron and muon reconstruction algorithms already discussed.

Most of the recent development regarding the particle flow paradigm in ATLAS has concerned the reconstruction of jets. The desire to combine tracks and clusters such that both charged and neutral particles are included in jets without double-counting of energy led to the ATLAS particle flow algorithm [183]. In this section, this algorithm will be briefly discussed, with its application to jet reconstruction given in the following section.

4.4.1 Particle flow algorithm

The particle flow algorithm aims for a least-biased reconstruction approach in which tracks and clusters are combined to form particle flow objects (PFOs). An individual PFO is either a track, or a topo-cluster modified by the particle flow algorithm, that ideally represents the deposit of a single particle with no overlap. The PFO reconstruction algorithm starts with ID tracks with $p_T < 40$ GeV satisfying a set of stringent criteria that are matched to topo-clusters. Each track may be matched to more than one topo-cluster if it is expected that the particle deposited its energy in multiple clusters. Since the topo-clusters in general may contain deposits from multiple particles, it is not possible to simply remove the matched topo-clusters to avoid overlap between the track and clusters in the final PFO collection. Instead, it is necessary to subtract the energy associated with the charged particle from the cluster. This is done by calculating the average expected energy deposited by a single charged pion, and then subtracting energy from matched topo-clusters at the EM scale outwards in rings of calorimeter cells around the extrapolated track position until all the expected energy has been removed. The remaining tracks and modified topo-clusters are referred to as charged and neutral PFOs respectively, and form the basis for jet reconstruction.

4.5 Jets

Jets were discussed in Section 1.2.4 in the context of QCD radiation and subsequent hadronisation. The detector-level signature of a jet is a collimated stream of tracks and clusters, or PFOs, corresponding to the deposits left by the hadrons that compose the jet.

4.5.1 Jet reconstruction

The jet definition is based on a jet clustering algorithm that groups the detector deposits into distinct jets in such a way that IR safety is respected. In ATLAS this is done with the anti-k_T algorithm [184], and in the particle flow approach the clustering is with respect to PFOs [183]. The anti-k_T algorithm is a sequential recombination algorithm based on the distance metrics

$$d_{ij} = \min\left(p_{\mathrm{T}i}^{-2}, p_{\mathrm{T}j}^{-2}\right)\left[\frac{\Delta R_{ij}}{R_0}\right]^2 \quad \text{and} \quad d_{iB} = p_{\mathrm{T}i}^{-2}, \tag{4.4}$$

where the indices i and j refer to any two objects in the event[3], ΔR_{ij} is the rapidity-based angular distance between the two objects, defined in Section 3.2.1, R_0 is a radius parameter, and B refers to the beam axis. The algorithm first calculates all possible distances. If the smallest distance is a d_{ij}, the object four-vectors are combined into a single four-vector, whilst if it is a d_{iB}, the object i is considered a jet and removed from the list of objects. This is repeated until there are no remaining objects. In the anti-k_T algorithm, the resulting hard jets are circular with radius R_0.

As mentioned previously, unlike other jet reconstruction algorithms that include only topo-clusters or only tracks, the particle flow approach combines both in a complementary fashion. The improved momentum resolution of low-energy particles provided by the tracker is exploited, and at the same time neutral deposits are accounted for. In addition, softer particles that may not be energetic enough to seed topo-clusters or are bent out of the calorimeter jet cone by the solenoid field are included. The inclusion of tracks also allows for matching to the HS vertex, which provides suppression of in-time PU, referred to as charged hadron subtraction (CHS). This can be achieved for example by placing a requirement on the longitudinal impact parameter z_0, defined in Section 4.1.1, of $|z_0 \sin\theta| < 2\,\mathrm{mm}$ for tracks prior to jet building, with the improvements relative to calorimeter jets shown in Figure 4.6a. In addition, whole jets likely to originate from PU interactions, referred to as fake jets, may be removed using the jet vertex tagger (JVT) approach [185]. For a given jet, the JVT uses the ratio of the scalar sum of the p_T of its tracks associated to the HS vertex to the scalar sum of the p_T of its tracks associated to any PV, known as the jet vertex fraction (JVF), in addition to the ratio of the scalar sum of the p_T of its tracks associated to the HS vertex to the p_T of the jet itself, to produce a combined discriminant. The particle flow approach already provides some level of fake jet rejection as shown in Figure 4.6b.

4.5.2 Jet calibration

Jets do not correspond to physical particles and so are only defined by the jet clustering algorithm. Most jet calibration therefore compares the jet energy scale and resolution between reconstructed and truth-level jets clustered with the same algorithm. Once jets are matched on both detector- and truth-level, the energy response, defined as the ratio of the detector-level jet energy to the truth-level jet energy, is calculated. The response typically follows a Gaussian distribution, with a mean referred to as the jet energy scale (JES) and a width referred to as the jet energy resolution (JER). There are a chain of calibration steps applied to correct the JES and minimise the JER [186].

---

[3]On the reconstruction level the objects could be PFOs or combinations of PFOs. On truth-level, they could be hadrons from generated events.
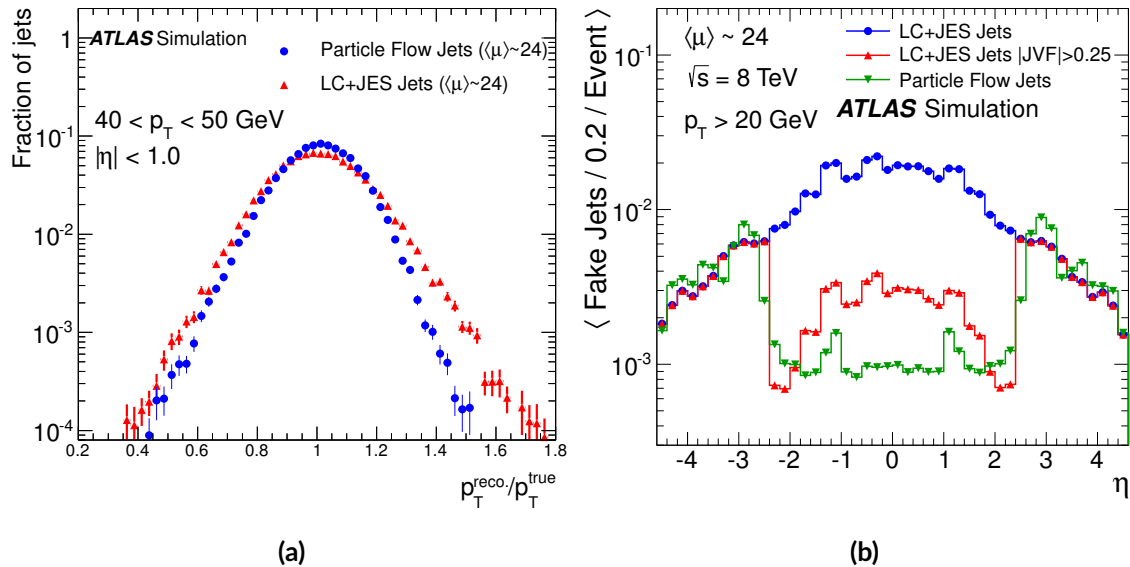
Figure 4.6: Jet reconstruction performance comparison for particle flow jets and calorimeter jets. Cluster jets use topo-clusters with a local cell (LC) weighting scheme applied to correct the energy scale [174], and are calibrated as described in the text. **a)** The jet response for low-p_T jets. **b)** The η distribution of fake jets. The red line shows calorimeter jets with an additional JVF PU suppression applied. Taken from [183].

Calibrations applied to both data and MC include subtractions of neutral PU in jets based on a per-event expected PU energy density, residual PU corrections to reduce the dependence on μ and the number of primary vertices in the event, N_{PV}, corrections for energy lost in the calorimeter due to inactive material or the detector geometry via particle-level comparisons, and a global sequential correction to reduce the dependence on auxiliary variables and improve the JER.

The final calibration step corrects for remaining differences between data and simulation. This is referred to as *in situ* calibration. The jet response is measured in data by balancing a fully MC-calibrated jet against another well-calibrated system such as a Z boson or photon. The response is then the average value of the ratio of the measured jet p_T to that of the reference system. The double ratio formed as the ratio of the responses in simulation and data is then used as the final jet energy scale correction factor, applied to the data. Additional smearing of the MC jet energy response based on the asymmetry in dijet events[4] provides the *in situ* JER correction.

4.5.3 Identification of *b*-jets

A significant background to the production of pairs of W bosons comes from $t\bar{t}$ events, where the top quarks decay as $t \rightarrow Wb$, with the bottom quarks producing jets, known as b-jets. An effective strategy to reduce this background is to reject events containing b-jets with significant energy. The identification of such jets uses the fact that B hadrons are relatively long-lived, and so produce secondary vertices at the point of their decay that are displaced from the PV by a resolvable amount. The impact parameter significances are correspondingly larger for tracks associated to B hadron decays than those from light hadrons. A host of low-level tagging algorithms exist to exploit

---

[4] Dijet events are those containing exactly two jets that are balanced in the transverse plane.

these and other features, whose outputs are used as inputs to high-level multivariate taggers that discriminate between b-jets and c- or light quark jets [187, 188]. The 85% b-tagging efficiency working point is used for the measurements presented in this thesis. Other working points are available that provide better rejection of background from light hadrons at the cost of a lower b-jet selection efficiency.

4.6 Missing transverse momentum

Missing transverse momentum, or p_T^{miss}, arises due to the inability of the ATLAS detector to reconstruct perfectly the transverse momentum of all the particles produced in a pp collision, as mentioned in Section 3.2.1. This may be due to the insensitivity of the detector to certain particles, for example neutrinos, or because the particles produced are too soft, or fall within inactive regions or outside the acceptance of the detector, or suffer from the limited detector resolution. Sometimes undetectable particles are said to generate genuine p_T^{miss}, whereas all other contributions produce fake p_T^{miss}.

4.6.1 Missing transverse momentum reconstruction

Since by definition p_T^{miss} leaves no detectable signal, its reconstruction relies on all the other physics objects in the event [189]. It is therefore the final analysis object to be reconstructed. The missing transverse momentum vector can be written as

$$\boldsymbol{p}_T^{miss} = -\sum_{\text{event}} \boldsymbol{p}_T \tag{4.5}$$

where the sum is over both hard and soft objects in the event. The hard objects include electrons, photons, muons, τ leptons and jets, and the soft objects include tracks or topo-clusters that do not enter the reconstruction of any hard object. Track soft term (TST) p_T^{miss} and cluster soft term (CST) p_T^{miss} correspond to the p_T^{miss} calculated using only tracks or only clusters in the soft term respectively. The vast majority of analyses use TST p_T^{miss} due to the inherent PU suppression.

The reconstruction of each hard object in ATLAS proceeds via an independent algorithm that applies a given particle or jet hypothesis to all detector signals in the event. As a result, a given set of detector signals may be reconstructed multiple times as different objects, and a scheme needs to be implemented to remove these overlaps to avoid double-counting of energy in the calculation of p_T^{miss} in Eq. (4.5). This is done with an ambiguity resolver, which first ranks the hard objects in order of reconstruction quality, starting with electrons and ending with jets, and then removes any lower-priority object that shares signal deposits with a selected higher-priority object. Muons typically do not overlap with other objects and so are considered to have the same priority as electrons. The overlap is determined on constituent-level, with two objects sharing at least one topo-cluster considered to be overlapping. The signals of the surviving objects are removed from the constituent list and replaced with the fully calibrated objects, with their associated systematic uncertainties propagated to the final result. The remaining signals form the soft term.

4.6.2   Missing transverse momentum response

The $p_\mathrm{T}^\mathrm{miss}$ response is determined in the comparison between the reconstructed $p_\mathrm{T}^\mathrm{miss}$ and that expected in a given event. Usually the response is evaluated in events with no genuine $p_\mathrm{T}^\mathrm{miss}$, such as $Z \to \mu\mu$ decays, which can be selected in data with a high signal-to-background ratio. Minor backgrounds with genuine $p_\mathrm{T}^\mathrm{miss}$, such as that arising from diboson events, may be reliably subtracted using MC simulation [189]. The presence of a non-zero $p_\mathrm{T}^\mathrm{miss}$ when averaged over many $Z \to \mu\mu$ events indicates biases in the event reconstruction arising from detector limitations as mentioned previously. The resolution in $Z \to \mu\mu$ events is given as the width of the reconstructed $p_\mathrm{T}^\mathrm{miss}$ distribution, and can be compared in both data and simulation.

5

Statistical methods

A variety of statistical techniques are needed for extracting useful information from data collected by the ATLAS detector. In this chapter, a brief overview of some essential statistics concepts will be given, followed by details of how statistical and systematic uncertainties may be combined, parameters estimated using profile LH fits, and how detector inefficiencies, resolution and acceptance effects may be corrected for via a process known as unfolding. The discussion in this chapter follows closely Refs. [190, 191].

5.1 Fundamental concepts

There are certain statistical methods that are ubiquitous throughout measurements in particle physics. In this section these concepts will be briefly reviewed. A summary of the specific statistical methods used in this thesis is given in the subsequent sections.

5.1.1 Frequentist and Bayesian methods

Most statistical methods are considered to be either frequentist or Bayesian. Frequentist probability is only defined up to an ensemble of events, whether real, hypothetical or simulated, where the probability of an outcome occurring is given as the number of times that outcome was observed divided by the number of trials. In contrast, the Bayesian interpretation of probability allows for including a subjective degree of belief that a certain statement is true. Bayesian inference is then based on Bayes' theorem

$$P(A|B) = \frac{P(B|A)}{P(B)}P(A), \tag{5.1}$$

which updates the probability of statement A being true, given the observations, B. Bayes' theorem holds for any definition of probability, but the interpretation of $P(A)$ as the prior probability

distribution, determined before an experiment is performed and updated with observations to produce a posterior distribution $P(A|B)$, is unique to Bayesian inference. The ATLAS collaboration has historically used frequentist methods for the majority of searches [192] and measurements. In most of the results presented in this thesis, frequentist methods are also used.

5.1.2 Correlation

In many instances, correlations exist between variables. The value of the correlation quantifies the extent to which changes in one variable affect another variable. For a given set of variables, $\boldsymbol{X}$, the covariance matrix is defined as

$$V_{ij} = \mathrm{Cov}(X_i, X_j) = \mathrm{E}[X_i X_j] - \mathrm{E}[X_i]\mathrm{E}[X_j], \tag{5.2}$$

where $\mathrm{E}[X_i]$ denotes the expectation value of X_i. For $i = j$, this expression reduces to the definition of the variance, and hence the on-diagonal entries of the covariance matrix are simply the variances. Uncorrelated variables result in a zero covariance, although a zero covariance does not necessarily imply independence. The correlation matrix is defined as

$$\rho_{ij} = \mathrm{Corr}(X_i, X_j) = \frac{\mathrm{Cov}(X_i, X_j)}{\sqrt{\mathrm{Var}(X_i)\mathrm{Var}(X_j)}}, \tag{5.3}$$

where $\mathrm{Var}(X_i)$ is the variance of X_i. Each entry of the correlation matrix is a number between -1 and $+1$, corresponding to fully negative and fully positive correlation respectively. The covariance matrix is needed when calculating functions of potentially correlated variables, as will be seen in the sections below.

5.1.3 Inference

The process of inference aims to determine the value of a set of parameters using observed data. The parameters may correspond to the properties of some true but unknown underlying distribution, with the inference making use of a finite set of observations.

Estimators

An estimator, $\hat{\theta}$, is a quantity calculated from a given set of observations whose value provides an estimate of the corresponding true parameter, θ. There are certain properties associated with estimators that quantify how well they represent the parameter they are designed to estimate. These include the consistency, which indicates whether $\hat{\theta}$ converges to θ as the number of observations increases, the bias, defined as the difference between $\mathrm{E}[\hat{\theta}]$ and θ, and the efficiency, which describes whether the variance on $\hat{\theta}$ is minimal. Sometimes an estimator is consistent, unbiased and efficient, although in many cases only a subset of these criteria is satisfied.

Likelihood

The LH is an essential quantity for parameter estimation and limit setting. It can be defined as

$$L(\boldsymbol{\theta}) = \prod_i f(x_i; \boldsymbol{\theta}), \qquad (5.4)$$

where $\boldsymbol{x}$ is a set of statistically independent observations following the same distribution, $f(x_i; \boldsymbol{\theta})$, and $\boldsymbol{\theta}$ is a set of parameters whose values are to be estimated. The LH therefore represents the joint probability distribution for observing the data, $\boldsymbol{x}$, given the parameters, $\boldsymbol{\theta}$.

The LH can be used to provide estimators for the parameters, $\boldsymbol{\theta}$. This is done by maximising the LH with respect to $\boldsymbol{\theta}$, under the reasoning that the parameter values most consistent with the observations are those that maximise the joint probability. The resulting estimates of the parameters are known as the maximum LH estimates (MLEs). The MLE is always consistent, but only unbiased and efficient in certain cases, or in the limit of large numbers of observations. Often the LH is written as its negative logarithm, known as the negative log-LH, and the minimum of this function corresponds to the MLE. The use of the LH in parameter estimation will be discussed further in Section 5.3.

It should be noted that the LH is not a probability distribution for the parameters, $\boldsymbol{\theta}$. This would be obtained as the posterior in a Bayesian inference, which would require knowledge of the prior distribution for $\boldsymbol{\theta}$.

5.2 Measurement uncertainties

Inherent to the presentation of any measurement result is an estimate of the associated uncertainty. In particle physics experiments, there are two classes of uncertainties, namely statistical uncertainties and systematic uncertainties. Measurements targeting rare processes suffer from relatively large statistical uncertainties, and are referred to as statistics-dominated. In contrast, measurements of processes for which a large amount of data is available, such as those presented in this thesis, are more sensitive to the values of systematic uncertainties, and are therefore said to be systematics-dominated.

5.2.1 Statistical uncertainties

Statistical uncertainties are random variations in the quantity of interest, which may be related to the underlying probabilistic nature of the pp scattering process and decays, as well as potentially other random effects associated with the detector response. Statistical uncertainties enter experimental results via the number of events measured in data or simulated with MC methods, in both signal and control regions.

Data statistical uncertainties are usually estimated by assuming the number of events observed in data over a given time interval, n_{data}, follows a Poisson probability distribution with a true mean and variance of ν_{data}. An unbiased estimator of ν_{data} is given by n_{data} itself. In the limit of a large number of events, the uncertainty, $\sqrt{n_{\text{data}}}$, corresponds to the $1\,\sigma$ variation of a Gaussian, with the interpretation that in approximately 68% of hypothetical repeated experiments the observed

number of events would be an integer lying between $n_{\text{data}} - \sqrt{n_{\text{data}}}$ and $n_{\text{data}} + \sqrt{n_{\text{data}}}$. For smaller numbers of events, the Poisson distribution may be needed [193].

Events generated via MC methods are associated with additional weights, which may come from the underlying generator as mentioned in Section 1.2.5, or from corrections that are applied to account for potential mismodelling of detector effects. Statistical uncertainties related to such events must account for these weights. Under the assumption that these weights are statistically independent and that the number of events follows a Poisson distribution[1], it can be shown [194, 195] that the appropriate variance on the weighted number of events is the sum of the squares of the weights. In the limit that all the weights are unity, this reduces to the statistical uncertainty calculated for data, as should be the case.

5.2.2 Systematic uncertainties

Systematic effects are associated with aspects of the measurement not directly related to statistical fluctuations in real or simulated data samples [196]. These effects include background estimates, detector resolution and calibration, underlying theoretical models, input parameters, and others. Uncertainties on the estimates of these systematic effects are referred to as systematic uncertainties. Systematic uncertainties may be on continuous parameters, such as the luminosity, or may be discrete, such as in the case where there are competing models for a given signal or background estimate. There is in general no universal prescription for how to estimate or handle such uncertainties. For continuous uncertainties, typically there are both *up* and *down* variations corresponding to $\pm 1\,\sigma$ deviations from the nominal, and the resulting uncertainty is taken as half the difference between the results obtained when conducting the measurement using the *up* and *down* variations as inputs. In the discrete case, where there is a preferred model and one other competing model, the difference in the result obtained from performing the measurement with each model separately is often taken as the uncertainty on the nominal result.

5.2.3 Error propagation

Observables are often calculated from a set of measured values with measurement uncertainties quantified by the covariance matrix, which takes into account potential correlations. The observable might be a simple function of the input values, such as their sum or product, for example when calculating the arithmetic mean, or when combining efficiencies. In such cases where the observable, f, is a known function of the input values, $\boldsymbol{X}$, its variance can be approximated as

$$\text{Var}\,(f) \approx \sum_{i,j} \left[\frac{\partial f}{\partial X_i} \frac{\partial f}{\partial X_j} \right]_{\boldsymbol{X}=\boldsymbol{\mu}} V_{ij}, \tag{5.5}$$

where $\boldsymbol{\mu} = \text{E}[\boldsymbol{X}]$. This result is valid up to higher order corrections coming from the non-linearity of f, and may be used to combine both statistical and systematic uncertainties. When there are no correlations between the variables, the covariance cross-terms are zero, and the standard sum of uncertainties in quadrature is recovered.

---

[1]Since a fixed number of MC events are generated, the correct distribution is in fact a binomial, but in the limit that the probability to enter the region of phase space in question is small, the Poisson approximation is valid.

In many cases f is unknown, or the linear approximation of Eq. (5.5) is not valid, and so other techniques must be used to estimate the uncertainty. One way, often used for systematic uncertainties, and as discussed in Section 5.2.2, is to vary the given input between its extreme values and use the resulting variation of the output as the final uncertainty. When the systematic uncertainty is fully correlated across multiple inputs it is necessary to vary all of them simultaneously to obtain the full effect of that uncertainty. Statistical uncertainties are often uncorrelated across different input variables, and so are usually dealt with differently. If the distribution of the statistical uncertainty on an input variable is known, or can be approximated for example as a Poisson or Gaussian, it may be possible to extract the corresponding uncertainty on the output using simulated data. This involves generating random data points according to the assumed distribution on the input, and obtaining a set of corresponding output data points from which the variance can be calculated.

5.3 Parameter estimation

Parameter estimation, also known as fitting, is an inference process where the model parameters for a function assumed to describe observations are estimated from the data. These parameters could for example be the slope and intercept for a straight line fit, or could be the normalisation of a signal process distribution whose shape is obtained from MC simulation. The MLE approach can be used for these problems. Since the fits used in this thesis are performed using binned distributions, the focus of this section will be on binned profile LH fits.

5.3.1 Binned profile likelihood fits

In the case where data is binned in a histogram, and the model assumed to describe the data contains both signal, S, and background, B, components, the LH may be written as

$$L(\boldsymbol{\mu}, \boldsymbol{\theta}) = \prod_i P(n_i | S_i(\boldsymbol{\mu}, \boldsymbol{\theta}) + B_i(\boldsymbol{\mu}, \boldsymbol{\theta})) \times \prod_j G(\theta_j). \tag{5.6}$$

Here, $P(n_i | S_i(\boldsymbol{\mu}, \boldsymbol{\theta}) + B_i(\boldsymbol{\mu}, \boldsymbol{\theta}))$ is the Poisson distribution for an observed number of events in the ith bin, n_i, given an expected number of events calculated as the sum of contributions from the signal and background processes, each of which depends on the model parameters. The parameters are divided into the so-called parameters of interest (PoIs), denoted $\boldsymbol{\mu}$, such as the normalisation of the signal and backgrounds, and the nuisance parameters (NPs), denoted $\boldsymbol{\theta}$, corresponding to variations of statistical or systematic uncertainties whose best-fit values are not of particular interest but whose contribution must nonetheless be included in the LH. Each NP, θ_j, is assumed to follow a distribution, $G(\theta_j)$, often taken to be a Gaussian, obtained in some auxiliary measurement or from theoretical constraints. There is one such constraint factor in the LH for each NP. In the case of shape-related systematic uncertainties, typically there are only nominal, *up* and *down* variations, so intermediate effects may be obtained using morphing techniques. Statistical uncertainties on the template distributions may be included as additional NPs that scale the associated signal or background component in each bin. They are typically included in the LH as additional uncorrelated Poisson or Gaussian constraints centred at one, and are referred to as γ parameters [197, 198].

Profiling

In principle, a numerical MLE method can be applied directly to the multidimensional LH in Eq. (5.6) to extract the best-fit values for both the PoIs and the NPs. However, usually it is also desirable to extract the uncertainties on the best-fit value of the PoIs, implicitly accounting for the effects of the NPs. This can be done in a process known as profiling, where the profile LH is defined as

$$L_p(\boldsymbol{\mu}) = L(\boldsymbol{\mu}, \hat{\hat{\boldsymbol{\theta}}}_{\boldsymbol{\mu}}), \quad \text{where} \quad \hat{\hat{\boldsymbol{\theta}}}_{\boldsymbol{\mu}} = \underset{\boldsymbol{\theta}}{\operatorname{argmax}} \, L(\boldsymbol{\mu}, \boldsymbol{\theta}), \tag{5.7}$$

that is $\hat{\hat{\boldsymbol{\theta}}}_{\boldsymbol{\mu}}$ corresponds to the MLE of the NPs under the conditional LH in which the PoIs, $\boldsymbol{\mu}$, are held fixed. The profile LH is therefore a function of $\boldsymbol{\mu}$ only. The MLE of $\boldsymbol{\mu}$ using $L_p(\boldsymbol{\mu})$ produces the same result as would be obtained by the MLE using the unprofiled LH. The profiled LH however allows for the estimation of uncertainties, with the effects of the NPs already folded in.

Uncertainties on fitted parameters

A given uncertainty interval, or confidence region, can be constructed by specifying the fraction, $1 - \alpha$, of hypothetical repeated experiments in which the resulting interval would contain the true values of the parameters. The value of $1 - \alpha$ is known as the confidence level (CL). The profiled LH can be used to find the confidence region by constructing the contour [199]

$$\ln L_p(\boldsymbol{\mu}) = \ln L_{\max} - \frac{1}{2} F_{\chi_N^2}^{-1}(1 - \alpha), \tag{5.8}$$

where $L_{\max} = L(\hat{\boldsymbol{\mu}}, \hat{\boldsymbol{\theta}})$ is the LH evaluated at the global best-fit values for the PoIs and NPs, and $F_{\chi_N^2}^{-1}$ is the inverse of the cumulative function, $F_{\chi_N^2}$, for a χ^2 distribution with N degrees of freedom, in this case corresponding to the number of PoIs. This result holds in the large-sample limit where the LH may be approximated as a Gaussian [200]. In the case where there is only one PoI, $F_{\chi_N^2}^{-1} = s^2$, where s is the number of standard deviations corresponding to the chosen CL. The confidence interval (CI) of a given parameter may then be determined by using the two points along that parameter axis where the contour defined by Eq. (5.8) is extremal, as shown in Figure 5.1. The presence of NPs can only ever increase the resulting uncertainty on the PoI relative to the case of no NPs.

Some NPs influence the resulting uncertainty on the PoIs more than others. The impact of a given NP may be quantified by calculating the change in the best-fit value of the PoI that arises by performing two separate fits in which the NP is fixed to either an upper or lower variation with respect to its MLE, which is also known as its postfit value. The size of the upper and lower variations may be taken as the uncertainty on the initial NP constraint function, resulting in the prefit impact, or as the final uncertainty of the fitted NP, resulting in the postfit impact. The postfit uncertainties may be smaller than the initial uncertainties in the case where the fit provides an additional constraint on the NP.
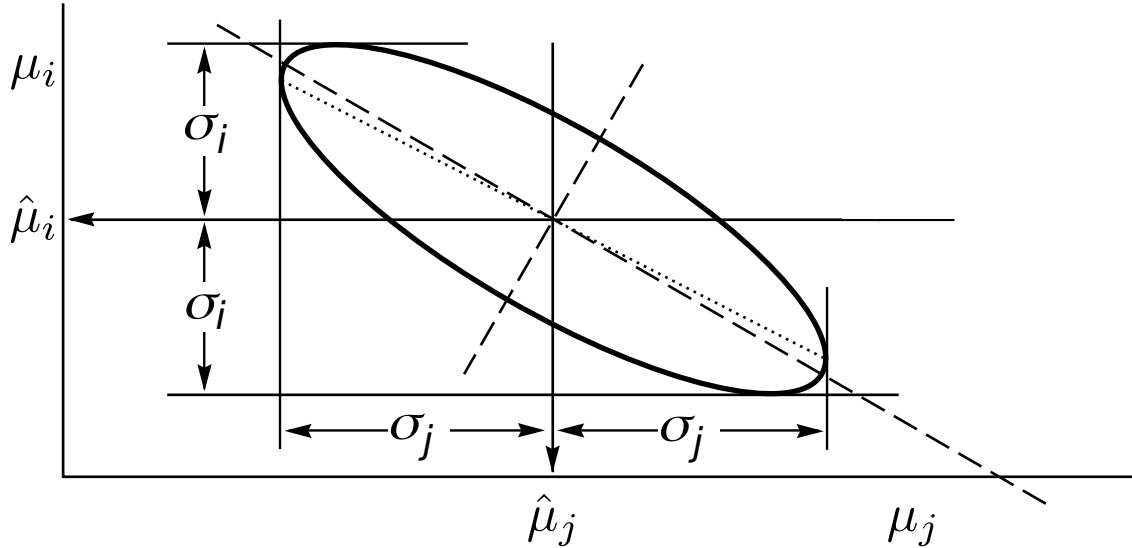
Figure 5.1: An example of the error ellipse defined by the contour of Eq. (5.8) in the case of two unprofiled PoIs, μ_i and μ_j. The centre of the ellipse corresponds to the minimum of the profiled negative log-LH, with the 68% confidence region given by the area inside the ellipse. σ_i and σ_j are the corresponding uncertainties on $\hat{\mu}_i$ and $\hat{\mu}_j$ respectively, and are seen to be larger than would be obtained if one of the PoIs was fixed at its best-fit value. Adapted from [22].

5.4 Unfolding

The data acquired by the ATLAS experiment consists of a number of reconstructed events passing some detector-level selection requirements and binned into histograms for a range of variables. In precision SM measurements, one of the aims is to compare the measured data with a range of theoretical predictions. Events generated using MC methods may be passed through a simulation of the ATLAS detector, as detailed in Section 3.2.6, followed by the reconstruction software and analysis selection, to produce detector-level theoretical predictions. This process may be referred to as folding, and requires a detailed knowledge of the ATLAS detector, reconstruction methods and event selection at the time that the measurement was made. These requirements can be circumvented by the reverse process, known as unfolding, which corrects for detector effects to produce a particle-level result, independent of the details of the detector. Comparisons can then be made directly on particle-level, both between measurements and theoretical predictions, and between measurements made by different collaborations. A variety of unfolding techniques are available, with the focus in this section on unparameterised methods used in the measurements presented in this thesis.

5.4.1 Unfolding as an inverse problem

Given a vector, $\boldsymbol{\mu}$, containing the expectation value of the number of particle-level events in each bin of some histogram, and a matrix, R, representing the response of the detector, the expectation value of the number of events in each bin on detector-level is given by

$$\boldsymbol{\nu} = \mathrm{E}[\boldsymbol{n}] = R\boldsymbol{\mu} + \boldsymbol{b}, \tag{5.9}$$

where $\boldsymbol{n}$ is the actual integer number of events observed, and $\boldsymbol{b}$ is the expected number of background events. An element, R_{ij}, of the response matrix can be understood intuitively as the conditional probability for a signal event to be reconstructed in detector-level bin i given it is generated in truth-level bin j. The aim of unfolding is then to obtain estimators for the components of $\boldsymbol{\mu}$, given information on R, $\boldsymbol{b}$ and $\boldsymbol{n}$. This is an inherently inverse problem, that is complicated by the fact that, during the folding process, information on the true distribution is generally lost due to the detector smearing. One choice of estimator is to simply invert the relationship given by Eq. (5.9) to give

$$\hat{\boldsymbol{\mu}} = R^{-1}(\boldsymbol{n} - \boldsymbol{b}), \tag{5.10}$$

where $\boldsymbol{n}$ is the MLE of $\boldsymbol{\nu}$ under the assumption that $\boldsymbol{n}$ follows a Poisson distribution. The estimator, $\hat{\boldsymbol{\mu}}$, is both unbiased and efficient [201]. It however assumes that the inverse matrix exists, which is generally true but may not always be the case [202]. Even in cases where the inverse is defined, this approach often produces very large variances. This can be understood intuitively as the loss of information, or smearing, associated with the folding process, where two very similar distributions on detector-level, perhaps distinguished by statistical fluctuations, may have been produced by two very different distributions on particle-level. The fact that the estimator is efficient means that there are no unbiased estimators for which the variance is smaller. Consequently, the focus of most unfolding efforts is on methods that introduce bias in an attempt to reduce the variance on the result.

5.4.2 Bin-by-bin unfolding

In order to use Eq. (5.10), it is necessary to calculate the full response matrix, which is usually done using MC simulations. However, in the case where the off-diagonal elements are expected to be small, that is events are unlikely to move from one truth-level bin to a different detector-level bin, it is possible to adopt a bin-by-bin approach where such elements are neglected. In this case the response matrix is assumed diagonal, and a single correction factor is calculated for each bin as

$$R_{ij}^{-1} \approx C_{ij} = \frac{\mu_i^{\text{MC}}}{\nu_j^{\text{MC}}} \delta_{ij}, \tag{5.11}$$

where μ_i^{MC} and ν_i^{MC} are the MC estimates for the expected number of signal events in the ith bin on particle- and detector-level respectively. The variance of the associated estimator is smaller than that obtained using the full response matrix, as expected, but the bias is non-zero in the case where the MC model does not match the true values [201]. However, in many cases, such as those where there is little smearing, perhaps due to the binning being suitably larger than the detector resolution, the bin-by-bin approach is sufficient, or at least can be used as a cross-check.

5.4.3 Iterative unfolding

The off-diagonal elements of the response matrix cannot always be neglected, in which case a different approach to the bin-by-bin method must be used. An iterative method [202, 203], sometimes called the iterative Bayesian unfolding method[2], is commonly used in ATLAS and other particle

---

[2]This name is somewhat misleading given that the method can be considered frequentist, and indeed tends to the MLE result in the limit of a large number of iterations [201].

physics experiments. It can be considered as a regularised approach to the direct matrix inversion, where the regularisation parameter, in this case the number of iterations, acts to suppress the large fluctuations at the cost of introducing bias.

The iterative unfolding algorithm starts with a set of initial guesses for the probabilities, $P_0(T_i)$, that a signal event is found in the ith bin on particle-, or truth-, level. This may be taken from an MC signal simulation, or even be considered to follow a uniform distribution. The estimator for the expected number of events in the ith bin on particle-level is then updated according to

$$\hat{\mu}_i = \frac{1}{\epsilon_i} \sum_j P(T_i|R_j) \times f_j \times (n_j - b_j), \tag{5.12}$$

where the sum is over the detector-level, also known as the reconstruction-level or reco-level, bins. ϵ_i is known as the efficiency correction, and is given as the ratio of the number of events passing both truth- and reco-level selections to those passing truth-level selections. It accounts for inefficiencies in the reconstruction, where true events may be missed due to detector imperfections. f_i is known as the fiducial correction, and is given as the ratio of the number of events passing both truth- and reco-level selections to those passing reco-level selections. It accounts for events that truly originate from outside the particle-level phase-space of interest, known as the fiducial region, but that may nonetheless be reconstructed in the reco-level region of interest. The remaining term, $P(T_i|R_j)$, is the conditional probability for an event to originate from a truth-level bin i, given it was reconstructed in a reco-level bin j. Bayes' theorem, given by Eq. (5.1), may to used to express this as

$$P(T_i|R_j) = \frac{P(R_j|T_i)}{P(R_j)}P(T_i), \tag{5.13}$$

where $P(R_j) = \sum_k P(R_j|T_k)P(T_k)$ is the probability to find an event in the jth reco-level bin. The matrix, $P(R_j|T_i)$, is referred to as the migration matrix, encoding the probability for events to move between bins, known as migrations, and is typically calculated using MC simulations. For the first iteration, $P(T_i) = P_0(T_i)$, and the corresponding result of Eq. (5.12) is used to update these probabilities for the next iteration. As the number of iterations increases, the bias due to the initial choice of probabilities is reduced as information from the number of events in data is included, but the variance related to statistical uncertainties increases. The iterative method can be understood to reduce to the matrix inversion method in the limit of a large number of iterations, which therefore becomes the regularisation parameter, as mentioned earlier. In an analysis, the number of iterations is optimised to reduce the bias whilst keeping statistical uncertainties small, as will be discussed in more detail in Section 6.7.4.

5.4.4   Uncertainties on unfolded results

Every unfolding procedure involves subtracting estimates for background processes from the measured number of events in data. Background estimate techniques relevant for the measurements presented in this thesis will be discussed in detail in Chapter 6, but are usually associated with a set of systematic and potentially statistical uncertainties that are propagated to the signal estimate on detector-level, that is $n - b$. Systematic uncertainties that also affect the MC signal estimate pro-

duce uncertainties on correction factors and migration matrices. Usually the unfolding procedure is repeated for each systematic variation, making sure to correlate systematic uncertainties across background and signal inputs where appropriate.

Statistical uncertainties may be propagated in different ways depending on the unfolding method. In the case of the bin-by-bin method, data and MC statistical uncertainties can be propagated using the simple formula given by Eq. (5.5). The iterative method introduces correlations between statistical uncertainties, and so more sophisticated techniques are usually used. In the case of data statistical uncertainties, multiple data samples simulated within the expected $\pm 1\,\sigma$ variations can be passed through the unfolding framework, with the spread of final results providing an uncertainty estimate. For MC statistical uncertainties, there are correlations between the efficiency and fiducial corrections, and elements of the migration matrix. In the case where the MC statistical uncertainties are expected to be small, their effect can be approximated using the bin-by-bin approach and neglecting off-diagonal elements. In other cases, techniques such as bootstrapping can be used, where multiple signal samples are generated by selecting, with replacement, events from the original signal sample. The corrections and migration matrices are recalculated with each of these generated samples, and again the variance of the set of unfolded results may be used as the estimate of the final uncertainty.

6

Measurements of W^+W^- production

Having discussed the theoretical and experimental aspects related to opposite sign W boson pair production, as well as the experimental environment and statistical techniques, in this chapter the most recent W^+W^- production cross section measurements performed using the ATLAS detector will be discussed in detail. The focus here will be on the detector-level event selection and distributions, including the methods used for estimating the dominant backgrounds. Details of the unfolding procedure, whereby data is corrected for detector effects, will also be given, and the final measurement uncertainties shown. Fiducial level integrated and differential cross sections will be presented in Chapter 7.

6.1   Analysis summary

As discussed extensively in Section 2.1, measurements of WW production cross sections provide an important test of the EW sector of the SM. The s-channel tree-level diagrams shown in Figure 2.1 indicate that this process is sensitive to the $W^+W^-\gamma$ and W^+W^-Z triple gauge couplings, which arise from the underlying SU(2)×U(1) gauge structure. Precision measurements can also be used to test higher order calculations involving both perturbative QCD and, more recently, EW corrections to the LO processes with and without hard jets in the final state, as detailed in Section 2.1.2. In addition, a detailed understanding of WW production can assist in high precision Higgs measurements, where non-resonant WW production can contribute a large background in resonant $H \rightarrow W^+W^-$ measurements [204]. Unlike all the previous measurements summarised in Section 2.2, this thesis showcases differential cross sections that have been obtained for the first time in fiducial phase spaces that are inclusive over jets. In particular, the measurements presented here are performed in a fiducial phase space with at least one hard jet [12], as well as in a fully jet inclusive phase space, where jet-related uncertainties are expected to be smaller.

The measurement strategy involves several components. Firstly a subset of events in data are selected according to some criteria designed to enhance contributions from the signal process, as will be detailed in Section 6.3. The dominant background processes must then be estimated, which is done using a range of data-driven and simulation techniques, as described in Section 6.4. The estimated background contributions are subtracted from the data to give the detector-level measurement for the number of signal events. All relevant systematic uncertainties are accounted for, as will be discussed further in Section 6.5, before detector-level distributions are presented in Section 6.6. Finally, as will be discussed in Section 6.7, signal events on the detector-level are unfolded to obtain particle-level integrated and differential fiducial cross sections. At this stage comparisons may be made to theoretical predictions.

6.1.1 Signal and background processes

The measurements described in this and the following chapter concern the production of pairs of oppositely charged W bosons in pp collisions at the LHC at $\sqrt{s} = 13\,\text{TeV}$. Measurements are made in the fully-leptonic final state, requiring exactly one electron and one muon of opposite charge, referred to as the $e\mu$ channel. The experimental signature for the signal process is therefore a pair of different flavour, opposite sign leptons, in addition to jets, and genuine p_T^miss from the W decay neutrinos. A set of criteria defining a signal region (SR), given in Section 6.3, is used in order to enhance contributions from the signal process.

Other processes can also enter the SR, perhaps because the final state particles are identical to, or are experimentally indistinguishable from, those of the signal process, or because the final state particles are misidentified. Such processes are referred to as background processes, and will be discussed in more detail in Section 6.4. The dominant background to WW production comes from top-related processes, including $t\bar{t}$ production and Wt, or single top, production. The $t\bar{t}$ process is dominant and has a much larger cross section than that for WW production due to the fact that the former process involves only QCD interactions at LO. Top quarks primarily decay as $t \to Wb$, with the bottom quark forming a b-jet, and so produce experimental signatures very similar to WW production. Usually a veto is placed on b-tagged jets to suppress this background, but such events can still enter the SR in cases where the b-jets are softer than the kinematic cut, are produced outside the detector acceptance, or are misidentified. The fraction of top events in jet inclusive SRs is typically larger than that in jet veto SRs. A dedicated data-driven method, detailed in Section 6.4.1, is therefore used for estimating the top contribution to allow for a precise signal measurement in jet inclusive phase spaces despite this enhancement.

Drell-Yan Z+jets events enter the SR mainly due to $Z \to \tau^+\tau^-$ processes where the τ lepton decays as $\tau^\pm \to e^\pm \nu_e \nu_\tau$ or $\tau^\pm \to \mu^\pm \nu_\mu \nu_\tau$. Even though four neutrinos are produced in the final state compared to only two for the signal process, the ATLAS detector can only be used to reconstruct the total neutrino momentum in the form of p_T^miss, as discussed in Section 4.6, meaning Drell-Yan Z+jets production has the same signature as the signal process. The $e\mu$ requirement greatly reduces $Z \to e^+e^-$ and $Z \to \mu^+\mu^-$ contributions.

Diboson processes including WZ, ZZ, $W\gamma$ and $Z\gamma$ production can also pass the SR criteria. In the case of WZ and ZZ, this is mainly due to leptonic decays, where one or two leptons are not

reconstructed. $W\gamma$ and $Z\gamma$ may contribute if the photon is misidentified as an electron. A smaller background arises from triboson production involving W and Z bosons, which enter the SR for similar reasons to those discussed for the diboson processes.

W+jets and dijet events may also be reconstructed as signal events if one or both of the jets are misidentified as leptons, or if the jet contains heavy-flavour hadrons that decay non-promptly to leptons. Although the misidentification rate is low, the cross section for such events is much larger than the WW production cross section. A data-driven method is used to estimate this background, as will be discussed in Section 6.4.3.

6.2 Data and nominal Monte Carlo samples

The measurements presented in this chapter use data recorded by the ATLAS detector at $\sqrt{s} = 13\,\mathrm{TeV}$ during the Run-II period from 2015 to 2018, corresponding to an integrated luminosity of $139\,\mathrm{fb}^{-1}$ after data quality criteria are applied [205].

A number of MC generated samples are used to describe the signal and background processes. In the case of the signal process, generated events are used for calculating correction factors and migration matrices in the unfolding procedure, and for the subtraction of signal events in control regions (CRs) used for background estimates. Background simulations may be used directly as background estimates in cases of less dominant backgrounds, or subtracted from CRs similarly to the signal simulations in data-driven approaches. There are both nominal samples used as the default estimate of the process, and alternative samples used for assessing modelling uncertainties. The former are summarised here, with the latter discussed in the context of systematic uncertainties in Section 6.5.

6.2.1 Nominal signal samples

The nominal signal simulation is performed with the SHERPA 2.2.2 [88] event generator. In the case of the $q\bar{q}$ channel, the prediction is accurate at NLO QCD for up to one additional parton, and at LO for two and three additional partons. For the gg-induced channel, which includes Higgs contributions, the prediction is accurate at LO for up to one additional parton. Virtual contributions are calculated using the OPENLOOPS [76] library. Higher parton multiplicities are accounted for by the PS, for which the default SHERPA simulation and tunes are used. The matching and merging to the hard ME is done with a MEPS@NLO [100] approach. The NNPDF3.0NNLO [31] set of PDFs is used, and the events use the generator normalisation, which is found to be in good agreement with the NNLO prediction [69].

6.2.2 Nominal background samples

The background coming from top events is formally divided into $t\bar{t}$ and Wt contributions. The nominal samples are simulated at NLO QCD using the POWHEG-BOX v2 [94, 95, 206–208] generator interfaced to PYTHIA 8.230 [90] for modelling of the PS. The NNPDF3.0NLO [31] set of PDFs is used for the fixed order calculation, whereas the NNPDF2.3LO [209] set of PDFs is used for modelling the PS using the A14 set of tuned parameters [210]. Beyond LO, the distinction

Process	Generator	PS	ME $\mathcal{O}(\alpha_s)$	Normalisation
$q\bar{q} \to W^+W^-$	SHERPA 2.2.2	SHERPA	NLO (0-1 jet), LO (2-3 jets)	Generator
$gg \to W^+W^-$	SHERPA 2.2.2	SHERPA	LO (0-1 jet)	Generator
$t\bar{t}$	POWHEG-BOX v2	PYTHIA 8	NLO	NNLO+NNLL
Wt	POWHEG-BOX v2	PYTHIA 8	NLO	NLO+NNLL
Z+jets	SHERPA 2.2.1	SHERPA	NLO (0-2 jets), LO (3-4 jets)	NNLO
WZ, ZZ	SHERPA 2.2.2	SHERPA	NLO (0-1 jet), LO (2-3 jets)	Generator
$W\gamma, Z\gamma$	SHERPA 2.2.8	SHERPA	NLO (0-1 jet), LO (2-3 jets)	Generator
VVV	SHERPA 2.2.2	SHERPA	NLO (0-1 jet), LO (2-3 jets)	Generator

Table 6.1: Summary of the nominal samples used to model the signal and background processes. The ME column indicates the order of the ME calculation in α_s relative to the base process. All samples use the NNPDF3.0 PDF sets, with the NNPDF2.3 PDFs used only to model the PS for POWHEG-BOX samples. Adapted from [12].

between $t\bar{t}$ and Wt processes is ambiguous as the two can overlap [211]. As a result, a diagram-removal scheme [212] is used in the nominal sample to distinguish the two processes. The $t\bar{t}$ and Wt processes are normalised to NNLO and NLO cross sections respectively, both including next-to-NLL (NNLL) resummation of soft-gluon terms[1] [213–220].

Drell-Yan Z+jets events are simulated using SHERPA 2.2.1 [88] at NLO QCD for up to two additional partons, and at LO for three and four additional partons, with inputs from the COMIX [221] and OPENLOOPS [76] packages. The prediction is matched and merged to the default SHERPA PS using the MEPS@NLO [100] method and the default SHERPA tunes. The NNPDF3.0NNLO [31] set of PDFs is used, and the events are normalised to the NNLO prediction [222].

WZ, ZZ and triboson (VVV) processes are simulated using SHERPA 2.2.2 [88], whilst $W\gamma$ and $Z\gamma$ use SHERPA 2.2.8. Both simulations use OPENLOOPS [76] and are generated at NLO QCD for up to one additional parton and at LO for two and three additional partons. The fixed order calculations are matched and merged to the default SHERPA PS. The NNPDF3.0NNLO [31] set of PDFs is used, and the events use the generator normalisation.

The nominal samples are summarised in Table 6.1. The decay of bottom and charm hadrons is modelled using the EVTGEN [223] program. As mentioned in Section 3.2.6, particle-level generated events are passed through a simulation of the ATLAS detector using GEANT4 [164]. PU was simulated by overlaying hits on the HS process from inelastic pp collisions generated with PYTHIA 8.186 [89] using the NNPDF2.3LO [209] set of PDFs and the A3 tunes [224].

6.3 Event selection

The event selection describes the set of criteria applied on the final state objects in an event, with the aim being to enhance contributions from the signal process whilst reducing those from backgrounds. Selections are applied on the reconstructed objects that enter the event, and on variables calculated from those objects.

---

[1]The soft-gluon terms are large logarithms that arise in regions of phase space where there is just enough energy to produce on-shell top quarks. The resummation is therefore also referred to as threshold resummation.

electrons	$p_\mathrm{T} > 27\,\mathrm{GeV}$, $|\eta| < 2.47$ and not $1.37 < |\eta| < 1.52$
	`Tight` identification
	`Gradient` isolation
	$|d_0/\sigma_{d_0}| < 5$, $|z_0 \sin\theta| < 0.5\,\mathrm{mm}$
muons	$p_\mathrm{T} > 27\,\mathrm{GeV}$, $|\eta| < 2.5$
	`Medium` identification
	`Tight_FixedRad` isolation
	$|d_0/\sigma_{d_0}| < 3$, $|z_0 \sin\theta| < 0.5\,\mathrm{mm}$
jets	$p_\mathrm{T} > 30\,\mathrm{GeV}$, $|\eta| < 4.5$
b-tagged jets	$p_\mathrm{T} > 20\,\mathrm{GeV}$, $|\eta| < 2.5$

Table 6.2: Definitions of the electron, muon and jet selections. Each event is required to have one electron and one muon satisfying the associated criteria, whilst the number of b-tagged jets is required to be zero, as described in the text. Adapted from [12].

6.3.1 Selections on reconstructed objects

As discussed in Sections 4.2.3 and 4.3.3, events are required to pass both the single electron and single muon triggers. Events are selected that have at least one reconstructed vertex with at least two tracks with $p_\mathrm{T} > 400\,\mathrm{MeV}$. The HS vertex is the vertex with the highest $\sum p_\mathrm{T}^2$ of its associated tracks, as mentioned in Section 4.1.1.

The electron selection requires candidates to pass the `Tight` LH-based identification criteria [177], have $p_\mathrm{T} > 27\,\mathrm{GeV}$ and $|\eta| < 2.47$. This excludes $1.37 < |\eta| < 1.52$ where there is a transition between the barrel and end-cap sections of the ECal and reconstruction quality is lower. As mentioned in Section 4.2.2, electron candidates are required to be isolated according to the `Gradient` working point. The muon selection similarly requires candidates to have $p_\mathrm{T} > 27\,\mathrm{GeV}$, and $|\eta| < 2.5$, in addition to satisfying the `Medium` identification criteria [181] and pass isolation criteria according to the `Tight_FixedRad` working point, as discussed in Section 4.3.2. Both electron and muon tracks are also required to be consistent with the HS vertex. This is achieved by requiring the transverse impact parameter significance, d_0/σ_{d_0}, to satisfy $|d_0/\sigma_{d_0}| < 3$ for electrons and $|d_0/\sigma_{d_0}| < 5$ for muons, as well as requiring the longitudinal impact parameter to satisfy $|z_0 \sin\theta| < 0.5\,\mathrm{mm}$. The definitions of both impact parameters were given in Section 4.1.1. The reconstructed leptons are required to match their respective trigger objects.

Jets are reconstructed and calibrated as described in Sections 4.5.1 and 4.5.2. For the distance metric in the anti-k_T algorithm, a radius parameter of $R_0 = 0.4$ is used. The JVT method [185] for suppressing contributions from PU is applied to jets with $p_\mathrm{T} < 60\,\mathrm{GeV}$ and $|\eta| < 2.4$. The nominal event selection requires jet candidates to have $p_\mathrm{T} > 30\,\mathrm{GeV}$ and $|\eta| < 4.5$. In addition, b-jets are identified using the b-tagging algorithms described in Section 4.5.3 at the 85% efficiency working point. Jets passing the standard requirements will be referred to as regular jets, with those additionally satisfying the b-jet requirements referred to as b-tagged jets. The definitions of the selections placed on reconstructed objects are summarised in Table 6.2.

As discussed in Section 4.6, different objects may be reconstructed from the same or overlapping sets of detector signals. To account for this overlap, a set of criteria are defined. Non-b-tagged

jets are removed if they are found within $\Delta R < 0.2$ of an electron candidate, or within the same distance of a muon candidate if the jet additionally has fewer than three tracks with $p_{\mathrm{T}} > 500\,\mathrm{MeV}$, a p_{T} less than twice the muon p_{T}, and the ratio of the muon p_{T} to the sum of the p_{T} of the tracks associated with the jet is greater than 0.7. The muon criteria are designed to remove jets that are reconstructed using hard bremsstrahlung radiation from a genuine muon. Electrons or muons within $\Delta R < 0.4$ of any remaining jet are rejected.

6.3.2 Signal region definition

The final selection, which defines the SR, is applied on events whose reconstructed objects satisfy the criteria discussed in the previous section. Events are required to have one electron and one muon of opposite charge according to the specified criteria, and no additional lepton with $p_{\mathrm{T}} > 10\,\mathrm{GeV}$ satisfying Loose isolation[2] and identification criteria. This third lepton veto reduces background contributions from WZ and ZZ production. Events are also rejected if they contain any b-tagged jets with $p_{\mathrm{T}} > 20\,\mathrm{GeV}$ and $|\eta| < 2.5$ to reduce top quark background.

Jet selections

A range of SRs with different requirements on the number of non-b-tagged jets are studied, as summarised in Table 6.3. The most recent ATLAS measurement [12] is performed in a phase space with at least one jet, referred to as the one jet inclusive phase space. In addition, results are shown for a fully inclusive measurement, where any number of jets are allowed, as well as a so-called dynamic jet veto phase space. In the dynamic jet veto selection, events are required to satisfy

$$H_{\mathrm{T}}^{\mathrm{jet}} < \max\left(H_{\mathrm{T,thresh}}^{\mathrm{jet}}, \xi H_{\mathrm{T}}^{\mathrm{lep}}\right), \tag{6.1}$$

where $H_{\mathrm{T}}^{\mathrm{jet}}$ is the scalar sum of the p_{T} of all selected jets in the event, $H_{\mathrm{T,thresh}}^{\mathrm{jet}}$ is some threshold value of $H_{\mathrm{T}}^{\mathrm{jet}}$ below which all events are kept, $H_{\mathrm{T}}^{\mathrm{lep}}$ is the scalar sum of the p_{T} of the charged leptons, and ξ is a parameter regulating the jet activity. This requirement is dynamic in the sense that the specific cut value placed to limit jet activity is a function of the other features of the event. Its purpose is to reject events where the energy within the event associated to jets is significantly larger than that associated with leptons, and is motivated by theoretical considerations. It has been shown [10] that in the high energy tails of certain distributions, for example the leading lepton p_{T}, topologies arise at NLO QCD where one of the W bosons becomes soft and can be considered to be radiated off a hard jet in the initial or final state. This is associated with a large logarithm that depends on the ratio of m_W to the energy scale of the jet. The opening up of this topology means the NLO contribution is larger than the LO contribution and so the K-factor, defined as the ratio of the NLO to the LO cross section, becomes large. This is known as a giant K-factor. Although these giant K-factors do not persist to all orders, their presence means that there are large theoretical uncertainties associated with mixed QCD and EW corrections. In order to avoid these regions, it was proposed that a cut similar to that of Eq. (6.1) should be applied[3], which was shown

---

[2]The Loose isolation criteria for both electrons and muons places a fixed requirement on the track and calorimeter isolation variables.

[3]In the original paper [10], there was no threshold for applying the veto, and $p_{\mathrm{T}}^{\mathrm{miss}}$ was included in the lepton p_{T} sum.

Jet selection	Definition	p_T^{jet} / GeV
Fully jet inclusive	No requirement on jet activity	-
One jet inclusive	≥ 1 jet	30
Jet veto	$= 0$ jets	30
Dynamic jet veto	$H_T^{\text{jet}} < \max\left(50\,\text{GeV},\, 0.4 H_T^{\text{lep}}\right)$	30
b-jet veto	$= 0$ b-tagged jets	20

Table 6.3: Summary of the jet selections used for the measurements. p_T^{jet} is the p_T threshold of the reconstructed jets used in the corresponding selection. H_T^{jet} and H_T^{lep} are defined in the text. The b-jet veto is applied for all regular jet selections.

to reduce the large differences between the calculation schemes for the mixed corrections. For the measurements presented here, the parameters are chosen as $H_{T,\text{thresh}}^{\text{jet}} = 50\,\text{GeV}$, consistent with the theoretical requirement that the event jet energy should be limited to being within the region of m_W to avoid large K-factors, and $\xi = 0.4$, which was modified from the theoretical study to account for the removal of p_T^{miss} from the H_T^{lep} definition for the experimental measurement. A value of $H_{T,\text{thresh}}^{\text{jet}} = 100\,\text{GeV}$ was also considered, although since the selection in this case is very similar to the selection with any number of jets, the lower threshold was chosen.

Finally, a jet veto phase space is considered, where events are rejected if they contain any jet with a p_T above $30\,\text{GeV}$. Historically this has been the phase space of interest for measurements of WW production due to the reduction in top quark background events, but here is mostly used for studying asymmetry variables, as will be discussed in Section 7.3. The jet veto phase space is also associated with large uncertainties on both theoretical predictions and experimental measurements, with the former suffering from large logarithms related to the jet p_T threshold, and the latter from jet response calibration effects.

Since the methods adopted to obtain the final results for each jet requirement are very similar, the results are presented together in the following sections. Distinctions in the measurement approaches will be highlighted where appropriate. The phase space with at least one jet will be referred to as the one jet inclusive phase space, whereas the phase space with any number of jets will be referred to as the fully inclusive phase space. References to methods used for the fully inclusive phase space also pertain to the dynamic jet veto and jet veto phase spaces, since the measurement approach for these three SRs is identical.

Event selection optimisation for Z+jets background rejection

Variables built from the reconstructed objects can be used to further suppress background contributions. In particular, contributions from Drell-Yan Z+jets can be reduced by placing kinematic cuts. A subset of variables, namely p_T^{miss}, the invariant mass of the dilepton system, $m_{e\mu}$, and the transverse momentum of the dilepton system, $p_{T,e\mu}$, were identified in the previous jet veto ATLAS measurement [8] as possible candidates for such a cut-based background rejection. The distributions for these variables are reproduced in Figure 6.1. p_T^{miss} was chosen since signal events contain neutrinos and therefore significant missing energy. Although Z+jets events with decays to

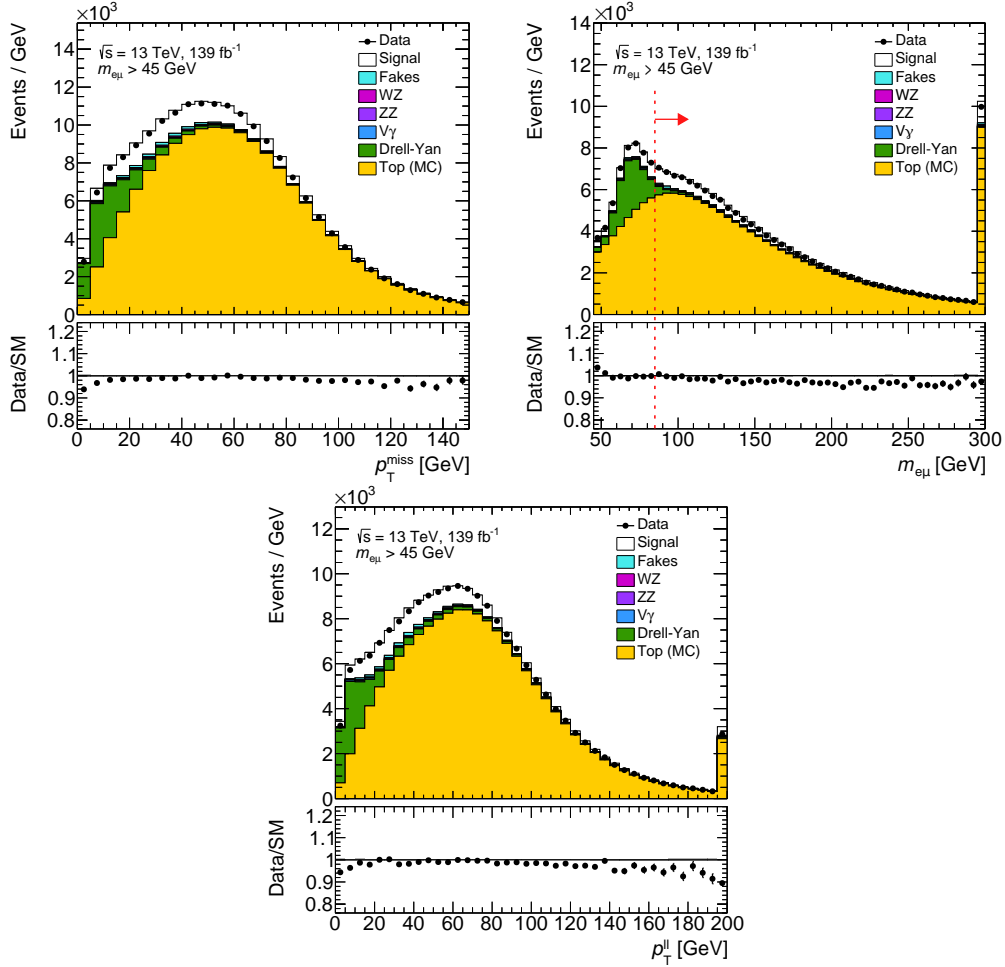**Figure 6.1:** Variables for SR cut optimisation and Drell-Yan Z+jets background rejection as described in the text using MC simulated samples. For these plots a pre-selection cut of $m_{e\mu} > 45\,\text{GeV}$ is applied, but there is no requirement on the number of regular or b-tagged jets. The red dotted line indicates the value of the cut applied, where the arrow points towards events that are kept in the SR. The final bin includes overflow events. Systematic and statistical uncertainties on the MC estimates are not shown.

τ leptons also contain neutrinos, the magnitude of the genuine p_T^{miss} is expected to be smaller than that of the signal process. A resonant enhancement in the $m_{e\mu}$ distribution is expected for Z+jets in the vicinity of the Z boson mass, so placing a kinematic cut to select events above this value can significantly reduce the background contribution. $p_{T,e\mu}$ is expected to be small for Z+jets events in the jet veto selection, again as a result of the smaller expected p_T^{miss} leading to a smaller recoil momentum of the dilepton system. For the signal process however, the leptons can recoil from the harder neutrino system, and so $p_{T,e\mu}$ can take higher values for this process. In the previous jet veto analysis, cuts were applied on all of these variables, with the following values: $p_T^{\text{miss}} > 20\,\text{GeV}$, $p_{T,e\mu} > 30\,\text{GeV}$ and $m_{e\mu} > 50\,\text{GeV}$. For the same analysis, the cut on $m_{e\mu}$ was mainly chosen to reduce signal contributions from $H \rightarrow W^+W^-$, a process for which there are dedicated measurements [204].

For the analysis using the full Run-II dataset, presented here, a further optimisation of these cuts was performed. The metrics for the optimisation were taken to be the number of simulated

p_T^{miss} / GeV	$m_{e\mu}$ / GeV	$p_{T,e\mu}$ / GeV	WW	Z+jets	$\frac{WW}{Z+\text{jets}}$
30	55	20	19,207	6,306	3.05
10	85	5	19,317	1,586	12.18
10	85	-	19,401	1,604	12.10
5	85	10	19,513	1,649	11.83
-	85	10	19,667	1,695	11.60
5	85	5	19,812	1,720	11.52
5	85	-	19,912	1,749	11.39
-	85	5	19,983	1,775	11.26
-	85	-	20,094	1,814	11.08

Table 6.4: Cut combinations with the largest signal to background ratio. The values for each variable correspond to lower cut thresholds, whilst the numbers for the WW and Z+jets columns indicate MC yields. The first row shows the cut combination for the previous jet veto measurement. Dashes indicate that no cut is applied on the corresponding variable.

signal events surviving the cut, known as the signal yield, as well as the ratio of this yield to that of Drell-Yan events. A scan was performed across all variables, with the optimisation maximising the signal to background ratio, whilst ensuring a signal yield greater than or equal to that obtained using the cut values from the previous measurement. The cut combinations satisfying the yield and signal to background ratio requirements are shown in order of decreasing signal to background ratio in Table 6.4. Only the eight combinations with the highest signal to background ratios are shown, in addition to the cut combination used for the most recent jet veto measurement. It is clear that by using a higher cut threshold on $m_{e\mu}$ of 85 GeV, it is possible to significantly improve the signal to background ratio. Additionally reducing the cut thresholds for p_T^{miss} and $p_{T,e\mu}$ increases the signal yield, but due to the relatively large uncertainties associated with p_T^{miss} reconstruction, combinations with no cut on p_T^{miss} are preferred. For this reason, and because cuts on $p_{T,e\mu}$ only introduce mild improvements in the signal to background ratio, the single cut of $m_{e\mu} > 85$ GeV is used for the analyses presented in this thesis.

The optimisation has only been performed for the jet veto selection, although it is anticipated that the presence of hard jets in the final state will not affect the outcome significantly. In particular, the cut on $m_{e\mu}$ is based on the position of the Z boson mass peak, which is expected to be insensitive to ISR. The signal and background yields are shown before and after the $m_{e\mu}$ cut in Table 6.5. There is a reduction in the expected Drell-Yan yield of about a factor of nine following the $m_{e\mu}$ cut, with a relatively minimal reduction in the signal yield. Also shown is the effect of applying the b-jet veto, where about 90% of the top background is removed whilst keeping about 95% of the signal. The jet inclusive SR, corresponding to the b-jet veto row in Table 6.5, is expected to have a signal purity of about 40%, with the top background making up about 45% of the total events, and 80% of the total background. The signal purity improves for the jet veto and dynamic jet veto selections, but deteriorates for the one jet inclusive selection.

Selection	Data	Total MC	WW	Top	Drell-Yan	Fakes	VZ/γ
Pre-selection	1,025,163	1,040,212	91,609	863,611	67,299	8,896	8,794
		-	9%	83%	7%	1%	1%
$m_{e\mu} > 85\,\text{GeV}$	695,890	712,086	65,058	628,467	7,179	6,224	5,154
		-	9%	88%	1%	1%	1%
b-jet veto	144,221	147,289	61,762	68,273	6,884	5,836	4,531
		-	42%	46%	5%	4%	3%
One jet inclusive	89,239	93,598	28,134	57,789	2,150	2,773	2,749
		-	30%	62%	2%	3%	3%
Jet veto	54,982	53,690	33,628	10,484	4,734	3,062	1,779
		-	63%	20%	9%	6%	3%
Dynamic jet veto	80,940	80,733	44,454	24,417	5,509	3,709	2,642
		-	55%	30%	7%	5%	3%

Table 6.5: Cutflow showing the number of events in data and the number of MC generated events for each process. Cuts in the upper rows are applied sequentially, whilst those in the lower three rows correspond to orthogonal regions. The fully jet inclusive selection coincides with that of the b-jet veto. The percentages show the expected relative proportions of each process for the given selection. The pre-selection includes all requirements placed on reconstructed leptons and jets, as discussed in Sections 6.3.1 and 6.3.2, in addition to a loose $m_{e\mu} > 10\,\text{GeV}$ cut. Here $V = W/Z$.

6.4 Background estimates

As is clear from Table 6.5, despite the event selection the SR still contains large background contributions, with the highest signal purity of 63% achieved for a jet veto phase space. As a result, in order to extract the signal component from data, estimates need to be made for the size of the contributions from backgrounds. The simplest approach would be to simply use the nominal MC estimates shown in Table 6.5. However, such estimates can be associated with large modelling uncertainties, or are perhaps expected to be poorly modelled, as in the case of the fake lepton background discussed in Section 6.4.3. This is of particular concern for the largest backgrounds, where associated uncertainties can dominate the measurement result. Therefore, in the measurements presented here a combination of data-driven and MC simulation methods are used.

6.4.1 Top quark background estimate

The largest background in all cases comes from top quark events, and so an accurate and precise data-driven method is used. As already mentioned, the top quark background is split into $t\bar{t}$ and Wt contributions, with the former accounting for about 80% of the total top contribution. Therefore, the focus of the data-driven approach is to obtain a precise estimate of the $t\bar{t}$ yield.

b-tag counting method

The method adopted for estimating the $t\bar{t}$ contribution in the SR is based on a recent $t\bar{t}$ cross section measurement [225], and is known as the b-tag counting method. The method defines two CRs, which have exactly the same selection as the nominal SR, but differ only in the requirement on the number of b-tagged jets. These are the one b-jet CR, with a requirement of exactly one b-tagged

jet, and the two b-jet CR, with a requirement of exactly two b-tagged jets. The b-tagged jets satisfy the requirements specified in Table 6.2. The CRs are dominated by top events, with an expected $t\bar{t}$ purity of 87% and 96% in the one and two b-jet CRs respectively for the one jet inclusive selection, as shown in Table 6.6. The remaining contributions are almost exclusively from single top events. The leading lepton p_T and jet multiplicity in the two $t\bar{t}$ CRs for the one jet inclusive selection are shown in Figure 6.2. There is a visible downwards slope in the ratio of data to the simulation. This is related to the modelling of $t\bar{t}$ events, for which the MC prediction is used in the plots, and is associated with a relatively large uncertainty. Such uncertainties are strongly reduced in the b-tag counting method, where there is limited reliance on the $t\bar{t}$ modelling.

The combination of data in the two CRs allows for the extraction of the $t\bar{t}$ yield in the SR via the following expressions for the numbers of $t\bar{t}$ events in each region

$$N_{1b}^{t\bar{t}} = N_{1b} - N_{1b}^{\text{non-}t\bar{t}} = \mathcal{L}\sigma_{t\bar{t}}\epsilon_{e\mu} \cdot 2\epsilon_b(1 - C_b\epsilon_b), \tag{6.2}$$

$$N_{2b}^{t\bar{t}} = N_{2b} - N_{2b}^{\text{non-}t\bar{t}} = \mathcal{L}\sigma_{t\bar{t}}\epsilon_{e\mu} \cdot C_b\epsilon_b^2, \tag{6.3}$$

$$\text{and} \quad N_{0b}^{t\bar{t}} = \mathcal{L}\sigma_{t\bar{t}}\epsilon_{e\mu} - N_{1b}^{t\bar{t}} - N_{2b}^{t\bar{t}} = \mathcal{L}\sigma_{t\bar{t}}\epsilon_{e\mu} \cdot (1 - 2\epsilon_b + C_b\epsilon_b^2), \tag{6.4}$$

where N_{ib} is the number of observed events in the region with i b-tagged jets, and $N_{ib}^{\text{non-}t\bar{t}}$ is the number of non-$t\bar{t}$ events in the same region, obtained from simulation. The expression, $\mathcal{L}\sigma_{t\bar{t}}\epsilon_{e\mu}$, combines the integrated luminosity, $\mathcal{L}$, the $t\bar{t}$ production cross section, $\sigma_{t\bar{t}}$, and the efficiency for selecting $t\bar{t}$ events with one electron and one muon in the final state, $\epsilon_{e\mu}$, in order to give the total number of $t\bar{t}$ events before any b-tagged jet selection[4]. Eq. (6.4) corresponds to the SR, containing exactly zero b-tagged jets. The b-jet selection efficiency, ϵ_b, corresponds to the efficiency to find and tag a given b-jet and therefore includes both acceptance effects and the efficiency of the b-tagging algorithm. Finally, the correction factor, C_b, accounts for possible correlation effects between selecting one and two b-jets. It is given as $C_b = \epsilon_{bb}/\epsilon_b^2$, where ϵ_{bb} is the efficiency for selecting two b-jets, and is obtained from MC simulation as

$$C_b = \frac{4N_{\text{MC}}^{t\bar{t}}N_{2b,\text{MC}}^{t\bar{t}}}{\left(N_{1b,\text{MC}}^{t\bar{t}} + 2N_{2b,\text{MC}}^{t\bar{t}}\right)^2}, \tag{6.5}$$

where $N_{\text{MC}}^{t\bar{t}}$ is the total number of MC simulated $t\bar{t}$ events across the zero, one and two b-tagged jet regions. The correction factor is typically close to one, with the differential distributions for the leading lepton p_T and the jet multiplicity shown in Figure 6.3. The distribution is fairly flat for the leading lepton p_T, and likewise for the jet multiplicity for two or more jets. The relatively low value for the one jet bin can be explained due to the reduced probability for finding and tagging both b-jets when at least one of them has a p_T below 30 GeV. Given the inputs, N_{ib}, $N_{ib}^{\text{non-}t\bar{t}}$, and C_b, it is possible to obtain $N_{0b}^{t\bar{t}}$ by solving Eqs. (6.2)–(6.4) simultaneously, with the result

$$N_{0b}^{t\bar{t}} = \frac{C_b}{4} \frac{\left(N_{1b}^{t\bar{t}} + 2N_{2b}^{t\bar{t}}\right)^2}{N_{2b}^{t\bar{t}}} - N_{1b}^{t\bar{t}} - N_{2b}^{t\bar{t}}. \tag{6.6}$$

---

[4]Strictly speaking, in order for Eqs. (6.2)–(6.4) to be consistent, this expression provides the total number of $t\bar{t}$ events with at most two b-tagged jets. The MC correlation factor, C_b, is estimated in accordance with this requirement.

Region	Observed	Predicted $\pm$ Error	Purity
$t\bar{t}$ CR $1b$	260,971	$268,000 \pm 19,000$	87%
$t\bar{t}$ CR $2b$	257,777	$267,000 \pm 21,000$	96%
Top VR	7,167	$7,000 \pm 1,000$	72%
Same-sign VR	5,095	$5,000 \pm 600$	25%
Drell-Yan VR	11,824	$13,000 \pm 1,600$	74%
VZ VR	14,770	$14,000 \pm 1,900$	94%
$V\gamma$ VR (OS)	2,720	$2,670 \pm 240$	63%
$V\gamma$ VR (SS)	2,401	$2,250 \pm 240$	76%

Table 6.6: Yields in the top CRs and all VRs. Here OS corresponds to the opposite-sign VR, whereas SS indicates the same-sign VR, and $V = W/Z$. The purity is with respect to the target process in each region, which for the same-sign VR is fake leptons. The regions in this table are for the one jet inclusive selection, although the purities are almost identical in the fully jet inclusive case, excluding the Drell-Yan VR where this increases to about 86%. The uncertainty on the prediction includes both statistical and systematic effects, excluding theoretical uncertainties on the signal. The $t\bar{t}$ CRs use simulated $t\bar{t}$ events, whilst the top VR uses the data-driven estimate. Adapted from [12].

This result only depends on the modelling of $t\bar{t}$ events via the correlation factor, C_b, and so associated theoretical and experimental uncertainties are reduced by about a factor of five compared to a pure MC simulation. The $t\bar{t}$ estimate is performed in each bin for differential distributions. Since the p_T threshold for the b-tagged jet selection is lower than that for non-b-tagged jets, as shown in Table 6.2, the b-tag counting method also works in regions of phase space where there is only one or even no jet passing the regular, higher p_T jet selection. That is, the one b-jet and two b-jet CRs may both in principle still be populated for the zero and one regular jet bins. The $t\bar{t}$ estimate demonstrates perfect closure in a test comparing the output of the estimate using simulated pseudodata to the detector-level expectation obtained from the same MC sample.

The remaining top contribution comes from Wt events. Given this contribution accounts for a much lower proportion of the top background in the SR, the number of such events is simply obtained from MC simulation. Including systematic variations, to be discussed in detail in Section 6.5, the total uncertainty on the top background in the one jet inclusive SR is 2.8%. This is reduced from about 15% for a pure MC estimate due to the relatively large reliance of the b-tag counting estimate on observed yields in the CRs, with $t\bar{t}$ modelling only entering via C_b, and because of a partial cancellation of uncertainties on the Wt contribution that are independent of the b-jet multiplicity, due to the anti-correlation between the Wt yield and the $t\bar{t}$ estimate.

Transfer factor method

Despite the b-tag counting method in principle still working in bins with zero or one regular jet, the number of events in data in the associated b-jet CRs can be very low, if not zero. This is particularly true for the high energy tails of distributions in the jet veto region, where for example the requirement of having two b-tagged jets with a p_T between $20\,\text{GeV}$ and $30\,\text{GeV}$, and at the same time high momentum leptons, is severely restrictive. In such bins, the data and MC statistical uncertainties can become very large, or the method itself might become inapplicable due to the
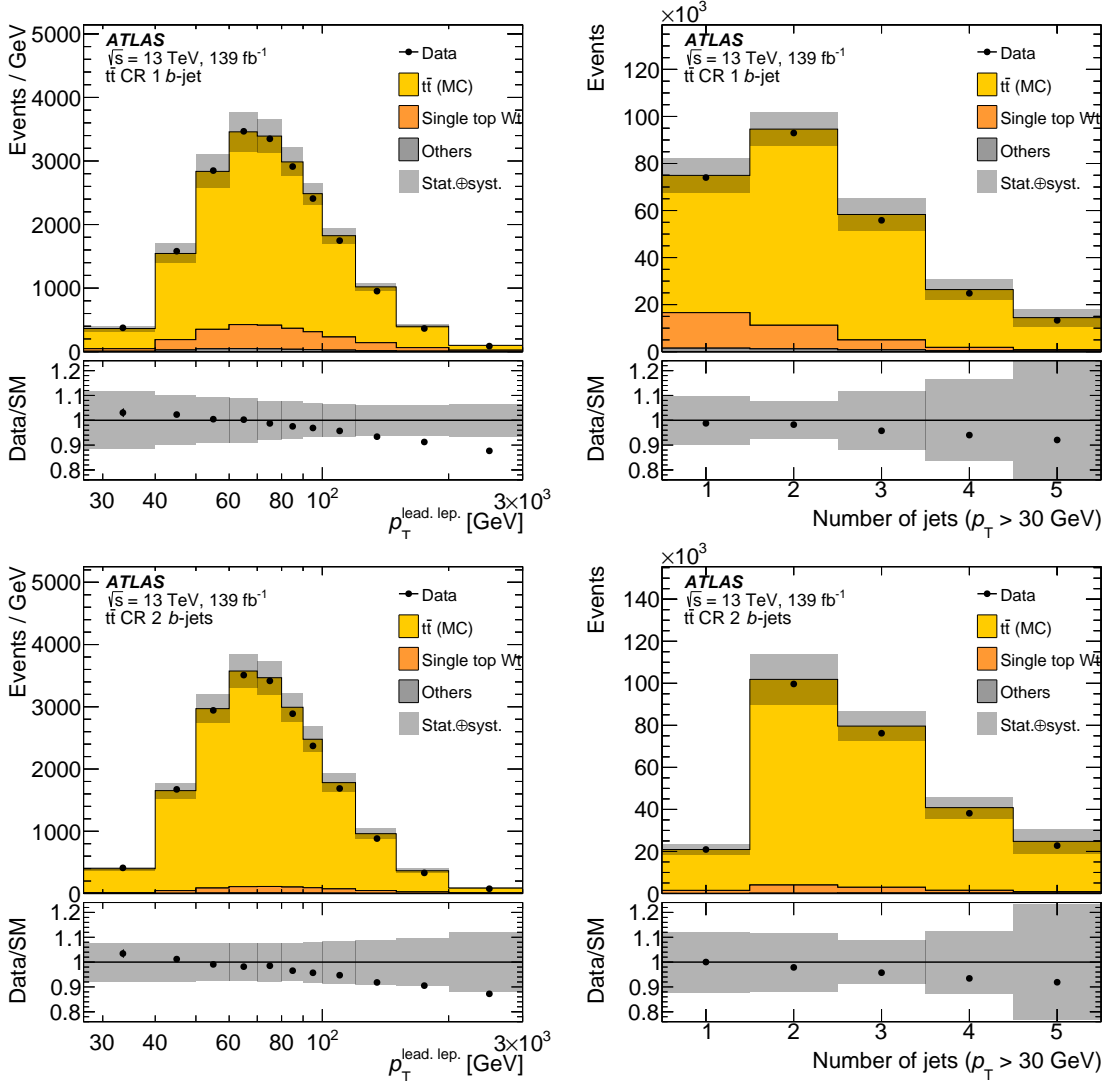
Figure 6.2: Distributions for the leading lepton p_T (left) and jet multiplicity (right) for the one jet inclusive selection in the CR with exactly one b-tagged jet (top) and exactly two b-tagged jets (bottom) showing $t\bar{t}$ and Wt predictions, as well as subdominant contributions. The grey band includes statistical and systematic uncertainties on the prediction. Taken from [12].

absence of any events in the CRs. A possible solution is to employ a transfer factor method for these bins, as will be described in this section. This method has only been adopted for the fully jet inclusive measurement, where the zero jet bin is introduced.

The transfer factor method is data-driven, with an extrapolation factor obtained from MC simulations. Unlike the b-tag counting estimate, the transfer factor approach estimates the combination of $t\bar{t}$ and Wt. The total number of top events in the SR is given as

$$N_{0b}^{top} = \frac{N_{0b,MC}^{top}}{N_{1b,\geq 0j,MC}^{top}} \cdot \left(N_{1b,\geq 0j} - N_{1b,\geq 0j,MC}^{non\text{-}top} \right), \tag{6.7}$$

where $N_{1b,\geq 0j}$ is the number of observed events in a CR with exactly one b-tagged jet and any number of regular jets. For the fully jet inclusive measurement, this region therefore differs from the SR only in the requirement on the number of b-tagged jets. Similarly to the b-tag counting estimate,
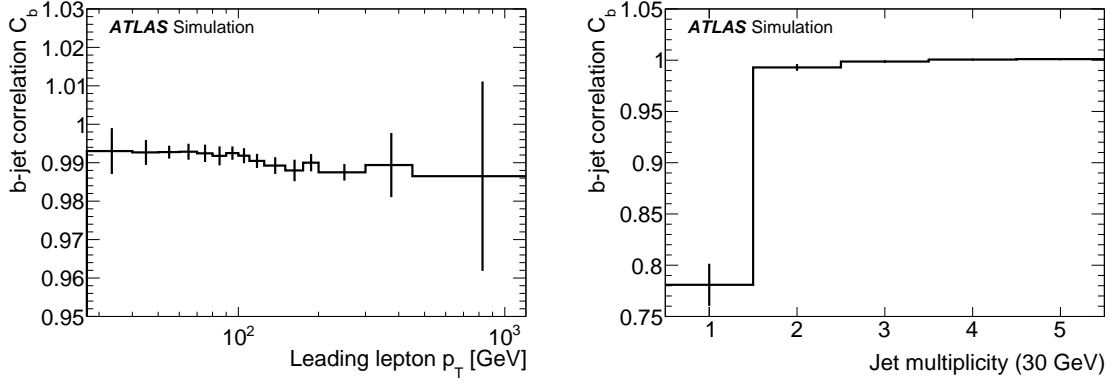
Figure 6.3: The correlation factor, C_b, for the leading lepton p_T (left) and the jet multiplicity (right). The uncertainties include both MC statistical uncertainties and systematic uncertainties. Taken from [12].

non-top background contributions are obtained using simulation and are subtracted from the number of observed events. The MC extrapolation factor then corrects to the expected number of top events in the SR. In general, the b-tag counting estimate provides reduced modelling and jet-related systematic uncertainties compared to both the pure MC estimate and the transfer factor method, although the latter does provide some reduction in the modelling and b-tagging uncertainties, and crucially is almost unaffected by data and MC statistical uncertainties. The complementary nature of the two estimates motivates a combination. The transfer factor method is chosen in a given bin if there are fewer than 100 observed events in the two b-jet CR. Whilst this does not always give the smallest uncertainty for all bins, it is a simple criterion to implement and performs well overall. Examples are shown in Figure 6.4, where the total relative uncertainty for the $t\bar{t}+Wt$ estimate is shown for both the b-tag counting method and the transfer factor method, as well as the combined approach.

Top estimate validation region

The top estimate is validated against data in a dedicated validation region (VR). This is chosen to be a subset of the one jet inclusive SR, where in addition to the nominal selection, the invariant mass of the leading jet and closest lepton, $m_{\ell j}$, is required to be less than 140 GeV, and the azimuthal angular separation between the electron and muon, $\Delta\phi(e, \mu)$, is required to be less than $\pi/2$. This creates a top-enriched region that is about 70% pure in top events. Good agreement is seen between the number of observed events and that predicted by the top estimate, both differentially as shown in Figure 6.5 and for the total number of events as shown in Table 6.6. The differential distributions show that the top estimate is valid for large leading lepton p_T and for up to at least five jets.

6.4.2 Drell-Yan background

The Drell-Yan Z+jets background is obtained from MC simulation, and contributes no more than 10% of the selected events, according to Table 6.5. The Drell-Yan contribution is strongly reduced by the different flavour requirement on the lepton pair, and enters the SR almost exclusively via $Z/\gamma^* \to \tau^+\tau^-$ events. The total uncertainty on the Z+jets background in the one jet inclusive
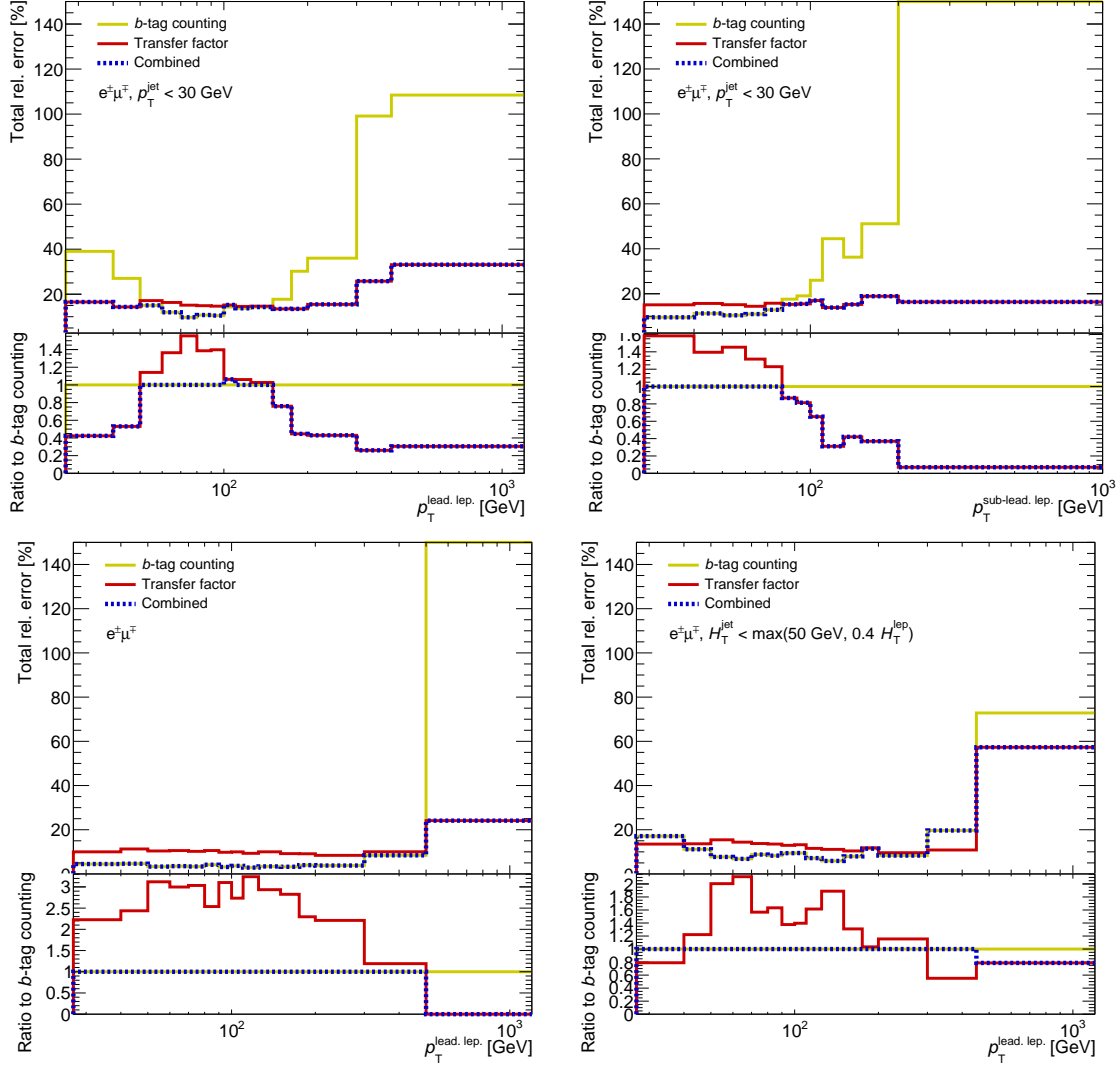
Figure 6.4: The total relative error including both systematic and statistical components in the $t\bar{t}+Wt$ estimate for the b-tag counting method, the transfer factor method, and the combined approach. Shown are the leading lepton p_T in the jet veto region (top left), the subleading lepton p_T in the jet veto region (top right), the leading lepton p_T in the fully jet inclusive region (bottom left), and the leading lepton p_T in the dynamic jet veto region (bottom right).

SR is found to be about 30%.

Drell-Yan validation region

The Drell-Yan validation region requires the b-jet veto from the SR, as well as a dilepton mass between 45 GeV and 80 GeV and either $p_{T,e\mu} < 30$ GeV or $p_T^{\text{miss}} < 20$ GeV. The requirement on the number of regular jets is the same as that of the corresponding SR. The purity for the one jet inclusive selection is about 74%, increasing to about 86% for the fully jet inclusive selection, and there is good agreement with the data, as shown in Table 6.6. This agreement is also seen in Figure 6.6, where the dilepton invariant mass, $m_{e\mu}$, and leading lepton p_T are shown for both the one jet inclusive and fully jet inclusive VRs.
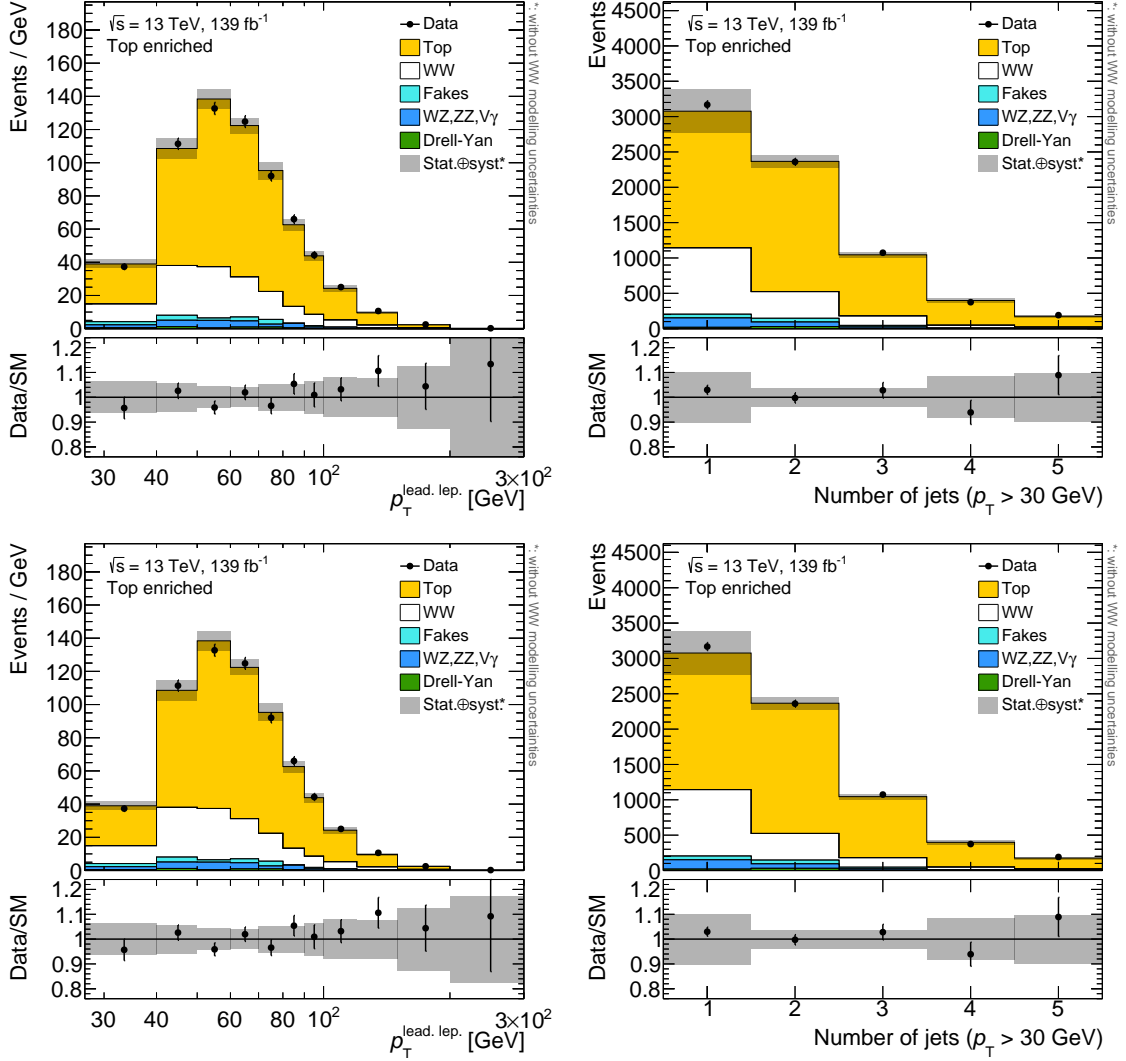
Figure 6.5: Distributions for the leading lepton p_T (left) and the jet multiplicity (right) in the top-enriched VR defined in the text with (bottom) and without (top) the transfer factor method. The plots of the number of jets are identical since the b-tag counting method is chosen in all bins shown. The grey band includes statistical and systematic uncertainties on the prediction. Modelling uncertainties on the WW signal prediction are not included. The final bin includes overflow events.

6.4.3 Backgrounds from non-prompt or misidentified leptons

As mentioned in Section 6.1.1, events in which jets are either misidentified as leptons, or contain heavy-flavour hadrons that decay to leptons, known as non-prompt leptons, may enter the SR. Misidentified or non-prompt leptons are collectively referred to as fakes. Most fakes arise from W+jets, although there are also contributions from single top and $t\bar{t}$ events that include only one prompt lepton. The fake background accounts for no more than 6% of selected events in the jet regions considered.

Fake factor method

In general, the efficiency for selecting non-prompt or misidentified leptons is expected to be poorly modelled [226], and so despite the relatively small contribution to the SR, a data-driven estimate
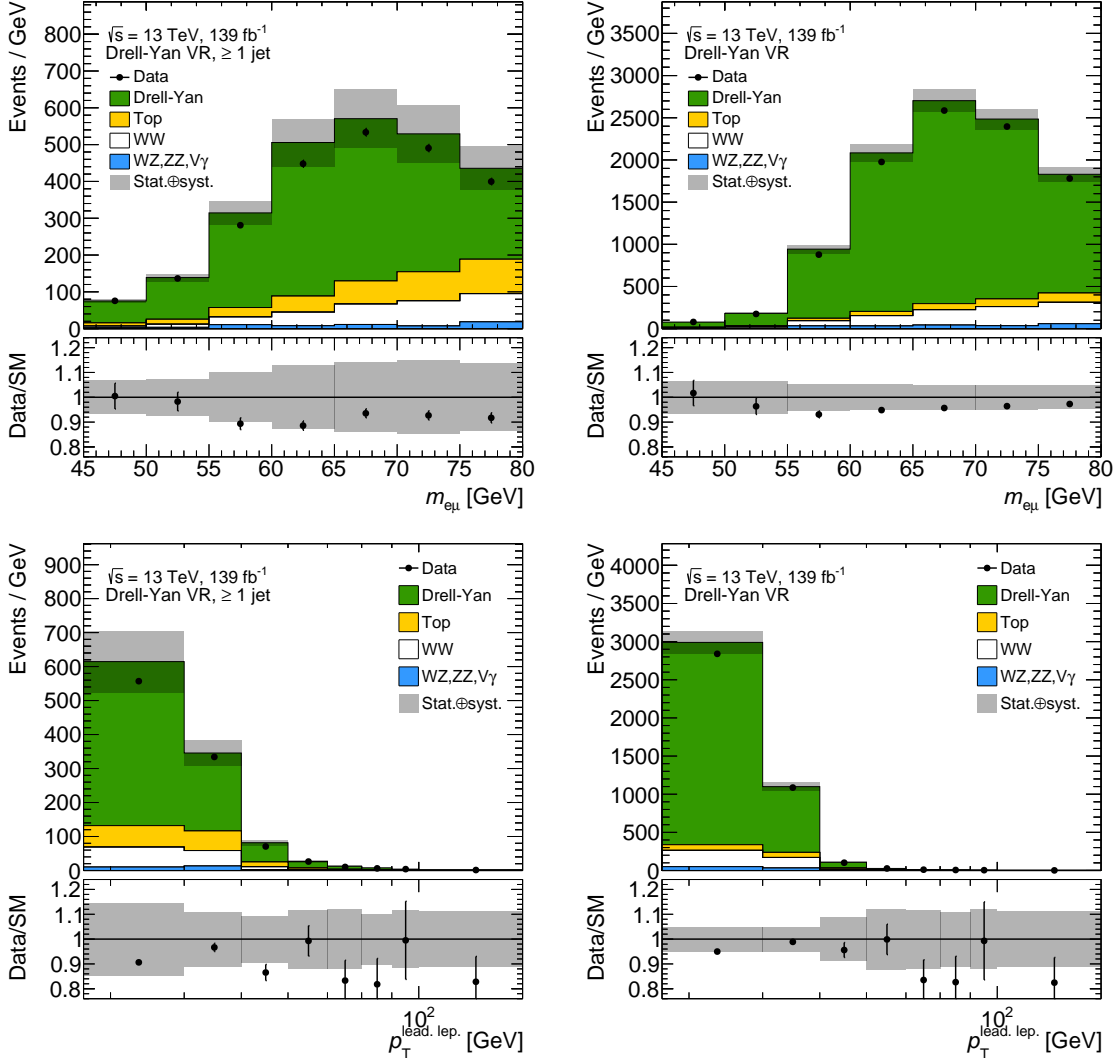
Figure 6.6: Distributions for the dilepton invariant mass, $m_{e\mu}$ (top), and the leading lepton p_T (bottom) in the Drell-Yan VR defined in the text for the one jet inclusive (left) and fully jet inclusive (right) selections. The grey band includes statistical and systematic uncertainties on the prediction. The final bin includes overflow events.

is used that follows closely the method applied in a recent same-sign WW analysis [227]. A CR is defined in which contributions from fake events are enhanced. One of the lepton candidates is required to fail the isolation and identification criteria of the SR, but pass a looser set of criteria designed to increase contributions from fake leptons. In every other respect, the fake CR is identical to the SR. In order to obtain the expected number of fake events in the SR, extrapolation factors are determined as functions of η, p_T and the lepton flavour and applied to events in the fake CR after background subtraction. The total uncertainty on the fake background in the one jet inclusive SR is about 40%.

The extrapolation factors themselves are determined in a separately defined region that is dominated by fake leptons. Events in this region are required to have one lepton candidate and one jet, where the azimuthal angular distance between the lepton and jet, $|\Delta\phi(\ell, j)|$, is required to be larger than 2.8 in order to enhance contributions from dijet events in which one of the jets fakes a lepton.

Contamination from W+jets events is reduced by placing upper cuts on p_T^{miss}. The fake factor is then obtained as the ratio of the number of events where the lepton candidate passes the SR lepton selection, to the number of events where it passes instead the looser selection defining the fake CR.

Fake estimate validation region

The fake estimate is validated in a same-sign VR where the opposite charge requirement of the SR is replaced with a same-sign requirement. This requirement enhances contributions from processes producing fake leptons, which are more often charge symmetric compared to SM processes. The purity in this region for the one jet inclusive selection, as shown in Table 6.6, is only 25%, but the dominant diboson background is known with a precision of about 10%, which allows for a reasonable validation of the fake background. The distributions of the leading lepton p_T and subleading lepton p_T in VRs with at least one jet and any number of jets are shown in Figure 6.7, where good agreement with the data is observed.

6.4.4 Other backgrounds

WZ, ZZ, $W\gamma$ and $Z\gamma$ production contribute about 3% of the total selected events for all jet selections. They are estimated using MC simulation. The dominant contribution comes from WZ events, which have been found to be well modelled by the nominal SHERPA simulation [228]. The background from simulated triboson events was found for the one jet inclusive selection to contribute less than 0.1% of the total selected events, and no more than 0.5% of events in a single bin. As a result, this background is neglected in all measurements. It should be noted that the simulated samples used to reach this conclusion only include leptonic boson decays, and in principle events including hadronic decays may contribute more significantly to the triboson background for more inclusive selections. Even though this contribution is not explicitly included, it is effectively treated as part of the signal in the analyses presented in this thesis.

Validation of other backgrounds

The VZ estimate is validated in a region requiring an additional lepton with $p_T > 10\,\text{GeV}$ that satisfies loosened identification criteria. The invariant mass of the same-flavour opposite-sign lepton pair is required to be within a $20\,\text{GeV}$ window around the Z boson mass, providing a very pure sample of diboson events, as seen in Table 6.6. The agreement between the data and the predictions is good, as shown for the p_T^{miss} and leading lepton p_T distributions in Figure 6.8. As mentioned in Section 6.1.1, $W\gamma$ and $Z\gamma$ processes enter the SR when the photon is misidentified as an electron. VRs are defined where the identification requirements on the electron are changed to enhance photon conversion contributions. Since photon conversions result in electron-positron pairs of opposite charge, one VR is defined with a same-sign requirement on the two leptons, and another with an opposite-sign requirement. These VRs are relatively pure in photon conversions, and as seen in Table 6.6 and in the electron candidate p_T and leading lepton p_T distributions in Figure 6.9, there is good agreement between the data and the predictions.
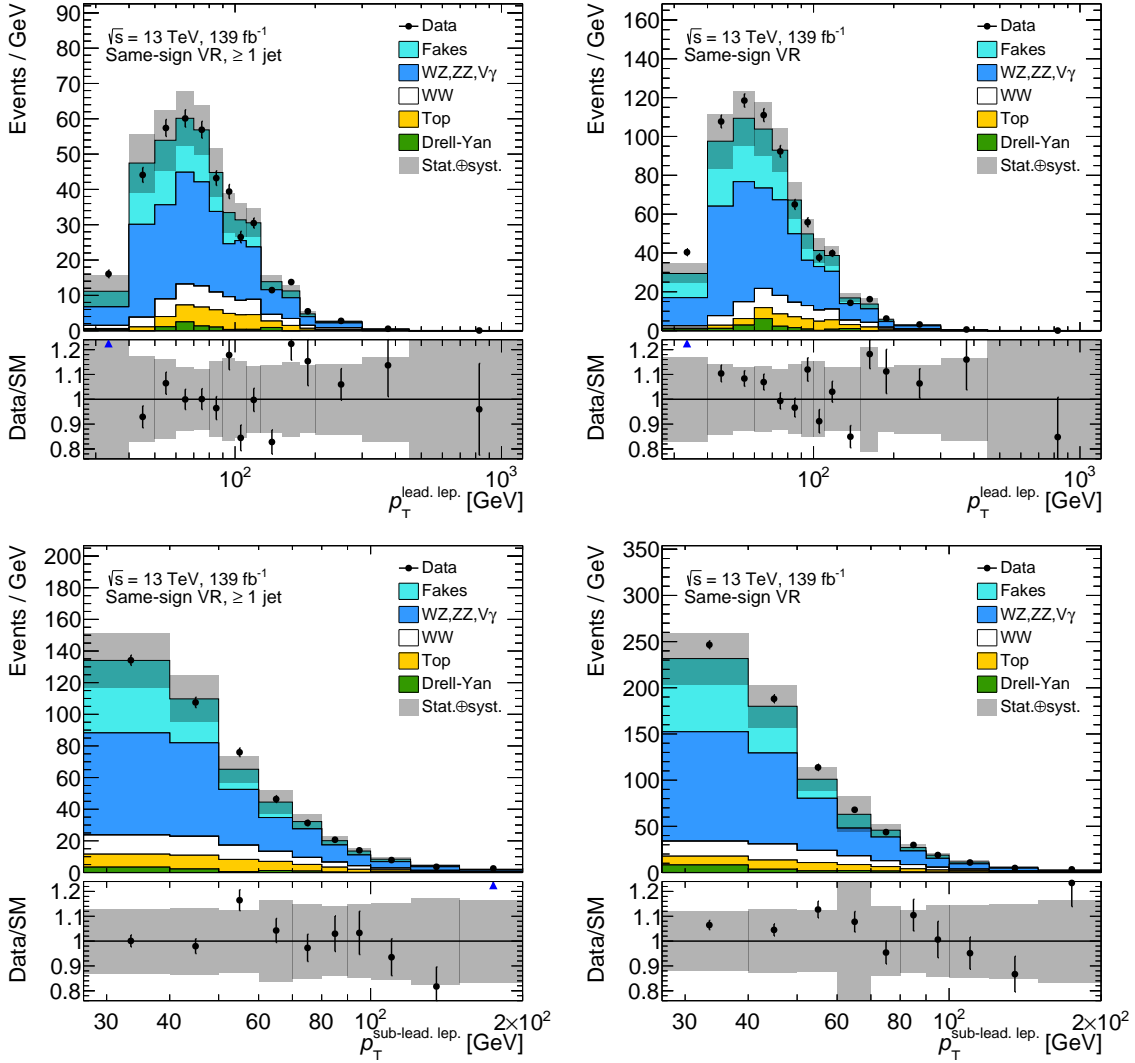
Figure 6.7: Distributions for the leading lepton p_T (top) and subleading lepton p_T (bottom) in the same-sign fake VR defined in the text for the one jet inclusive (left) and fully jet inclusive (right) selections. The grey band includes statistical and systematic uncertainties on the prediction. The final bin includes overflow events.

6.5 Systematic uncertainties

Systematic uncertainties were discussed in general terms in Section 5.2.2. There are many systematic uncertainties that affect the measurements discussed here, including those related to experimental sources, signal modelling and background estimates. A selection of the most important systematic uncertainties are discussed in this section. The effect of systematic uncertainties is evaluated coherently for all aspects of the measurement, thereby correctly taking into account correlations.

6.5.1 Experimental systematic uncertainties

A number of uncertainties relate to the reconstruction and identification of analysis objects, and are typically referred to as experimental uncertainties. They include uncertainties associated with
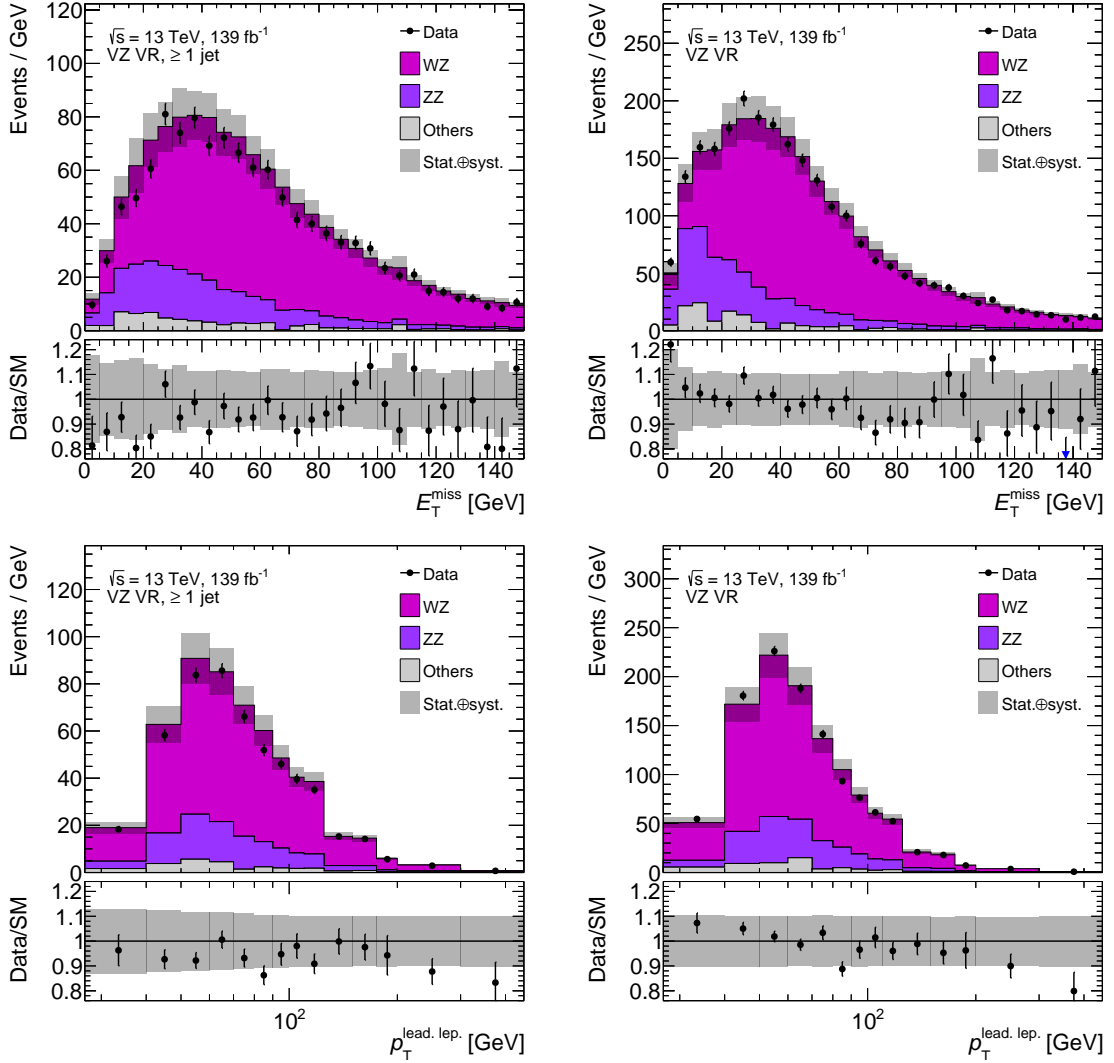
Figure 6.8: Distributions for p_T^{miss} (top) and the leading lepton p_T (bottom) in the VZ VR defined in the text for the one jet inclusive (left) and fully jet inclusive (right) selections. The grey band includes statistical and systematic uncertainties on the prediction. The final bin includes overflow events.

jets, leptons and p_T^{miss}, as well as PU and b-jet identification.

Luminosity: The integrated full Run-II luminosity of $139\,\text{fb}^{-1}$ has an uncertainty of 1.7% [229] that was determined in van der Meer scans using the LUCID-2 detector [230]. The luminosity uncertainty is a flat uncertainty applied on MC generated signal and background predictions.

Pile-up: The MC samples used in the analysis are reweighted such that the distribution of the number of pp collisions per bunch crossing matches that in data. There are systematic uncertainties associated with this reweighting related to the modelling of PU events.

Jet reconstruction: Relatively large uncertainties enter the measurement via calibration of the JES and the JER. The calibration procedure was briefly discussed in Section 4.5.2. For the JES, an MC-based jet flavour composition uncertainty is applied to account for the imprecise knowledge on
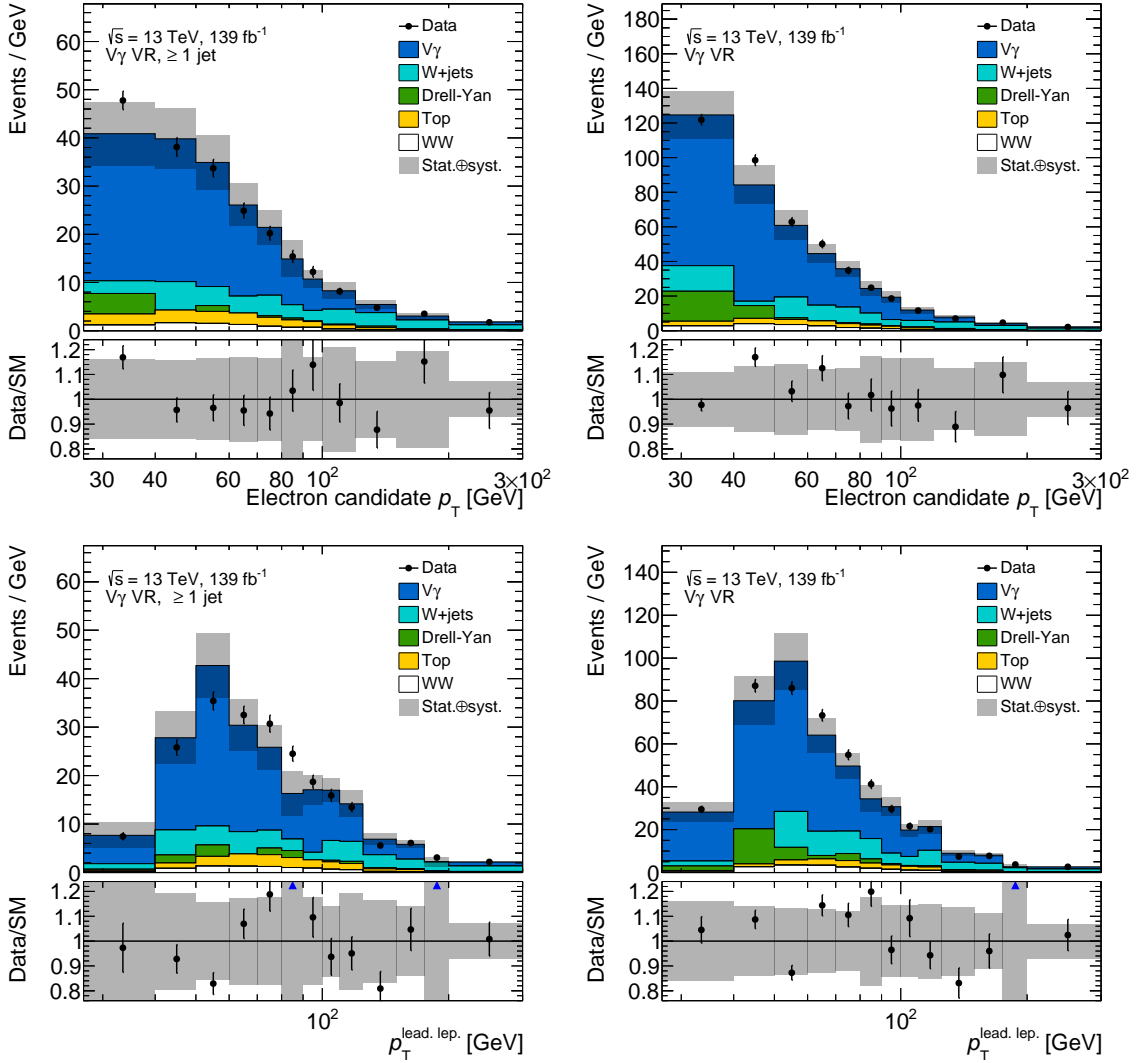
Figure 6.9: Distributions for the electron candidate p_T (top) and the leading lepton p_T (bottom) in the opposite-sign $V\gamma$ VR defined in the text for the one jet inclusive (left) and fully jet inclusive (right) selections. The grey band includes statistical and systematic uncertainties on the prediction. The final bin includes overflow events.

the gluon fraction in data in the SR, as well as an MC-based jet flavour response uncertainty to account for modelling uncertainties in the calorimeter response for gluon-initiated jets. Uncertainties specific to the b-jet energy scale are also included. PU corrections to the JES are associated with MC uncertainties. Modelling uncertainties from the η-intercalibration method used to equalise the detector response in all η regions influence the JES as well as the JER. An uncertainty arising from the absolute resolution difference between data and MC is additionally applied to the JER. A reduced set of effective NPs which combine various uncertainties affect both the JES and the JER [186].

Lepton reconstruction: There are systematic uncertainties related to the calibration of reconstruction, identification and isolation efficiencies for electrons and muons. Additional uncertainties account for the energy scale and resolution of electrons and the momentum scale and resolution of muon tracks. The calibration of electron and muon energies and momenta was discussed in

Sections 4.2.1 and 4.3.1.

Flavour tagging: Flavour tagging in the context of the measurements presented here corresponds to the tagging of b-jets. There are experimental uncertainties on the scale factors associated to the calibration of the efficiency [231] and mis-tag rates [232].

Missing transverse momentum: The p_T^{miss} response was discussed in Section 4.6.2. Systematic uncertainties on the response arising from the soft term are obtained using differences between data and MC simulations [189]. Systematic uncertainties from hard objects are excluded to avoid double-counting.

6.5.2 Signal systematic uncertainties

Systematic uncertainties related to the signal modelling enter during the unfolding process. In addition to uncertainties on the nominal PDF, there are uncertainties from the choice generator, and scale uncertainties.

Generator: The uncertainty from the choice of generator for the signal is estimated using an alternative sample for $q\bar{q} \rightarrow W^+W^-$ generated using Powheg-Box v2 [94, 95, 206, 233], which provides MEs at NLO QCD. The PS, hadronisation and UE are modelled using Pythia 8.186 [89], with the AZNLO set of tuned parameters [234]. For the fixed order prediction, the CT10nlo PDF set [235] is used, whereas the CTEQ6L1 PDF set [236] is used in the PS simulation. The events are normalised to the NNLO QCD prediction [68]. No alternative sample is used for the gluon-induced channel, since it is expected to contribute only about 5% to the signal prediction.

Scale variations: As mentioned in Section 1.2.3, missing higher order terms in theoretical predictions introduce an uncertainty that can be estimated using the residual dependence of such predictions on the renormalisation and factorisation scales. The usual prescription is to generate seven-point scale variations, where the nominal scale values are multiplied by factors of two or one half, either keeping one scale fixed or varying both scales simultaneously. Each MC event then has a nominal event weight, along with an additional six weights corresponding to variations about the nominal. For each scale variation and variable, the differential distribution is plotted on truth-level and the difference from the nominal found. For each bin in the distribution, the weights corresponding to the pair of scale variations that lead to the largest positive and negative deviations from the nominal are used to determine the uncertainty in that bin. In this way the scale uncertainty envelopes are formed, as shown in Figure 6.10. The selected event weights are then applied to events in the corresponding bins and propagated through all the signal unfolding inputs, with the final deviations from the nominal unfolded result taken as the *up* and *down* uncertainties. Unfolding of the detector-level distributions will be discussed in detail in Section 6.7. Currently the scale uncertainties are calculated at NLO, although NNLO accurate variations are becoming available [102, 237].
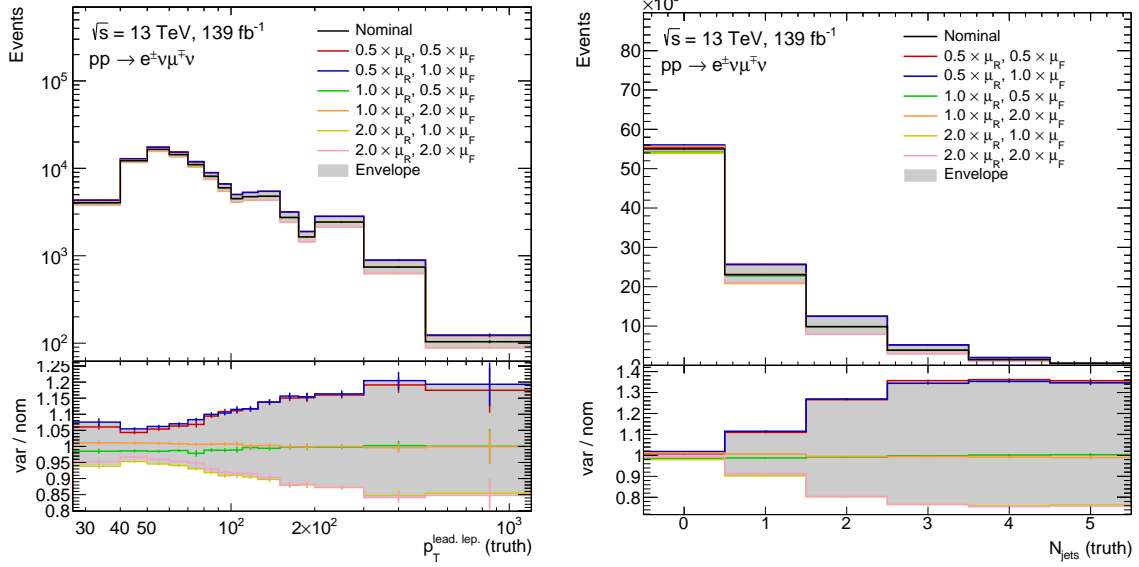
Figure 6.10: Signal truth-level distributions for the leading lepton p_T (left) and the jet multiplicity (right) for the fully jet inclusive selection. Shown in each bin is the nominal value, as well as six values corresponding to scale variations. μ_R is the renormalisation scale and μ_F is the factorisation scale. The numbers correspond to multiplicative factors with respect to the nominal scale. The grey region shows the uncertainty envelope formed by taking the largest positive and negative deviations from the nominal in each bin as the uncertainty. The scale variations shown are calculated at NLO accuracy.

6.5.3 Background systematic uncertainties

In this section the systematic uncertainties related to the various background estimates, including modelling and theoretical uncertainties, as well as some experimental uncertainties for data-driven methods, will be summarised.

Top background: Systematic uncertainties related to the ME and PS are estimated with alternative generators. The uncertainty related to the matching of the NLO MEs to the PS is estimated by comparing to an alternative sample generated using MADGRAPH5_aMC@NLO 2.6.2 [238] with the NNPDF2.3NLO PDF set [209] interfaced to PYTHIA 8.230 [90]. The normalisation is the same as for the nominal samples. The uncertainty related to the PS and hadronisation model is estimated by comparing to a sample generated with the nominal POWHEG-BOX v2 [94, 95, 206–208] generator interfaced to HERWIG 7.04 [91, 92], using the H7UE tuned parameters [92] and the MMHT2014LO PDF set [239]. Uncertainties due to ISR and missing higher order QCD contributions in $t\bar{t}$ events are estimated using the nominal sample with simultaneous variations of the ISR modelling parameters and the factorisation and renormalisation scales. Uncertainties on the FSR are accounted for with additional event weights that vary the renormalisation scale for final-state parton emissions. Replacement of the diagram-removal scheme with a diagram-subtraction scheme [211] is used to assess the uncertainty coming from $t\bar{t}$ and Wt overlap. An uncertainty of about 5% is associated with the Wt cross section. The presence of additional b-jets in $t\bar{t}$ events can influence the b-tag counting estimate. To account for potential mismodelling of these additional heavy-flavour jets, events with more than two truth-level b-jets are reweighted to increase their relative contribution

following the procedure of recent $t\bar{t}$ cross section measurements [240, 241]. The dominant top uncertainties on the integrated cross section come from those related to the PS modelling, in particular from Wt, as well as uncertainties on the matching of the ME to the PS, the resolution of the overlap between $t\bar{t}$ and Wt, and flavour tagging.

Drell-Yan background: Uncertainties on the Z+jets prediction arise from PDF uncertainties, missing higher-order QCD corrections, and the PS. For the one jet inclusive measurement, these are encapsulated by an alternative simulation. MADGRAPH5_aMC@NLO 2.2.2 [238] and the NNPDF2.3LO PDF set [209] are used, which include MEs at LO in QCD for up to four final-state partons, and are interfaced to PYTHIA 8.186 [89] with the A14 tunes [210]. The CKKW-L merging procedure [97, 98] is used. The normalisation is the same as for the nominal sample. For the fully jet inclusive measurements, scale variations are used instead of an alternative simulation as the uncertainties are expected to be much smaller. Variations of the renormalisation and factorisation scales, as well as scales related to ME and PS matching and the resummation of soft gluons, are used to quantify the modelling uncertainties [242]. An additional uncertainty is associated with the Z+jets cross section.

Fake background: The largest uncertainty in the fake estimate comes from the subtraction of prompt lepton backgrounds in the fake CR. The modelling of the efficiency for prompt leptons to fail the SR identification requirements but to pass a looser set of requirements is checked in a CR requiring two b-tagged jets, which is dominated by prompt leptons from the decay of top quark pairs. The efficiency is found to be poorly modelled, and so a flat 25% uncertainty is applied to the fake estimate to cover the differences between simulation and data. A 20% relative uncertainty is applied on the signal simulation used to estimate the signal contamination in the fake CR. The size of this uncertainty is taken as the typical size of the largest deviations between the measured and predicted differential cross sections. Uncertainties are also applied on the normalisation of the prompt background subtracted in the region used to derive the extrapolation factors, and variations are made on the selection in this region in order to estimate uncertainties related to differences in the composition of fake sources compared to the fake CR. Uncertainties on the prompt background subtraction in the fake CR are correlated with those in the SR.

Other backgrounds: Similarly to the Z+jets background, uncertainties from PDF uncertainties, missing higher-order QCD corrections, and the PS are estimated using alternative simulations. For WZ and ZZ production the alternative simulation uses the same setup as for the alternative signal simulation. The events are normalised to the NNLO QCD predictions [243–246]. The scale uncertainty in the NNLO diboson cross section of about 10% is also included [247, 248]. No alternative simulation is used for the $W\gamma$ or $Z\gamma$ contributions, which are subdominant to the WZ and ZZ contributions.

6.6 Detector-level distributions

The yields for data and the background estimates, as well as the expected signal yield, in the various SRs are shown in Table 6.7. Figures 6.11 and 6.12 show the detector-level distributions including

the data and background estimates for the one jet inclusive selection. The nominal signal prediction is also shown to allow comparison to data. Distributions for the fully jet inclusive selection are shown in Figures 6.13 and 6.14, and for the dynamic jet veto selection in Figures 6.15 and 6.16. The following variables are considered:

- the leading lepton transverse momentum, $p_{\mathrm{T}}^{\mathrm{lead.\,lep.}}$

- the subleading lepton transverse momentum, $p_{\mathrm{T}}^{\mathrm{sublead.\,lep.}}$

- the leading jet transverse momentum, $p_{\mathrm{T}}^{\mathrm{lead.\,jet}}$

- the jet multiplicity

- the invariant mass of the dilepton system, $m_{e\mu}$

- the transverse momentum of the dilepton system, $p_{\mathrm{T},e\mu}$

- the scalar sum of the jet transverse momenta, $H_{\mathrm{T}}^{\mathrm{jet}}$

- the scalar sum of the jet, electron and muon transverse momenta, S_{T}

- the transverse mass of the dilepton system and missing transverse momentum[5], $m_{\mathrm{T},e\mu}$

- the rapidity of the dilepton system, $y_{e\mu}$

- the azimuthal separation between the electron and muon, $\Delta\phi(e,\mu)$

- $\cos\theta^* = |\tanh(\Delta\eta(e,\mu)/2)|$, which is sensitive to the spin structure of the W boson pair [249]

Overall there is good agreement between the data and the expected background and signal yields and shapes of the distributions. For the one jet inclusive selection, small excesses are observed at low values of the leading lepton p_{T}, which are expected to be covered by theory uncertainties on the signal, not shown in the figures. The distributions for the dynamic jet veto are very similar to those for the fully jet inclusive selection, as expected. There is a disagreement between the data and prediction at low values of $\Delta\phi(e,\mu)$ for the dynamic jet veto selection, which was also observed in the previous ATLAS measurement in a jet veto phase space [8].

6.7 Unfolding detector-level distributions

Unfolding was discussed in a general context in Section 5.4. The main purpose of unfolding is to obtain particle-level results for integrated and differential cross sections that can be compared more easily to results from other experiments and to theoretical predictions.

---

[5]The transverse mass is defined as $m_{\mathrm{T},e\mu} = \sqrt{(E_{\mathrm{T},e\mu} + p_{\mathrm{T}}^{\mathrm{miss}})^2 - (\boldsymbol{p}_{\mathrm{T},e\mu} + \boldsymbol{p}_{\mathrm{T}}^{\mathrm{miss}})^2}$, where $E_{\mathrm{T},e\mu} = \sqrt{|\boldsymbol{p}_{\mathrm{T},e\mu}|^2 + m_{e\mu}^2}$ and $\boldsymbol{p}_{\mathrm{T},e\mu}$ and $m_{e\mu}$ are the transverse momentum and invariant mass of the dilepton system respectively.
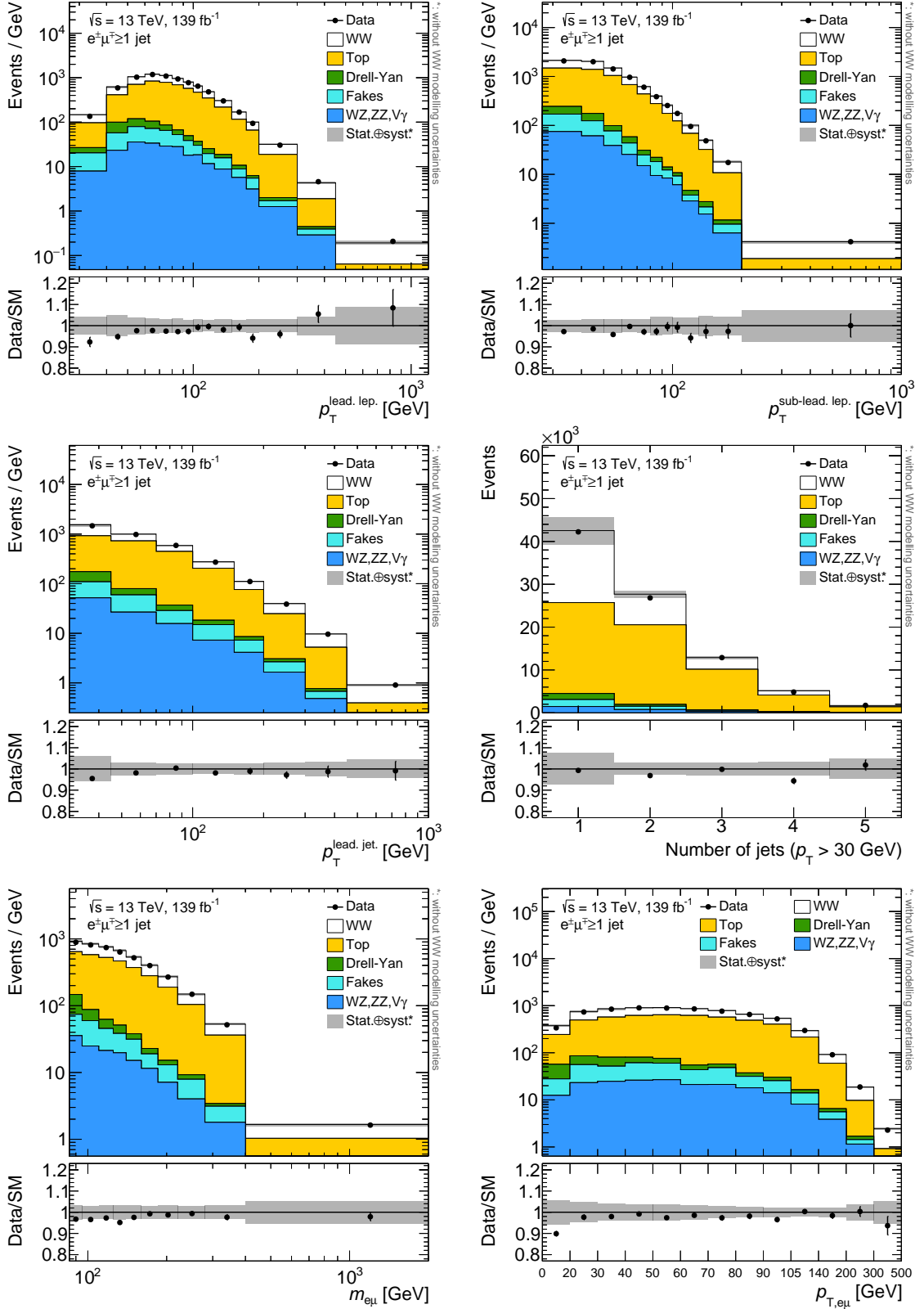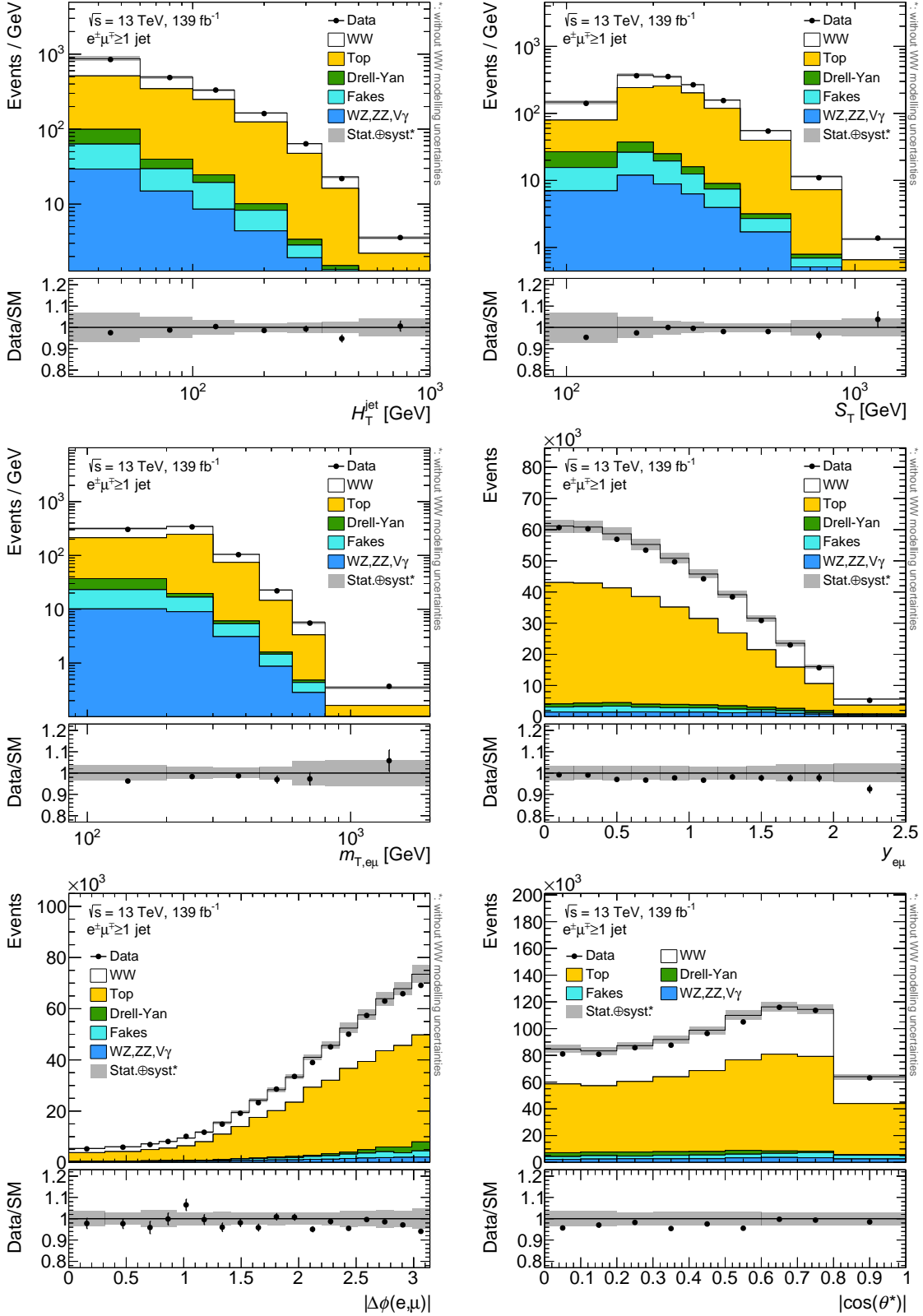
Figure 6.11: Detector-level distributions for the one jet inclusive selection showing data alongside the background estimates and nominal signal prediction. Shown are the leading lepton p_T (top left), the subleading lepton p_T (top right), the leading jet p_T (middle left), the jet multiplicity (middle right), the invariant mass of the dilepton system (bottom left), and the transverse momentum of the dilepton system (bottom right). The grey band includes both statistical and systematic uncertainties, but signal theory uncertainties are not included. Overflow events are not included.
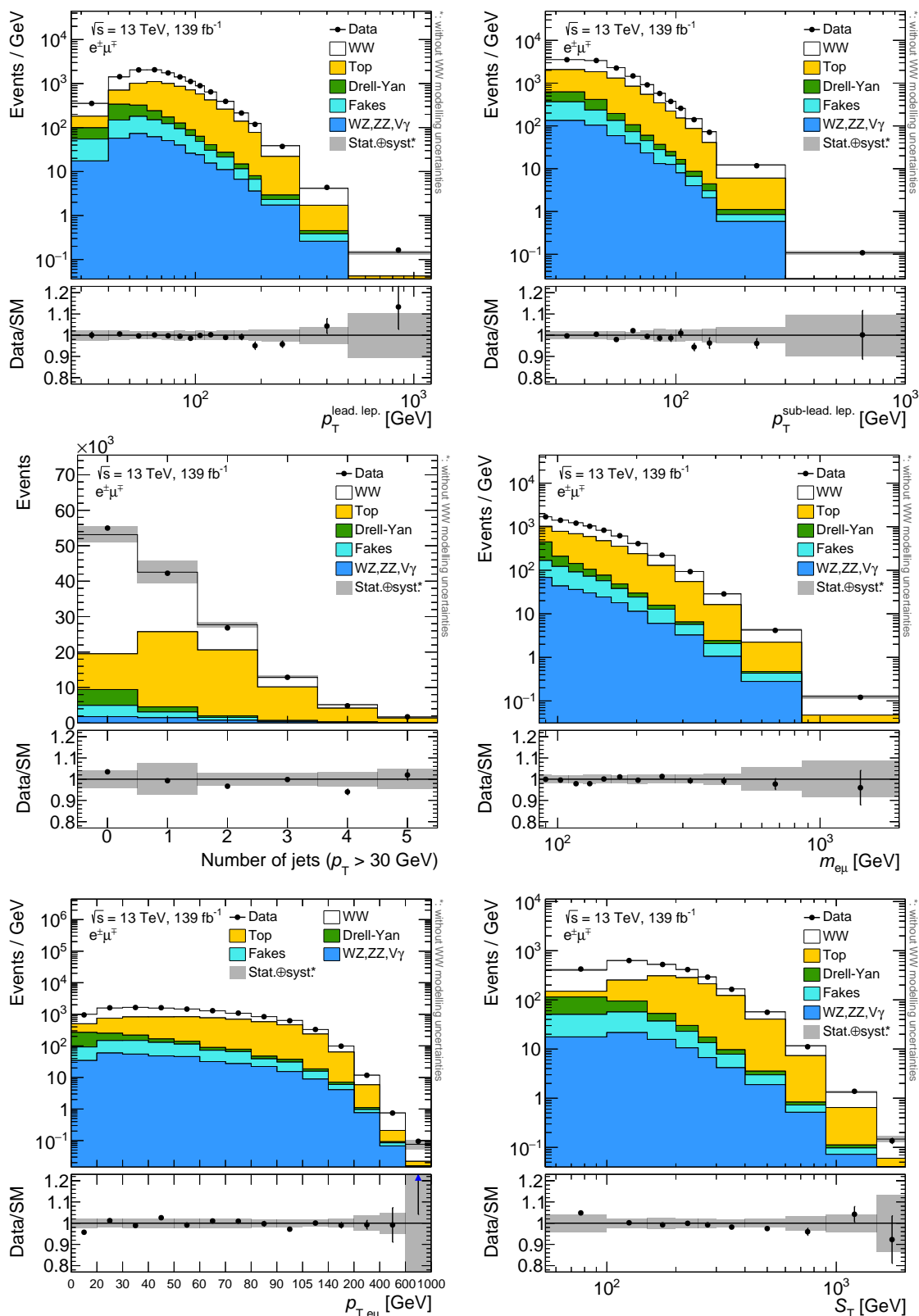
Figure 6.12: Detector-level distributions for the one jet inclusive selection showing data alongside the background estimates and nominal signal prediction. Shown are H_T^{jet} (top left), S_T (top right), the transverse mass (middle left), the rapidity of the dilepton system (middle right), the azimuthal separation of the two leptons (bottom left), and $\cos\theta^*$ (bottom right). The grey band includes both statistical and systematic uncertainties, but signal theory uncertainties are not included. Overflow events are not included.

Figure 6.13: Detector-level distributions for the fully jet inclusive selection showing data alongside the background estimates and nominal signal prediction. Shown are the leading lepton p_T (top left), the subleading lepton p_T (top right), the jet multiplicity (middle left), the invariant mass of the dilepton system (middle right), the transverse momentum of the dilepton system (bottom left), and S_T (bottom right). The grey band includes both statistical and systematic uncertainties, but signal theory uncertainties are not included. Overflow events are not included.
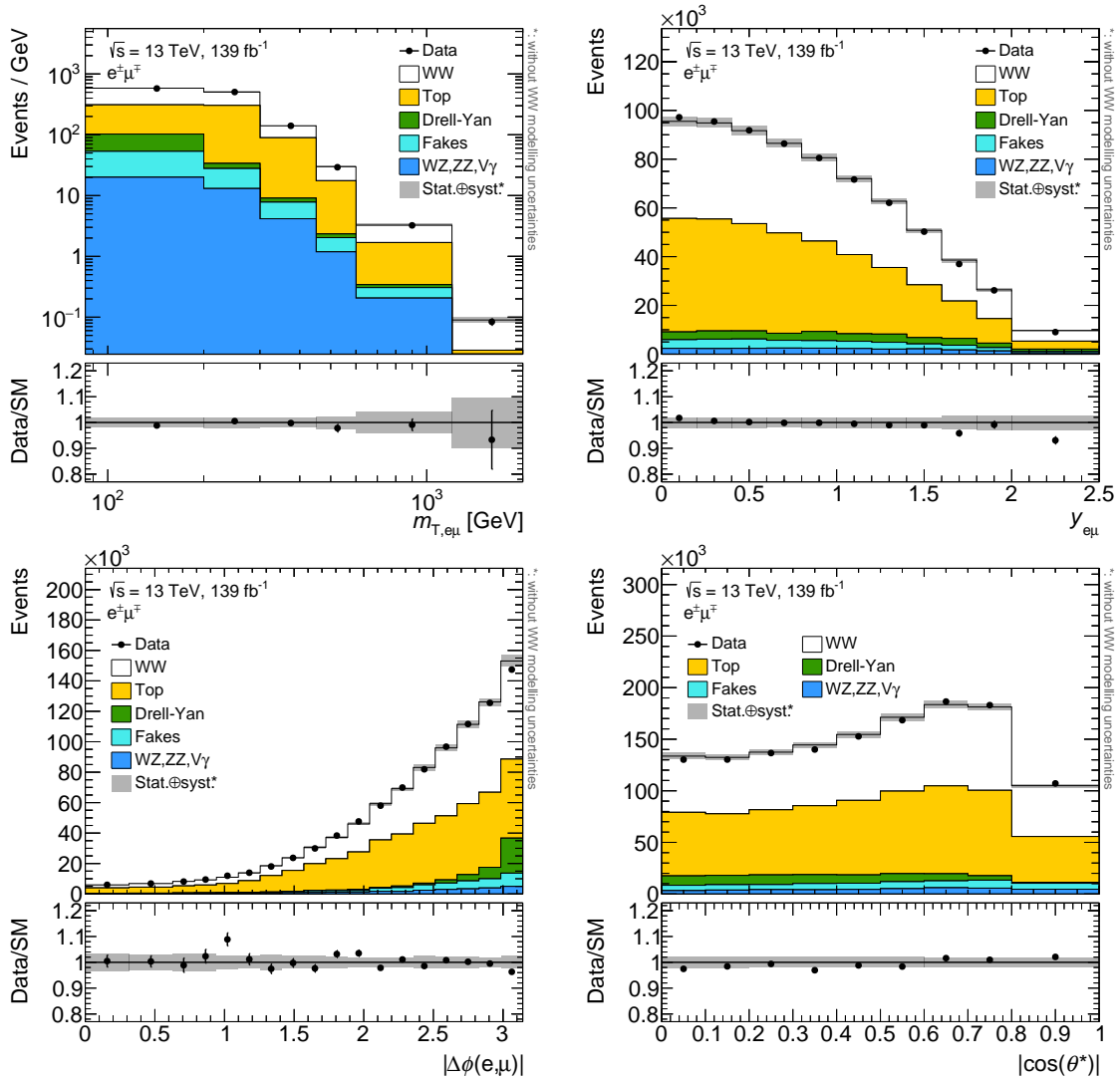
Figure 6.14: Detector-level distributions for the fully jet inclusive selection showing data alongside the background estimates and nominal signal prediction. Shown are the transverse mass (top left), the rapidity of the dilepton system (top right), the azimuthal separation of the two leptons (bottom left), $\cos\theta^*$ (bottom right). The grey band includes both statistical and systematic uncertainties, but signal theory uncertainties are not included. Overflow events are not included.
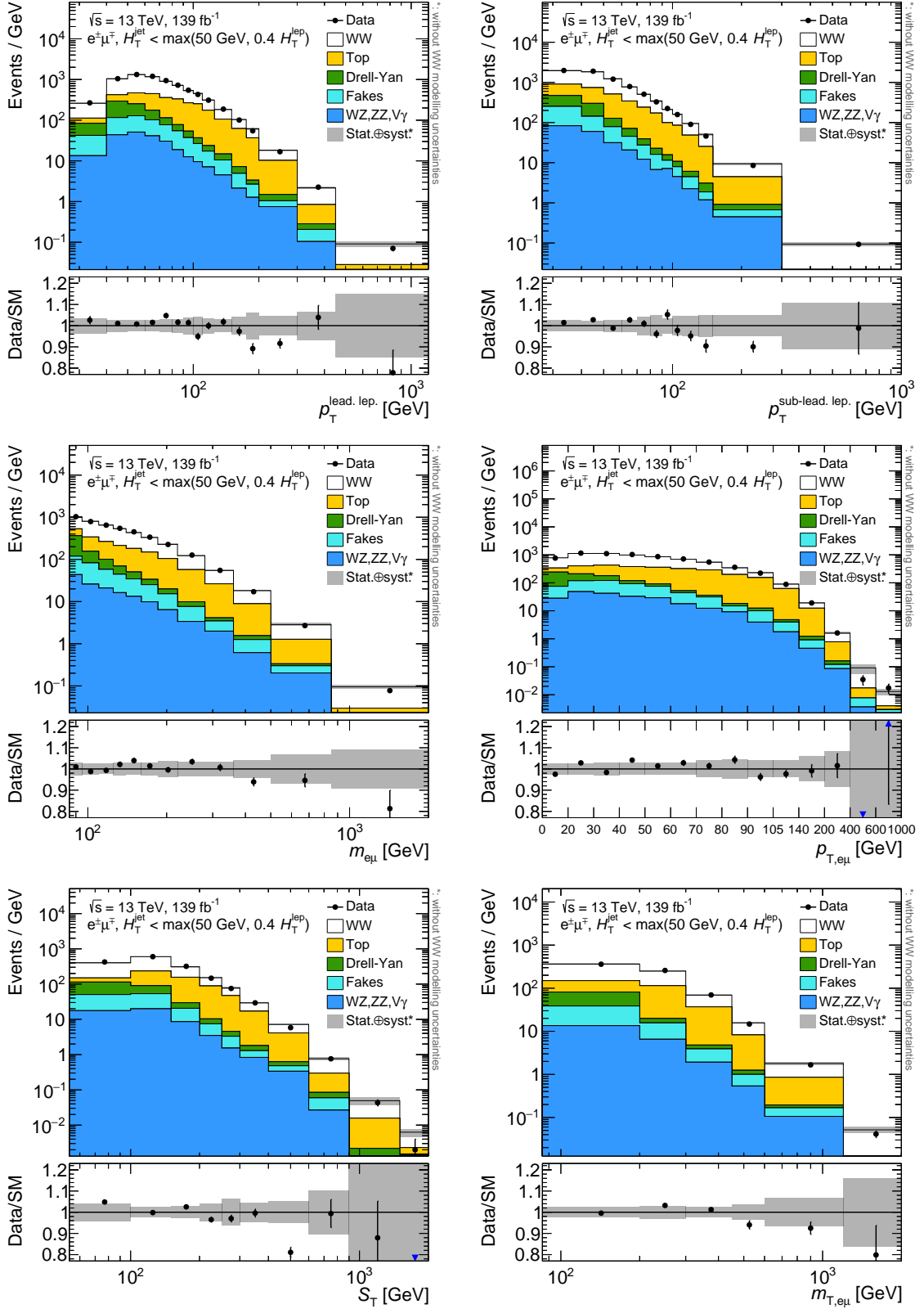
Figure 6.15: Detector-level distributions for the dynamic jet veto selection showing data alongside the background estimates and nominal signal prediction. Shown are the leading lepton p_T (top left), the subleading lepton p_T (top right), the invariant mass of the dilepton system (middle left), the transverse momentum of the dilepton system (middle right), S_T (bottom left), and the transverse mass (bottom right). The grey band includes both statistical and systematic uncertainties, but signal theory uncertainties are not included. Overflow events are not included.
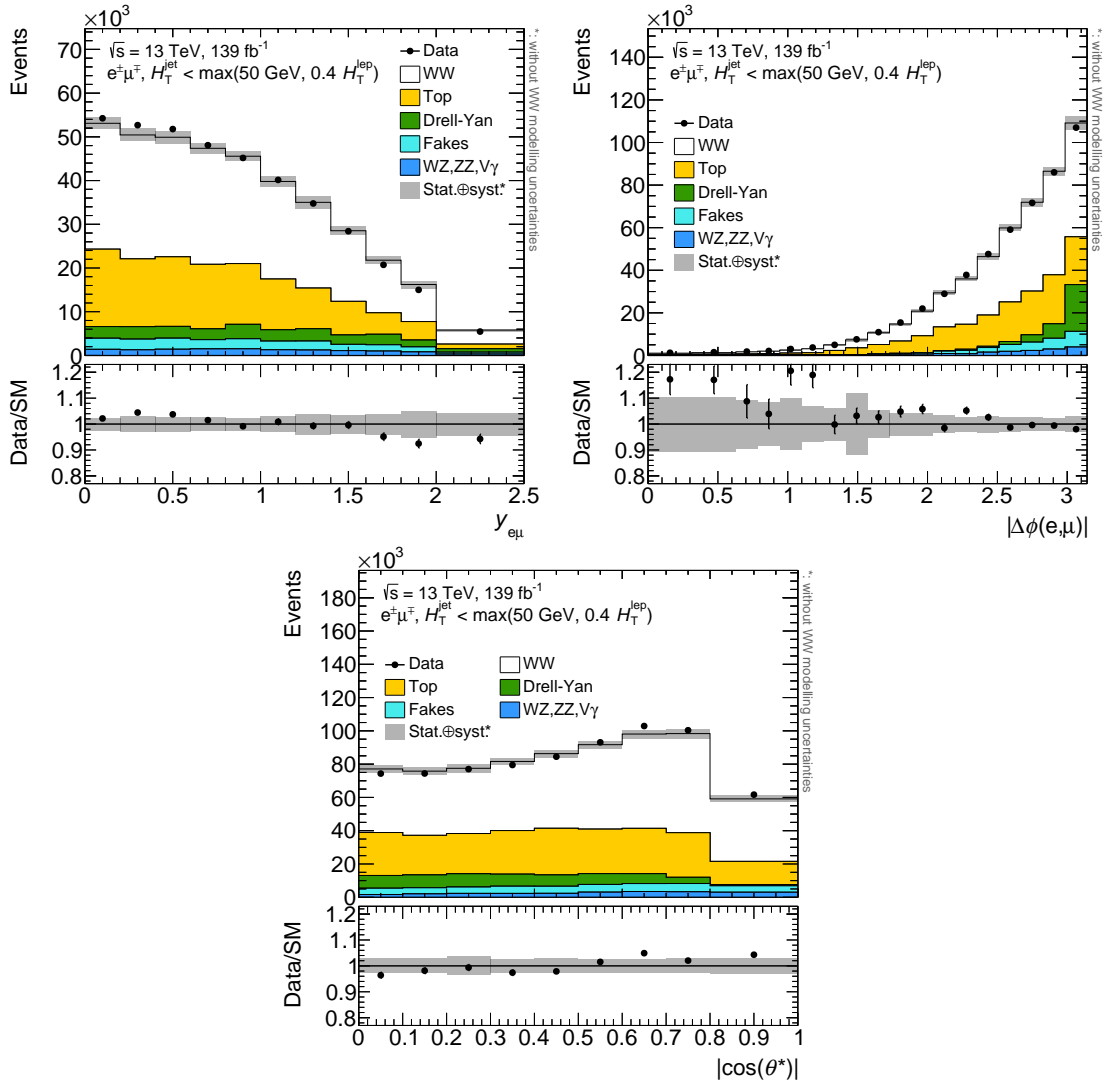
Figure 6.16: Detector-level distributions for the dynamic jet veto selection showing data alongside the background estimates and nominal signal prediction. Shown are the rapidity of the dilepton system (top left), the azimuthal separation of the two leptons (top right), and cos θ^* (bottom). The grey band includes both statistical and systematic uncertainties, but signal theory uncertainties are not included. Overflow events are not included.

	Fully jet inclusive	One jet inclusive	Jet veto	Dynamic jet veto
Data	144,221	89,239	54,982	80,940
Total SM	$144{,}900 \pm 3{,}100$	$91{,}500 \pm 2{,}800$	$53{,}300 \pm 2{,}400$	$80{,}500 \pm 2{,}200$
WW	$61{,}800 \pm 1{,}100$	$28{,}100 \pm 1{,}500$	$33{,}600 \pm 1{,}700$	$44{,}500 \pm 1{,}300$
	43%	31%	63%	55%
Total bkg.	$83{,}200 \pm 2{,}900$	$63{,}300 \pm 1{,}800$	$19{,}700 \pm 1{,}400$	$36{,}100 \pm 2{,}000$
	57%	69%	37%	45%
Top	$66{,}000 \pm 1{,}900$	$55{,}800 \pm 1{,}600$	$10{,}100 \pm 600$	$23{,}600 \pm 1{,}200$
	46%	61%	19%	29%
Drell-Yan	$6{,}500 \pm 400$	$2{,}030 \pm 240$	$4{,}500 \pm 400$	$5{,}500 \pm 400$
	4%	2%	8%	7%
Fakes	$6{,}100 \pm 2{,}300$	$2{,}700 \pm 1{,}100$	$3{,}300 \pm 1{,}300$	$4{,}300 \pm 1{,}600$
	4%	3%	6%	5%
$VZ, V\gamma$	$4{,}500 \pm 700$	$2{,}800 \pm 500$	$1{,}780 \pm 270$	$2{,}600 \pm 400$
	3%	3%	3%	3%

Table 6.7: The final yields for the background estimates and simulated signal contributions in each of the SRs. The uncertainties include both statistical and systematic effects, but signal modelling uncertainties are not included. The percentages show the expected relative contribution of each process to the total number of events in each region. Here $V = W/Z$.

6.7.1 Fiducial phase space definition

Usually the unfolding is performed with respect to a fiducial phase space. This is defined on particle-level, and is chosen to match as closely as possible the detector-level SR in order to re-duce extrapolation and signal modelling biases. The fiducial phase space is thus different to a completely inclusive phase space in which a relatively large extrapolation is made to regions in-accessible to the detector, or to decay topologies not directly measured. The fiducial phase space of the $WW \to e^{\pm}\nu\mu^{\mp}\nu$ decay channel used for the unfolding and the final cross section mea-surements is summarised in Table 6.8. Simulated signal events are required to contain one prompt electron and one prompt muon. Events involving decays of τ leptons are not included to simplify comparisons with theoretical predictions, although in principle such events are present in the data, and in fact account for about 9% of the expected signal events in the one jet inclusive case. The fiducial correction used in the unfolding procedure therefore mostly corrects for events in data that involve τ lepton decays, and so must originate from outside the particle-level fiducial phase space. Simulated photons emitted in a cone of radius $\Delta R = 0.1$ around the leptons are added to the lepton momentum, effectively accounting for photon FSR that would not be distinguished in the detector. The truth-level $p_{\mathrm{T}}^{\mathrm{miss}}$ value is calculated by summing the transverse momenta of neutrinos. The recoil is not used since the main quantity of interest in this analysis is the transverse vector sum of invisible particles, for which the reconstructed detector-level $p_{\mathrm{T}}^{\mathrm{miss}}$ is an experimental proxy. Jets are formed by clustering remaining stable final-state particles according to the anti-k_{T} algorithm with radius parameter $R_0 = 0.4$, as for particle flow jets on detector-level. No b-jet veto is applied on signal events at particle-level in the nominal fiducial phase space definition, although a set of results additionally including a veto on b-jets with $p_{\mathrm{T}} > 20\,\mathrm{GeV}$ have been made available for the

leptons	$p_T > 27\,\text{GeV}$
	$|\eta| < 2.5$
	$m_{e\mu} > 85\,\text{GeV}$
jets	$p_T > 30\,\text{GeV}$
	$|y| < 4.5$

Table 6.8: $WW \to e^{\pm}\nu\mu^{\mp}\nu$ fiducial phase space definition for the properties of leptons and jets. Events are required to have one prompt electron and one prompt muon, and requirements on the number of particle-level jets coincide with those of the given detector-level phase space. Adapted from [12].

Selection	$C \pm \Delta C$
Fully jet inclusive	0.657 ± 0.019
One jet inclusive	0.747 ± 0.061
Jet veto	0.611 ± 0.028
Dynamic jet veto	0.651 ± 0.024

Table 6.9: Correction factors for the extrapolation from the reco-level event selection to the fiducial phase space. Uncertainties include systematic and statistical sources. Values for the one jet inclusive selection taken from [12].

one jet inclusive selection[6]. The requirement on the number of regular jets matches that of the detector-level selection.

The integrated fiducial cross section is obtained using an extrapolation factor derived from MC simulations, and is given as

$$\sigma^{\text{fid}} = \frac{N_{\text{data}} - N_{\text{bkg}}}{C \times \mathcal{L}}, \tag{6.8}$$

where N_{data} is the number of observed events, N_{bkg} is the number of estimated background events in the detector-level phase space, and C is the MC extrapolation factor between the detector-level phase space and the fiducial phase space. The numerical values for the different regions are summarised in Table 6.9. The uncertainties in each case are dominated by the generator choice, luminosity, scale variations, jet calibration and PU modelling.

6.7.2   Iterative unfolding inputs

For differential distributions, with more than one bin, the iterative unfolding method discussed in Section 5.4.3 is used in order to account for migrations of events between bins. Eqs. (5.12) and (5.13) indicate that in addition to the data and background estimates, four inputs are needed, namely the efficiency corrections, fiducial corrections, migration matrices, and prior. These are all obtained from MC simulations. The prior is taken as the nominal SHERPA simulation, with the alternative POWHEG simulation used to assess generator uncertainties and signal model bias. The efficiency and fiducial corrections are calculated for each bin of every distribution, with some examples shown in Figure 6.17. The migration matrix encodes the probability for an event to be reconstructed in a detector-level bin, given it was generated in a truth-level bin, and is usually displayed with
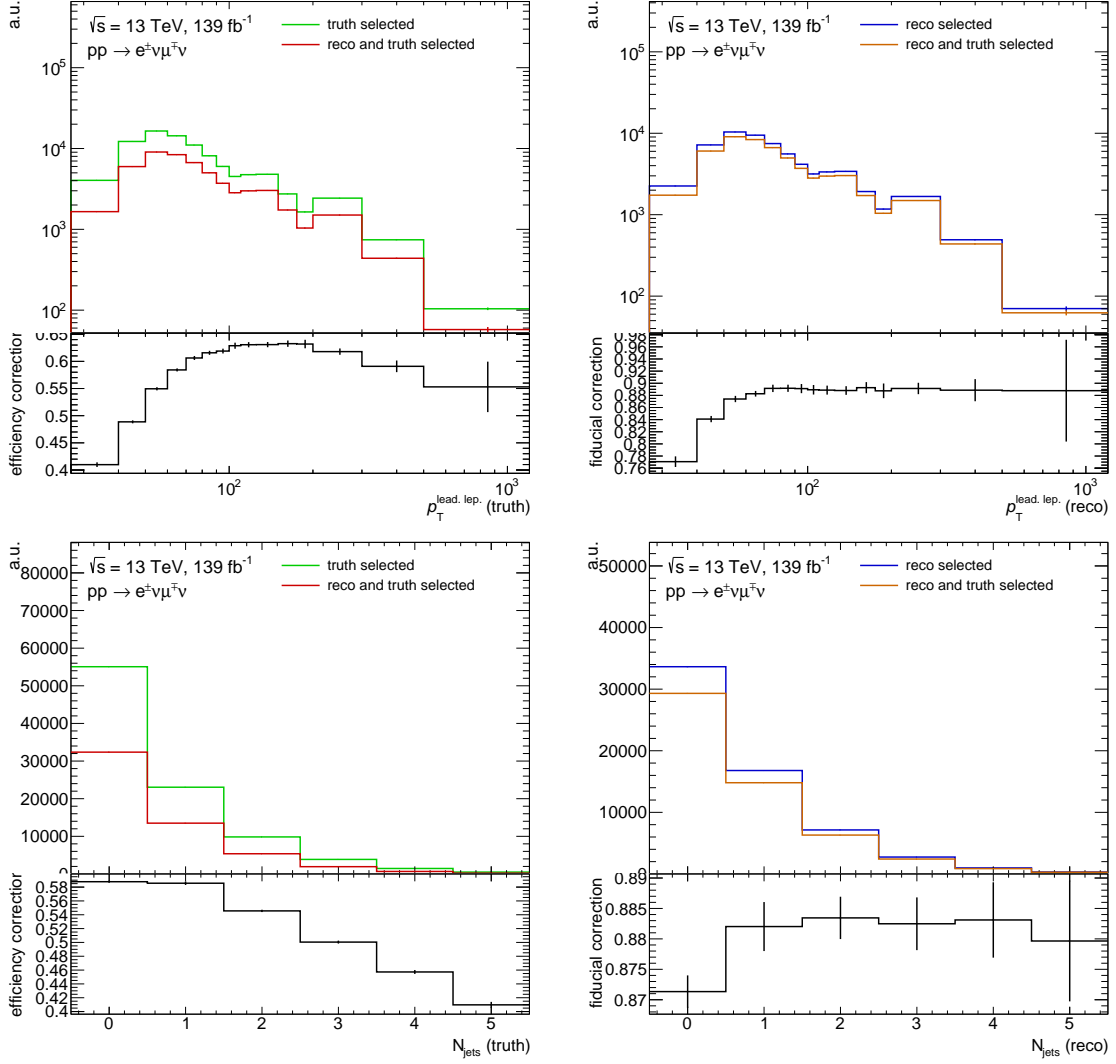
---

[6]https://www.hepdata.net/record/100511

Figure 6.17: Efficiency (left) and fiducial (right) corrections for the leading lepton p_T (top) and jet multiplicity (bottom) for the fully jet inclusive selection. The lower panel shows the correction as the ratio of either the truth (left) or reco (right) selected events to those events passing both the reco and truth selection. Vertical error bars correspond to MC statistical uncertainties.

the reco-level bins as columns and the truth-level bins as rows. Therefore, events in a given cell of the migration matrix are normalised to the total number of events in the corresponding row. Example migration matrices are shown in Figure 6.18. The stability, also known as the migration efficiency, is defined as the percentage of events in a given truth-level bin that are reconstructed in the same reco-level bin, and can be obtained from the diagonal of the migration matrix. The binning for each variable listed in Section 6.6 is chosen where possible such that the migration matrices have a minimum stability across all bins of around 50-60% to limit migrations. In addition, the expected number of reco-level events in each bin is required to be at least about 20 to limit statistical uncertainties, with a maximum of around 100 events in the highest bins of the energy-based variables.
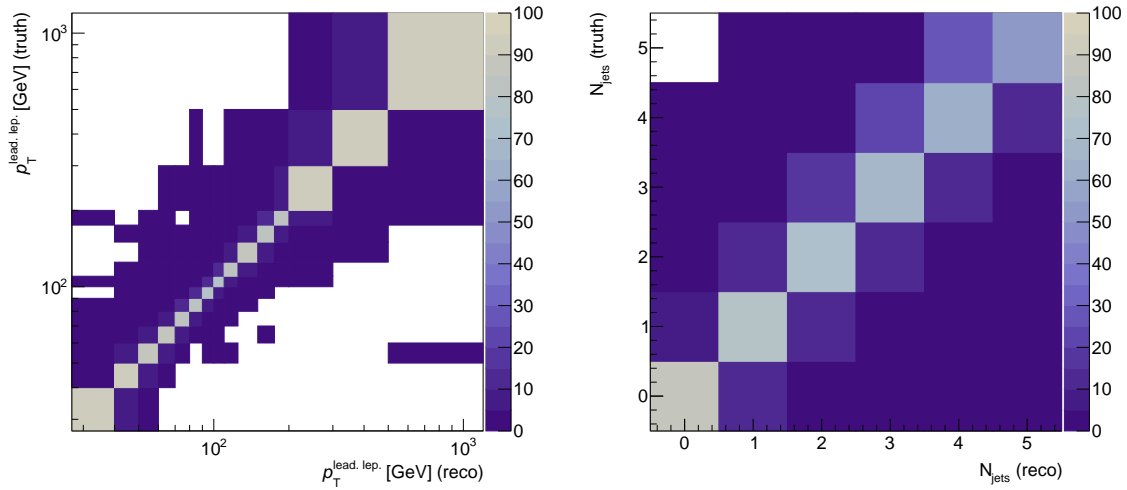
Figure 6.18: Migration matrices for the leading lepton p_T (left) and jet multiplicity (right) for the fully jet inclusive selection. The colours indicate the migration as a percentage, with zero values shown as white cells. Overflow bins are not shown.

6.7.3 Iterative unfolding closure and bias tests

In order to validate the unfolding method, tests are performed using MC and data-driven methods. Firstly, the convergence of the method is confirmed by unfolding each distribution with increasingly many iterations and demonstrating that successive iterations provide smaller relative corrections. Another test involves folding the nominal signal model on particle-level to produce a reco-level distribution that is then unfolded with the nominal unfolding setup, with the result agreeing exactly with the original particle-level prediction. The data-driven closure test involves reweighting the nominal signal prediction on particle-level with a smooth function, such that it closely matches data on reco-level. This reweighted reco-level distribution is then unfolded using the nominal unfolding setup, with the result compared to the reweighted particle-level distribution. The resulting non-closure as a result of the bias introduced by the unfolding is found to be negligible.

6.7.4 Iterative unfolding optimisation

It was mentioned that the number of iterations in the unfolding procedure acts as a regularisation parameter, where more iterations reduce the ability to regularise large statistical uncertainties but reduce the prior bias. It is therefore necessary to optimise the number of iterations to balance these two effects. The uncertainty arising from the difference in signal model is used for assessing the prior bias. All sources of statistical uncertainty are considered together. An example optimisation is given for the jet multiplicity, where the difference between the nominal SHERPA signal model and the alternative POWHEG model is relatively large, with the latter modelling the high jet multiplicity region poorly. In Figure 6.19, the effect of the number of unfolding iterations on the final uncertainties is shown. It is evident for this variable that two iterations is the optimum in terms of reducing the final uncertainty overall, with the signal modelling uncertainty significantly reduced in high jet multiplicity bins whilst keeping statistical uncertainties relatively low. A similar opti-
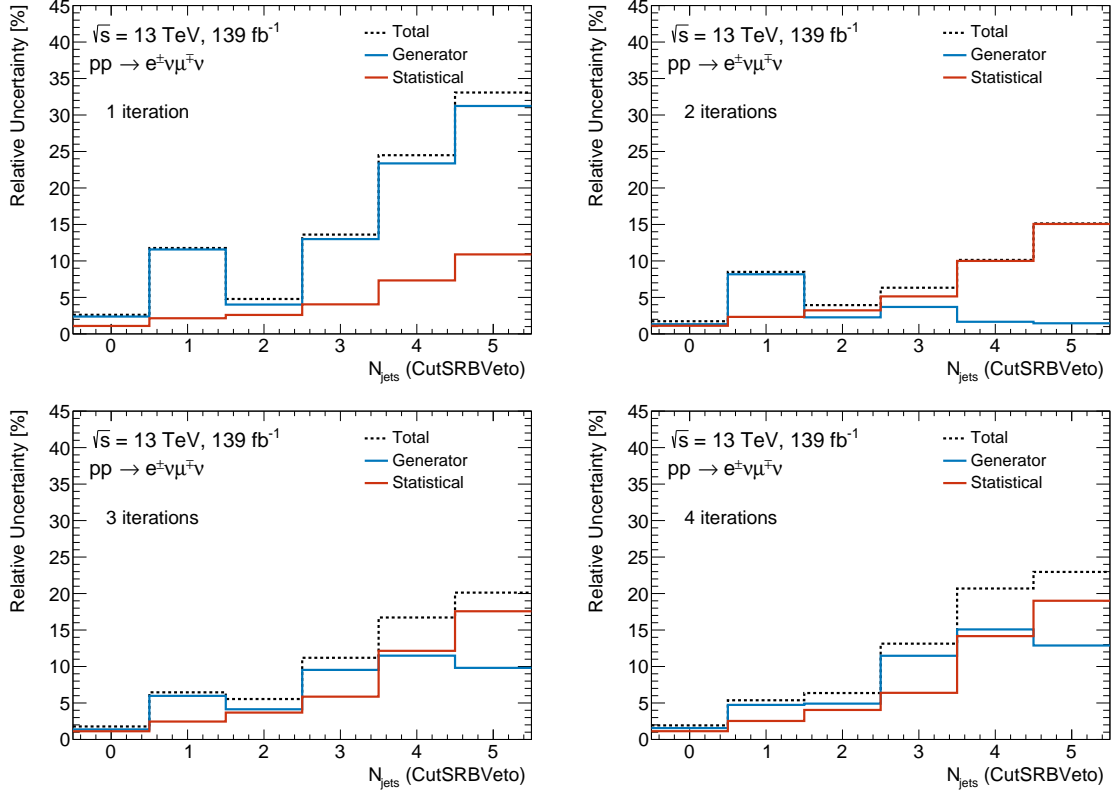
Figure 6.19: Relative uncertainty on the unfolded jet multiplicity. The generator uncertainty and statistical uncertainty, which includes both MC and data components, are shown in blue and red respectively, with the combined uncertainty shown as a black dashed line. The number of iterations used for the unfolding increases from one in the top left to four in the bottom right.

misation is performed for the other variables. In the case of the one jet inclusive selection, two iterations are used for the jet multiplicity, H_T^{jet}, S_T and the leading jet p_T due to the associated large modelling uncertainties, whilst only one iteration is used for the other variables, where large statistical uncertainties are found to dominate any reduction in modelling uncertainties. This can be understood due to the more consistent modelling of these observables, which also closely matches the data, such that subsequent iterations do not update the prior significantly.

6.7.5 Unfolding error propagation

Uncertainty propagation through the unfolding framework was discussed in Section 5.4.4. Systematic uncertainties are propagated by varying both signal and background inputs according to the *up* and *down* variations, or alternative variation for two-point systematic uncertainties, and repeating the unfolding. In the case where either the signal or background input is not affected by the systematic, the nominal for that input is used. For systematic uncertainties with *up* and *down* variations, the signed error on the nominal from that systematic is taken as half the difference between the results obtained with *up* and *down* variations separately, assuming the variations straddle the nominal[7]. In the case where both the *up* and *down* variations are on the same side of the nomi-

---

[7]It is possible for the *up* variation to be smaller than the *down* variation, in which case the error is negative. It is essential to keep track of the signs to calculate correctly the covariance matrix.

nal, the error associated with the variation with the largest absolute deviation from the nominal is used. For two-point systematic uncertainties, the error is simply taken as the difference between the result from the variation and the nominal result. All systematic uncertainties are treated as fully correlated across bins, with a correlation coefficient of $+1$ or -1 in each bin depending on whether the error is positive or negative, in accord with Eq. (5.3). There are assumed to be no correlations between different systematic uncertainties, so the combined covariance matrix is found by simply adding the covariances of the separate systematic uncertainties. The total systematic uncertainty in a given bin is then then simply the sum in quadrature of the uncertainties coming from each individual systematic uncertainty in that bin.

Data statistical uncertainties are propagated using 2000 simulated data samples where the number of events in each bin is drawn from a Poisson distribution with an expectation value equal to the observed number of events in that bin. This procedure allows for the accounting of correlations introduced by the iterative unfolding procedure. Each simulated data sample is effectively treated as a systematic uncertainty, fully correlated across all bins and with no correlations amongst samples. A separate covariance matrix is formed in the same way to the systematic uncertainties described above, and all 2000 covariance matrices are added to produce the final data statistical covariance matrix. MC statistical uncertainties on the background estimates, as well as data uncertainties from the CRs used in the fake and top estimates, are propagated in a similar way, and treated as uncorrelated amongst themselves and with those from the data in the SR.

Signal MC statistical uncertainties are correlated across the unfolding inputs, since the same events are used in the efficiency and fiducial corrections, as well as the migration matrices. This is handled with a bootstrapping technique, where separate signal samples are generated by sampling, with replacement, events from the nominal signal sample. These events are then in principle used to calculate the corrections and fill the migration matrices, with the unfolding procedure repeated on each sample and the variance of the outputs taken as the final uncertainty. The resampling procedure can however be approximated in the limit of a large number of events by attaching a weight to each event that is randomly generated according to a Poisson distribution with an expectation value of 1. This is due to the large sample approximation

$$\lim_{n \to \infty} \text{Binomial}(n, 1/n) = \text{Poisson}(1), \tag{6.9}$$

where n is the number of sampled events. In this case, the unique number that is associated to each simulated signal event, known as the event number, can be used to seed a random number generator based on this Poisson distribution. Each event then has a set of weights and the unfolding inputs can be calculated for each weight separately, with the final spread of unfolded results taken to quantify the signal MC uncertainty. The final absolute uncertainty is shown for the leading lepton p_T and jet multiplicity for the one jet inclusive selection in Figure 6.20. Although the method properly accounts for correlations between the statistical uncertainties, the final uncertainty is fairly small and very similar to that obtained using a simpler bin-by-bin approach, where the MC statistical uncertainty is propagated through extrapolation factors according to Eq. (5.5) with no migrations and hence correlations taken into account. The bootstrap method is therefore only adopted for the one jet inclusive selection, with the bin-by-bin approach used for the jet inclusive measurements.
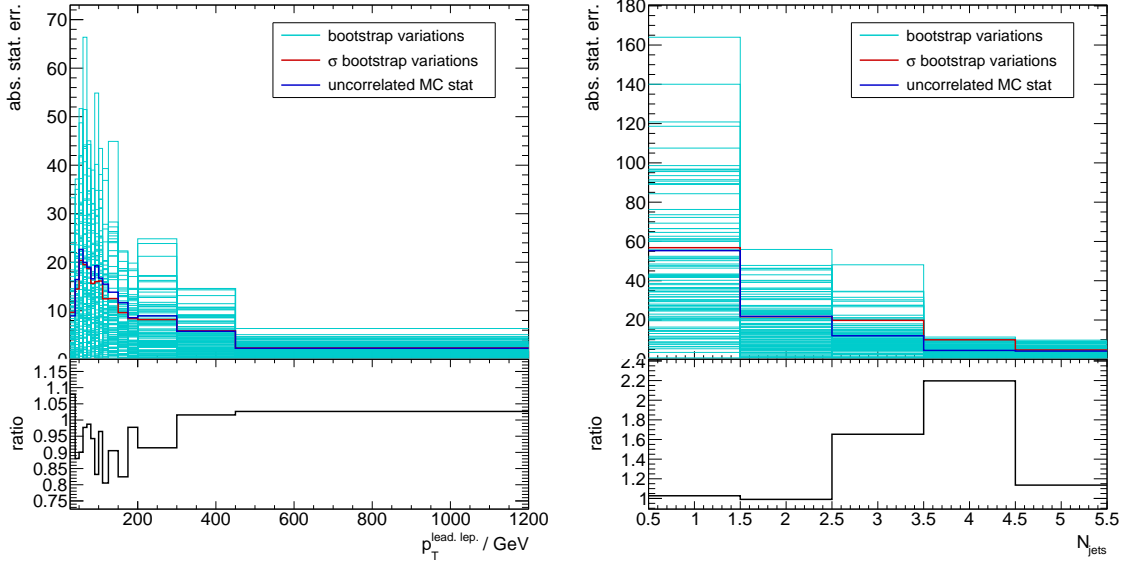
Figure 6.20: Absolute signal MC statistical uncertainty on the leading lepton p_T (left) and jet multiplicity (right) for 100 bootstrap variations. The standard deviation of the variations is shown in red, with the uncorrelated bin-by-bin estimate shown in blue. The bottom panel shows the ratio of the standard deviation of the bootstrap variations to the result from the bin-by-bin estimate.

6.7.6 Final uncertainties

The breakdown of the final uncertainty on the integrated fiducial cross section result for each region is shown in Table 6.10. It is clear that the one jet inclusive result produces the largest overall uncertainty, which is driven by a relatively large jet calibration uncertainty, as well as top modelling and fake background uncertainties. The large jet calibration uncertainty relative to the fully jet inclusive and dynamic jet veto phase spaces can be understood as arising from the hard cut on the number of jets in the former case. There is no such cut for the fully inclusive selection, and the dynamic jet veto tends to place cuts only on jets of higher p_T, for which the relative effect of jet calibration uncertainties is smaller. The top modelling uncertainty is lowest for the jet veto phase space, due to the relatively small contribution from top events, but largest for the one jet inclusive selection where the relative top contribution is highest, as was shown in Table 6.7. Flavour tagging uncertainties follow a similar pattern to the top modelling uncertainties, and may be explained using similar reasoning. The relatively large uncertainty from the fake estimate for the one jet inclusive selection is due to the fact that the 25% flat uncertainty on the mismodelling of prompt leptons passing the selection requirements in the fake CR, as discussed in Section 6.5.3, is removed for the zero jet, fully jet inclusive, and dynamic jet veto measurements in anticipation of an improved estimate of this uncertainty. The overall conclusions without including this uncertainty are assumed to be unchanged. The signal modelling uncertainty is smallest for the jet veto phase space, where the difference between the nominal and alternative predictions is smaller. Some of the reduction in the uncertainty on the other backgrounds can be explained by the change to using scale variations for the Drell-Yan uncertainty rather than an alternative simulation. Given the POWHEG generator is used for the alternative prediction on the WZ and ZZ predictions, a similar argument as for the differences in the signal modelling uncertainties can also be made here. The zero jet phase space

Uncertainty source	Fully jet inclusive	One jet inclusive	Jet veto	Dynamic jet veto
Total uncertainty	5.1%	10%	6.0%	5.1%
Statistical uncertainty	0.8%	1.6%	1.2%	1.1%
Jet calibration	0.7%	6.3%	4.4%	1.6%
Top modelling	2.5%	4.5%	0.9%	2.0%
Fake-lepton background	2.6%	4.3%	2.6%	2.6%
Signal modelling	2.3%	2.7%	1.8%	2.7%
Other background	1.1%	2.3%	0.8%	0.8%
Flavour tagging	1.5%	2.3%	0.8%	0.5%
Luminosity	1.8%	1.9%	1.8%	1.7%
Other uncertainties	0.5%	0.6%	1.2%	0.7%

Table 6.10: The uncertainty breakdown on the integrated fiducial cross section result. The statistical uncertainty combines both signal and background MC statistical uncertainties, as well as data statistical uncertainties from the SR and data-driven background estimates. Jet calibration uncertainties include uncertainties on the jet response. Top modelling and signal modelling uncertainties include uncertainties on the theoretical predictions of the respective processes. The fake-lepton background uncertainty includes all uncertainties on the fake estimate. Other background uncertainties include uncertainties on minor prompt lepton backgrounds. The flavour tagging uncertainty includes uncertainties in both the b-tag efficiency and mis-tag rate. The luminosity is the uncertainty on the measured integrated luminosity. Other uncertainties include all remaining systematic effects. One jet inclusive result taken from [12].

is more sensitive to the modelling of PU, which explains the relatively large uncertainty coming from other systematic sources, which include PU reweighting uncertainties.

The previous ATLAS jet veto measurement discussed in Section 2.2.3 had a final uncertainty of about 7%. There is therefore a reduction in the uncertainty in this phase space in the current measurement, benefiting in part from the improved top estimate.

Future improvements to the measurement are anticipated that may reduce the uncertainties shown in Table 6.10 further. This would at least include reducing the relatively large uncertainty related to the prompt lepton selection efficiency in the fake CR by using a dedicated data-driven calibration. As already mentioned, this uncertainty has been removed in the table for all selections apart from the one jet inclusive selection to provide a rough comparison of the effects of this reduction. A further reduction in the fake uncertainty may be achieved by using the final measured uncertainty on the detector-level signal yield for the subtraction of signal events in the fake CR, following an iterative approach. Reductions in the signal modelling uncertainties are also anticipated by a replacement of the nominal SHERPA signal model with a recent POWHEG MINNLO [102, 237] prediction interfaced to PYTHIA 8.245 [90]. The scale uncertainties of this prediction could be used in place of an alternative generator comparison. Using scale uncertainties for the diboson background in place of the current generator comparison would similarly help to reduce uncertainties on this background. As mentioned in Section 6.5.3, the dominant uncertainties on the top background arise from modelling effects, which could perhaps be partly mitigated in future by switching to a more unified description of the $t\bar{t}$ and Wt process that correctly accounts for interference effects [250]. Run-III measurements have the potential to further benefit from improvements to jet and

lepton calibrations and flavour tagging, as well as increased statistics.

In addition to the uncertainty on the integrated cross section, uncertainties are calculated per bin for each distribution. The uncertainty for the leading lepton p_T and the leading jet p_T in the one jet inclusive phase space are shown in Figure 6.21. In general the jet-related uncertainties decrease with the jet p_T, whilst statistical uncertainties increase at higher energies where there are fewer events. This leads to a minimum uncertainty at intermediate values of both the leading lepton p_T and the leading jet p_T. The associated correlation matrices including all uncertainties, which may be used for calculating χ^2 values that quantify the agreement between the measurement results and the theoretical predictions, are shown in Figure 6.22. The uncertainties for the leading lepton p_T and S_T for the fully jet inclusive selection are also shown in Figure 6.21. The statistical uncertainties in the final bin of the leading lepton p_T for the one jet inclusive selection are larger than those for the fully inclusive selection in part because the top estimate for the former selection does not use the transfer factor approach designed to reduce such uncertainties, in contrast to the fully jet inclusive case.
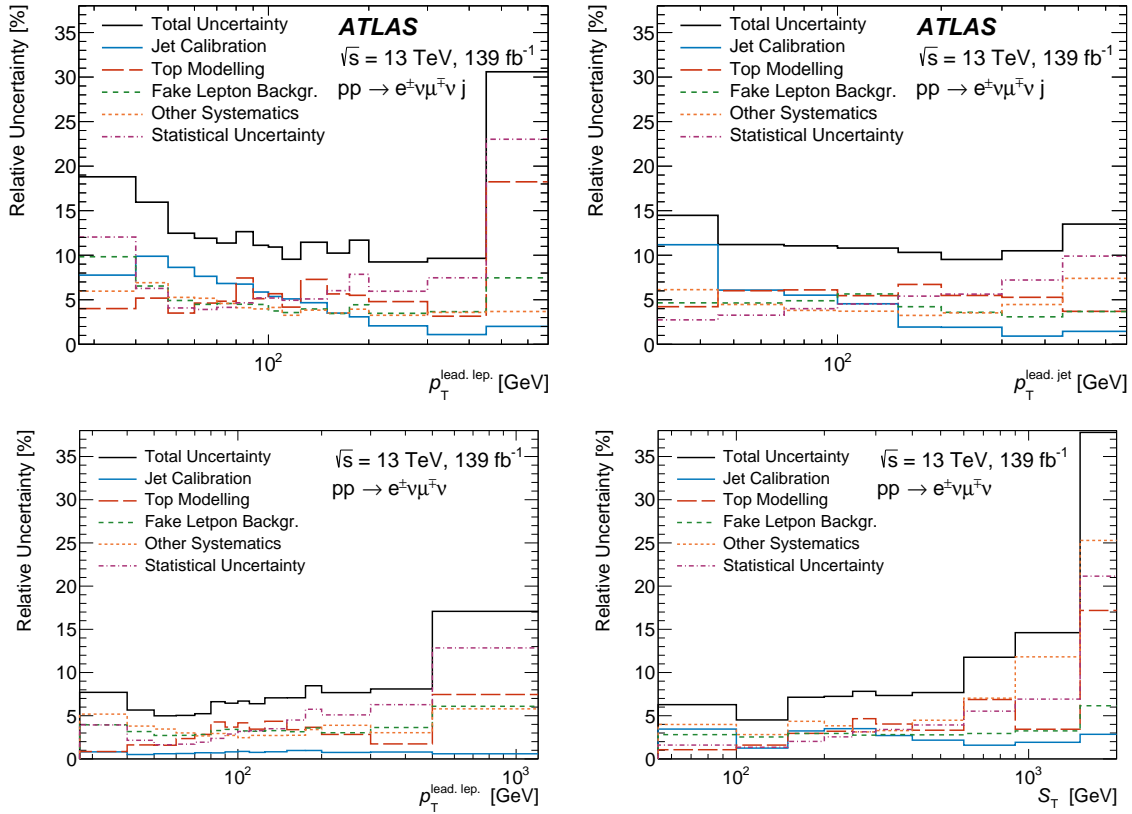
Figure 6.21: Distributions of the relative uncertainty breakdown. Shown are the unfolded leading lepton p_T (top left) and leading jet p_T (top right) for the one jet inclusive selection, and the leading lepton p_T (bottom left) and S_T (bottom right) for the fully jet inclusive selection. Jet calibration uncertainties include uncertainties on the jet response. Top modelling uncertainties include uncertainties on the theoretical top quark background prediction. The fake-lepton background uncertainty includes all uncertainties on the fake estimate. Other systematic uncertainties include uncertainties on the signal modelling, minor prompt lepton backgrounds, flavour tagging and luminosity as well as uncertainties from other remaining systematic effects. The statistical uncertainty combines both signal and background MC statistical effects, as well as data statistical uncertainties from the SR and data-driven background estimates. For the one jet inclusive distributions, only the b-tag counting method is used in the top estimate. Top plots taken from [12].
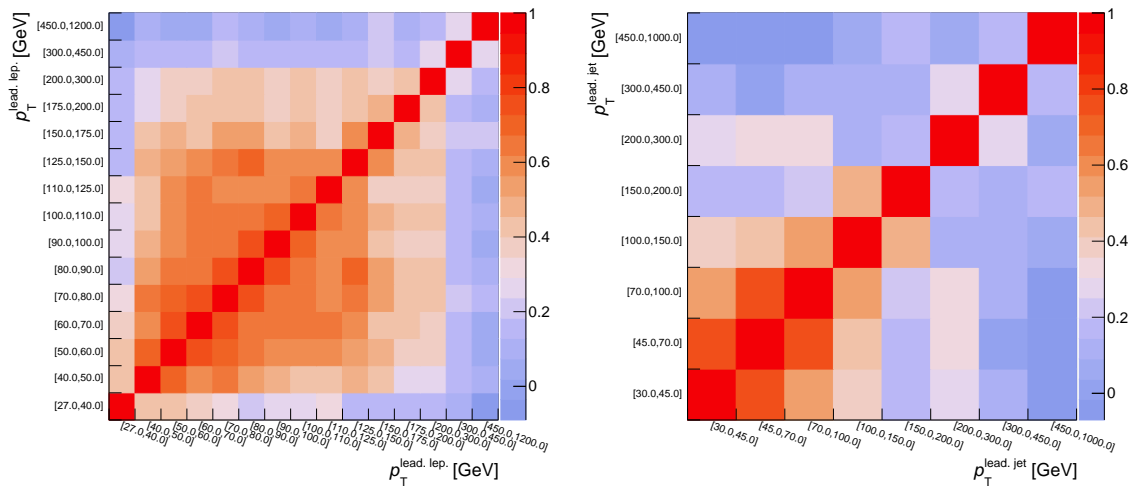
Figure 6.22: Correlation matrices for the leading lepton p_T (left) and leading jet p_T (right) for the one jet inclusive selection. The colours correspond to the correlation. Both statistical and systematic uncertainties are included as discussed in Section 6.7.5.

7

Results

In the previous chapter, details were given of the event selection and background estimates leading to detector-level distributions for observables related to W^+W^- production. The unfolding procedure used to obtain fiducial-level results and the final uncertainties was also discussed. In this chapter, the final fiducial integrated and differential cross sections will be presented. Results for a fit-based measurement, as well as studies on the sensitivity to the W^+W^- charge asymmetry, will also be shown.

7.1 Cross section results

Fixed-order and PS-matched theoretical predictions for W^+W^- production cross sections were discussed in Section 2.1.2. Such predictions can easily be compared to the unfolded results obtained in the measurements described.

7.1.1 One jet inclusive results

The measured integrated fiducial cross section for the one jet inclusive phase space is

$$\sigma^{\text{fid}}(pp \rightarrow W^+W^- \rightarrow e^\pm \nu_e \mu^\mp \nu_\mu, \sqrt{s} = 13\,\text{TeV}) = 258 \pm 4\,(\text{stat.}) \pm 25\,(\text{syst.})\,\text{fb},$$

with a total relative uncertainty of about 10%. This is compared to the range of theoretical predictions summarised in Table 7.1, with the results shown in Figure 7.1a. Differential cross sections are shown in Figures 7.2 and 7.3 and compared to the same theoretical predictions. Overall very good agreement is observed between the predictions and the measurement within the uncertainties. The $\chi^2/\text{d.o.f.}$ values calculated with respect to the nominal SHERPA prediction are all below one. Slight discrepancies are observed in the highest multiplicity bin of the jet multiplicity, and

Process	Generator	PS	ME $\mathcal{O}(\alpha_s)$
$q\bar{q} \rightarrow W^+W^-$	MATRIX 2.0	-	NNLO
$gg \rightarrow W^+W^-$	MATRIX 2.0	-	NLO
$q\bar{q} \rightarrow W^+W^-$	SHERPA 2.2.2	SHERPA	NLO (0-1 jet), LO (2-3 jets)
$q\bar{q} \rightarrow W^+W^-$	POWHEG MiNLO	PYTHIA 8	NLO (0-1 jet)
$q\bar{q} \rightarrow W^+W^-$	MADGRAPH 2.3.3	PYTHIA 8	NLO (0-1 jet)
$gg \rightarrow W^+W^-$	SHERPA 2.2.2 + OPENLOOPS	SHERPA	LO (0-1 jet)

Table 7.1: Summary of the theoretical predictions used to compare against the measured cross sections for the one jet inclusive phase space. The ME column indicates the order of the ME calculation in α_s relative to the base process. All predictions use the NNPDF3.0 PDF sets. An additional prediction not listed combines the MATRIX result with NLO EW corrections as described in the text. Adapted from [12].

the highest energy bins of the H_T^jet and S_T distributions.

The MATRIX [11, 68, 69, 77] fixed-order inclusive cross section prediction shown in Figure 7.1a and the differential distributions is accurate to NNLO QCD for $q\bar{q} \rightarrow W^+W^-$ and NLO for $gg \rightarrow W^+W^-$. Since the gg-induced component formally contributes at $\mathcal{O}(\alpha_s^3)$, this combination is written nNNLO to indicate the result is an approximation to the full N^3LO prediction. The requirement of at least one jet means the calculation is only accurate to NLO for the quark-induced channel and LO for the gluon-induced channel. The NNPDF3.1NNLO [31] set is used for these predictions, with the nominal renormalisation and factorisation scales set to m_W. The same prediction additionally including NLO EW corrections generated with SHERPA 2.2.2 + OPENLOOPS [76, 78, 88] is also considered.

For predictions interfaced to a PS, the nominal SHERPA 2.2.2 prediction is used, as well as a POWHEG MiNLO [251] prediction interfaced to PYTHIA 8.244 [90], and a MADGRAPH 2.3.3 [238] prediction interfaced to PYTHIA 8.212 using FxFx merging [99]. The $q\bar{q} \rightarrow W^+W^-$ ME for each of these predictions is NLO accurate for at least one jet, and the NNPDF3.0 PDF set is used. The gg-induced channel is included in each case with SHERPA 2.2.2 + OPENLOOPS, normalised to the total NLO cross section [11]. Uncertainties arise in each case from the PDF and scale variations. From Figure 7.1a it can be seen that the uncertainty from scale variations is dominant, with the largest effect for the nominal SHERPA prediction. This is because this prediction uses MEs accurate only at LO for two to three jets, and so the scale dependence for these contributions to the integrated cross section is larger. Uncertainties associated to the PS are not included.

7.1.2 Fully inclusive and dynamic jet veto results

The result for the fully jet inclusive selection is

$$\sigma^\text{fid}(pp \rightarrow W^+W^- \rightarrow e^\pm\nu_e\mu^\mp\nu_\mu, \sqrt{s} = 13\,\text{TeV}) = 668 \pm 5\,(\text{stat.}) \pm 34\,(\text{syst.})\,\text{fb},$$

with a relative uncertainty of about 5%. For the dynamic jet veto, the result is

$$\sigma^\text{fid}(pp \rightarrow W^+W^- \rightarrow e^\pm\nu_e\mu^\mp\nu_\mu, \sqrt{s} = 13\,\text{TeV}) = 496 \pm 5\,(\text{stat.}) \pm 25\,(\text{syst.})\,\text{fb},$$
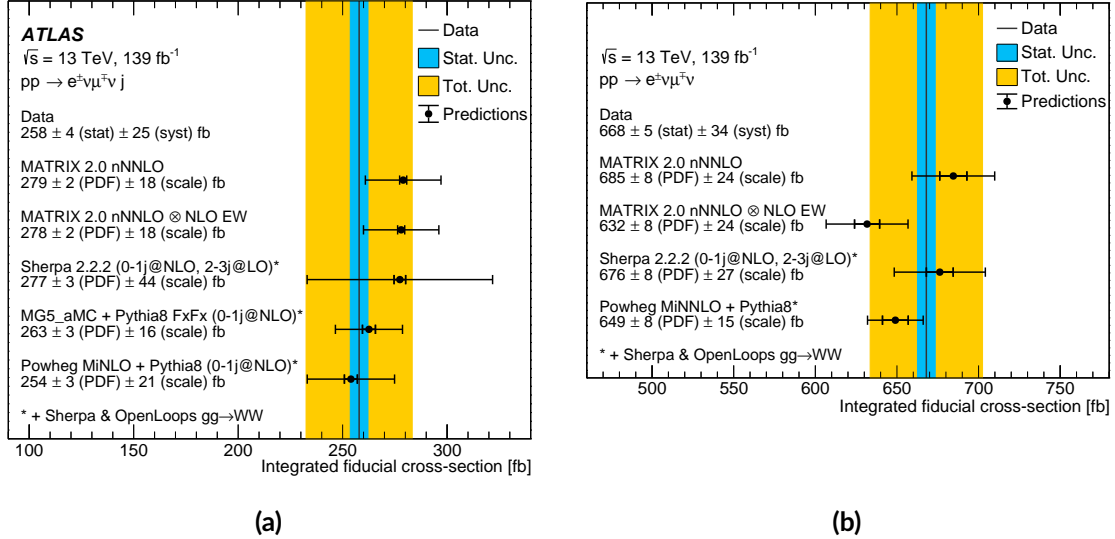
Figure 7.1: **(a)** Integrated fiducial cross section for the one jet inclusive selection measured in data and calculated with a range of theoretical predictions as discussed in the text. The data is shown as a vertical line, with the statistical uncertainty band in blue, and the band also including systematic uncertainties shown in yellow. For the theoretical predictions, the inner uncertainty bars include PDF uncertainties, whilst the outer error bars also include uncertainties from scale variations. Taken from [12]. **(b)** Integrated fiducial cross section for the fully inclusive selection.

also with a relative uncertainty of about 5%. There is good agreement between these measured integrated fiducial cross sections and a range of theoretical predictions, as summarised in Figure 7.1b. The same MATRIX and SHERPA calculation schemes as for the one jet inclusive measurement are considered, as well as the POWHEG MINNLO [102, 237] prediction interfaced to PYTHIA 8.245 [90] mentioned in Section 6.7.6. The MINNLO prediction is accurate at NNLO QCD for zero jets and inclusive observables, and is therefore expected to have reduced scale uncertainties compared to the MINLO [251] prediction, which was considered in the one jet inclusive measurement. Differential results are shown for the fully jet inclusive selection in Figures 7.4 and 7.5, and the dynamic jet veto selection in Figures 7.6 and 7.7. In all cases, one iteration is used in the unfolding, which uses the nominal SHERPA prediction. Good agreement is observed overall in both the integrated and differential fiducial cross sections.

The main motivation for measuring cross sections in the dynamic jet veto phase space was to reduce theoretical uncertainties coming from mixed QCD and EW corrections, as discussed in Section 6.3.2. In Figure 7.8, a selection of results for this phase space are compared to a MINNLO prediction that additionally includes multiplicative NLO EW corrections calculated with MATRIX 2.0. The correction is calculated only for the $q\bar{q}$ initial state, differentially for each observable in the fiducial phase space. As expected, the EW corrections lead to a reduction in the predicted cross section at large energies, and an improved description of the shape. The rate reduction however worsens the agreement between the prediction and the data. A partial explanation is related to a possible double-counting of the EM component of the NLO EW corrections between the MINNLO and MATRIX predictions. Both predictions are calculated on the basis of dressed leptons, whereby the momenta of photons radiated within a cone of $\Delta R < 0.1$ are added to the lepton momentum.
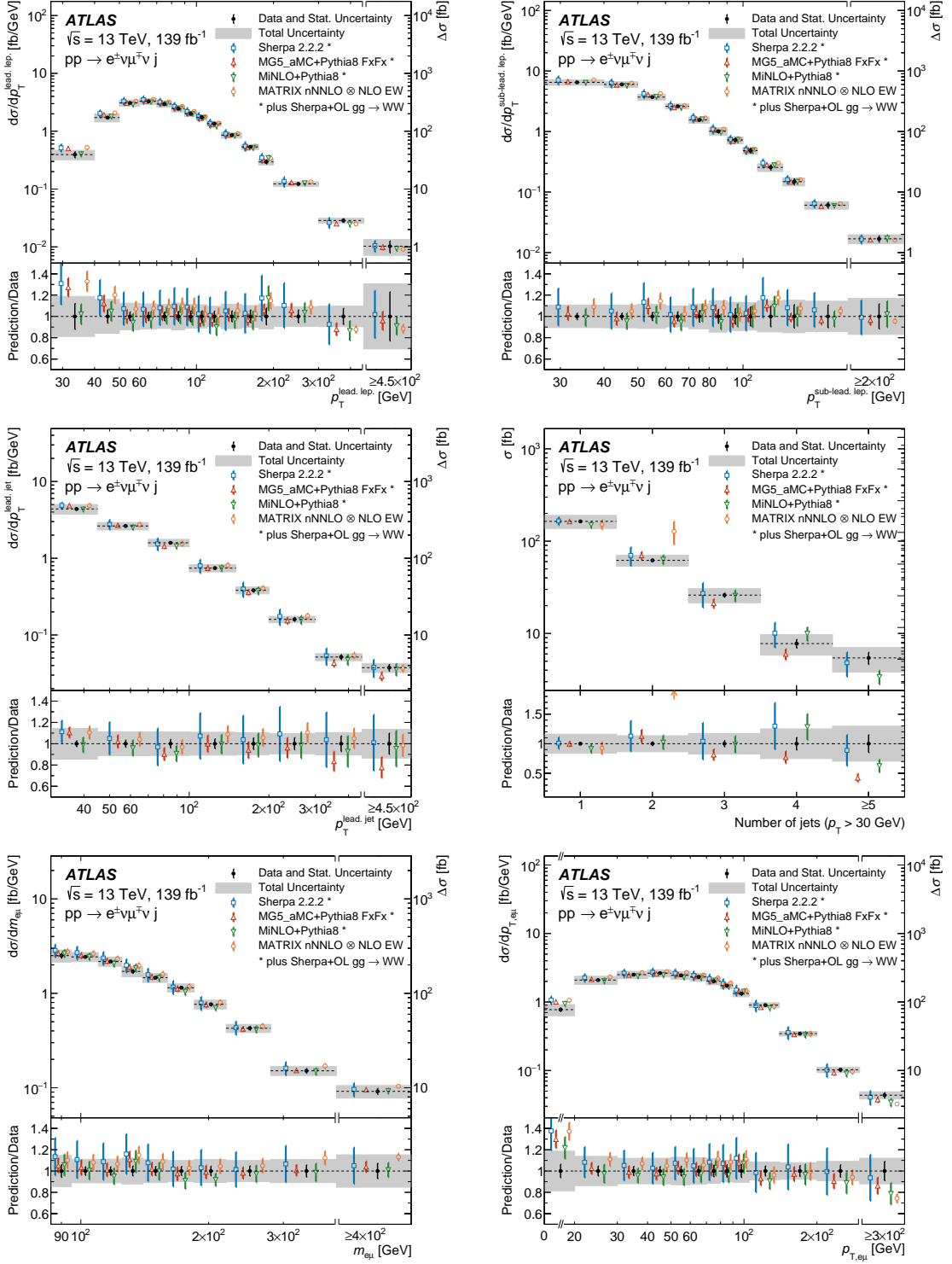
Figure 7.2: Measured differential fiducial cross sections for the one jet inclusive selection compared to theoretical predictions. Shown are the leading lepton p_T (top left), subleading lepton p_T (top right), leading jet p_T (middle left), jet multiplicity (middle right), invariant mass of the dilepton system (bottom left) and the transverse momentum of the dilepton system (bottom right). The statistical uncertainty on the measured cross section is shown by the vertical lines on the data points, with the grey band including both statistical and systematic uncertainties. The error bars on the theoretical predictions include both scale variation uncertainties and PDF uncertainties. The final bin of each distribution is inclusive in the observable where applicable, with the integrated cross section indicated by the right-hand axis. Taken from [12].
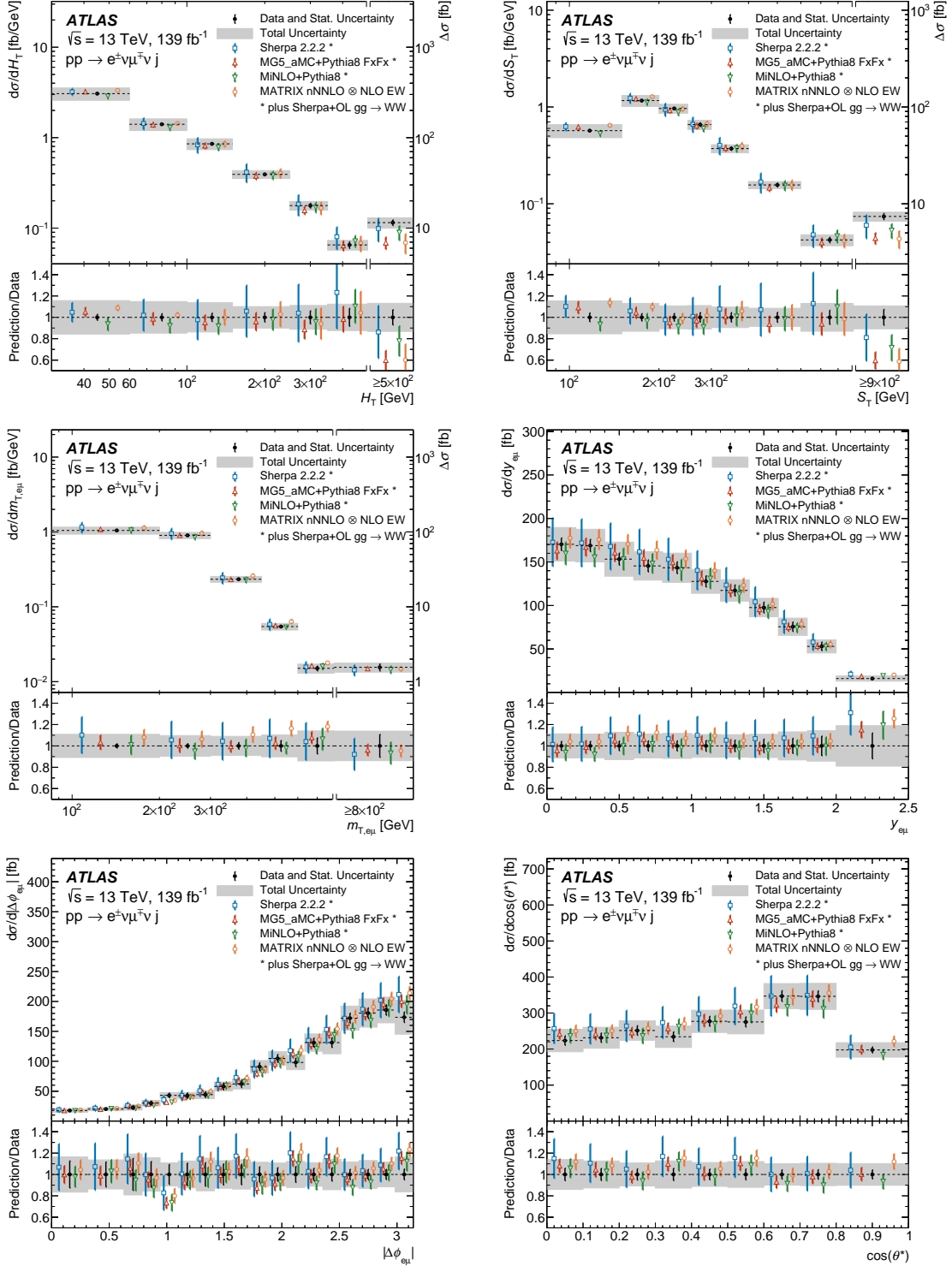
Figure 7.3: Measured differential fiducial cross sections for the one jet inclusive selection compared to theoretical predictions. Shown are H_T^{jet} (top left), S_T (top right), the transverse mass (middle left), the rapidity of the dilepton system (middle right), the azimuthal separation between the two leptons (bottom left) and $\cos\theta^*$ (bottom right). The statistical uncertainty on the measured cross section is shown by the vertical lines on the data points, with the grey band including both statistical and systematic uncertainties. The error bars on the theoretical predictions include both scale variation uncertainties and PDF uncertainties. The final bin of each distribution is inclusive in the observable where applicable, with the integrated cross section indicated by the right-hand axis. Taken from [12].
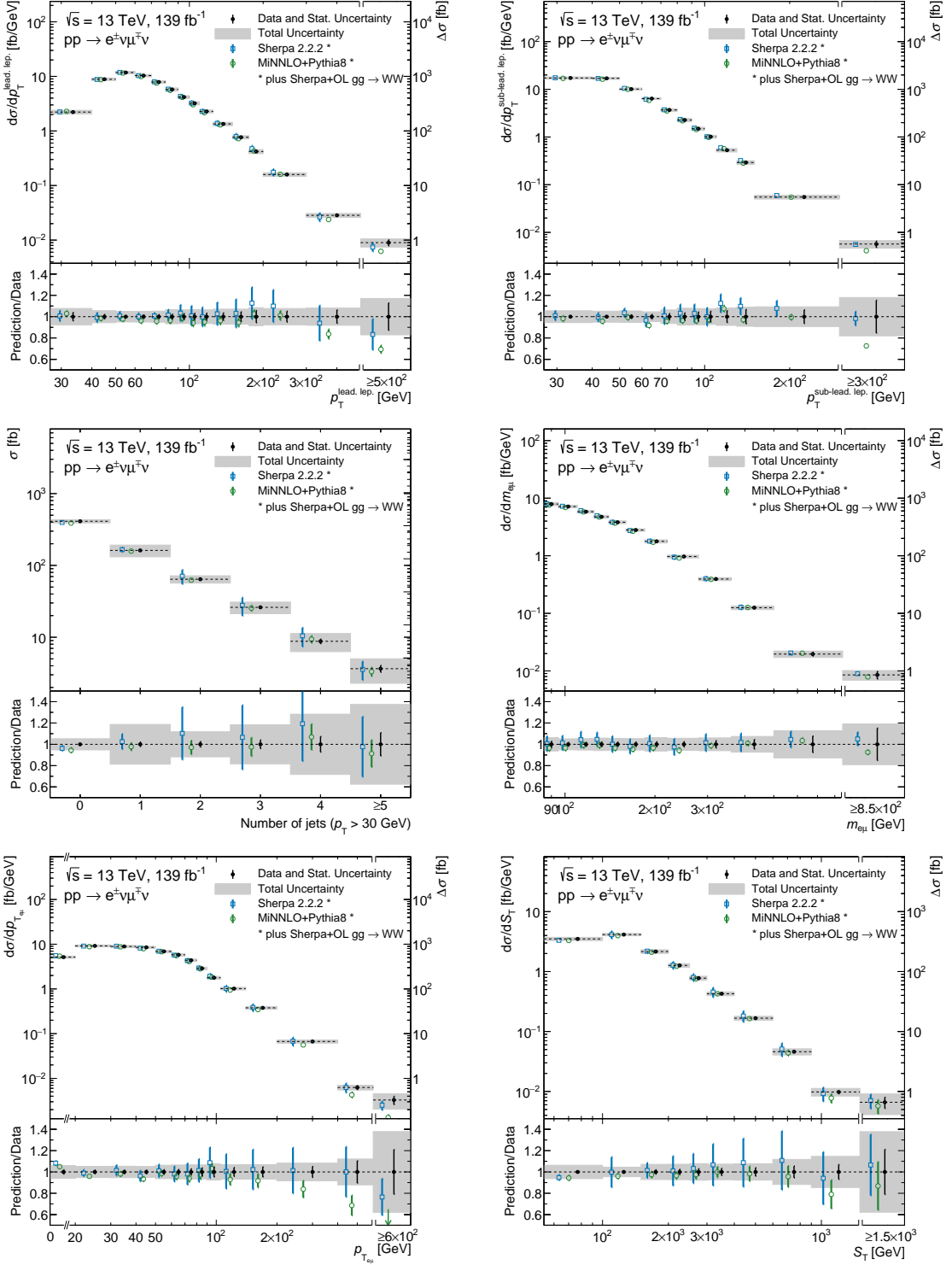
Figure 7.4: Measured differential fiducial cross sections for the fully jet inclusive selection compared to theoretical predictions. Shown are the leading lepton p_T (top left), subleading lepton p_T (top right), jet multiplicity (middle left), invariant mass of the dilepton system (middle right), the transverse momentum of the dilepton system (bottom left), and S_T (bottom right). The statistical uncertainty on the measured cross section is shown by the vertical lines on the data points, with the grey band including both statistical and systematic uncertainties. Uncertainties on the theoretical predictions include both scale variation uncertainties and uncertainties on the PDF. The final bin of each distribution is inclusive in the observable where applicable, with the integrated cross section indicated by the right-hand axis.
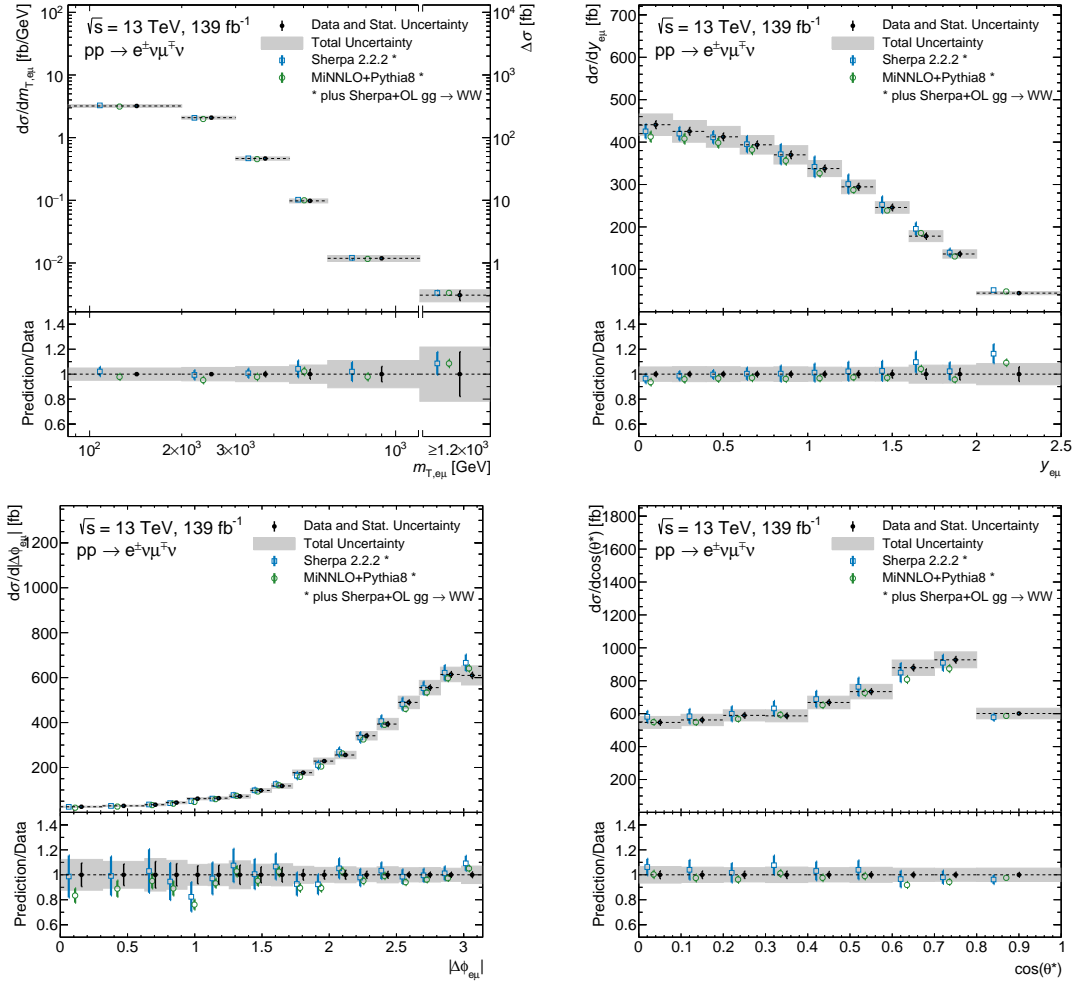
Figure 7.5: Measured differential fiducial cross sections for the fully jet inclusive selection compared to theoretical predictions. Shown are the transverse mass (top left), the rapidity of the dilepton system (top right), the azimuthal separation between the two leptons (bottom left), $\cos\theta^*$ (bottom right). The statistical uncertainty on the measured cross section is shown by the vertical lines on the data points, with the grey band including both statistical and systematic uncertainties. Uncertainties on the theoretical predictions include both scale variation uncertainties and uncertainties on the PDF. The final bin of each distribution is inclusive in the observable where applicable, with the integrated cross section indicated by the right-hand axis.
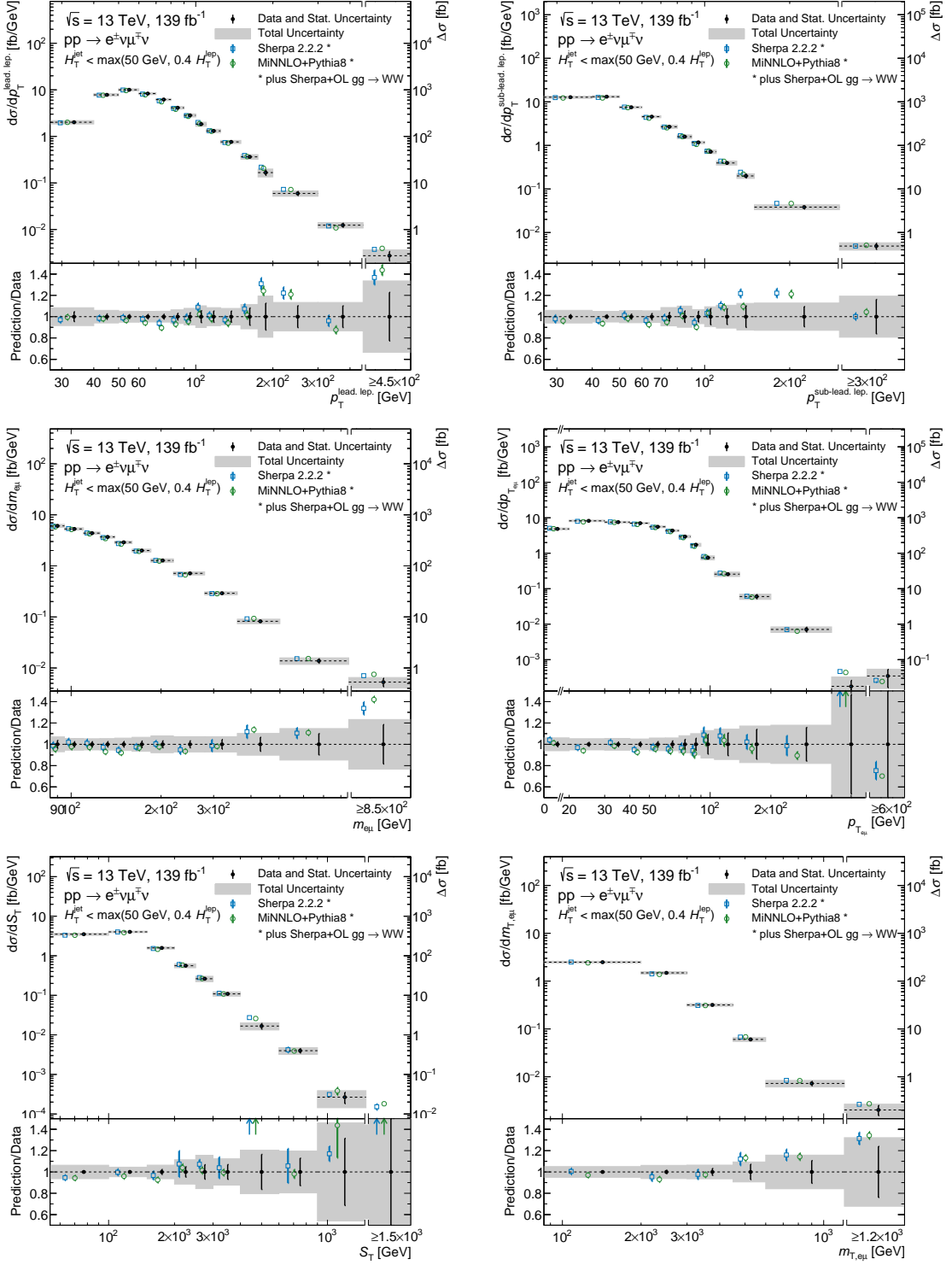
Figure 7.6: Measured differential fiducial cross sections for the dynamic jet veto selection compared to theoretical predictions. Shown are the leading lepton p_T (top left), subleading lepton p_T (top right), invariant mass of the dilepton system (middle left), the transverse momentum of the dilepton system (middle right), S_T (bottom left), and the transverse mass (bottom right). The statistical uncertainty on the measured cross section is shown by the vertical lines on the data points, with the grey band including both statistical and systematic uncertainties. Uncertainties on the theoretical predictions include both scale variation uncertainties and uncertainties on the PDF. The final bin of each distribution is inclusive in the observable where applicable, with the integrated cross section indicated by the right-hand axis.
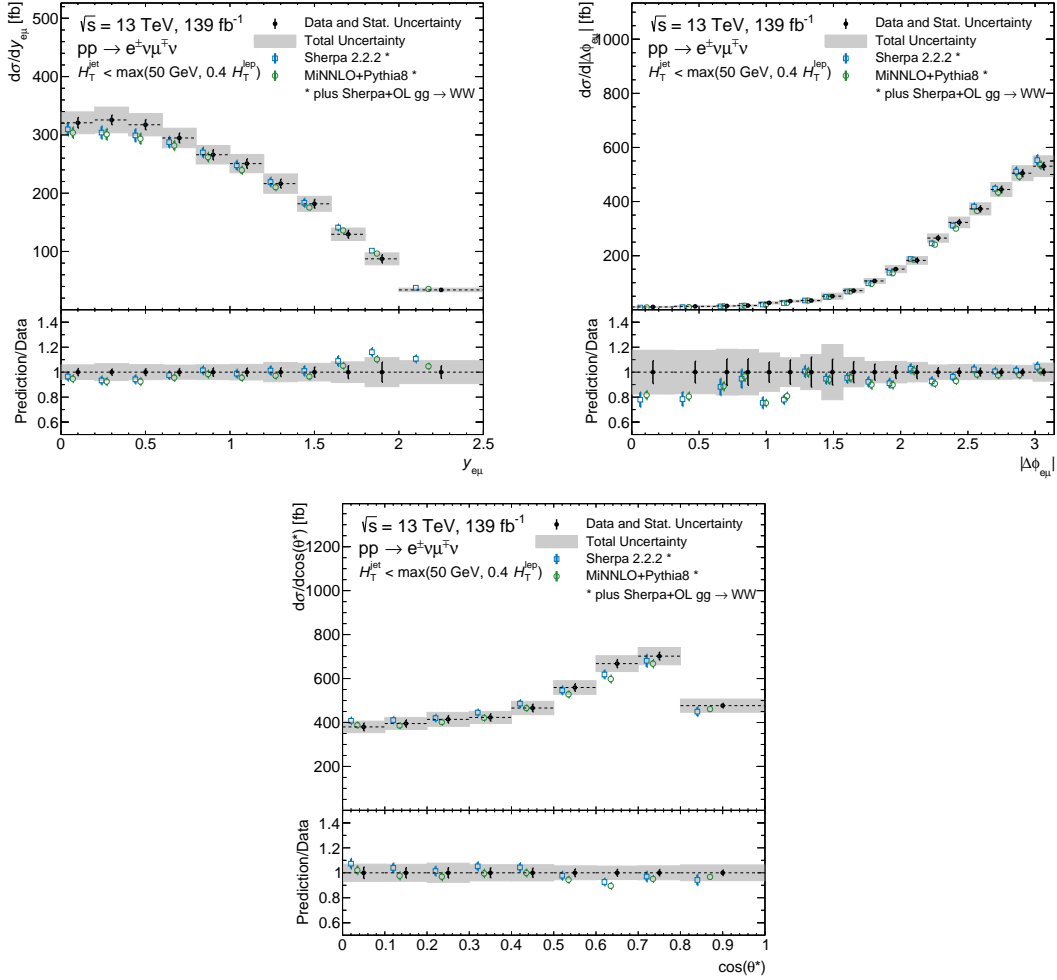
Figure 7.7: Measured differential fiducial cross sections for the dynamic jet veto selection compared to theoretical predictions. Shown are the rapidity of the dilepton system (top left), the azimuthal separation between the two leptons (top right), and $\cos\theta^*$ (bottom). The statistical uncertainty on the measured cross section is shown by the vertical lines on the data points, with the grey band including both statistical and systematic uncertainties. Uncertainties on the theoretical predictions include both scale variation uncertainties and uncertainties on the PDF. The final bin of each distribution is inclusive in the observable where applicable, with the integrated cross section indicated by the right-hand axis.

It is also possible in both cases for FSR photons to escape the dressing cone. These arise from the PYTHIA PS in the case of the MiNNLO prediction. This effect, which reduces the lepton energy, is therefore double-counted in the combination of the two predictions. It typically amounts to a correction of the cross section by a few percent [228]. Such double-counting could be avoided by considering only fixed-order NNLO QCD predictions, or by switching off the EM radiation component in PYTHIA.

7.2 Fit-based measurements

In addition to the method described in the preceding sections for obtaining fiducial cross sections by extrapolating the background subtracted data to the fiducial phase space, an alternative approach can be adopted in which the normalisation of the signal estimate is extracted in a profile LH fit. Constraints on systematic uncertainties that arise when the data in the fitting region is able to fix the nuisance parameter better than the auxiliary measurement can lead to a reduction in the final uncertainty. The introduction of anti-correlations between systematic uncertainties in the LH, can also lead to smaller overall uncertainties. This can be understood from Eq. (5.5), where the generated anti-correlations between two systematic effects lead to a variance that is smaller than simply their sum in quadrature. Since the fitting method requires a signal model whose normalisation is to be determined, it is more model-dependent than the nominal analysis strategy.

7.2.1 Profile likelihood fits for the one jet inclusive selection

Binned profile LH fits are performed in the one jet inclusive phase space. The fit uses template distributions for the leading lepton p_T for both signal and background contributions in the SR defined in Section 6.3.2. Apart from the top and W+jets contributions, these templates are obtained from MC simulation. The top contribution is taken from the nominal top estimate discussed in Section 6.4.1, whereas the W+jets contribution is estimated using the fake factor data-driven approach discussed in Section 6.4.3. The nominal SHERPA prediction is used for the signal template. Figure 7.9a shows the distribution in data, alongside the signal and background templates, before the fit is performed. This is known as the prefit plot. Fits are then performed in which either the signal normalisation, or both the signal and top normalisations, are taken as PoIs. Systematic uncertainties are included in the fit model as described in Section 5.3.1 in terms of NPs, with γ parameters used for the MC and data statistical uncertainties on the background estimates. Two-point systematic uncertainties are symmetrised as for the unfolding. Systematic uncertainties with separate *up* and *down* variations are constrained to be within the corresponding envelope around the nominal. Some smoothing may be applied to the systematic uncertainties in order to reduce fluctuations arising from limited statistics that otherwise could lead to double counting of statistical uncertainties, or artificial pulls and constraints on NPs. For the fit results shown in this section, the default smoothing algorithm of the fitting software was used. The effects on some example jet and top modelling related systematic uncertainties are shown in Figure 7.10. It is clear that in some bins the applied smoothing is too harsh. Alternative results with no smoothing applied were also considered, but the difference in the fitted PoIs between the case with smoothing and that without
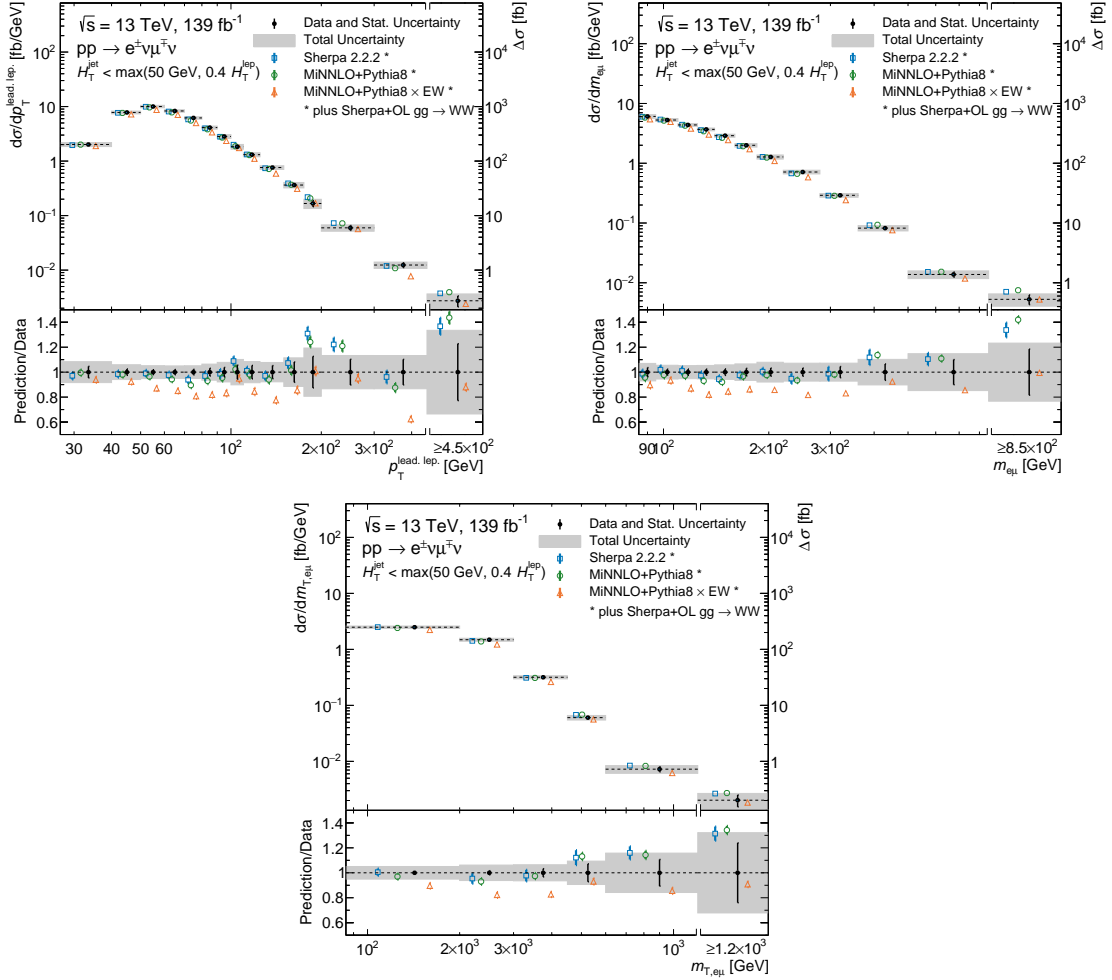
Figure 7.8: Measured differential fiducial cross sections for the dynamic jet veto selection compared to theoretical predictions, including the MiNNLO prediction with multiplicative NLO EW corrections. Shown are the leading lepton p_T (top left), the invariant mass of the dilepton system (top right), and the transverse mass (bottom). The statistical uncertainty on the measured cross section is shown by the vertical lines on the data points, with the grey band including both statistical and systematic uncertainties. Uncertainties on the theoretical predictions include both scale variation uncertainties and uncertainties on the PDF. The final bin of each distribution is inclusive in the observable, with the integrated cross section indicated by the right-hand axis.
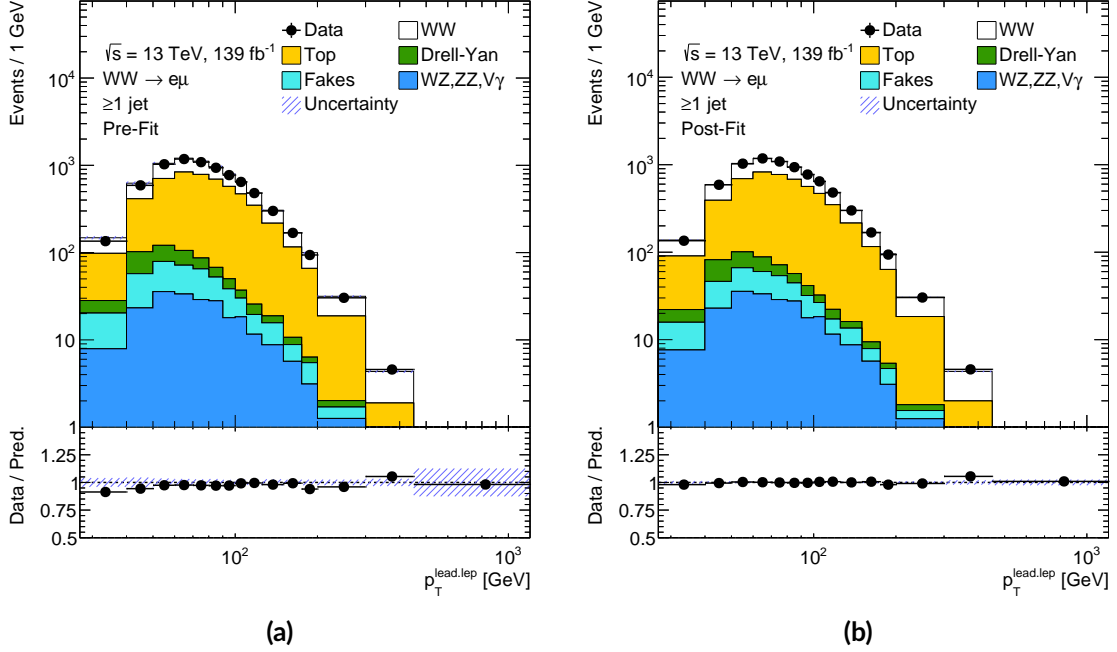
Figure 7.9: **(a)** The prefit leading lepton p_T distribution, showing data, and the signal and background predictions. The uncertainty on the predictions includes statistical and systematic uncertainties, excluding signal modelling uncertainties. **(b)** The postfit leading lepton p_T distribution for the fit to real data.

smoothing was found to be small, with the latter producing a slightly smaller uncertainty as a result of the increased flexibility of the fit.

An initial fit of the signal normalisation is performed using so-called Asimov data [252]. This involves replacing the expectation value of the actual data in each bin with the value obtained by setting the signal and background yields equal to their nominal values. The Asimov dataset then perfectly matches the nominal prediction. The best fit value for the normalisations in such a fit should be exactly one, with the NPs fit to their nominal values. The Asimov fit can be used to provide an estimate for the uncertainty on the final fitted result, as well as to check for any potential technical problems with the fit. The effect of the fit on the systematic uncertainties via their NPs can be determined with pull plots. The pull indicates how far the best fit value of the NP is from its nominal value, as well as to what extent its postfit uncertainty agrees with its prefit uncertainty. The pull plot for the fit to Asimov data is shown in Figure 7.11a, where the NPs are ranked according to their impact, as defined in Section 5.3.1. One NP is present for each of the systematic uncertainties relevant for the measurement, described in Section 6.5, excluding those related to theoretical uncertainties on the signal. It is clear that jet-related uncertainties have the largest impacts, as well as the uncertainty on the luminosity, and some modelling uncertainties related to top and diboson backgrounds. Overall there are no non-zero pulls or large constraints on the NPs, which provides some validation for the method. The uncertainty related to the top ISR modelling is constrained slightly by the fit, as is the flat 25% uncertainty applied on the fake estimate to account for the mismodelling of the prompt subtraction in the fake CR. The relatively large constraint on the latter suggests that the estimate of this uncertainty is too conservative. The two γ
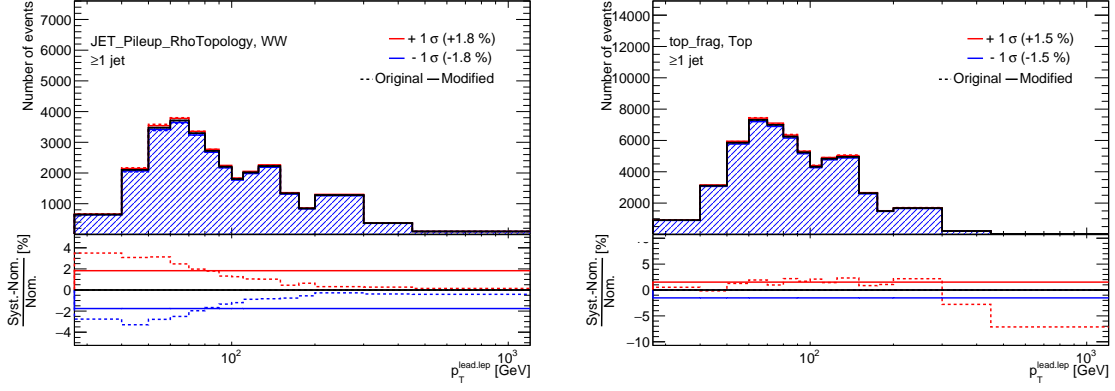
Figure 7.10: Effects of smoothing on the jet PU correction (left) and top ISR modelling (right) systematic uncertainties on the signal and top predictions respectively. The original systematic uncertainty, or pair of systematic uncertainties, are shown as dashed lines, with the smoothed results shown as solid lines. The nominal distribution is shown as a solid black line.

PoI	Asimov	Data
$\hat{\mu}_{WW}$	1.000 ± 0.076	0.954 ± 0.075
$\hat{\mu}_{WW}$	1.000 ± 0.093	0.958 ± 0.092
$\hat{\mu}_{\text{top}}$	1.000 ± 0.045	0.996 ± 0.045

Table 7.2: Summary of the best fit values and uncertainties on the PoIs for fits to both Asimov and real data. The top row shows the result for a fit in which only the signal normalisation, μ_{WW}, is free to float. The bottom row shows the results when both the signal normalisation and top normalisation, μ_{top}, are free to float.

parameters present in the ranking correspond to data statistical uncertainties in the two penultimate bins from the CRs of the top estimate, which for the one jet inclusive selection shown here is based entirely on the b-tag counting method. In these bins, the number of events in data in the top CRs is likely to be small, meaning the relative statistical uncertainties are large. This could lead to a relatively large impact on the fitted signal normalisation coming from these bins since the top contribution here is still substantial. The same cannot be said for the final bin, where the equivalent γ parameter has a smaller impact.

Following the Asimov fit, a similar fit is performed using real data, with the postfit plot shown in Figure 7.9b. The strong reduction in the total uncertainty relative to the prefit plot is evident. The corresponding ranking plot is shown in Figure 7.11b, where the constraints are similar to the Asimov fit, with some small pulls observed. The best fit value and uncertainty on the signal PoI are shown for the Asimov and real data fits in the top row of Table 7.2. The uncertainty is about 8%, to be compared with the 10% uncertainty on the one jet inclusive result obtained with the nominal analysis strategy. This suggests a more precise measurement may be possible with a fitting approach, at the cost of an increased model dependence.

An additional fit is performed where both the signal and top background normalisations are considered as PoIs. The results are displayed in the bottom row of Table 7.2. Since the top background template is obtained using the b-tag counting method, this fit can be considered as an additional validation for the top estimate, with the best fit value of 0.996 ± 0.045 consistent with one.

Pre-fit impact on μ:
□ θ = θ̂+Δθ □ θ = θ̂−Δθ
Post-fit impact on μ:
■ θ = θ̂+Δθ̂ ■ θ = θ̂−Δθ̂
—●— Nuis. Param. Pull
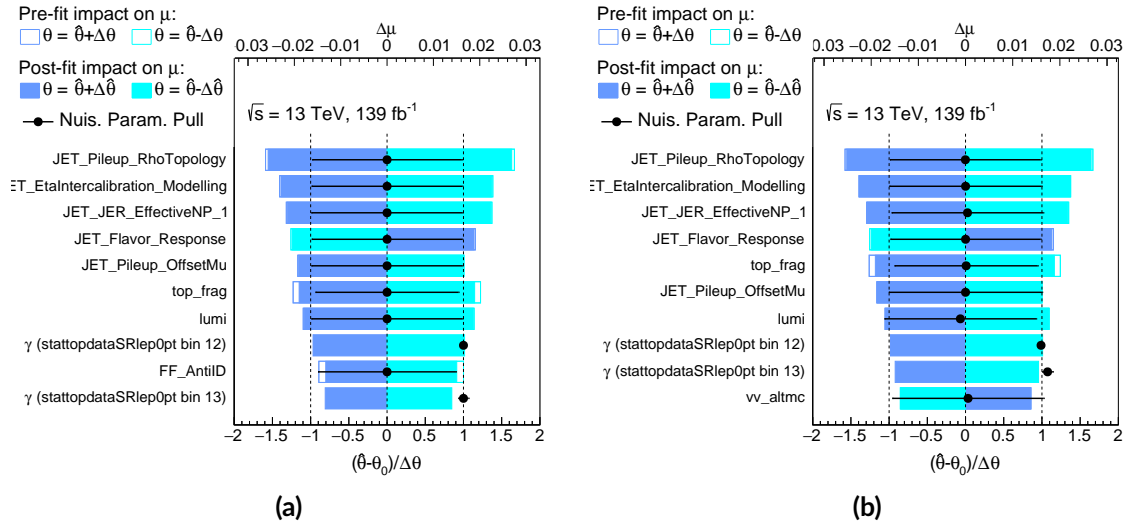
$\sqrt{s}$ = 13 TeV, 139 fb^{-1}

(a)

(b)

Figure 7.11: (a) Pulls and impacts for a subset of NPs for the fit to Asimov data. The lower horizontal axis measures the normalised pull, shown as the black circle, which is defined as the difference between the postfit value of the NP, $\hat{\theta}$, and its nominal value, θ_0, divided by the prefit uncertainty, $\Delta\theta$. The black horizontal lines indicate the postfit uncertainties, whilst the vertical dashed lines correspond to the prefit uncertainties. γ parameters related to finite MC and data statistics have nominal values of one, and are seen to be strongly constrained around this value. The impact on the signal PoI, $\Delta\mu$, is measured by the upper horizontal axis, with the empty and filled boxes corresponding to the prefit and postfit impacts respectively. NPs are ranked in order of decreasing impact, with lower impact NPs not shown. **(b)** Pulls and impacts for a subset of NPs for the fit to real data.

7.3 W^+W^- charge asymmetry

Larger numbers of observed signal events provide the possibility not only for more precise differential measurements, but also improved sensitivity to quantities such as the W^+W^- charge asymmetry, which may be able to provide a constraint on the proton quark PDFs. The sensitivity to this observable is expected to be larger in the zero jet phase space, where kinematic effects from jets and the opening up of new production topologies are reduced, but measurements are presented in this section also for the fully jet inclusive and dynamic jet veto selections.

7.3.1 Charge asymmetry phenomenology

The LO Feynman diagrams for $q\bar{q} \to W^+W^-$ were shown in Figure 2.1. Near threshold the t-channel diagram dominates and there is an enhancement of the differential cross section when each W boson travels in the direction of the incoming quark or antiquark carrying the same charge [253, 254]. Since the off-diagonal elements of the CKM matrix are small, quark mixing is suppressed and so the dominant $q\bar{q}$-induced channels will be those where the quarks are the same flavour. At relatively large momentum fractions, up quarks have the largest PDF, as shown in Figure 1.2. Since up quarks are positively charged, it is therefore expected that the W^+ boson will have a larger longitudinal momentum than the W^- boson, and hence be more forward in the detector. The opposite is true for the contribution from down quarks, but their PDF and therefore resulting cross section is smaller. The difference in the $W^\pm$ boson directions is known as the charge asymmetry,

and can be quantified for on-shell bosons using the observable

$$A_C^W = \frac{\sigma(|y_{W^+}| > |y_{W^-}|) - \sigma(|y_{W^+}| < |y_{W^-}|)}{\sigma(|y_{W^+}| > |y_{W^-}|) + \sigma(|y_{W^+}| < |y_{W^-}|)},$$ (7.1)

where $y_{W^\pm}$ is the rapidity of the $W^\pm$ boson. For protons, simulations predict a positive asymmetry [255], as expected. However, the momenta of the W bosons are not directly accessible experimentally due to the inability to reconstruct the momenta of the two neutrinos, so a charged lepton asymmetry variable is defined instead as

$$A_C^\ell = \frac{\sigma(|y_{\ell^+}| > |y_{\ell^-}|) - \sigma(|y_{\ell^+}| < |y_{\ell^-}|)}{\sigma(|y_{\ell^+}| > |y_{\ell^-}|) + \sigma(|y_{\ell^+}| < |y_{\ell^-}|)},$$ (7.2)

where y_{ℓ^+} and y_{ℓ^-} are respectively the rapidities of the positively and negatively charged leptons from the W boson decays. The non-zero asymmetry is found to persist even for the lepton case [255], although its value is reduced and in fact changes sign with respect to A_C^W. This can be argued as arising from the left-handed nature of W boson interactions, and is shown schematically in Figure 7.12. Since the colliding quark must be left-handed, and the antiquark right-handed, the W boson travelling in the direction of the quark is more likely to have left-handed polarisation [253, 256, 257]. In the case of a $u\bar{u}$ initial state, this means that the W^+ boson is left-handed, whilst the W^- boson is right-handed. The opposite is true in the case of a $d\bar{d}$ initial state. Left-handed W^+ bosons decay primarily such that the neutrino travels in the direction of the W boson, whilst the charged anti-lepton ends up more central. The same is true for the W^- boson, and this acts to effectively cancel the original asymmetry for the $u\bar{u}$ contribution. In contrast, in the $d\bar{d}$ initial state, since the down quark is negatively charged, the same line of reasoning means that the charged leptons tend to follow the directions of their parent W bosons, preserving the asymmetry from this contribution. In combination with the suppression of the $u\bar{u}$ contribution, this can lead to an overall negative asymmetry. The extent to which this happens depends on the kinematic cuts applied on the leptons, with the inclusion of more forward regions expected to improve the sensitivity to the asymmetry [255].

7.3.2 Asymmetry sensitivity studies

A study of the sensitivity to the W boson asymmetry using the full Run-II dataset is presented in this section. The asymmetry is defined according to Eq. (7.2), with the rapidity replaced by the pseudorapidity, which coincides with the rapidity in the massless lepton limit, as discussed in Section 3.2.1. For studies using data, the cross section is substituted for the unfolded number of events, since the two are related via the luminosity, as given by Eq. (3.2). The experimental observable is then

$$A_C^{\ell,\eta} = \frac{N(|\eta_{\ell^+}| > |\eta_{\ell^-}|) - N(|\eta_{\ell^+}| < |\eta_{\ell^-}|)}{N(|\eta_{\ell^+}| > |\eta_{\ell^-}|) + N(|\eta_{\ell^+}| < |\eta_{\ell^-}|)} = \frac{N_+ - N_-}{N_+ + N_-},$$ (7.3)

where η_{ℓ^+} and η_{ℓ^-} are respectively the pseudorapidities of the positively and negatively charged leptons and N is the number of events. For brevity, the notation $N_\pm = N(|\eta_{\ell^\pm}| > |\eta_{\ell^\mp}|)$ is used.
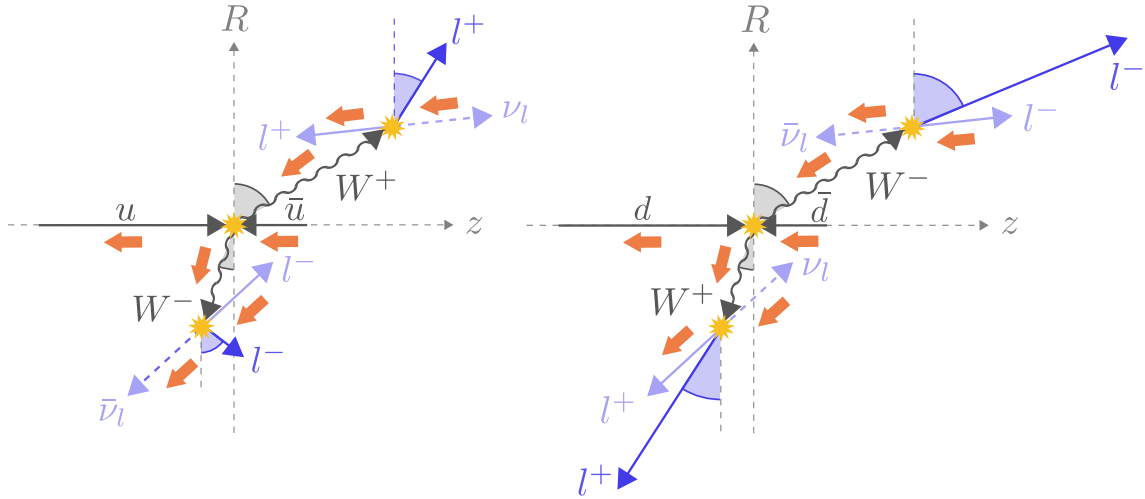
Figure 7.12: An example of how the charged lepton asymmetry may be reversed with respect to the initial W boson asymmetry. The left-hand diagram shows a $u\bar{u}$ initial state, where the W^+ is more forward, whereas the right-hand diagram shows a $d\bar{d}$ initial state, where the W^- is more forward. The red arrows indicate the directions of the helicities of the corresponding particles. The light blue lepton arrows show the corresponding particle momenta in the W boson rest frames. The dark blue charged lepton arrows show the momenta in the laboratory frame, where in the $u\bar{u}$ initial state it is clear that the original asymmetry in $|\eta_W|$ is lost on the level of leptons, whereas in the $d\bar{d}$ initial state it is preserved.

The absolute values of η for the two charged leptons are shown for the jet veto, fully jet inclusive and dynamic jet veto selections on both detector- and unfolded-level in Figures 7.13–7.15, whilst the difference between the absolute η values for the two leptons, $|\eta_{\ell^+}| - |\eta_{\ell^-}|$, is shown in Figure 7.16. The nominal values for the jet veto selection indicate a larger expected asymmetry compared to the fully jet inclusive selection, although this is visually consistent with zero within the uncertainties, whose statistical component is larger for the jet veto phase space. The dynamic jet veto region also displays a relatively large asymmetry, and has smaller uncertainties compared to the jet veto phase space. There is also a slight asymmetry visible for the background contributions, driven largely by Drell-Yan events. This arises from the different coupling strengths of the Z to left- and right-handed particles, as were shown in Table 2.2. Indeed, there is an observed preference for negatively charged leptons to travel in the direction of the incoming quark in the Z/γ^* rest frame at the relatively large centre-of-mass energies that arise in the SR due to the $m_{e\mu} > 85\,\text{GeV}$ selection [258]. Since the incoming quark is more likely an up quark, which has the largest average longitudinal momentum fraction of all partons, the negatively charged lepton is more likely to be forward in the laboratory frame, with the positively charged lepton more central.

The asymmetry is calculated according to Eq. (7.3) for particle-level events obtained using the nominal SHERPA simulation with the NNPDF3.0NLO PDF set. The expected asymmetries for each of the jet selections are shown in the upper rows of Table 7.3. As expected from the discussion in Section 7.3.1, the asymmetry values are all negative, and the fully jet inclusive selection presents the smallest absolute asymmetry. The PDF uncertainties on each nominal prediction are evaluated by calculating the asymmetry for each of the PDF variations, with the distributions for each of the jet selections shown in Figure 7.17. Given the distributions appear non-Gaussian, the confidence
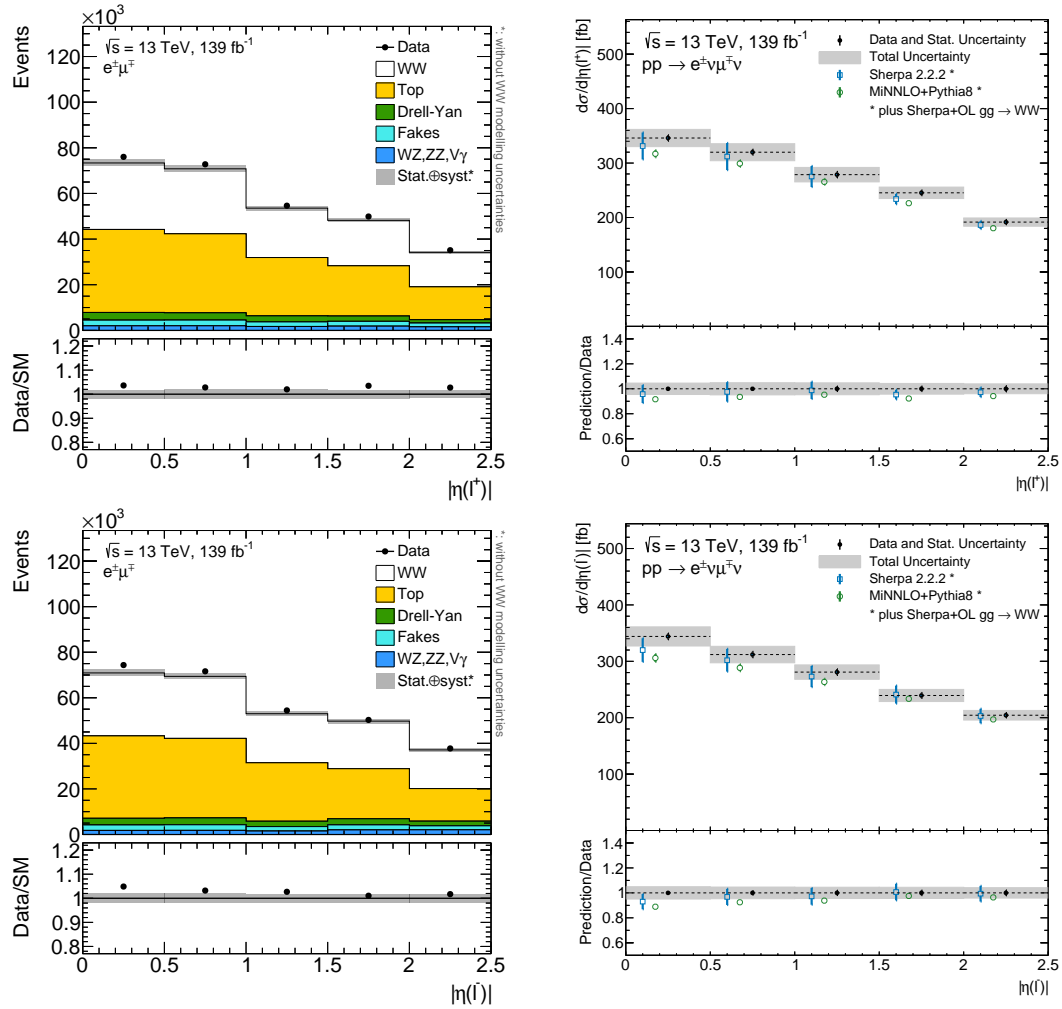
Figure 7.13: Absolute η values of positively (top) and negatively (bottom) charged leptons for the fully inclusive selection. The left column shows the number of observed and expected events on detector-level, whilst the right column shows the unfolded distributions. The unfolded data value is shown with its statistical uncertainty as the black vertical line, and its total uncertainty as a grey band. Also shown are the predictions from the SHERPA and MINNLO generators. Given the lepton kinematic cuts, the maximum possible absolute η value is 2.5, so there are no events in the overflow bins.

Figure 7.14: Absolute η values of positively (top) and negatively (bottom) charged leptons for the jet veto selection. The left column shows the number of observed and expected events on detector-level, whilst the right column shows the unfolded distributions. The unfolded data value is shown with its statistical uncertainty as the black vertical line, and its total uncertainty as a grey band. Also shown are the predictions from the SHERPA and MINNLO generators. Given the lepton kinematic cuts, the maximum possible absolute η value is 2.5, so there are no events in the overflow bins.
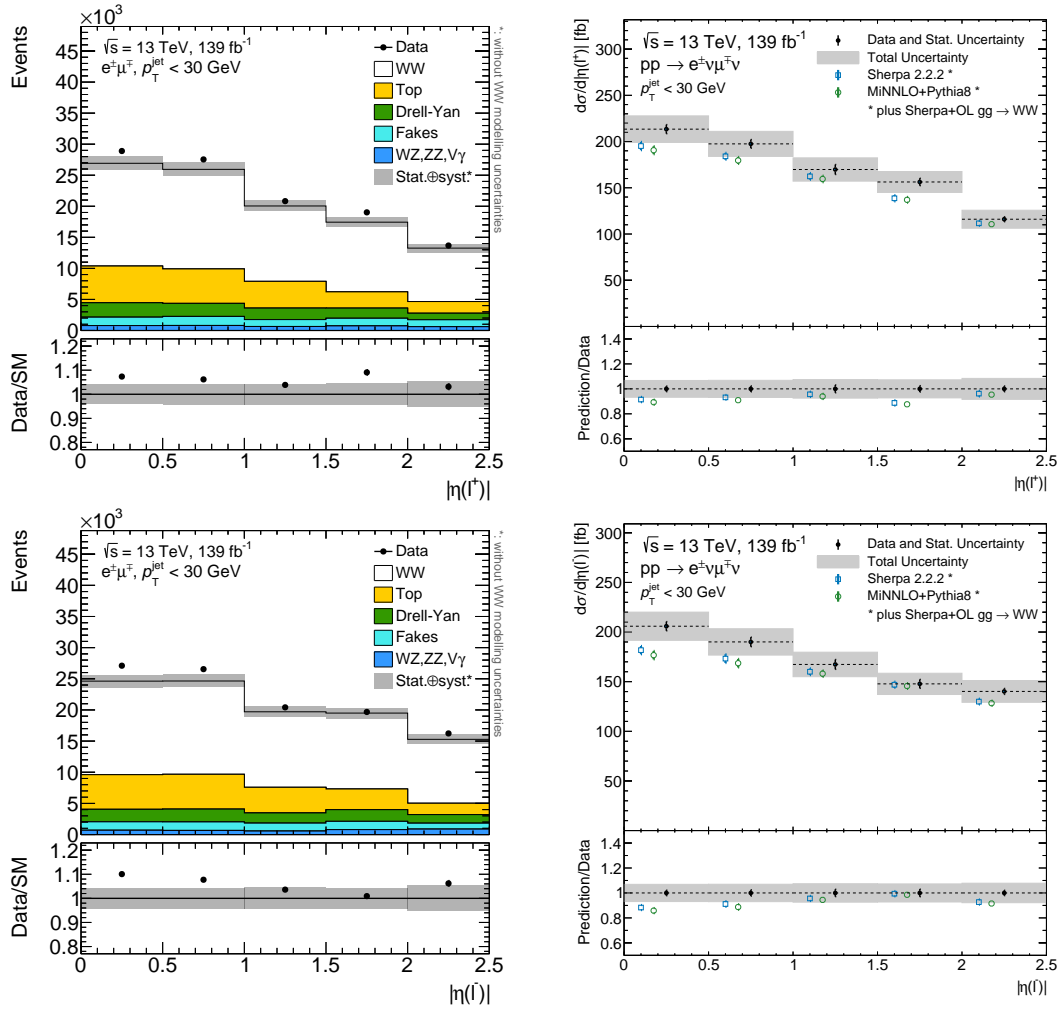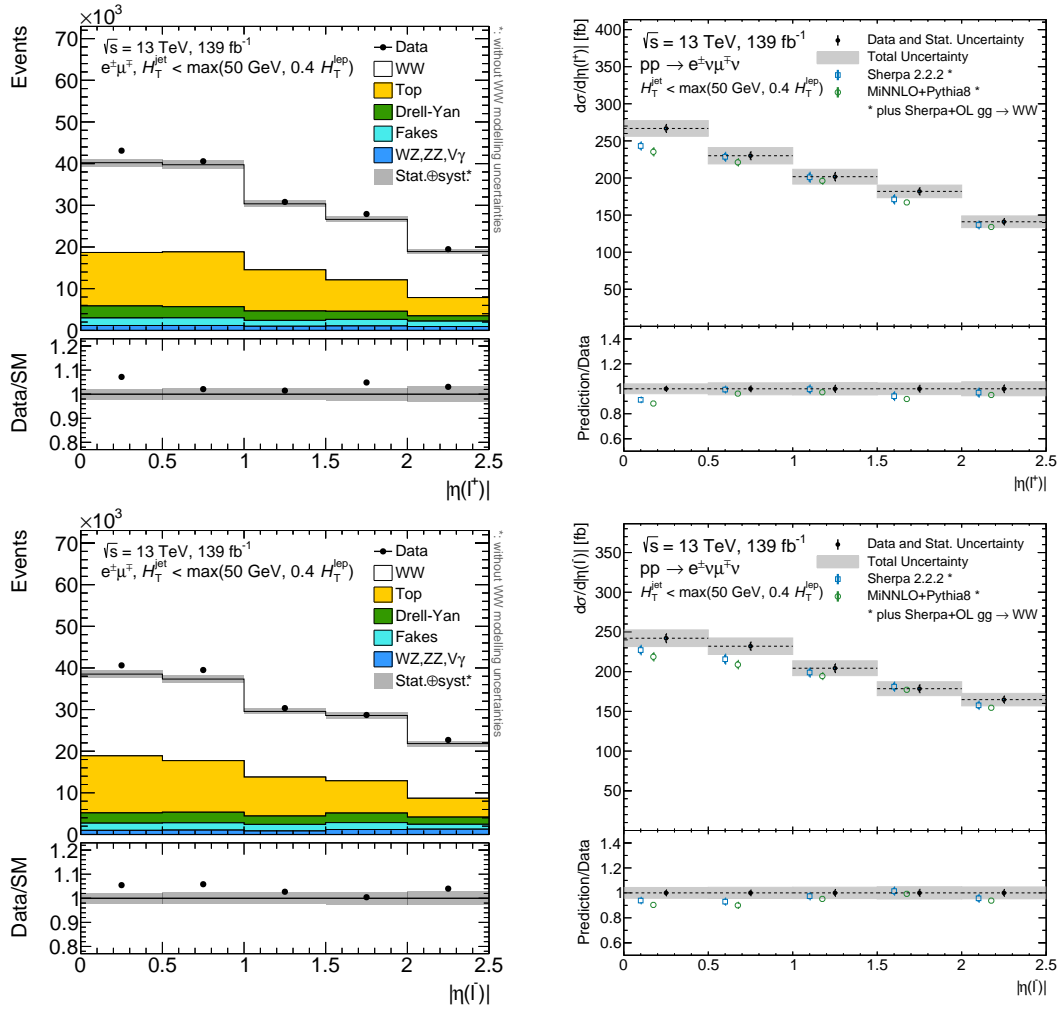
Figure 7.15: Absolute η values of positively (top) and negatively (bottom) charged leptons for the dynamic jet veto selection. The left column shows the number of observed and expected events on detector-level, whilst the right column shows the unfolded distributions. The unfolded data value is shown with its statistical uncertainty as the black vertical line, and its total uncertainty as a grey band. Also shown are the predictions from the Sherpa and MiNNLO generators. Given the lepton kinematic cuts, the maximum possible absolute η value is 2.5, so there are no events in the overflow bins.
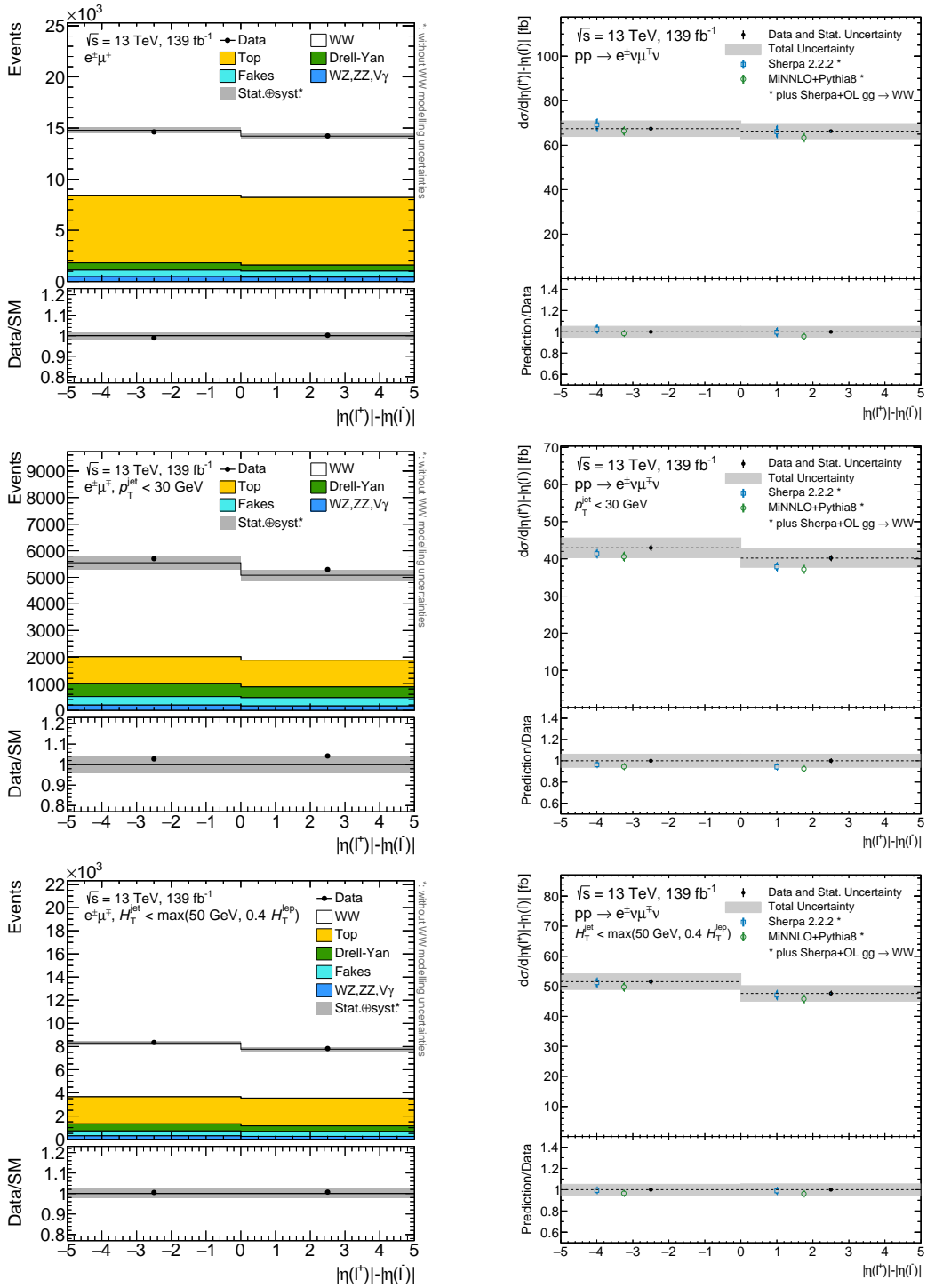
Figure 7.16: Differences in the absolute η values of the charged lepton pair for the fully jet inclusive (top), jet veto (middle), and dynamic jet veto (bottom) selections. The left column shows the number of observed and expected events on detector-level, whilst the right column shows the unfolded distributions. The unfolded data value is shown with its statistical uncertainty as the black vertical line, and its total uncertainty as a grey band. Also shown are the predictions from the SHERPA and MiNNLO generators. Given the lepton kinematic cuts, the maximum possible absolute η difference is 2.5, so there are no events in the overflow bins.

Expected	N_+	N_-	$A_C^{\ell,\eta}$	68% CI	95% CI
Fully jet inclusive	46,701	48,843	-0.022	[-0.025, -0.019]	[-0.032, -0.005]
Jet veto	26,908	29,329	-0.043	[-0.047, -0.039]	[-0.053, -0.028]
Dynamic jet veto	33,440	36,305	-0.041	[-0.045, -0.037]	[-0.050, -0.021]

Data	N_+	N_-	$A_C^{\ell,\eta}$	$\sigma_{\text{stat.}}$	$\sigma_{\text{syst.}}$	$|A_C^{\ell,\eta}|/\sigma_{\text{stat.}}$	$|A_C^{\ell,\eta}|/\sigma_{\text{tot.}}$
Fully jet inclusive	46,088	46,862	-0.008	0.008	0.005	1.0	0.8
Jet veto	27,939	29,864	-0.033	0.012	0.007	2.8	2.5
Dynamic jet veto	33,089	35,818	-0.040	0.011	0.005	3.7	3.3

Table 7.3: Asymmetries calculated on particle-level and in data. The nominal asymmetry value is shown for each jet selection, as well as the 68% and 95% CIs for the particle-level predictions, and the statistical uncertainty, $\sigma_{\text{stat.}}$, and systematic uncertainty, $\sigma_{\text{syst.}}$, for the results in data. Also shown for the results in data are the sensitivities with respect to the statistical uncertainty and the combined statistical and systematic uncertainty, $\sigma_{\text{tot.}}$.

region is expected to be asymmetric about the nominal. The region is obtained by finding the asymmetry values above and below the nominal beyond which a fraction $\alpha/2$ of the variations lie, where $1 - \alpha \approx 0.68$ for the 1σ uncertainty. The 95% uncertainty interval is likewise found by choosing $1 - \alpha \approx 0.95$. The CIs are summarised in Table 7.3. The uncertainty related to QCD scale variations is not included. In the absence of a prescription for calculating this uncertainty with correlations correctly taken into account, a conservative estimate could in principle be made by treating the numerator and denominator as uncorrelated.

The asymmetry is also calculated in data using unfolded events for each of the jet selections. Systematic uncertainties are propagated to the final result assuming they are fully correlated across both bins. Uncorrelating the signal scale variation uncertainties was found to have a negligible impact on the final uncertainty. Different systematic sources are treated as uncorrelated so their effects on the final asymmetry result are simply added in quadrature. Statistical uncertainties may be propagated according to

$$\sigma_{\text{stat.}}^2 \approx \frac{4 \left(N_+^2\, \sigma_{N_-}^2 + N_-^2\, \sigma_{N_+}^2 - 2N_+N_-V_{+-} \right)}{(N_+ + N_-)^4}, \tag{7.4}$$

where $\sigma_{N_\pm}$ is the statistical uncertainty on $N_\pm$, and V_{+-} is the off-diagonal element of the statistical covariance matrix. The statistical covariance matrix is obtained from the unfolding procedure, and there is found to be a correlation coefficient of about -0.03 between each bin for the jet veto selection, and about -0.01 for the fully jet inclusive and dynamic jet veto selections. The small correlation coefficient means the covariance term can safely be neglected. The expression in Eq. (7.4) is obtained using Eq. (5.5), and so assumes non-linear terms are negligible, which is reasonable given the relatively large number of events and small associated statistical uncertainties. An alternative method uses simulated data samples to estimate the statistical uncertainty, also allowing for the Gaussianity of the final result to be tested. 10,000 values for both N_+ and N_- are generated using Gaussian distributions with means corresponding to the nominal values for each number and standard deviations corresponding to their statistical uncertainties. For each simulated dataset the
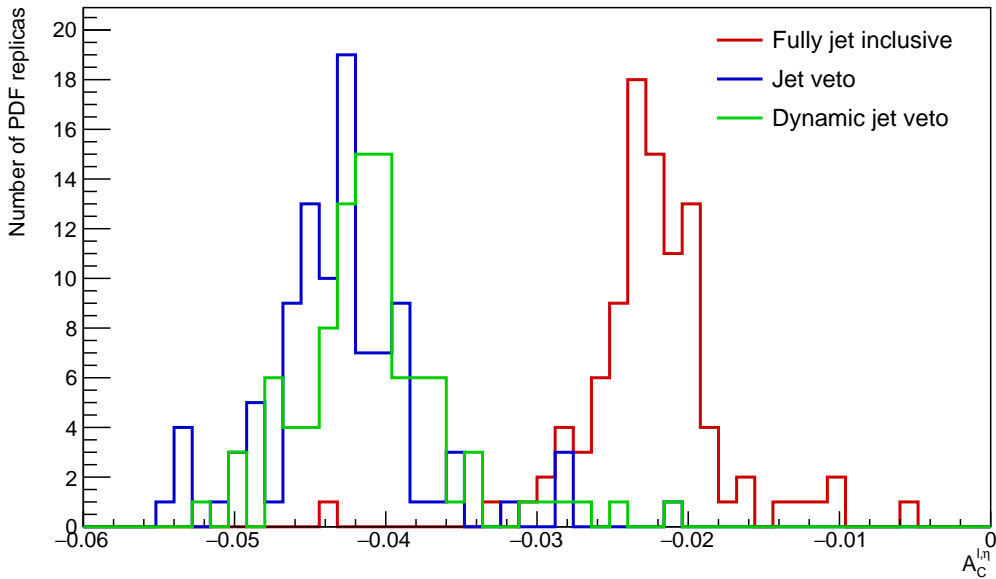
Figure 7.17: Distributions of the asymmetry calculated using 100 PDF variations for the fully jet inclusive (red), jet veto (blue) and dynamic jet veto (green) selections.

value of the asymmetry is calculated. The mean of these values gives $A_C^{\ell,\eta}$, and the standard deviation is used as an estimate of the uncertainty. The correlation induced by the unfolding process is neglected in this method, but the uncertainty is found to nonetheless agree closely with that obtained from Eq. (7.4). The distribution of the difference between the asymmetry value calculated with each simulated data sample and the mean value, normalised by the standard deviation, is compared to a reference Gaussian in Figure 7.18, clearly demonstrating that the statistical uncertainties on $A_C^{\ell,\eta}$ follow a Gaussian distribution.

The unfolded event numbers and the asymmetries along with their uncertainties for each jet selection are shown in the bottom rows of Table 7.3. The nominal value is negative in every case as expected from the discussion in Section 7.3.1. The significances relative to the statistical uncertainty, and the uncertainty combining both statistical and systematic effects, are also shown. For the jet veto and fully inclusive selections, these are found to be smaller than three, defined as the threshold for claiming a non-zero value. This is despite the strong cancellation of the systematic uncertainties, and is due to the relatively large statistical uncertainties. The asymmetry for the jet inclusive selection is significantly smaller than for the jet veto phase space, as expected. The nominal asymmetry value is largest for the dynamic jet veto phase space, and is considered significantly different from zero given the smaller statistical and systematic uncertainties compared to the jet veto phase space. The size of the total uncertainty on the measured results corresponds roughly to that of the 95% PDF uncertainty CI on truth-level, also shown in Table 7.3. This suggests that with the reduction in statistical uncertainties anticipated from the full Run-III dataset, and an optimisation to perhaps include more forward regions, it may be possible to constrain the proton PDFs, in addition to measuring the asymmetries differentially, for example as a function of $||\eta_{l+}| - |\eta_{l-}||$ or $m_{e\mu}$.
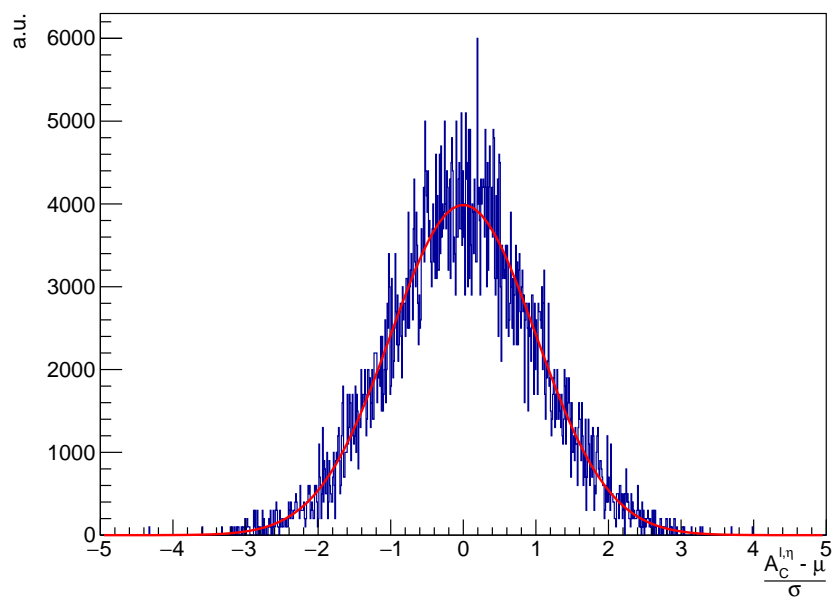
Figure 7.18: Distribution of the asymmetry values calculated using 10,000 simulated data samples. Plotted is the deviation of the asymmetry from the mean of all the samples, μ, normalised by the standard deviation of those samples, σ. For each simulated sample, N_+ and N_- are allowed to vary independently within their statistical uncertainties. The mean and variance of the plotted distribution are almost exactly 0 and 1 respectively, with a normalised Gaussian shown in red for reference.

Summary

In this thesis, measurements of cross sections for the production of pairs of oppositely charged W bosons in pp collisions have been presented. The data used was recorded by the ATLAS detector, corresponding to the full Run-II dataset of $139\,\text{fb}^{-1}$. Cross section measurements were made in a fiducial phase space containing exactly one electron and one muon of opposite charge, as well as different requirements on the number of hadronic jets. The measurements performed in a phase space with at least one jet have recently been published [140]. These represent the first measurements of WW production in which differential cross sections were obtained in a jet inclusive region. After estimates were made for the background contributions, an iterative unfolding method was employed to obtain a selection of differential fiducial cross sections. The integrated fiducial cross section was obtained as

$$\sigma^{\text{fid}}(pp \to W^+W^- \to e^{\pm}\nu_e\mu^{\mp}\nu_{\mu}, \sqrt{s} = 13\,\text{TeV}) = 258 \pm 4\,(\text{stat.}) \pm 25\,(\text{syst.})\,\text{fb},$$

with a total relative uncertainty of about 10%. The agreement with theoretical calculations at fixed order, and those matched to a PS, was found to be very good, providing confirmation of the SM prediction in this phase space. The dominant uncertainty in the measurement comes from jet-related sources due to the requirement of at least one jet. The relatively small total uncertainty in the cross section, despite the large background from top quark events, is possible due to an accurate and precise data-driven method for estimating this contribution. The approach was found to reduce the uncertainty by a factor of about five relative to an estimate based purely on MC simulations.

Results for cross section measurements in a fully jet inclusive fiducial phase space were also presented, with the integrated fiducial cross section result found to be

$$\sigma^{\text{fid}}(pp \to W^+W^- \to e^{\pm}\nu_e\mu^{\mp}\nu_{\mu}, \sqrt{s} = 13\,\text{TeV}) = 668 \pm 5\,(\text{stat.}) \pm 34\,(\text{syst.})\,\text{fb},$$

with an uncertainty of about 5%. The reduction in uncertainty relative to the one jet inclusive result is largely due to the smaller jet-related systematic uncertainties. This result represents the most precise measurement of inclusive WW production in pp collisions performed to date, and does not rely to the same extent as previous measurements on an extrapolation to the full phase space. Additional results were shown for a phase space in which the cut placed to limit jet activity was allowed to vary on an event-by-event basis. This selection, referred to as the dynamic jet veto selection, was used mainly to avoid regions of phase space in which theoretical predictions have large uncertainties from mixed QCD and EW corrections. The results in both jet phase spaces

indicate an overall good agreement with the theoretical predictions. Future improvements to the precision of the measured result are anticipated from updates to the estimate of the background from misidentified or non-prompt leptons, as well the use of a more precise signal prediction and potential reductions in modelling uncertainties related to the top background.

A fit-based measurement technique in which the signal normalisation is extracted using a template distribution was also investigated. It was shown that the measurement uncertainty may be reduced using this method, which however introduces a larger model dependence than the nominal technique.

Finally, a study on the sensitivity to the WW charge asymmetry was presented. The asymmetry is related to the nature of the proton PDFs, and was found to have negative values in accord with theoretical expectations. The significance was found to be larger than three standard deviations for the dynamic jet veto selection. There is optimism that with larger datasets, the measurement uncertainty may become smaller than the PDF uncertainty on the prediction, potentially allowing for the asymmetry measurement to provide constraints on the proton PDFs. Using the existing Run-II dataset, it may also be possible to perform differential measurements in some energy-based variable, such as the dilepton invariant mass.

In conclusion, the measurements presented in this thesis provide some of the highest precision measurements of WW production in pp collisions, in addition to the first jet inclusive differential measurements of this process. All results were found to be in agreement with a variety of the latest and most precise theoretical predictions, providing yet further valuable confirmation of the perturbative QFT paradigm and the SM.

Abbreviations

ALEPH   Apparatus for LEP pHysics at CERN

ALICE   A Large Ion Collider Experiment

AOD   Analysis Object Data

ATLAS   A Toroidal LHC ApparatuS

BR   Branching Ratio

BSM   Beyond the Standard Model

CB   Combined (muon type)

CDF   Collider Detector at Fermilab

CERN   European Organisation for Nuclear Research

CHS   Charged Hadron Subtraction

CI   Confidence Interval

CKM   Cabibbo-Kobayashi-Maskawa

CL   Confidence Level

CMS   Compact Muon Solenoid

CR   Control Region

CSC   Cathode Strip Chambers

CST   Cluster Soft Term

DAOD   Derived AOD

DELPHI   DEtector with Lepton, Photon and Hadron Identification

DGLAP   Dokshitzer-Gribov-Lipatov-Altarelli-Parisi

ECal   EM Calorimeter

EM   Electromagnetic

EMEC   Electromagnetic End-cap

ESD   Event Summary Data

EW   Electroweak

EWSB   Electroweak Symmetry Breaking

FCal   Forward Calorimeter

FSR   Final State Radiation

GSF   Gaussian Sum Filter

HCal   Hadronic Calorimeter

HEC   Hadronic End-cap

HL-LHC   High Luminosity LHC

HLT   High-Level Trigger

HS   Hard Scatter

IBL   Insertable B-Layer

ID   Inner Detector

IO   Inside-Out Combined (muon type)

IP   Interaction Point

IR   Infrared

ISR   Initial State Radiation

JER   Jet Energy Resolution

JES   Jet Energy Scale

JVF   Jet Vertex Fraction

JVT   Jet Vertex Tagger

KLN   Kinoshita-Lee-Nauenberg

LC   Local Cell

LEP   Large Electron-Positron

LH   Likelihood

LHC   Large Hadron Collider

LHCb   LHC beauty

Linac4   Linear Accelerator 4

LL   Leading Logarithmic

LO   Leading Order

LS   Long Shutdown

MC Monte Carlo

MDT Monitored Drift Tubes

ME Matrix Element

MIP Minimum-Ionising Particle

MLE Maximum LH Estimate

MPI Multiple Parton Interactions

MS Muon Spectrometer

N^{3}LO Next-to-NNLO

NLL Next-to-LL

NLO Next-to-LO

NNLL Next-to-NLL

NNLO Next-to-NLO

NP Nuisance Parameter

OPAL Omni-Purpose Apparatus for LEP

PDF Parton Distribution Function

PFO Particle Flow Object

PMT Photomultiplier Tube

PoI Parameter of Interest

PS Proton Synchrotron

PS Parton Shower

PSB Proton Synchrotron Booster

PU Pile-up

PV Primary Vertex

QCD Quantum Chromodynamics

QFT Quantum Field Theory

RDO Raw Data Object

RF Radio Frequency

RoI Region of Interest

RPC Resistive Plate Chambers

SCT Semiconductor Tracker

SM Standard Model

SPS Super Proton Synchrotron

SR Signal Region

TDAQ Trigger and Data Acquisition

TGC Thin Gap Chambers

TRT Transition Radiation Tracker

TST Track Soft Term

UE Underlying Event

VEV Vacuum Expectation Value

VR Validation Region

References

[1] G. Gabrielse et al., *Towards an improved test of the Standard Model's most precise prediction*, Atoms **7** (2019) 45, arXiv: 1904.06174 [quant-ph].

[2] B. Abi et al., *Measurement of the positive muon anomalous magnetic moment to 0.46 ppm*, Phys. Rev. Lett. **126** (2021) 141801, arXiv: 2104.03281 [hep-ex].

[3] LHCb Collaboration, *Test of lepton universality in beauty-quark decays*, Nature Phys. **18** (2022) 277, arXiv: 2103.11769 [hep-ex].

[4] ATLAS Collaboration, *The ATLAS experiment at the CERN Large Hadron Collider*, JINST **3** (2008) S08003.

[5] L. Evans and P. Bryant, *LHC machine*, JINST **3** (2008) S08001, URL: https://doi.org/10.1088/1748-0221/3/08/s08001.

[6] ATLAS Collaboration, *Measurement of W^+W^- production in pp collisions at $\sqrt{s} = 7$ TeV with the ATLAS detector and limits on anomalous WWZ and $WW\gamma$ couplings*, Phys. Rev. D **87** (2013) 112001, arXiv: 1210.2979 [hep-ex].

[7] CMS Collaboration, *Measurement of the W^+W^- cross section in pp collisions at $\sqrt{s} = 7$ TeV and limits on anomalous $WW\gamma$ and WWZ couplings*, Eur. Phys. J. C **73** (2013) 2610, arXiv: 1306.1126 [hep-ex].

[8] ATLAS Collaboration, *Measurement of fiducial and differential W^+W^- production cross-sections at $\sqrt{s} = 13$ TeV with the ATLAS detector*, Eur. Phys. J. C **79** (2019) 884, arXiv: 1905.04242 [hep-ex].

[9] CMS Collaboration, *W^+W^- boson pair production in proton-proton collisions at $\sqrt{s} = 13$ TeV*, Phys. Rev. D **102** (2020) 092001, arXiv: 2009.00119 [hep-ex].

[10] M. Grazzini et al., *NNLO QCD + NLO EW with Matrix+OpenLoops: precise predictions for vector-boson pair production*, JHEP **02** (2020) 087, arXiv: 1912.00068 [hep-ph].

[11] M. Grazzini et al., *W^+W^- production at the LHC: NLO QCD corrections to the loop-induced gluon fusion channel*, Phys. Lett. B **804** (2020) 135399, arXiv: 2002.01877 [hep-ph].

[12] ATLAS Collaboration, *Measurements of $W^+W^- + \geq 1$ jet production cross-sections in pp collisions at $\sqrt{s} = 13$ TeV with the ATLAS detector*, JHEP **06** (2021) 003, arXiv: 2103.10319 [hep-ex].

[13] S. L. Glashow, *Partial symmetries of weak interactions*, Nucl. Phys. **22** (1961) 579.

[14] A. Salam and J. C. Ward, *Electromagnetic and weak interactions*, Phys. Lett. **13** (1964) 168.

[15] S. Weinberg, *A model of leptons*, Phys. Rev. Lett. **19** (1967) 1264.

[16] H. Fritzsch, M. Gell-Mann, and H. Leutwyler, *Advantages of the color octet gluon picture*, Phys. Lett. B **47** (1973) 365.

[17] D. J. Gross and F. Wilczek, *Ultraviolet behavior of non-abelian gauge theories*, Phys. Rev. Lett. **30** (1973) 1343.

[18] H. D. Politzer, *Reliable perturbative results for strong interactions?*, Phys. Rev. Lett. **30** (1973) 1346.

[19] G. S. Guralnik, C. R. Hagen, and T. W. B. Kibble, *Global conservation laws and massless particles*, Phys. Rev. Lett. **13** (1964) 585.

[20] P. W. Higgs, *Broken symmetries and the masses of gauge bosons*, Phys. Rev. Lett. **13** (1964) 508.

[21] F. Englert and R. Brout, *Broken symmetry and the mass of gauge vector mesons*, Phys. Rev. Lett. **13** (1964) 321.

[22] P. A. Zyla et al., *Review of particle physics*, PTEP **2020** (2020) 083C01.

[23] The KATRIN Collaboration, *Direct neutrino-mass measurement with sub-electronvolt sensitivity*, Nature Phys. **18** (2022) 160, arXiv: 2105.08533 [hep-ex].

[24] M. D. Schwartz, *Quantum Field Theory and the Standard Model*, Cambridge University Press, 2013.

[25] J. C. Collins, D. E. Soper, and G. F. Sterman, *Factorization for short distance hadron-hadron scattering*, Nucl. Phys. B **261** (1985) 104.

[26] J. C. Collins, D. E. Soper, and G. F. Sterman, *Factorization of hard processes in QCD*, Adv. Ser. Direct. High Energy Phys. **5** (1988) 1, arXiv: 0409313 [hep-ph].

[27] V. N. Gribov and L. N. Lipatov, *Deep inelastic ep-scattering in perturbation theory*, Sov. J. Nucl. Phys. **15** (1972) 438, URL: http://cds.cern.ch/record/427157.

[28] L. N. Lipatov, *The parton model and perturbation theory*, Sov. J. Nucl. Phys. **20** (1975) 94, URL: http://cds.cern.ch/record/400357.

[29] Yuri L. Dokshitzer, *Calculation of the structure functions for deep inelastic scattering and e^+e^- annihilation by perturbation theory in quantum chromodynamics.*, Sov. Phys. JETP **46** (1977) 641.

[30] G. Altarelli and G. Parisi, *Asymptotic freedom in parton language*, Nucl. Phys. B **126** (1977) 298.

[31] The NNPDF Collaboration, *Parton distributions for the LHC run II*, JHEP **04** (2015) 40, arXiv: 1410.8849 [hep-ph], URL: https://doi.org/10.1007/JHEP04(2015)040.

[32] R. K. Ellis, W. J. Stirling, and B. R. Webber, *QCD and Collider Physics*, Cambridge Monographs on Particle Physics, Nuclear Physics and Cosmology, Cambridge University Press, 1996.

[33] T. Kinoshita, *Mass singularities of Feynman amplitudes*, J. Math. Phys. **3** (1962) 650.

[34] T. D. Lee and M. Nauenberg, *Degenerate systems and mass singularities*, Phys. Rev. **133** (1964) B1549.

[35] A. Buckley et al., *General-purpose event generators for LHC physics*, Phys. Rep. **504** (2011) 145, arXiv: `1101.2599 [hep-ph]`.

[36] A. Schälicke et al., *An event generator for particle production in high-energy collisions*, Prog. Part. Nucl. Phys. **53** (2004) 329, arXiv: `0311270 [hep-ph]`.

[37] B. Andersson et al., *Parton fragmentation and string dynamics*, Phys. Rep. **97** (1983) 31.

[38] D. Amati and G. Veneziano, *Preconfinement as a property of perturbative QCD*, Phys. Lett. B **83** (1979) 87.

[39] R. W. Brown and K. O. Mikaelian, W^+W^- and Z^0Z^0 *pair production in* e^+e^-, *pp, and* $p\bar{p}$ *colliding beams*, Phys. Rev. D **19** (1979) 922.

[40] U. Baur, E. W. N. Glover, and J. J. van der Bij, *Hadronic production of electroweak vector boson pairs at large transverse momentum*, Nucl. Phys. B **318** (1989) 106.

[41] V. Barger et al., *Pair production of* $W^{\pm}$, γ, *and* Z *in association with jets*, Phys. Rev. D **41** (1990) 2782.

[42] N. Cabibbo, *Unitary symmetry and leptonic decays*, Phys. Rev. Lett. **10** (1963) 531.

[43] M. Kobayashi and T. Maskawa, *CP-violation in the renormalizable theory of weak interaction*, Prog. Theor. Phys. **49** (1973) 652.

[44] C. S. Wu et al., *Experimental test of parity conservation in beta decay*, Phys. Rev. **105** (1957) 1413.

[45] R. P. Feynman and M. Gell-Mann, *Theory of the Fermi interaction*, Phys. Rev. **109** (1958) 193.

[46] E. C. G. Sudarshan and R. E. Marshak, *Chirality invariance and the universal fermi interaction*, Phys. Rev. **109** (1958) 1860.

[47] F. J. Hasert et al., *Search for elastic muon neutrino electron scattering*, Phys. Lett. B **46** (1973) 121.

[48] F. J. Hasert et al., *Observation of neutrino-like interactions without muon or electron in the Gargamelle neutrino experiment*, Phys. Lett. B **46** (1973) 138.

[49] UA1 Collaboration, *Experimental observation of isolated large transverse energy electrons with associated missing energy at* $\sqrt{s} = 540\,\mathrm{GeV}$, Phys. Lett. B **122** (1983) 103.

[50] UA2 Collaboration, *Observation of single isolated electrons of high transverse momentum in events with missing transverse energy at the CERN* $p\bar{p}$ *collider*, Phys. Lett. B **122** (1983) 476.

[51] UA1 Collaboration, *Experimental observation of lepton pairs of invariant mass around* $95\,\mathrm{GeV/c^2}$ *at the CERN SPS collider*, Phys. Lett. B **126** (1983) 398.

[52]   UA2 Collaboration, *Evidence for $Z_0 \to e^+e^-$ at the CERN $p\bar{p}$ collider*, Phys. Lett. B **129** (1983) 130.

[53]   B. W. Lee, C. Quigg, and H. B. Thacker, *Weak interactions at very high energies: The role of the Higgs-boson mass*, Phys. Rev. D **16** (1977) 1519.

[54]   ATLAS Collaboration, *Observation of a new particle in the search for the Standard Model Higgs boson with the ATLAS detector at the LHC*, Phys. Lett. B **716** (2012) 1, arXiv: 1207. 7214 [hep-ex], URL: https://www.sciencedirect.com/science/article/pii/ S037026931200857X.

[55]   CMS Collaboration, *Observation of a new boson at a mass of 125 GeV with the CMS experiment at the LHC*, Phys. Lett. B **716** (2012) 30, arXiv: 1207.7235 [hep-ex].

[56]   J. Ohnemus, *Order-α_s calculation of hadronic W^-W^+ production*, Phys. Rev. D **44** (1991) 1403.

[57]   S. Frixione, *A next-to-leading order calculation of the cross section for the production of W^+W^- pairs in hadronic collisions*, Nucl. Phys. B **410** (1993) 280.

[58]   J. Ohnemus, *Hadronic ZZ, W^-W^+, and $W^{\pm}Z$ production with QCD corrections and leptonic decays*, Phys. Rev. D **50** (1994) 1931, arXiv: 9403331 [hep-ph].

[59]   L. Dixon, Z. Kunszt, and A. Signer, *Helicity amplitudes for $\mathcal{O}(\alpha_s)$ production of W^+W^-, $W^{\pm}Z$, ZZ, $W^{\pm}\gamma$, or $Z\gamma$ pairs at hadron colliders*, Nucl. Phys. B **531** (1998) 3.

[60]   L. Dixon, Z. Kunszt, and A. Signer, *Vector boson pair production in hadronic collisions at $\mathcal{O}(\alpha_s)$: lepton correlations and anomalous couplings*, Phys. Rev. D **60** (1999) 114037, arXiv: 9907305 [hep-ph].

[61]   J. M. Campbell and R. K. Ellis, *Update on vector boson pair production at hadron colliders*, Phys. Rev. D **60** (1999) 113006, arXiv: 9905386 [hep-ph].

[62]   B. Biedermann et al., *Next-to-leading-order electroweak corrections to $pp \to W^+W^- \to 4$ leptons at the LHC*, JHEP **06** (2016) 065, arXiv: 1605.03419 [hep-ph].

[63]   E. W. N. Glover and J. J. van der Bij, *Vector boson pair production via gluon fusion*, Phys. Lett. B **219** (1989) 488.

[64]   C. Kao and D. A. Dicus, *Production of W^+W^- from gluon fusion*, Phys. Rev. D **43** (1991) 1555.

[65]   T. Binoth et al., *Gluon-induced WW background to Higgs boson searches at the LHC*, JHEP **2005** (2005) 065, arXiv: 0503094 [hep-ph].

[66]   T. Binoth et al., *Gluon-induced W-boson pair production at the LHC*, JHEP **2006** (2006) 046, arXiv: 0611170 [hep-ph].

[67]   J. M. Campbell, R. K. Ellis, and C. Williams, *Gluon-gluon contributions to W^+W^- production and Higgs interference effects*, JHEP **10** (2011) 005, arXiv: 1107.5569 [hep-ph].

[68]   T. Gehrmann et al., *W^+W^- production at hadron colliders in next to next to leading order QCD*, Phys. Rev. Lett. **113** (2014) 212001, arXiv: 1408.5243 [hep-ph].

[69] M. Grazzini et al., *W^+W^- production at the LHC: fiducial cross sections and distributions in NNLO QCD*, JHEP **08** (2016) 140, arXiv: 1605.02716 [hep-ph].

[70] F. Caola et al., *QCD corrections to W^+W^- production through gluon fusion*, Phys. Lett. B **754** (2016) 275, arXiv: 1511.08617 [hep-ph].

[71] A. Denner and S. Pozzorini, *One loop leading logarithms in electroweak radiative corrections. 1. Results*, Eur. Phys. J. C **18** (2001) 461, arXiv: 0010201 [hep-ph].

[72] A. Bierweiler et al., *Electroweak corrections to W-boson pair production at the LHC*, JHEP **93** (2012) 093, arXiv: 1208.3147 [hep-ph].

[73] J. Baglio, L. D. Ninh, and M. M. Weber, *Massive gauge boson pair production at the LHC: a next-to-leading order story*, Phys. Rev. D **88** (2013) 113005, arXiv: 1307.4331 [hep-ph].

[74] S. Gieseke, T. Kasprzik, and J. H. Kühn, *Vector-boson pair production and electroweak corrections in HERWIG++*, Eur. Phys. J. C **74** (2014) 2988, arXiv: 1401.3964 [hep-ph].

[75] S. Kallweit et al., *NLO QCD+EW predictions for $2\ell2\nu$ diboson signatures at the LHC*, JHEP **11** (2017) 120, arXiv: 1705.00598 [hep-ph].

[76] F. Cascioli, P. Maierhöfer, and S. Pozzorini, *Scattering amplitudes with Open Loops*, Phys. Rev. Lett. **108** (2012) 111601, arXiv: 1111.5206 [hep-ph].

[77] M. Grazzini, S. Kallweit, and M. Wiesemann, *Fully differential NNLO computations with MATRIX*, Eur. Phys. J. C **78** (2017) 537, arXiv: 1711.06631 [hep-ph].

[78] F. Buccioni et al., *OpenLoops 2*, Eur. Phys. J. C **79** (2019) 7306, arXiv: 1907.13071 [hep-ph].

[79] J. M. Campbell, R. K. Ellis, and G. Zanderighi, *Next-to-leading order predictions for WW+jet distributions at the LHC*, JHEP **2007** (2007) 056, arXiv: 0710.1832 [hep-ph].

[80] S. Dittmaier, S. Kallweit, and P. Uwer, *Next-to-leading-order QCD corrections to WW+jet production at hadron colliders*, Phys. Rev. Lett. **100** (2008) 062003, arXiv: 0710.1577 [hep-ph].

[81] S. Dittmaier, S. Kallweit, and P. Uwer, *NLO QCD corrections to $pp/p\bar{p} \to WW$+jet+X including leptonic W-boson decays*, Nucl. Phys. B **826** (2010) 18, arXiv: 0908.4124 [hep-ph].

[82] J. M. Campbell, D. J. Miller, and T. Robens, *Next-to-leading order predictions for WW+jet production*, Phys. Rev. D **92** (2015) 014033, arXiv: 1506.04801 [hep-ph].

[83] W. Li et al., *NLO QCD and electroweak corrections to WW+jet production with leptonic W-boson decays at LHC*, Phys. Rev. D **92** (2015) 033005, arXiv: 1507.07332 [hep-ph].

[84] S. Bräuer et al., *Fixed-order and merged parton-shower predictions for WW and WWj production at the LHC including NLO QCD and EW corrections*, JHEP **2020** (2020) 159, arXiv: 2005.12128 [hep-ph].

[85] T. Melia et al., *Next-to-leading order QCD corrections for W^+W^- pair production in association with two jets at hadron colliders*, Phys. Rev. D **83** (2011) 114043, arXiv: 1104.2327 [hep-ph].

[86] N. Greiner et al., *NLO QCD corrections to the production of W^+W^- plus two jets at the LHC*, Phys. Lett. B **713** (2012) 277, arXiv: 1202.6004 [hep-ph].

[87] F. F. Cordero, P. Hofmann, and H. Ita, *W^+W^-+3-jet production at the Large Hadron Collider in next-to-leading-order QCD*, Phys. Rev. D **95** (2017) 034006, arXiv: 1512.07591 [hep-ph].

[88] E. Bothmann et al., *Event generation with Sherpa 2.2*, SciPost Phys. **7** (2019) 034, arXiv: 1905.09127 [hep-ph].

[89] T. Sjöstrand, S. Mrenna, and P. Skands, *A brief introduction to PYTHIA 8.1*, Comput. Phys. Commun. **178** (2008) 852, arXiv: 0710.3820 [hep-ph].

[90] T. Sjöstrand et al., *An introduction to PYTHIA 8.2*, Comput. Phys. Commun. **191** (2015) 159, arXiv: 1410.3012 [hep-ph].

[91] M. Bähr et al., *Herwig++ physics and manual*, Eur. Phys. J. C **58** (2008) 639, arXiv: 0803.0883 [hep-ph].

[92] J. Bellm et al., *Herwig 7.0/Herwig++ 3.0 release note*, Eur. Phys. J. C **76** (2016) 196, arXiv: 1512.01178 [hep-ph].

[93] S. Frixione and B. R. Webber, *Matching NLO QCD computations and parton shower simulations*, JHEP **06** (2002) 029, arXiv: 0204244 [hep-ph].

[94] P. Nason, *A new method for combining NLO QCD with shower Monte Carlo algorithms*, JHEP **2004** (2004) 040, arXiv: 0409146 [hep-ph].

[95] S. Frixione, P. Nason, and C. Oleari, *Matching NLO QCD computations with parton shower simulations: the POWHEG method*, JHEP **2007** (2007) 070, arXiv: 0709.2092 [hep-ph].

[96] P. Skands, *Introduction to QCD*, 2013, arXiv: 1207.2389 [hep-ph].

[97] S. Catani et al., *QCD matrix elements + parton showers*, JHEP **2001** (2001) 063, arXiv: 0109231 [hep-ph].

[98] L. Lönnblad, *Correcting the colour-dipole cascade model with fixed order matrix elements*, JHEP **2002** (2002) 046, arXiv: 0112284 [hep-ph].

[99] R. Frederix and S. Frixione, *Merging meets matching in MC@NLO*, JHEP **2012** (2012) 061, arXiv: 1209.6215 [hep-ph].

[100] S. Höche et al., *QCD matrix elements + parton showers. The NLO case*, JHEP **2013** (2013) 027, arXiv: 1207.5030 [hep-ph].

[101] K. Hamilton, *MINLO: multi-scale improved NLO*, JHEP **2012** (2012) 155, arXiv: 1206.3572 [hep-ph].

[102] P. F. Monni et al., *MiNNLOPS: a new method to match NNLO QCD to parton showers*, JHEP **2020** (2020) 143, arXiv: 1908.06987 [hep-ph].

[103] S. Myers, *The LEP Collider, from design to approval and commissioning*, CERN, 1991, URL: https://cds.cern.ch/record/226776.

[104] *Design Report Tevatron 1 project*, 1984, URL: https://cds.cern.ch/record/1478620.

[105] ALEPH Collaboration, *ALEPH: Technical Report 1983*, 1983, URL: https://cds.cern.ch/record/300680.

[106] DELPHI Collaboration, *DELPHI: Technical Proposal*, 1983, URL: https://cds.cern.ch/record/300668.

[107] OPAL Collaboration, *The OPAL Detector: Technical Proposal*, 1983, URL: https://cds.cern.ch/record/300669.

[108] L3 Collaboration, *Technical Proposal: L3*, 1983, URL: https://cds.cern.ch/record/297266.

[109] L3 ALEPH DELPHI, OPAL Collaborations, and the LEP Electroweak Working Group, *Electroweak measurements in electron-positron collision at W-boson-pair energies at LEP*, Phys. Rep. **532** (2013) 119, arXiv: 1302.3415 [hep-ex].

[110] S. Jadach et al., *The Monte Carlo event generator YFSWW3 version 1.16 for W-pair production and decay at LEP2/LC energies*, Comput. Phys. Commun. **140** (2001) 432, arXiv: 0103163 [hep-ph].

[111] A. Denner et al., *Electroweak radiative corrections to $e^+e^- \to WW \to 4$ fermions in double-pole approximation — the RacoonWW approach*, Nucl. Phys. B **587** (2000) 67, arXiv: 0006307 [hep-ph].

[112] D. Bardin et al., *GENTLE/4fan v. 2.0 A program for the semi-analytic calculation of predictions for the process $e^+e^- \to 4f$*, Comput. Phys. Commun. **104** (1997) 161.

[113] CDF Collaboration, *The CDF-II Detector: Technical Design Report*, 1996, URL: https://cds.cern.ch/record/1478626.

[114] V. M. Abazov et al., *DØ Run IIB Upgrade Technical Design Report*, 2002.

[115] CDF Collaboration, *Observation of top quark production in $p\bar{p}$ collisions with the Collider Detector at Fermilab*, Phys. Rev. Lett. **74** (1995) 2626, arXiv: 9503002 [hep-ex].

[116] DØ Collaboration, *Observation of the top quark*, Phys. Rev. Lett. **74** (1995) 2632, arXiv: 9503003 [hep-ex].

[117] CDF Collaboration, *Evidence for W^+W^- production in $p\bar{p}$ collisions at $\sqrt{s} = 1.8$ TeV*, Phys. Rev. Lett. **78** (1997) 4536.

[118] DØ Collaboration, *Measurement of the WW production cross section in $p\bar{p}$ collisions at $\sqrt{s} = 1.96$ TeV*, Phys. Rev. Lett. **94** (2005) 151801.

[119] DØ Collaboration, *Measurement of the WW production cross section with dilepton final states in $p\bar{p}$ collisions at $\sqrt{s} = 1.96$ TeV and limits on anomalous trilinear gauge couplings*, Phys. Rev. Lett. **103** (2009) 191801.

[120] CDF Collaboration, *Measurement of the W^+W^- production cross section in $p\bar{p}$ collisions at $\sqrt{s} = 1.96$ TeV using dilepton events*, Phys. Rev. Lett. **94** (2005) 211801, arXiv: 0501050 [hep-ex].

[121] CDF Collaboration, *Measurement of the W^+W^- production cross section and search for anomalous $WW\gamma$ and WWZ Couplings in $p\bar{p}$ collisions at $\sqrt{s} = 1.96$ TeV*, Phys. Rev. Lett. **104** (2010) 201801, arXiv: 0912.4500 [hep-ex].

[122] CDF Collaboration, *Measurement of the production and differential cross sections of W^+W^- bosons in association with jets in pp collisions at $\sqrt{s} = 1.96$ TeV*, Phys. Rev. D **91** (2015) 111101, arXiv: 1505.00801 [hep-ex].

[123] M. L. Mangano et al., *ALPGEN, a generator for hard multiparton processes in hadronic collisions*, JHEP **2003** (2003) 001, arXiv: 0206293 [hep-ph].

[124] CMS Collaboration, *Measurement of W^+W^- production and search for the Higgs boson in pp collisions at $\sqrt{s} = 7$ TeV*, Phys. Lett. B **699** (2011) 25, arXiv: 1102.5429 [hep-ex].

[125] ATLAS Collaboration, *Measurement of the W^+W^- cross section in $\sqrt{s} = 7$ TeV pp collisions with ATLAS*, Phys. Rev. Lett. **107** (2011) 041802, arXiv: 1104.5225 [hep-ex].

[126] ATLAS Collaboration, *Measurement of the WW cross section in $\sqrt{s} = 7$ TeV pp collisions with the ATLAS detector and limits on anomalous gauge couplings*, Phys. Lett. B **712** (2012) 289, arXiv: 1203.6232 [hep-ex].

[127] CMS Collaboration, *Measurement of the W^+W^- and ZZ production cross sections in pp collisions at $\sqrt{s} = 8$ TeV*, Phys. Lett. B **721** (2013) 190, arXiv: 1301.4698 [hep-ex].

[128] ATLAS Collaboration, *Measurement of total and differential W^+W^- production cross sections in proton-proton collisions at $\sqrt{s} = 8$ TeV with the ATLAS detector and limits on anomalous triple-gauge-boson couplings*, JHEP **2016** (2016) 029, arXiv: 1603.01702 [hep-ex].

[129] CMS Collaboration, *Measurement of the W^+W^- cross section in pp collisions at $\sqrt{s} = 8$ TeV and limits on anomalous gauge couplings*, Eur. Phys. J. C **76** (2016) 4219, arXiv: 1507.03268 [hep-ex].

[130] ATLAS Collaboration, *Measurement of W^+W^- production in association with one jet in proton–proton collisions at $\sqrt{s} = 8$ TeV with the ATLAS detector*, Phys. Lett. B **763** (2016) 114, arXiv: 1608.03086 [hep-ex].

[131] ATLAS Collaboration, *Measurement of the W^+W^- production cross section in pp collisions at a centre-of-mass energy of $\sqrt{s} = 13$ TeV with the ATLAS experiment*, Phys. Lett. B **773** (2017) 354, arXiv: 1702.04519 [hep-ex].

[132] L. Arnaudon et al., *Linac4 Technical Design Report*, 2006, URL: https://cds.cern.ch/record/1004186.

[133] O. S. Brüning et al., *LHC Design Report*, CERN Yellow Reports: Monographs, CERN, 2004, URL: http://cds.cern.ch/record/782076.

[134] ALICE Collaboration, *The ALICE experiment at the CERN LHC*, JINST **3** (2008) S08002.

[135] CMS Collaboration, *The CMS experiment at the CERN LHC*, JINST **3** (2008) S08004.

[136] LHCb Collaboration, *The LHCb Detector at the LHC*, JINST **3** (2008) S08005.

[137]   E. Mobs, *The CERN accelerator complex - 2019.*, 2019, URL: http://cds.cern.ch/record/2684277.

[138]   W. Herr and B. Muratori, *Concept of luminosity*, 2006, URL: https://cds.cern.ch/record/941318.

[139]   S. van der Meer, *Calibration of the effective beam height in the ISR*, 1968, URL: https://cds.cern.ch/record/296752.

[140]   ATLAS Collaboration, *ATLAS Luminosity Public Results Run 2*, URL: https://twiki.cern.ch/twiki/bin/view/AtlasPublic/LuminosityPublicResultsRun2.

[141]   J. Pequenao, *Computer generated image of the whole ATLAS detector*, 2008, URL: https://cds.cern.ch/record/1095924.

[142]   J. Gallicchio and Y. T. Chien, *Quit using pseudorapidity, transverse energy, and massless constituents*, 2018, arXiv: 1802.05356 [hep-ph].

[143]   Images compiled from code made available under CC BY-SA 4.0 by Izaak Neutelings. Source code from: https://github.com/IzaakWN/CodeSnippets/blob/master/LaTeX/TikZ/axis3D_CMS.tex and https://github.com/IzaakWN/CodeSnippets/blob/master/LaTeX/TikZ/axis2D_pseudorapidity.tex. (Accessed 2021/12/28).

[144]   ATLAS Collaboration, *ATLAS Inner Detector: Technical Design Report, 1*, 1997, URL: https://cds.cern.ch/record/331063.

[145]   ATLAS Collaboration, *ATLAS Inner Detector: Technical Design Report, 2*, 1997, URL: https://cds.cern.ch/record/331064.

[146]   ATLAS Collaboration, *Experiment briefing: keeping the ATLAS inner detector in perfect alignment*, 2020, URL: https://cds.cern.ch/record/2723878.

[147]   G. Aad et al., *ATLAS pixel detector electronics and sensors*, JINST 3 (2008) P07007.

[148]   N. Wermes and G. Hallewel, *ATLAS Pixel Detector: Technical Design Report*, 1998, URL: http://cds.cern.ch/record/381263.

[149]   M. Capeans et al., *ATLAS Insertable B-layer Technical Design Report*, 2010, URL: https://cds.cern.ch/record/1291633.

[150]   A. Ahmad et al., *The silicon microstrip sensors of the ATLAS semiconductor tracker*, Nucl. Instrum. Meth. A 578 (2007) 98.

[151]   ATLAS TRT Collaboration, *The ATLAS transition radiation tracker (TRT) proportional drift tube: design and performance*, JINST 3 (2008) P02013.

[152]   ATLAS Collaboration, *Performance of the ATLAS transition radiation tracker in Run 1 of the LHC: tracker properties*, JINST 12 (2017) P05002, arXiv: 1702.06473 [hep-ex].

[153]   ATLAS Collaboration, *ATLAS Calorimeter Performance: Technical Design Report*, 1996, URL: https://cds.cern.ch/record/331059.

[154] J. Pequenao, *Computer generated image of the ATLAS calorimeter*, 2008, URL: https://cds.cern.ch/record/1095927.

[155] R. Wigmans, *Calorimetry*, Oxford University Press, 2000.

[156] ATLAS Collaboration, *ATLAS Liquid-Argon Calorimeter: Technical Design Report*, 1996, URL: https://cds.cern.ch/record/331061.

[157] C. W. Fabjan and F. Gianotti, *Calorimetry for particle physics*, Rev. Mod. Phys. **75** (2003) 1243.

[158] ATLAS Collaboration, *ATLAS Tile Calorimeter: Technical Design Report*, 1996, URL: https://cds.cern.ch/record/331062.

[159] ATLAS Collaboration, *ATLAS Muon Spectrometer: Technical Design Report*, 1997, URL: https://cds.cern.ch/record/331068.

[160] J. Pequenao, *Computer generated image of the ATLAS Muons subsystem*, 2008, URL: https://cds.cern.ch/record/1095929.

[161] ATLAS Collaboration, *Performance of the ATLAS trigger system in 2015*, Eur. Phys. J. C **77** (2016) 317, arXiv: 1611.09661 [hep-ex].

[162] ATLAS Collaboration, *The ATLAS simulation infrastructure*, Eur. Phys. J. C **70** (2010) 823, arXiv: 1005.4568 [physics.ins-det].

[163] ATLAS Collaboration, *ATLAS Computing: Technical Design Report*, 2005, URL: https://cds.cern.ch/record/837738.

[164] S. Agostinelli et al., *GEANT4 – a simulation toolkikt*, Nucl. Instrum. Meth. A **506** (2002) 250.

[165] M. Dobbs and J. B. Hansen, *The HepMC C++ Monte Carlo event record for high energy physics*, Comput. Phys. Commun. **134** (2001) 41.

[166] ATLAS Collaboration, *Performance of the ATLAS silicon pattern recognition algorithm in data and simulation at* $\sqrt{s} = 7\,\text{TeV}$, CERN, 2010, URL: http://cds.cern.ch/record/1281363.

[167] T. G. Cornelissen et al., *Concepts, design and implementation of the ATLAS new tracking (NEWT)*, CERN, 2007, URL: https://cds.cern.ch/record/1020106.

[168] R. Frühwirth, *Application of Kalman filtering to track and vertex fitting*, Nucl. Instrum. Meth. A **262** (1987) 444.

[169] T. G. Cornelissen et al., *The global* χ^2 *track fitter in ATLAS*, J. Phys. Conf. Ser. **119** (2008) 032013.

[170] ATLAS Collaboration, *ATLAS Detector and Physics Performance: Technical Design Report, 1*, 1999, URL: https://cds.cern.ch/record/391176.

[171] R. L. Gluckstern, *Uncertainties in track momentum and direction, due to multiple scattering and measurement errors*, Nucl. Instrum. Meth. **24** (1963) 381.

[172] ATLAS Collaboration, *Muon reconstruction performance of the ATLAS detector in proton–proton collision data at $\sqrt{s}$=13 TeV.*, Eur. Phys. J. C **76** (2016) 292, arXiv: 1603.05598 [hep-ex].

[173] ATLAS Collaboration, *Performance of primary vertex reconstruction in proton-proton collisions at $\sqrt{s}$ =7 TeV in the ATLAS experiment*, CERN, 2010, URL: http://cds.cern.ch/record/1281344.

[174] ATLAS Collaboration, *Topological cell clustering in the ATLAS calorimeters and its performance in LHC Run 1.*, Eur. Phys. J. C **77** (2016) 490, arXiv: 1603.02934 [hep-ex].

[175] W. Lampl et al., *Calorimeter clustering algorithms: description and performance*, CERN, 2008, URL: https://cds.cern.ch/record/1099735.

[176] ATLAS Collaboration, *Electron reconstruction and identification in the ATLAS experiment using the 2015 and 2016 LHC proton-proton collision data at $\sqrt{s} = $ 13 TeV*, Eur. Phys. J. C **79** (2019) 639, arXiv: 1902.04655 [hep-ex].

[177] The ATLAS Collaboration, *Electron and photon performance measurements with the ATLAS detector using the 2015-2017 LHC proton-proton collision data*, JINST **14** (2019) P12006, arXiv: 1908.00005 [hep-ex].

[178] ATLAS Collaboration, *Improved electron reconstruction in ATLAS using the Gaussian Sum Filter-based model for bremsstrahlung*, CERN, 2012, URL: https://cds.cern.ch/record/1449796.

[179] ATLAS Collaboration, *Electron and photon energy calibration with the ATLAS detector using 2015-2016 LHC proton-proton collision data*, JINST **14** (2018) P03017, arXiv: 1812.03848 [hep-ex].

[180] ATLAS Collaboration, *Performance of electron and photon triggers in ATLAS during LHC Run 2*, Eur. Phys. J. C **80** (2019) 47, arXiv: 1909.00761 [hep-ex].

[181] ATLAS Collaboration, *Muon reconstruction and identification efficiency in ATLAS using the full Run 2 pp collision data set at $\sqrt{s} = $ 13 TeV*, Eur. Phys. J., C **81** (2020) 578, arXiv: 2012.00578 [hep-ex].

[182] ATLAS Collaboration, *Performance of the ATLAS muon triggers in Run 2*, JINST **15** (2020) P09015, arXiv: 2004.13447 [physics.ins-det].

[183] ATLAS Collaboration, *Jet reconstruction and performance using particle flow with the ATLAS Detector*, Eur. Phys. J. C **77** (2017) 466, arXiv: 1703.10485 [hep-ex].

[184] M. Cacciari, G. P. Salam, and G. Soyez, *The anti-k_{T} jet clustering algorithm*, JHEP **2008** (2008) 063, arXiv: 0802.1189 [hep-ph].

[185] ATLAS Collaboration, *Performance of pile-up mitigation techniques for jets in pp collisions at $\sqrt{s} = $ 8 TeV using the ATLAS detector*, Eur. Phys. J. C **76** (2015) 581, arXiv: 1510.03823 [hep-ex].

[186] ATLAS Collaboration, *Jet energy scale and resolution measured in proton–proton collisions at $\sqrt{s} = 13$ TeV with the ATLAS detector*, Eur. Phys. J. C **81** (2020) 689, arXiv: 2007.02645 [hep-ex].

[187] ATLAS Collaboration, *Optimisation and performance studies of the ATLAS b-tagging algorithms for the 2017-18 LHC run*, CERN, 2017, URL: https://cds.cern.ch/record/2273281.

[188] ATLAS Collaboration, *ATLAS b-jet identification performance and efficiency measurement with $t\bar{t}$ events in pp collisions at $\sqrt{s} = 13$ TeV*, Eur. Phys. J. C **79** (2019) 970, arXiv: 1907.05120 [hep-ex].

[189] ATLAS Collaboration, *Performance of missing transverse momentum reconstruction with the ATLAS detector using proton-proton collisions at $\sqrt{s} = 13$ TeV*, Eur. Phys. J. C **78** (2018) 903, arXiv: 1802.08168 [hep-ex].

[190] G. Cowan, *Statistical Data Analysis*, Clarendon Press, 1998.

[191] R. Barlow et al., *Data Analysis in High Energy Physics*, ed. by O. Behnke et al., John Wiley and Sons, Ltd, 2013.

[192] D. Casadei, *Statistical methods used in ATLAS for exclusion and discovery*, 2011, arXiv: 1108.2288 [physics.data-an].

[193] R. Aggarwal and A. Caldwell, *Error bars for distributions of numbers of events*, Eur. Phys. J. Plus **127** (2012) 12024, arXiv: 1112.2593 [physics.data-an].

[194] G. Cowan, *Statistical tests with weighted Monte Carlo events*, (Accessed 2022/01/24), 2012, URL: https://www.pp.rhul.ac.uk/~cowan/stat/notes/weights.pdf.

[195] G. Cowan, *Error analysis with weighted events*, (Accessed 2022/01/24), 2014, URL: https://www.pp.rhul.ac.uk/~cowan/stat/notes/errors_with_weights.pdf.

[196] R. Wanke, "How to Deal with Systematic Uncertainties", *Data Analysis in High Energy Physics*, John Wiley and Sons, Ltd, 2013, chap. 8 263.

[197] R. Barlow and C. Beeston, *Fitting using finite Monte Carlo samples*, Comput. Phys. Commun. **77** (1993) 219.

[198] K. Cranmer et al., *HistFactory: A tool for creating statistical models for use with RooFit and RooStats*, 2012, URL: https://cds.cern.ch/record/1456844.

[199] O. Behnke and L. Moneta, "Parameter Estimation", *Data Analysis in High Energy Physics*, John Wiley and Sons, Ltd, 2013, chap. 2 27.

[200] S. S. Wilks, *The large-sample distribution of the likelihood ratio for testing composite hypotheses*, Ann. Math. Stat. **9** (1938) 60.

[201] G. Cowan, *A survey of unfolding methods for particle physics*, Conf. Proc. C **0203181** (2002) 248.

[202] G. D'Agostini, *A multidimensional unfolding method based on Bayes' theorem*, Nucl. Instrum. Meth. A **362** (1995) 487.

[203] G. D'Agostini, *Improved iterative Bayesian unfolding*, 2010, arXiv: 1010.0632 [physics.data-an].

[204] ATLAS Collaboration, *Measurements of gluon–gluon fusion and vector-boson fusion Higgs boson production cross-sections in the $H \rightarrow WW^* \rightarrow e\nu\mu\nu$ decay channel in pp collisions at $\sqrt{s} = 13$ TeV with the ATLAS detector*, Phys. Lett. B **789** (2019) 508, arXiv: 1808.09054 [hep-ex].

[205] ATLAS Collaboration, *ATLAS data quality operations and performance for 2015–2018 data-taking*, JINST **15** (2020) P04003, arXiv: 1911.04632 [physics.int-det].

[206] S. Alioli et al., *A general framework for implementing NLO calculations in shower Monte Carlo programs: the POWHEG BOX*, JHEP **2010** (2010) 043, arXiv: 1002.2581 [hep-ph].

[207] S. Frixione, G. Ridolfi, and P. Nason, *A positive-weight next-to-leading-order Monte Carlo for heavy flavour hadroproduction*, JHEP **2007** (2007) 126, arXiv: 0707.3088 [hep-ph].

[208] E. Re, *Single-top Wt-channel production matched with parton showers using the POWHEG method*, Eur. Phys. J. C **71** (2011), arXiv: 1009.2450 [hep-ph].

[209] R. D. Ball et al., *Parton distributions with LHC data*, Nucl. Phys. B **867** (2013) 244, arXiv: 1207.1303 [hep-ph].

[210] ATLAS Collaboration, *ATLAS Pythia 8 tunes to 7 TeV data*, CERN, 2014, URL: https://cds.cern.ch/record/1966419.

[211] S. Frixione et al., *Single-top hadroproduction in association with a W boson*, JHEP **2008** (2008) 029, arXiv: 0805.3067 [hep-ph].

[212] ATLAS Collaboration, *Studies on top-quark Monte Carlo modelling for Top2016*, CERN, 2016, URL: https://cds.cern.ch/record/2216168.

[213] M. Beneke et al., *Hadronic top-quark pair production with NNLL threshold resummation*, Nucl. Phys. B **855** (2012) 695, arXiv: 1109.1536 [hep-ph].

[214] M. Cacciari et al., *Top-pair production at hadron colliders with next-to-next-to-leading logarithmic soft-gluon resummation*, Phys. Lett. B **710** (2012) 612, arXiv: 1111.5869 [hep-ph].

[215] P. Bärnreuther, M. Czakon, and A. Mitov, *Percent-level-precision physics at the Tevatron: next-to-next-to-leading order QCD corrections to $q\bar{q} \rightarrow t\bar{t} + X$*, Phys. Rev. Lett. **109** (2012) 132001, arXiv: 1204.5201 [hep-ph].

[216] M. Czakon and A. Mitov, *NNLO corrections to top-pair production at hadron colliders: the all-fermionic scattering channels*, JHEP **2012** (2012) 054, arXiv: 1207.0236 [hep-ph].

[217] M. Czakon and A. Mitov, *NNLO corrections to top pair production at hadron colliders: the quark-gluon reaction*, JHEP **2013** (2013) 080, arXiv: 1210.6832 [hep-ph].

[218] M. Czakon, P. Fiedler, and A. Mitov, *Total top-quark pair-production cross section at hadron colliders through $\mathcal{O}(\alpha_s^4)$*, Phys. Rev. Lett. **110** (2013) 252004, arXiv: 1303.6254 [hep-ph].

[219] M. Czakon and A. Mitov, *Top++: A program for the calculation of the top-pair cross-section at hadron colliders*, Comput. Phys. Commun. **185** (2014) 2930, arXiv: 1112.5675 [hep-ph].

[220] N. Kidonakis, *Two-loop soft anomalous dimensions for single top quark associated production with a W^- or H^-*, Phys. Rev. D **82** (2010) 054018, arXiv: 1005.4451 [hep-ph].

[221] T. Gleisberg and S. Höche, *Comix, a new matrix element generator*, JHEP **2008** (2008) 039, arXiv: 0808.3674 [hep-ph].

[222] C. Anastasiou et al., *High-precision QCD at hadron colliders: Electroweak gauge boson rapidity distributions at next-to-next-to leading order*, Phys. Rev. D **69** (2004) 094008, arXiv: 0312266 [hep-ph].

[223] D. J. Lange, *The EvtGen particle decay simulation package*, Nucl. Instrum. Meth. A **462** (2001) 152.

[224] ATLAS Collaboration, *The Pythia 8 A3 tune description of ATLAS minimum bias and inelastic measurements incorporating the Donnachie-Landshoff diffractive model*, CERN, 2016, URL: https://cds.cern.ch/record/2206965.

[225] ATLAS Collaboration, *Measurement of the $t\bar{t}$ production cross-section and lepton differential distributions in $e\mu$ dilepton events from pp collisions at $\sqrt{s} = 13$ TeV with the ATLAS detector*, Eur. Phys. J. C **80** (2020) 7907, arXiv: 1910.08819 [hep-ex].

[226] J. Alison, "The road to discovery: Detector alignment, electron identification, particle misidentification, WW physics, and the discovery of the Higgs boson", CERN Thesis, 2015, URL: https://cds.cern.ch/record/1536507.

[227] ATLAS Collaboration, *Observation of electroweak production of a same-sign W boson pair in association with two jets in pp collisions at $\sqrt{s} = 13$ TeV with the ATLAS Detector*, Phys. Rev. Lett. **123** (2019) 161801, arXiv: 1906.03203 [hep-ex].

[228] ATLAS Collaboration, *Measurement of $W^\pm Z$ production cross sections and gauge boson polarisation in pp collisions at $\sqrt{s} = 13$ TeV with the ATLAS detector*, Eur. Phys. J. C **79** (2019) 7027, arXiv: 1902.05759 [hep-ex].

[229] ATLAS Collaboration, *Luminosity determination in pp collisions at $\sqrt{s} = 13$ TeV using the ATLAS detector at the LHC*, CERN, 2019, URL: https://cds.cern.ch/record/2677054.

[230] G. Avoni et al., *The new LUCID-2 detector for luminosity measurement and monitoring in ATLAS*, JINST **13** (2018) P07017.

[231] ATLAS Collaboration, *Measurements of b-jet tagging efficiency with the ATLAS detector using $t\bar{t}$ events at $\sqrt{s} = 13$ TeV*, JHEP **2018** (2018) 089, arXiv: 1805.01845 [hep-ex].

[232] ATLAS Collaboration, *Calibration of light-flavour b-jet mistagging rates using ATLAS proton-proton collision data at $\sqrt{s} = 13$ TeV*, CERN, 2018, URL: https://cds.cern.ch/record/2314418.

[233] P. Nason and G. Zanderighi, *W^+W^-, WZ and ZZ production in the POWHEG-BOX-V2*, Eur. Phys. J. C **74** (2014) 2702, arXiv: 1311.1365 [hep-ph].

[234] ATLAS Collaboration, *Measurement of the Z/γ^* boson transverse momentum distribution in pp collisions at $\sqrt{s} = 7$ TeV with the ATLAS detector*, JHEP **2014** (2014) 145, arXiv: 1406.3660 [hep-ex].

[235] H. L. Lai et al., *New parton distributions for collider physics*, Phys. Rev. D **82** (2010) 074024, arXiv: 1007.2241 [hep-ph].

[236] J. Pumplin, *New generation of parton distributions with uncertainties from global QCD analysis*, JHEP **2002** (2002) 012, arXiv: 0201195 [hep-ph].

[237] D. Lombardi, M. Wiesemann, and G. Zanderighi, *W^+W^- production at NNLO+PS with MINNLOPS*, JHEP **2021** (2021) 230, arXiv: 2103.12077 [hep-ph].

[238] J. Alwall et al., *The automated computation of tree-level and next-to-leading order differential cross sections, and their matching to parton shower simulations*, JHEP **2014** (2014) 079, arXiv: 1405.0301 [hep-ph].

[239] L. A. Harland-Lang et al., *Parton distributions in the LHC era: MMHT 2014 PDFs*, Eur. Phys. J. C **75** (2015) 3397, arXiv: 1412.3989 [hep-ph].

[240] ATLAS Collaboration, *Measurement of the $t\bar{t}$ production cross-section using $e\mu$ events with b-tagged jets in pp collisions at $\sqrt{s} = 13$ TeV with the ATLAS detector*, Phys. Lett. B **772** (2017) 879.

[241] ATLAS Collaboration, *Measurements of inclusive and differential fiducial cross-sections of $t\bar{t}$ production with additional heavy-flavour jets in proton-proton collisions at $\sqrt{s} = 13$ TeV with the ATLAS detector*, JHEP **2019** (2019) 046, arXiv: 1811.12113 [hep-ex].

[242] J. K. Anders and M. D'Onofrio, *V+jets theoretical uncertainties estimation via a parameterisation method*, CERN, 2016, URL: https://cds.cern.ch/record/2125718.

[243] F. Cascioli et al., *ZZ production at hadron colliders in NNLO QCD*, Phys. Lett. B **735** (2014) 311, arXiv: 1405.2219 [hep-ph].

[244] M. Grazzini, S. Kallweit, and D. Rathlev, *ZZ production at the LHC: fiducial cross sections and distributions in NNLO QCD*, Phys. Lett. B **750** (2015) 407, arXiv: 1507.06257 [hep-ph].

[245] M. Grazzini et al., *$W^\pm Z$ production at hadron colliders in NNLO QCD*, Phys. Lett. B **761** (2016) 179, arXiv: 1604.08576 [hep-ph].

[246] M. Grazzini et al., *$W^\pm Z$ production at the LHC: fiducial cross sections and distributions in NNLO QCD*, JHEP **2017** (2017) 139, arXiv: 1703.09065 [hep-ph].

[247] *Multi-boson simulation for 13 TeV ATLAS analyses*, CERN, 2016, URL: https://cds.cern.ch/record/2119986.

[248] M. Grazzini, S. Kallweit, and D. Rathlev, *$W\gamma$ and $Z\gamma$ production at the LHC in NNLO QCD*, JHEP **85** (2015) 085, arXiv: 1504.01330 [hep-ph].

[249] A. J. Barr, *Measuring slepton spin at the LHC*, JHEP **2006** (2006) 042, arXiv: 0511115 [hep-ph].

[250] T. Ježo et al., *An NLO+PS generator for $t\bar{t}$ and Wt production and decay including non-resonant and interference effects*, Eur. Phys. J. C **76** (2016), arXiv: 1607.04538 [hep-ph].

[251] K. Hamilton et al., *Merging WW and WW+jet with MiNLO*, JHEP **2016** (2016) 057, arXiv: 1606.07062 [hep-ph].

[252] G. Cowan et al., *Asymptotic formulae for likelihood-based tests of new physics*, Eur. Phys. J. C **71** (2011) 1554, arXiv: 1007.1727 [physics.data-an].

[253] K. Hagiwara et al., *Probing the weak boson sector in $e^+e^- \rightarrow W^+W^-$*, Nucl. Phys. B **282** (1987) 253.

[254] S. Dittmaier, *Theoretical aspects of W pair production in e^+e^- collisions*, 1997, arXiv: 9610529 [hep-ph].

[255] E. Re, M. Wiesemann, and G. Zanderighi, *NNLOPS accurate predictions for W^+W^- production*, JHEP **2018** (2018) 121, arXiv: 1805.09857 [hep-ph].

[256] Z. Bern et al., *Left-handed W bosons at the LHC*, Phys. Rev. D **84** (2011) 034008, arXiv: 1103.5445 [hep-ph].

[257] A. Denner and G. Pelliccioli, *Polarized electroweak bosons in W^+W^- production at the LHC including NLO QCD effects*, JHEP **2020** (2020) 164, arXiv: 2006.14867 [hep-ph].

[258] LHCb Collaboration, *Measurement of the forward-backward asymmetry in $Z/\gamma^* \rightarrow \mu^+\mu^-$ decays and determination of the effective weak mixing angle*, JHEP **11** (2015) 190, arXiv: 1509.07645 [hep-ex].